UNIVERSITY OF SOUTHAMPTON

FACULTY OF ENGINEERING AND THE ENVIRONMENT

Engineering Sciences

Identification of Plastic Strain using Thermoelastic Stress Analysis

by

Geoffrey Howell

Thesis for the degree of Doctor of Philosophy

May 2017

ABSTRACT

UNIVERSITY OF SOUTHAMPTON

FACULTY OF ENGINEERING AND THE ENVIRONMENT

Engineering Materials

Thesis for the degree of Doctor of Philosophy

IDENTIFICATION OF PLASTIC STRAIN USING THERMOELASTIC STRESS ANALYSIS

By Geoffrey Peter Howell

Identification of regions containing plastic strain arising from the welding process is performed through the application of thermoelastic stress analysis (TSA) and finite element (FE) modelling. An approach is developed that removes the requirement to have a physical reference specimen for the component studied by developing a "synthetic reference bitmap" using finite element analysis. The regions containing plastic strain can be identified with TSA by collecting data from a 'reference' plastic strain free specimen from the TSA data and creating a resultant bitmap. Here, a synthetic bitmap is developed that mimics the thermoelastic response of a physical reference specimen. The approach is validated against physical reference specimens of different geometries and materials (AL2024 and 316L stainless steel) and is shown to accurately model the thermoelastic response. The newly developed synthetic bit map approach is applied to specimens containing welds and it is shown that the regions that contain plastic strain in the heat affected zone (HAZ) of a double bead welded 316L stainless steel specimen can be revealed. The predicted changes in thermoelastic response are compared to plastic strain predictions generated by thermomechanical modelling of the welded specimen and the distribution of plastic strain found by the TSA matches that given by the model.

The relationship between the change in thermoelastic response and plastic strain has been investigated and the results suggest there is a change in the thermoelastic response as a result of plastic straining. However, uncertainties in the data resulting from detector noise and other errors mean that further development of the experiments and the equipment is required to provide a conclusive and quantitative relationship.

It has also been demonstrated that TSA can be used outside of the laboratory in onsite trials in two coal fired power stations. Thermoelastic data was successfully recorded from pipe welds in-situ. To achieve this a new means of loading the pipes was devised based on vibration excitation, and the difficulties of performing surface measurements on heavily corroded pipes were overcome. The results from the onsite tests show that TSA can be used as an in-situ assessment technique and that is no longer restricted to being a laboratory based technique.

Table of Contents

List of Tables

List of Figures

DECLARATION OF AUTHORSHIP

I, Geoffrey Peter Howell, declare that this thesis and the work presented in it are my own and has been generated by me as the result of my own original research.

Identification of Plastic Strain using Thermoelastic Stress Analysis

I confirm that:

1. This work was done wholly or mainly while in candidature for a research degree at this University;
2. Where any part of this thesis has previously been submitted for a degree or any other qualification at this University or any other institution, this has been clearly stated;
3. Where I have consulted the published work of others, this is always clearly attributed;
4. Where I have quoted from the work of others, the source is always given. With the exception of such quotations, this thesis is entirely my own work;
5. I have acknowledged all main sources of help;
6. Where the thesis is based on work done by myself jointly with others, I have made clear exactly what was done by others and what I have contributed myself;
7. Part of this work has been published as: Please see List of Conference Papers

Signed: .....

Date: .....

LIST OF CONFERENCE PAPERS

[1] Howell, G., Dulieu-Barton, J.M., Achintha, M., Robinson, A.F., "A stress free model for residual stress assessment using thermoelastic stress analysis", *Proceedings of SPIE – The International Society for Optical Engineering,* 2015

[2] Howell, G., Dulieu-Barton, J.M., Achintha, M., *"Validation of a synthetic bitmap for the development of residual stress assessment using thermoelastic stress analysis", Conference: 10th International Conference on Advances in Experimental Mechanics,* 2015

Acknowledgements

I would like to thank my supervisors Professor Janice Dulieu-Barton and Dr Mithila Achintha for their support and advice throughout the PhD. I would also like to thank Andy, Duncan, Rachael, and James for an unending amount of questions.

I would like to recognise the financial support provided by Innovate UK who provided the funding for the RESIST project. Thanks are also due to the project partners who provided invaluable feedback and insight throughout the course of the PhD: Dr Philip Tyler (EPT), Professor Mike Smith (EPT [University of Manchester]), Dr Jerry Lord (formerly NPL), Dr Marcus Warwick (TWI), Dr Ruth Sanderson (TWI), Dr Sabrina Blackwell (formerly TWI), Dr Nicholas O'Meara (TWI), Dr Steve Bate (AMEC Foster Wheeler), and Professor Andy Morris (EDF).

To my fellow PhD students on the RESIST project, Elise and Vishnu, we'll all get there in the end!

Thanks go to my parents, for hours spent on the phone not understand a word coming out of my mouth but always willing to lend an ear when required, and to the rest of my family for all the support they provided in so many other ways.

Thanks go to my friends made during my PhD: Sami, Chloe, Theo, Andy, Duncan, Rachael, James, Elise, Vishnu. You've all helped so much, even if you haven't always known it. Sam, Emma, Jamie, and Ben thanks for all the support through this crazy endeavour. A special thanks to SUKDS, for providing a safe location where hitting things and letting go of tension go hand in hand!

Special thanks go to Sophie, for supporting me during these last 6 months of the PhD. When things were getting me down, you didn't let me give up or give in.

Thanks to you all!

Definitions and Abbreviations

e – Emissivity
C_p – Specific heat at constant pressure
E – Young's modulus
K – Thermoelastic constant
K_0 – Thermoelastic constant at 0% plastic strain
M_P – Melting point
T – Surface temperature
T_0 – Original surface temperature
$\dot{T}$ – Rate of change of temperature
ΔT – Change in temperature
$\frac{\Delta T}{T}$ – Thermoelastic response
α – Coefficient of thermal expansion
$\varepsilon_1, \varepsilon_2$ – Principal strain in the 1 and 2 directions
$\varepsilon_{p_{ij}}$ – Plastic strain invariant
ν – Poisson's ration
ρ – Density
$\sigma_1, \sigma_2, \sigma_3$ – Principal stress in the 1, 2, and 3 directions
$\sigma_x, \sigma_y, \sigma_z$ – Stress components in the x-, y-, z- directions as defined by the coordinate system within Abaqus
σ_m – Mean stress
σ_{kk} – First stress invariant

CAD – Computer aided design
CMM – Coordinate measuring machine
DIC – Digital image correlation
DL – Digital level
DSPI – Digital speckle pattern interferometry
EDM – Electro-discharge machining
EPT – Enabling process technologies
FE – Finite element
FEA – Finite element analysis
FFT – Fast Fourier transform
HAZ – Heat affected zone
IR – Infra red
LI – Lock in
MU-A – Mock-up A
MU-C – Mock-up C
NeT – European network on neutron techniques standardisation of structural integrity
NPL – National physical laboratories
PEEQ – Plastic strain equivalent
RESIST – Residual stress and structural integrity studies using thermography
RS – Residual stress
SCF – Stress concentration factor
SiC – Silicon carbide
TSA – Thermoelastic stress analysis

Chapter 1: Introduction

1.1 Background and Motivation

The purpose of the PhD is to develop a means of assessing the amount of plastic strain a component has experienced during a welding process using the thermoelastic stress analysis (TSA) technique [1]. The PhD is a part of a larger research project entitled "REsidual Stress and structural Integrity Studies using Thermography" (RESIST) funded through Innovate UK and partnered with TWI Ltd Cambridge, Enabling Process Technologies (EPT), AMEC Foster Wheeler, National Physical Laboratory (NPL), and EDF West Burton. The overall aim of the RESIST project is to develop a cheaper, quicker, more flexible method of residual stress assessment using the thermoelastic effect for use in an onsite capacity targeted at the energy production industry, but in general the work has applicability over a wide range of industries. The material used for the experiments in the PhD is 316L stainless steel, this was chosen for two reasons. The first is the nuclear industry focus of the RESIST project, 316L is used by the nuclear industry for pressure vessels and pipe work due to the creep resistance of 316L up to 600°C. Secondly, 316L is an austenitic steel, which is very ductile and can experience large amounts of plastic strain prior to failure. It also remains entirely in the austenitic phase despite the large temperature changes and rapid cooling experienced during welding.

During manufacturing, residual stresses can be caused in a variety of ways, the most common being, during forming and welding processes, and from surface treatments of the component [2]. In these processes, residual stresses arise from deformation and plastic straining of the material. The residual stresses generated during forming and welding processes are usually undesirable and can adversely affect the performance of a component so where possible an attempt to remove them through heat treatment is made. The stresses created during surface treatment are normally intentional as the surface treatment is chosen to result in a specific stress state, i.e. the opposite of the in-service stresses to counteract their effect.

If unevaluated and have nothing to counteract them, residual stresses can lead to early failure of components because the in-service stresses and residual stresses can combine to be greater than the yield stress of the material [3] and hence promote early failure particularly during fatigue loading. As plastic straining is a precursor to residual stress, it is proposed that TSA can be used to assess the amount of plastic strain a material has experienced and link this to the residual stresses. The overall outlook being a new means of determining the levels of residual stress in components caused by manufacturing processes, such as plastic forming and welding.

There are currently several methods for obtaining residual stresses by measuring strain release within a component such as hole drilling [4] and contour method [5] or identifying residual stress through the measurement of strain in relation to a reference specimen such as X-ray diffraction [3] and ultrasound [6]. Hole drilling and the contour method are either semi-destructive or destructive, can be time consuming, and can require the component to be removed from service and processed through a laboratory. In regions with high residual stress gradients, such as in the vicinity of a weld, the residual stress becomes more difficult to repeatedly and accurately measure using hole drilling [7]. X-ray diffraction and ultrasound, whilst non-destructive, are very time consuming and therefore expensive. When used with 316L stainless steel, X-ray diffraction produces large scatter in measurements taken close to the heat-affected zones around welds [8]. This is due to the relatively small grain sizes developed during the welding process. Depending on the source used in diffraction, the equipment required can be very expensive, as well as not being portable. Ultrasound is a non-destructive evaluation tool that is currently taken onsite to detect defects. Some work is being conducted on evaluating residual stresses, but this in largely in development and it is unable to separate the different stress components. Ultrasound also currently requires a period of off-site computation to be performed, so although a portable technique it is not a quick system of residual stress assessment. There is clearly an opportunity for a relatively inexpensive, quick, robust, full-field measurement system that allows the non-destructive evaluation of the plastic strain distribution in a component and hence a means of residual stress assessment, without the need to remove the component from service. Developing TSA firstly as a tool to obtain the plastic straining a component has undergone and thereby any residual stresses contained in the component is a very attractive proposition.

TSA [1] is a full-field, non-destructive stress analysis technique, which is based on the measurement of small temperature changes resulting from elastic loading. For a linear, isotropic, homogenous material, the temperature change is directly proportional to the change in the sum of the principal surface stresses.

$$\Delta T = -KT\Delta(\sigma_1 + \sigma_2) \tag{1-1}$$

where ΔT is the change in temperature resulting from the thermoelastic response, T is surface temperature, and K is the thermoelastic constant. $K = \frac{\alpha}{\rho C_p}$ where α, ρ, C_p are the coefficient of thermal expansion, density, and specific heat respectively. The loading is performed cyclically to ensure adiabatic conditions prevail; also ΔT is a very small quantity, so averaging over a number of loading cycles is required to aid in detecting it. Equation (1-1) gives a simple, linear relationship between ΔT (the thermoelastic response) and the change in stress. Inspection of equation (1-1) shows that there is no dependence on the mean stress of the applied cyclic load. This means any pre-existing (residual) stresses cannot be extracted

from TSA. However, in developing equation (1-1) certain assumptions were made, which if re-examined might provide a route for residual stress assessment.

In deriving equation (1-1), it was assumed that the elastic constants (Young's modulus and Poisson's ratio) were independent of temperature. TSA has previously been proposed [9] as a means for residual stress measurement based on the temperature dependence of the Young's modulus of materials, which generates a thermoelastic response from the mean stress rather than the stress change, known as the 'mean stress effect'. However, here the focus is on 316L stainless steel; it has been shown that steels in general [10] [11] and in particular stainless steel [12] show little dependence on the mean applied stress. Interestingly, in previous thermoelastic work [12] [13], it has been shown that steel components that have undergone plastic straining show a change in the thermoelastic response when compared to unstrained material. The conclusion was that the change in the response occurred as a result of a change in the thermoelastic constant, K, caused by the plastic straining. The primary purpose of the current PhD is to explore this further and establish if it is possible to assess the level of plastic strain experienced by a component using TSA.

The proposed approach differs from that described in [9], where the mean stress (or residual stress) is obtained directly from the thermoelastic response. However, this has only been demonstrated on simple uniaxial components where the applied stresses are known. Without a known uniaxial stress change, it is not possible to decouple the residual stress from the mean and applied stresses. In a general component, the mean stress will vary as well as the applied stress hence a very accurate residual stress/plastic strain free experimental or numerical model will be required to extract the residual stresses from the thermoelastic data. For the work in the present PhD such a model will also be required. By creating a stress/strain free reference specimen of identical geometry to that of the actual component under investigation it is possible to identify regions containing residual stress and plastic strain. The approach is not limited by the geometry of the component and the type of stress field developed as long as a reference dataset can be generated.

In [10], it was shown that regions in a component containing plastic strain could be identified using TSA in a mild steel EN1A component. A comparison between the thermoelastic response from a deformed component, i.e. having undergone plastic strain, to a component machined to the same shape as the deformed component and containing no plastic strain, i.e. the reference component, was made. It was shown that there was a clear difference in the thermoelastic response between the two components, which was attributed to the plastic straining. It is important to note that in [10], it was shown that the change in response was not due the mean stress effect and this opened the possibility of examining materials such as 316L stainless steel, where the elastic constants are not dependent enough on temperature.

The work in [10] forms the basis of the idea that to use TSA to identify regions where components have undergone plastic straining, it is necessary to manufacture a "reference component" of identical material and geometry to the component under investigation. By obtaining the response from the reference component and comparing this to the response from the actual component, the resultant thermoelastic response reveals the regions that contain plastic strain. However, for actual in service components such a reference component will not be available. Therefore, in the thesis a finite element approach is developed to produce a synthetic bitmap of the thermoelastic response to act as a 'reference specimen'. Subtracting the reference data in the synthetic bitmap from the experimental data containing plastic strain allows regions containing plastic strain to be identified. To construct the thermoelastic bitmap from the finite element model, a value of thermoelastic constant needs to be known. Here, the thermoelastic constant is experimentally derived for the material under investigation via the technique described in [14].

The difference in the thermoelastic response between the reference and the component under investigation is very small (6-10 mK [15]), and therefore is very sensitive to experimental conditions that might introduce uncertainty and bias into the recorded dataset. Potential sources of uncertainty including surface finish, application of the paint coating required for TSA, and heat treatment of the test specimens potentially modifying material properties are investigated in the thesis.

To quantify the amount of plastic straining a component has experienced, it is necessary to adopt a procedure, where the thermoelastic response of a known level of plastic strain is established. A key part of the thesis is devising techniques that calibrate the change in the thermoelastic constant against the known level of plastic straining. To study the effectiveness of the proposed technique, a welded mock-up has been developed which contains plastic strain in the heat-affected zone around a weld bead. The change in thermoelastic response of the 316L between two weld beads is compared to the plastic strain predictions of a thermo-mechanical model and a similar pattern of change in thermoelastic response and plastic strain distribution is observed.

A key part of the procedure is to be able to apply TSA on actual in-service components. The TSA equipment was taken onsite at two EDF coal-fired power stations and successfully set up on location. The procedure for obtaining the plastic strain distribution from the onsite tests was carried out; the initial proof of process that TSA can be carried out in a challenging onsite environment was a success with stress concentrations and potential welding defects identified.

1.2 Aims and Objectives

The aim of the PhD is to develop a hybrid method using TSA and finite element modelling to identify regions of plastic straining in a component and establish the level of plastic strain a component has experienced. This is achieved by using thermoelastic data and a synthetic, plastic strain free bitmap to identify regions containing plastic strain. Then, an approach is developed to assess if the amount of plastic strain experienced can be quantified. The hybrid method is being developed so that it can be used as an in-situ analysis tool.

To achieve the aim, the following objectives must be addressed

1. Establish a methodology that uses a synthetic bitmap of the thermoelastic response as a replacement for plastic strain-free reference specimens to identify regions of plastic strain.
2. Demonstrate the approach on a welded mock-up and show the approach is applicable to welded structures.
3. Define a procedure for establishing the relationship between the thermoelastic response and changes in plastic strain and evaluate the effects of material heat treatment on the response.
4. Establish the limitations of the technique within the current framework of detector sensitivity, paint coating application and surface finish, alongside other factors such as changes in material behaviour resulting from heat treatments.
5. Demonstrate that the TSA technique can be used away from the laboratory environment in an onsite application.

As the PhD is part of the RESIST project, it is interconnected with the other PhD projects and activities within the larger RESIST project. The development of the welded mock-up was performed in partnership with PhD student Elise Chevallier, a thermomechanical model was provided by Chevallier that predicted the strain induced by the welding and cutting processes. The industrial visits were a team effort, the role of the current PhD was to develop the calibration procedures and assess the effect of the paint coating and surface condition on the thermoelastic response. In Figure 1-1, the structure of the PhD is shown and how the objectives listed above interact with the other parts of RESIST project and build on one another.

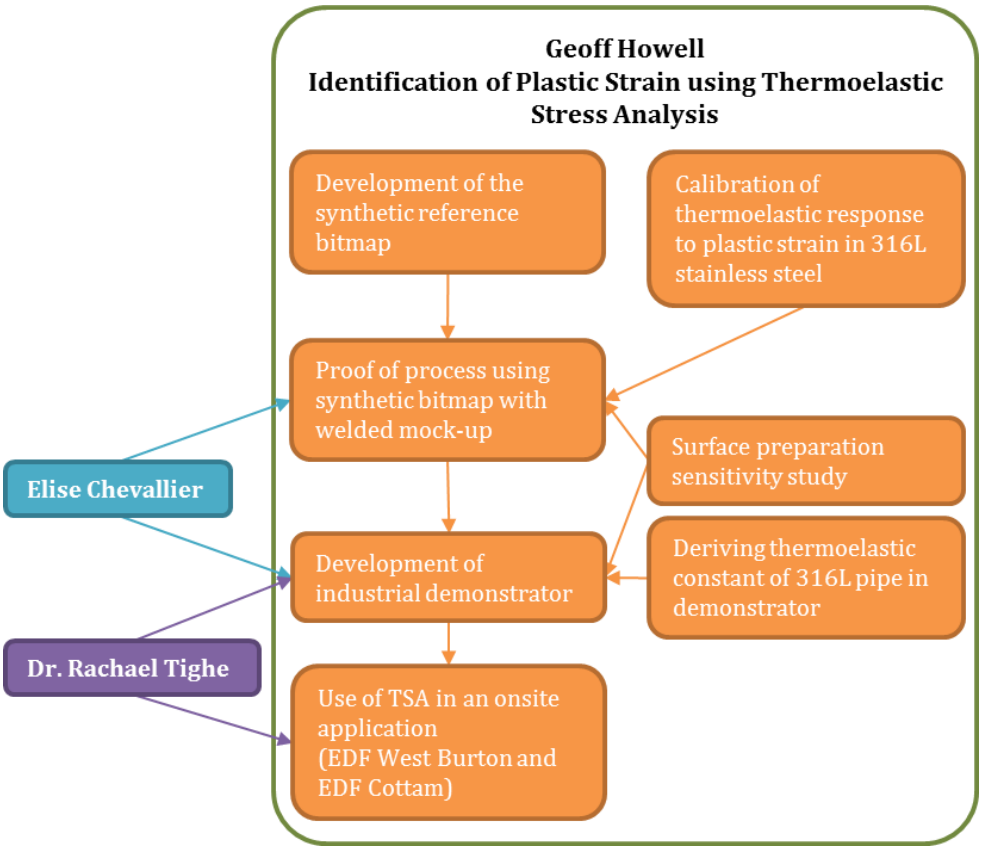

Figure 1-1 – Flowchart showing the subprojects of the PhD. Also shown are where work created by Elise Chevallier and Dr. Rachael Tighe has been contributed as part of the RESIST project.

1.3 Novelty

Previous work that extracted residual stresses using TSA were based on materials where the mean stress dependence of the response was strong [9] [15] [16]. In the present thesis, an approach is proposed that can be used on 316L stainless steel where the thermoelastic response shows no mean stress dependence [12] [13]. To successfully apply the approach to a general component, it is necessary to devise a synthetic reference specimen that is stress/strain free. This is done using a finite element (FE) model to simulate the sum of the principal stresses in a component, the results of which are manipulated by a Matlab programme specifically devised for this purpose. Thermoelastic data has not been simulated previously in this way for this purpose, so the development of the synthetic bitmap is one of the novel aspects of the work described in the thesis. The approach has application beyond that described in the thesis, and would be useful in identifying anomalies in the thermoelastic response such as localised plasticity, and nonlinearities caused by inhomogeneous material. The approach is demonstrated on a welded mock-up and regions are identified in the vicinity of the welds that provide a different thermoelastic response to that of the reference (both synthetic and physical). This is the first time such an approach has been taken on a welded

component representing a novel achievement, particularly considering that very little TSA work on welded components is reported in the literature.

The synthetic bitmap enables regions that have experienced plastic straining to be revealed but does not quantify the level of plastic strain a component has experienced. To extract the plastic strain values, a relationship between plastic strain and thermoelastic response must be established. Some preliminary work was carried out in [17]. These are further explored in the thesis and a new approach is developed to identify the relationship between the change in the thermoelastic response and the plastic straining. To this end, new specimens were designed that contain a strain gradient to quantify any variations in a single specimen. For the first time, the new specimens determine the sensitivity of the thermoelastic response to plastic strain. In the previous work, it has not been discussed why the thermoelastic response of a material might change with plastic straining, apart from saying the K value has changed. Here, each component of K is examined and a thorough review of the associated literature is provided in Chapter 2.

In previous work [18], an assessment of the effect of paint coating on the thermoelastic response was made. Here, a more detailed coverage of the effect of paint coatings on steel and stainless steel is carried out, examining a range of paints and paint coating thicknesses. The relative emissivity of each paint coating is established alongside its effect on the thermoelastic response. This is conducted alongside calibration exercises to obtain K from material with different surface texture and level of corrosion.

To demonstrate the industrial relevance of the technique, it was required to take the TSA equipment onsite and show it could be used outside of a controlled, laboratory setting. To this end, two visits to power stations were performed where TSA was used to assess pipes of various sizes and welds of different geometries (mostly T-section welds and mid-section welds joining two pipes together). This was a first for the technique, and generated usable data from which stress concentrations and potential weld defects could be quantified.

In summary, the novel aspects of the PhD are

- The creation and use of a residual-stress free, finite element model from which a synthetic bitmap of a reference thermoelastic response can be created.
- Combining this with data acquired through the use of TSA to find a map of the differences in thermoelastic response and comparing them to thermomechanical simulations of the welded mock-ups.
- Identification of the relationship between plastic strain and thermoelastic response.
- Using TSA onsite at power stations and recording data showing stress concentration around welds highlighting potential weld defects.

1.4 Structure of Thesis

In Chapter 2, a literature survey of the subjects relevant to this PhD is presented. These subjects are a background to residual stress, the current measurement techniques, and how residual stresses are formed in welds; and thermoelastic stress analysis, how it can be used to assess residual stress, and the current limitations of the technique. Also researched is the material changes that take place with plastic strain, specifically those in relation to the thermoelastic constant used in thermoelastic stress analysis.

The development of the synthetic bitmap is investigated in Chapter 3. A comprehensive study into the need for submodelling and the effects of 2D vs 3D modelling is carried out, before a validation of the synthetic bitmap approach against the thermoelastic response measured in a physical reference specimen made from AL2024 is carried out.

Chapter 4 investigates experimental variables and the attempts to control them. These variables include a deeper investigation into the effect of paint coating on the thermoelastic response, an investigation into different surface preparations for multiple test pieces, and an investigation into the boundary conditions within an experimental set up and defining a means to control them.

Chapter 5 develops the use of the synthetic bitmap through an investigation into the heat affected zones in a welded 316L stainless steel industrial mock-up. Here the work of Elise Chevallier is used to validate the approach by comparing the results TSA and synthetic bitmap approach to plastic strain predictions made from a thermomechanical model.

In Chapter 6, a study is carried out to investigate the relationship between plastic strain and changes in thermoelastic response. The work investigated the approach used in [17]; however, the complex shape and loading conditions of the test specimens used created problems with repeatability. Therefore, a refined geometry was developed that allowed the relationship between tensile plastic strain and changes in thermoelastic response to be investigated.

Finally, Chapter 7 describes the use of thermoelastic stress analysis for plastic strain assessment in a real-life industrial setting. Two visits to EDF power stations, where thermoelastic stress analysis was performed in-situ on real pipes, allowed data to be gathered that was later transformed into stress distribution maps around actual welded pipes.

Chapter 2: Current residual stress measurement techniques and progress in application of TSA to residual stress assessment: a review

2.1 Strategy

The purpose of the review is to set the scene and justify the motivation for devising a means of obtaining residual stresses with TSA as the basis. Therefore, in the following sections a brief description of the nature of residual stress is presented, alongside a description of the current methods for measuring residual stress, and also the theory and current state-of-the-art of TSA is presented.

The first section begins with a review of residual stresses, how they arise, and what they mean from an engineering perspective. The different techniques that can be used to evaluate residual stresses are reviewed; these are presented in two categories, destructive and non-destructive. The different advantages to each technique, as well as their limitations are reviewed, and the opportunity for a novel, quick, non-destructive technique using TSA is proposed.

The second section of the chapter briefly describes the background to TSA and focuses on the progress to date in using TSA for assessing residual stresses. The background section provides the basis for understanding TSA, by presenting the theory and the equipment required for TSA hence enabling the approach adopted in the thesis to be understood. To define the novelty of the work presented here, the progress in using TSA to obtain residual stresses and plastic strain is described in detail. After this, the effect plastic strain has on the thermoelastic response and the role this will have in the proposed assessment of plastic strain on the thermoelastic response is investigated.

2.2 Residual Stress

Residual stresses are the “locked-in” stresses found in nearly every manufactured component; they can be created through the forming processes and also during installation of the component. Residual stresses come from the build-up of a strain mismatch within the structure of a material, rather than in-service stresses which are caused by external forces

acting on the material. Residual stresses are most commonly developed during the following stages [2]:

1. Material manufacture; deformation of the material through rolling of metal ingots into sheets and plates, or differences in thermal expansion can cause residual stresses to be input.
2. Component manufacture; the deformation processes used during the production of a component (e.g. forging, rolling, cutting, etc.), or the heat treatments used during the later stages of component manufacture.
3. Surface treatment; post manufacturing processes used to provide a beneficial surface stress state to resist in-service stresses applied to a component.
4. Assembly or installation; mechanical fixation can deform components and embed stresses within the material of individual components, alternatively thermal processes (e.g. welding) can cause residual stresses through thermal gradients and differences in cooling rates.

Some residual stresses are useful from an engineering perspective, e.g. cold hole expansion embed compressive stresses that counteract the large tensile stresses generated around holes in component geometries, whilst others, usually unknown residual stresses, are detrimental and when combined with in-service stresses can lead to premature failure of a component. If the component contained a high level of compressive residual stress, then a much smaller applied compressive stress would be required to cause plastic deformation [3]; however, if the component was to be loaded with tensile stresses, the compressive residual stress would be a benefit as this would act to increase the amount of tensile stress the component could be loaded with before plastic deformation occurred. Therefore, it is important to know the distribution of residual stresses within components; if it is known then external forces can be applied to take advantage of beneficial stresses and to avoid over-stressing regions containing large amounts of residual stress. It is this principle that is exploited when finishing processes such as shot peening, laser peening, surface carburisation of steels and cold expansion are performed during the component manufacture [19]. The motivation behind these treatments is to create high, localised compressive stresses in regions that are predicted to see high tensile in-service stress to reduce the likelihood of crack growth and yielding of the material. Mechanical treatments that are used to induce favourable residual stress states include shot peening of surfaces to inhibit crack growth [19], strain-peening of springs [20], over-speeding of rotating discs whilst restricting their ability to deform [21], and autofrettaging of pressure vessels [22]. As well as mechanical treatments, there are many non-mechanical treatments including carburising, nitriding, and induction

hardening [23]; these exploit differences in material properties to produce beneficial stress fields in the local area.

Residual stresses have been categorised [3] by the length scale over which they act; in doing so, three types of residual stress were defined. Type 1 stresses act over very large distances and are known as macro-stresses. These are often induced through large scale deformation or through thermal processes such as heat treatments or welding. Type 2 stresses act at the scale of material grains and are known as intergranular stresses. These are due to dissimilar thermal, elastic or plastic properties of neighbouring grains, often due to different grain orientations. Type 3 stresses are those that occur due to coherency between strain fields at dislocations and interfaces. Type 2 and 3 stresses can be assumed negligible for component life assessment [3]; therefore, only residual macro-stresses are investigated in the present PhD (e.g. those generated by different heating and cooling rates found around welds).

2.2.1 Residual stress in welds

Many metal components in the energy industry are joined using a welding process. The introduction of large temperature differences, as well as additional materials, cause residual stresses within the component. It is important to study how the residual stresses are distributed within a weld zone because residual stresses in the region of welds can increase the likelihood of brittle fracture or fatigue cracking occurring [24]. The residual stresses in welds are caused by localised heating around the weld bead, and subsequent cooling [2]. As well as causing an uneven thermal gradient within the area around the weld (i.e. thermal mismatch), the heating of the material can cause phase changes within the surrounding material [25]. This difference in temperature causes a residual stress field to be established around the weld after cooling.

Figure 2-1 shows a cut through of a bead in notch weld. When welding occurs, there is a large thermal gradient between the weld metal, D, and the base metal, E. This thermal gradient causes the metal along the heat path to expand by different amounts dependent on the temperature reached by the metal. The differing amounts of expansion, and the constraint on the material by the bulk metal around the weld, causes plastic strain to be developed through the heat affected zone (HAZ), C. The difference in strain between the material in the HAZ and the material outside the HAZ causes a residual stress field to be developed in the welded component.

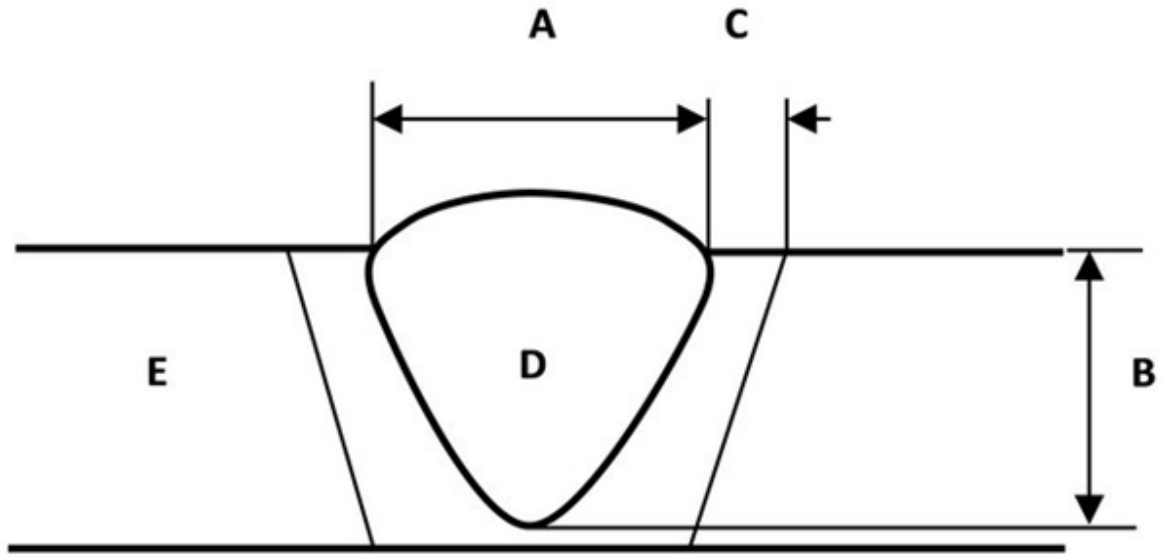

Figure 2-1 – Schematic of a simple weld bead shape. A: Bead width; B: Depth of penetration; C: Heat affected zone width; D: Weld metal; E: Base metal [26].

The previous sections have described various techniques for residual stress assessment, and some of these are capable of measuring the stress field around a weld bead. X-ray diffraction is capable of measuring the stress field around the weld bead, however, the phase change of the metal near to the weld bead can cause errors in the measurement since the diffractor requires a homogeneous crystal structure for measurements [25]. Of the destructive techniques, the hole drilling method is best used for investigating residual stresses around welds [3]. The hole drilling method allows the strain at different distances from the hole to be measured, and with incremental and deep hole drilling, a measure of the strain state through the thickness of the metal around the weld can be taken. From both of these approaches, the residual stress field around the weld can be calculated. However, both of these approaches provide single points of data and many such data points need to be taken to resolve the residual stress field around a weld. Using TSA provides the potential for much greater data density to be gathered in a shorter amount of time.

Finite element modelling of weld stresses

Finite element modelling is a very important tool used for predicting residual stress around welds. The thermomechanical modelling approach has been used to simulate the welding process and resultant stresses in many different studies [27] [28]. Through simulation of the changes in mechanical behaviour during welding, the residual stress can be calculated. To construct the model, a heat input profile needs to be created using thermocouple data gathered during manufacture and the input parameters of the welding torch [29]. The heat transference and material expansion it causes can then be modelled to provide the final predicted residual stress and plastic strain values.

A study from the members of the European network NeT compared different modelling approaches using different shapes of heat input and different hardening models [30]. The results of the study revealed that the most accurate predictions could be achieved using mixed isotropic-kinematic hardening models. In the round robin study conducted by NeT, and other studies, the predictions of the models were compared against a variety of residual stress measurement techniques including centre hole drilling, X-ray diffraction, and neutron diffraction [30] [31]. A key part of the RESIST project is the development, by Elise Chevallier, of a thermomechanical FE model of the range of welded mock-ups. The models provide reference datasets to compare with the experimental results gathered using the proposed TSA-based approach.

2.3 Residual stress measurement

2.3.1 Destructive techniques

Measuring residual stresses can be done through a variety of means. These can be divided into two general groups: destructive or non-destructive [3]. When choosing a residual stress assessment technique, it is important to consider which type (1, 2, or 3) of residual stress is being measured, how accessible the location is for the stress test to be performed, and whether the component can be removed from service or not (and if so, how long can the component be removed for).

In this section, the destructive methods for residual stress measurement are described. These methods usually involve the measurement of small geometric changes due to stress relaxation within the component. These geometric differences are typically discovered through material removal, which allows stress relaxation to occur and the residual stresses originally locked into the component can be calculated from a measured deformation that occurs during the relaxation process. The stress relaxation may only occur as a localised effect, so the amount of material removed is a key parameter for the destructive methods. The destructive methods are relatively inexpensive; however, they often require the component to be removed from service. The nature of these test methods means the component is damaged during the testing, sometimes to failure, so are not always suitable for testing components in-service.

Curvature method

For this method a thin layer of material from the surface of the specimen is removed, this allows residual stresses from surface coatings and surface layers of a component to be assessed [32]. The removal of material causes a deformation in the surface of the specimen as

the stresses are redistributed to maintain equilibrium within the specimen. The change in curvature can be measured via either contact (i.e. strain gauges [33]) or non-contact (i.e. video/image assessment [34]) methods. This change in curvature is then used to calculate the residual stress that existed between cut piece and the remaining, bulk material. This process is limited to only assessing the residual stresses within the surface of the component, and is usually performed on narrow strips (width/length < 0.2) so the effects of multiaxial curvature are avoided [32]. For stress depth profile measurements, incremental removal of layers can be performed; however, this can lead to the destruction of the component. Through the removal of the strip of material, extra strain from cutting can be induced into the cut surface resulting in a biased measurement of surface deformation [35].

Centre hole drilling

There are two hole drilling methodologies, incremental hole drilling that measures the residual stresses near the surface of a specimen, and deep hole drilling that measures the residual stress profile through the thickness of a specimen [3].

Incremental hole drilling

Incremental hole drilling is often used by both industry and in research settings. A hole is drilled into a component near the region of interest; as a result of the drilling, the stress state within the specimen relaxes to a new stable distribution. Through the measurement of the change in strain distribution local to the hole, the original residual stress state can be back calculated. The changes in strain can be measured using strain gauge rosettes, Digital Speckle Pattern Interferometry (DSPI) [4], or DIC techniques [36]. In small samples, this is a destructive technique, however, for a larger specimen, this can be considered as only a semi-destructive technique. The holes formed can either be ignored and left as they are, or can be back filled afterwards with filler material. For example, in the analysis of buildings, the incremental hole drilling technique is used to measure the residual stresses and compressive strength in concrete sections and steel supports [37]; the holes are filled afterwards with a sealing material to prevent corrosion damage.

Deep hole drilling

Deep hole drilling is used to assess the residual stress distribution throughout the thickness of a component. A hole is drilled through the component and its internal dimensions are accurately measured; afterwards, a trepanning tool is used to cut a larger core from the component containing the original hole. The residual stress will be relaxed in the new core, and the internal dimensions will change. Through comparison of the original dimensions of the hole against the new ones, the residual stresses that were within the material can be

calculated. This method has been improved through the use of water jets to reduce machining induced stresses [38]; however, if the residual stresses are greater than 50% of the yield stress, localised yielding can occur causing unreliable measurements [39].

Crack compliance

The crack compliance method [40] is similar in principle to the incremental hole drilling method since both techniques involve the removal of material over time. However, crack compliance utilises a small slot rather than a drilled hole. The strain relaxation around the slot is measured using strain gauges on the surface; by gradually increasing the depth of cut it is possible to resolve the stress field normal to the cut as a function of the depth [41]. Strain gauges provide an average strain value over the surface area of the wire grid; therefore, large strain gradients can be misrepresented by the gauges. This method generally results in the component being unsuitable for future use.

Contour method

The contour method [5] is a derivation of crack compliance. The specimen is sectioned, usually via Electro-Discharge Machining (EDM) [42], and the cut faces are carefully measured for deflections using a Coordinate Measuring Machine (CMM). The cut surfaces are modelled using the finite element (FE) method with displacement boundary conditions applied to force the free surfaces back into their original, pre-cut shape [43]. The stresses that result from this deformation procedure are equal but opposite to the residual stresses within the original component before sectioning took place. The technique allows the residual stress map to be constructed from the FE model; however, there are certain assumptions that have to be made in order to obtain the residual stress. For instance, the cut through the material will invariably result in some form of material removal and localised plastic deformation of the specimen. This is very difficult to measure in practice, so an assumption that the displacement in the cut plane is solely due to stress relaxation is made. Also, only the residual stress normal to the cut can be calculated, therefore multiple cuts will be required to model all stress components. The contour method is a wholly destructive technique that is mostly used in lab studies rather than with industrial components.

2.3.2 Non-destructive techniques

Non-destructive techniques measure the residual stresses without affecting the stress distribution through removal of material [3]. They tend to be more expensive than the destructive techniques already described, but they leave the components intact for future use. The diffraction methods are generally difficult to use in-situ as the equipment required is usually not portable, although a new X-ray diffraction system has been developed in the last

few years that allows for in-situ analysis. Diffraction techniques can only resolve surface or near surface residual stresses. For residual stresses through the thickness of a component, ultrasound techniques can be used. For the most part these techniques are non-contact and measure the residual stress distribution by comparing the measured results against a known value from a stress free reference sample.

Diffraction methods

Laboratory X-ray diffraction

Diffraction techniques can be split into three groups based on the method of residual stress detection: neutron diffraction [44], high-energy synchrotron X-ray diffraction [44], and lower energy X-ray diffraction [45]. In the diffraction method, strains within the structure of the material are measured using the crystal structure, see Figure 2-2, and from the strain the residual stresses can be calculated. The X-rays impinge on the specimen and both the incident beam and the backscatter results are captured on a photographic plate. The intensity and approach angle of the scattered beams are compared back to the incident beam angle to gauge diffraction based upon the crystal structure.

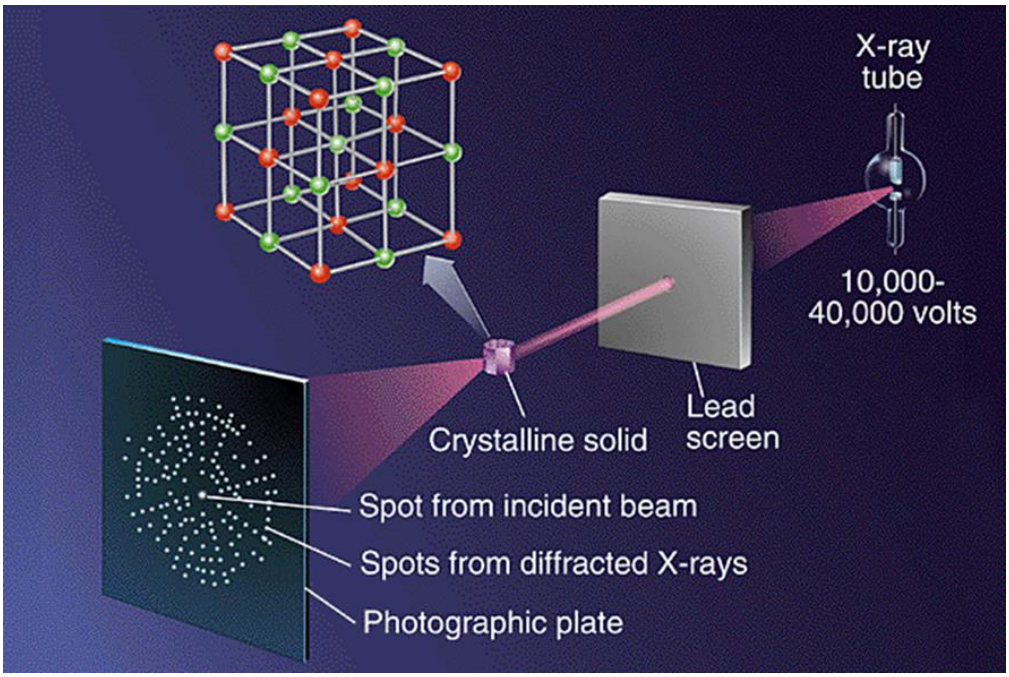

Figure 2-2 – A diagram of the basic principle behind X-ray diffraction [46].

There are two general methods for calculating residual stress through X-ray diffraction: the $sin^2\psi$ method that can be applied to neutron, synchrotron X-ray sources, as well as laboratory X-ray sources [47]; and the $\cos\alpha$ method [48] see Figure 2-3. This method is an improvement over the $sin^2\psi$ method because it is capable of measuring the elastic strains

held in the lattice structure from a single position, reducing the measurement time to around 90 seconds [49], see Figure 2-3.

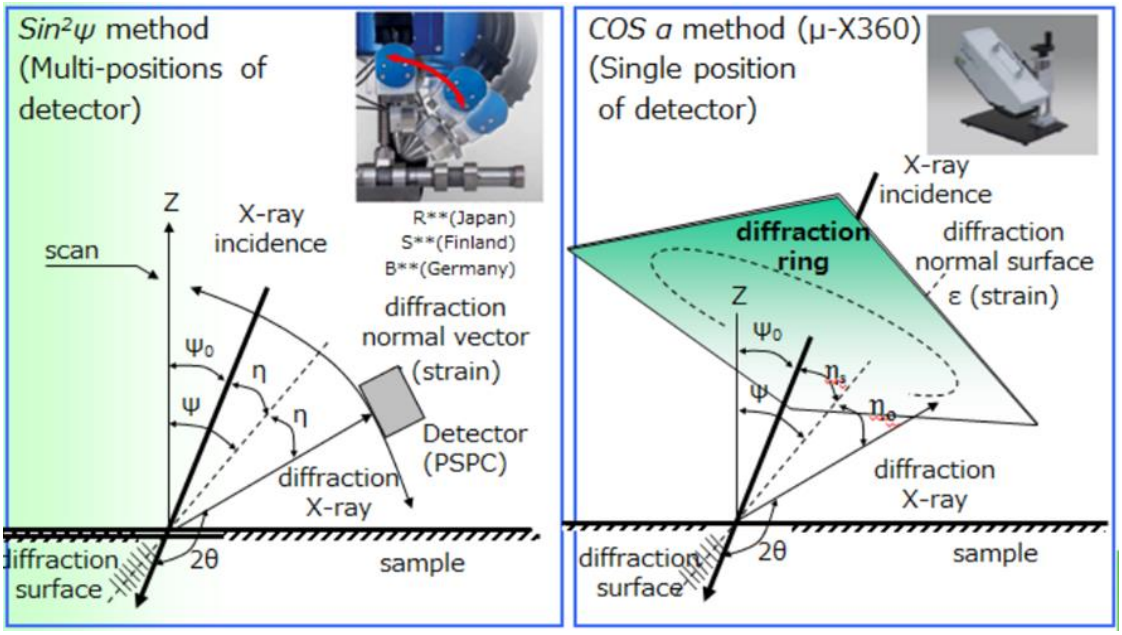

Figure 2-3 – A comparison of the *sin²ψ* method and the *cos α* X-ray diffraction techniques. The cos *α* technique allows a static x-ray source, thereby greatly reducing the space required to measure residual stress [48].

Synchrotron X-ray diffraction

Synchrotron X-ray diffraction is a very powerful X-ray diffraction technique and can penetrate to much greater depths (up to 7 mm in iron compared to 0.004 mm for laboratory generated X-ray diffraction [50]); however, this comes at the expense of scattering angle and spatial resolution. Synchrotron diffraction is also significantly more expensive, and only a few facilities globally are able to provide synchrotron capabilities so using this technique as part of a maintenance strategy is not practical.

Neutron diffraction

Neutron diffraction is very similar in process to X-ray diffraction with the key difference that the neutrons diffract due to interaction with the nucleus of atoms rather than the electron cloud. This allows deeper penetration of metal structures and also lower absorption rates of the incident beam by the material under investigation. To generate the neutrons a nuclear reactor is required, this limits the technique to being an offsite method so components for investigation have to be removed from service for a considerable length of time. It also requires a relatively large crystal size that is challenging to create and may not be present in the component being analysed.

Neutron diffraction and $sin^2\psi$ X-ray diffraction are both expensive methods of residual stress measurement, neutrons because of the reactor required to generate them, and $sin^2\psi$ X-ray diffraction because of the long scan time required to take repeat measurements increasing labour costs of the technique. The $\cos\alpha$ approach is a much quicker method for taking X-ray diffraction measurements. Diffraction methods allow for non-destructive residual stress measurements of crystalline materials; however, they are time consuming processes because only single points of discrete data are measured each time [51] so a scan of many points of the surface is required. Using TSA has the potential to provide full-field data across an entire surface with a single measurement.

Ultrasound

When a material is stressed there is a change in ultrasonic speed [52]; this change is a result of the stress averaged over the path of the sound wave. This method measures the large macroscopic stresses in the bulk of the material. Ultrasonic waves have their speed varied due to microstructural changes in metals; these can be caused by residual stress [53] [54]. Using different frequencies of ultrasonic probe it is possible to investigate the residual stress fields at different depths through a material [55]. However, only the residual stresses longitudinal to the direction of the wave between the ultrasonic source and the receiver can be determined. A series of tests are required to build a full-field stress distribution within a component, with the associated increase in the time taken for the inspection.

2.3.3 Summary of residual stress measurement techniques

The destructive techniques described in 2.3.1 rely on the removal of material, or the sectioning of the specimen, in order to make a measurement. The curvature method, hole drilling, and crack compliance are all similar in that they measure the surface strain relaxation around an area of material removal. This strain measurement can then be used to back calculate the residual stress before the cut was made. These strains can be gathered through either contact methods (e.g. strain gauges) or non-contact methods (e.g. DIC). The contour method requires the sectioning of the specimen to measure the stress field parallel to the surface through the thickness of the specimen. The contour method only allows the measurement of the residual stress component perpendicular to the cross section [43]; there is no further calculation step as the residual stresses can be calculated directly from the FE model. The assumptions used to create the FE model need to be fully understood to provide the limitations of the contour method.

The techniques described in 2.3.2 can be placed into two broad categories, diffraction methods and ultrasound. X-ray diffraction is currently the best non-destructive surface

residual stress assessment technique. There is no requirement for the large, expensive energy sources neutron and synchrotron X-ray diffraction require, and it is a well understood technique that is able to discern multi-axial stress states within the material unlike ultrasound analysis. However, X-ray diffraction still suffers from a major disadvantage, it requires the component be removed from service and taken to a laboratory for testing. This results in considerable down time for the equipment and components under investigation. The $sin^2\psi$ method requires a large amount of time to evaluate residual stress. The newer system, utilising the $\cos\alpha$ method, will result in measurement times of only 90 seconds; however, there are yet to be published trials where this new system has been used onsite. Ultrasound is a technique mostly used to inspect pipework for defects rather than residual stresses. Only residual stress fields longitudinal to the direction of travel of the sound waves can be investigated by ultrasound, therefore multiple measurements are required to establish the full stress field within a specimen.

None of the current experimental methods are particularly suitable for the post weld assessment of residual stresses around welds, or residual stress assessment in general, so a new method needs to be investigated. It is proposed that thermoelastic stress analysis can be used to investigate plastic strain, with the intention that the residual stress can be calculated from the plastic strain field in the future. Since the technique is non-contact, it does not lead to the destruction of the component. It also utilises the surface thermal emissions of the material, eliminating a measurement error seen in X-ray diffraction results coming from changes in orientation of the crystal structure. It is proposed, that through comparing the thermoelastic response of a component to the thermoelastic response of a plastic strain free reference specimen, an assessment of the plastic strain distribution can be carried out. The technique is then further developed to remove the physical reference specimen, and develop a computer generated synthetic bitmap of the reference thermoelastic response instead. The results will be compared to predictions of plastic strain calculated from thermomechanical finite element models of the welding process developed by Elise Chevallier.

2.4 Thermoelastic Stress Analysis

TSA [1] is a stress analysis technique which utilises infra-red (IR) thermography. John Gough first observed the principle which forms the basis of what is now called the thermoelastic effect in the early 19th century [56]. Then in the 1850s, Lord Kelvin established the foundation theory of thermoelasticity [57]. It was not until the 1980s, due to the advent of IR detectors, that the change in temperature of a specimen, ΔT, could be measured. With this capability the development of TSA as a non-contact, full-field stress analysis technique was possible. TSA is based upon the small changes in temperature that arise due to a material

being subjected to a change in elastic strain; this is generally referred to as the thermoelastic effect.

When a specimen in placed under cyclic loading conditions, the change in strain creates a cyclic variation in temperature. This temperature change, ΔT (known as the thermoelastic response) can be related to the change in the first stress invariant, $\Delta(\sigma_1 + \sigma_2 + \sigma_3)$, i.e. the sum of the principal stresses [1]. In actuality only $\Delta(\sigma_1 + \sigma_2)$ is used because the IR detector only detects in plane changes in temperature so only the change in the in plane stresses can be assessed, i.e. at the surface $\Delta\sigma_3 = 0$. This limits TSA to being a surface technique only; it is not able to measure changes through the thickness of the material. An IR detector is used to measure the change in temperature, and from this the stresses, $\Delta(\sigma_1 + \sigma_2)$, can be calculated using the relationship given in equation (1-1) [1].

Equation (1.1) is valid for linear, elastic, isotropic, homogenous materials where the temperature change has taken place under adiabatic conditions [1]. The equation cannot be used directly for residual stress assessment, however, residual stress causes a change in plastic strain and a change in plastic strain causes a measurable change in the thermoelastic constant [13]. Therefore, through comparison of the thermoelastic response from a specimen with an unknown level of residual stress against a residual stress free reference thermoelastic response it will be possible to obtain the difference in thermoelastic response. Using the difference in thermoelastic response it should be possible to calculate a value of plastic strain and the residual stress causing that plastic strain can be back calculated; thereby allowing an assessment of the residual stress from the thermoelastic response.

In 1988, Wong et al. [11] proposed that the general theory stated in equation (1-1) be reviewed to include 2nd order effects due to temperature dependence of the elastic properties and resulted in the following:

$$\dot{T} = \frac{T_0}{\rho C_p}\left[-\left(\alpha + \left(\frac{\nu}{E^2}\frac{\partial E}{\partial T} - \frac{1}{E}\frac{\partial \nu}{\partial T}\right)\sigma_{kk}\right)\dot{\sigma}_{kk} + \left(\frac{(1+\nu)}{E^2}\frac{\partial E}{\partial T} - \frac{1}{E}\frac{\partial \nu}{\partial T}\right)\sigma_{ij}\dot{\sigma}_{ij}\right] \qquad (2\text{-}1)$$

where $\dot{T}$ is the rate of change of temperature, E is Young's modulus of the material, ν is Poisson's ratio, and σ_{kk} is the first stress invariant. Equation (2-1) is known as the 'revised higher order theory'. To utilise (2-1) for residual stress analysis, it is necessary to establish a case of pure uniaxial loading (where $\sigma_{11} = \sigma_{kk}$ and $\sigma_{22} = \sigma_{33} = \sigma_{12} = \sigma_{13} = \sigma_{23} = 0$). This assumption causes (2-1) to be reduced to:

$$\dot{T} = \frac{T_0}{\rho C_p}\left[\left(\alpha - \frac{1}{E^2}\frac{\partial E}{\partial T}\sigma_{11}\right)\dot{\sigma}_{11}\right] \qquad (2\text{-}2)$$

which shows the rate of change of temperature is a function of the applied stress and the rate of change of applied stress. For TSA, σ_{11} could be considered a mean stress, and through integration of equation (2-2), from the initial state to the final state, the relationship between change in temperature and change in applied stress can be described:

$$\Delta T = \frac{T_0}{\rho C_p}\left[\left(\alpha - \frac{1}{E^2}\frac{\partial E}{\partial T}\sigma_m\right)\Delta\sigma_{11}\right] \tag{2-3}$$

(2-3) shows that the temperature response is dependent on both the applied stress and the mean stress. Since a residual stress would change the mean stress, it would also change the thermoelastic response.

A validation of the revised thermoelastic equation was completed by comparing the thermoelastic signal of two uniaxially loaded aluminium specimens [9]. One specimen was a simple bar specimen, the other was manufactured into a curve and then straightened to create a specimen of the same geometry, but one which contained residual stress. Thermoelastic data was taken from both specimens and showed there was a difference between the specimens. Strain gauges were used to map the areas of compressive and tensile stress in the straightened specimen. Comparing the difference in thermoelastic response and the strain gauge data allowed the change to be attributed to the residual stress driving the difference.

Further studies confirmed that it was possible to measure the mean stress effect in aluminium (2024), steel (4340), and titanium (Ti-6Al-4V) [58]. Values of mean stress dependence were reported as $\frac{\partial K}{\partial \sigma_m}\frac{1}{K} = 0.31, 0.11, \text{and } 0.45\ \text{GPa}^{-1}$ for each metal. Further work carried out in [12] [59] [60] showed there was a significant mean stress dependence in titanium alloys, nickel alloys (Inconel 718), TIMETAL, and nickel-titanium alloys. The work of [12] also showed that the mean stress in stainless steel was negligible. Therefore, a different approach is required to investigate stainless steels, which leads to devising the approach investigated in this PhD.

2.4.1 Infra-red system and typical experimental procedure

The IR system used in the PhD project was manufactured by FLIR and comprises three parts: the IR camera (including, the detector, lenses and analogue to digital converter), a computer system for data processing, and two software packages, Altair and Altair LI (Lock In). Altair is used for the detector control, and also the capture and viewing of the thermal data via the IR detector, whilst Altair LI is used to process the captured video files into a set of three collated image files, the surface temperature data averaged across the loading cycle (T), the change in

temperature averaged across the loading cycle (ΔT), and the time-phase of the thermal cycle to the loading cycle.

The IR camera used is the FLIR Silver 480M model, see Figure 2-4; it has two over-laid 320 x 256 element Indium Antimonide (InSb) detector arrays that are cooled internally using a Stirling engine, and two internal buffer arrays so that sequential storage from each detector is possible. This setup allows high frame rates to be recorded through the overlaying of the two detector arrays, up to 383 frames per second at full viewing window size. The system has a lock-in signal feed, coming from an analogue output on the servo-hydraulic test machine, which allows the software to average the data captured at the loading frequency only and to remove the data taken at all other points in time. This is necessary for TSA to be performed as only the change in temperature caused by a change in stress is to be recorded and used; this also reduces the noise in the data significantly.

For the system to gather enough thermal information a suitable integration time needs to be set in the software. This is equivalent to how quickly the shutter in a traditional camera opens and shuts. Having a small integration time, so having a shorter time period when data is being captured, reduces the effect of motion in the data collected; however, this reduces the amount of photons gathered by each pixel each time it is recording. When performing TSA on a stiff material (316L) these is very little motion of the specimen, <0.1 pixel movement between maximum load and minimum load, therefore, the integration time can be greater to allow a larger amount of data to be gathered.

Each element on the detector measures a voltage, this is converted into a digital signal by an internal processor; the output from the camera is an uncalibrated signal known as digital level, *DL*. On the computer, there are various calibration files stored for different temperature ranges, lens configurations, and integration times. Altair uses these to convert the *DL* data into temperature data for initial presentation. Altair LI then processes through the video file to extract three outputs: mean temperature data file, temperate magnitude data file, and the signal phase data file. These data files can then be exported to a third-party software package for data processing, e.g. Excel or Matlab.

During the setup of the experiment, it is necessary to perform a non-uniformity correction; this corrects for irregularities between pixels across the arrays. It is also possible that errors may come into the measurement due to the thermal reflection of the detector itself being visible in the images. Through the experimental set up (e.g. without the IR camera in the reflective path and specimen's surface preparation) thermal reflections can be prevented.

TSA provides a measure of the surface response under loading, and it is sensitive to the surface conditions of the specimen. For metals, it is required that the surface has a thin layer

of matt black paint applied to decrease reflectivity and increase thermal emissivity, see Figure 2-4. The paint layer needs to be thin, to prevent thermal lag but thick enough to prevent reflections from the metal surface being recorded as part of the TSA data. It also requires good contact to the substrate to allow an accurate transfer of the thermal response to the surface of the paint. The paint should have a high, consistent emissivity and a non-reflective finish. These conditions were all defined in [18]. The paint also needs to be uniform across the area being investigated; otherwise there will be differences in transit time of the thermal response from the substrate surface to the paint surface [18]. This will result in a thermal "lag" across the surface of the specimen and the ΔT could not be equated to $\Delta(\sigma_1 + \sigma_2)$ because the thermal response would be out of phase with the loading cycle. To further reduce the effect of reflections from external sources of IR radiation, a heavy black curtain is hung around the test machine and the IR camera. This prevents heat sources from the surroundings being correlated into the response from the specimen as unwanted reflections.

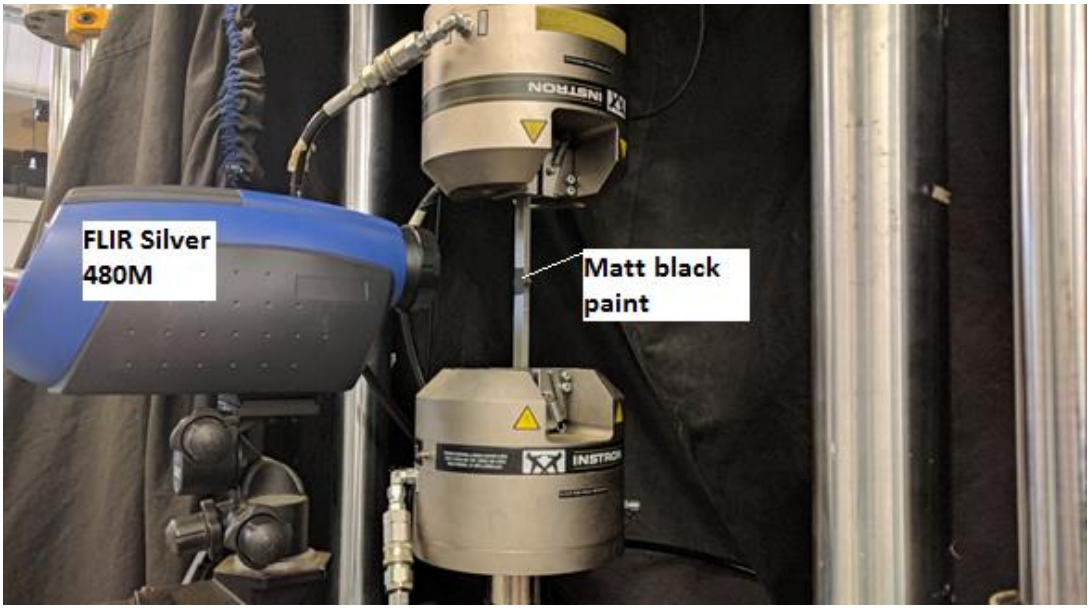

Figure 2-4 – A typical thermoelastic stress analysis setup. The IR detector is positioned in front of a specimen prepared with matt black paint applied to the region of interest.

Robinson et al. [18] performed a study into paint coatings, with both the type of paint and the thickness of the paint being investigated. The study looked into paints from Hammerite, Plasti-kote, and RS Components and found that RS matt black aerosol paint provided the most accurate and consistent thermoelastic response. Paint thickness was investigated in number of hand sprayed passes, from 1 to 6 passes. Results showed that 2 or 3 passes provided the ideal thermal response at a range of loading frequencies from 2.5 to 35 Hz. These pass numbers were measured using a paint thickness gauge and showed that the ideal thickness

was a 15 to 25 μm layer to provide a uniform and high emissivity. In [13] no attempt was made to evaluate the emissivity of the paint or the effect of surface condition. As the measurements sought in the present work require the measurement of very small changes this effect of the paint and the surface requires further evaluation.

The thermoelastic constant, K, in equation (1-1) can be obtained experimentally by cyclically loading specimens with a known applied stress and obtaining the thermoelastic response, $\frac{\Delta T}{T}$ experimentally [14] [15] [17]. By dividing $\frac{\Delta T}{T}$ by the applied stress, the thermoelastic constant can be calculated. A theoretical estimate of the thermoelastic constant for a material can be calculated from literature material values of α, ρ, and C_p. An experimental calibration allows a specimen specific evaluation of the thermoelastic constant to be made.

As a cyclic loading is required for TSA, there is the potential for relative motion to occur between the stationary IR camera and the moving test specimen. To reduce the effect of relative motion, a 'motion compensation' procedure can be followed. Two main approaches exist to provide motion compensation, the first calculates a global displacement vector frame-by-frame and applies this to each image taken by the IR camera [61]. The motion compensation is performed using proprietary software called 'Random Motion' in the Altair toolbox, supplied with the IR camera system. It functions by having the user position two 'markers' on the surface of the specimen, these must provide a strong contrast to the thermal image. After identifying the markers, the software tracks the position through every frame to calculate the translation, rotation, and deformation vectors. The software then applies the calculated vectors to every frame such that it appears that the test specimen is unmoving. It is possible that noise can be introduced via this method due to interpolation of subpixel motion. The second approach uses DIC data to provide the change in the displacement field frame-by-frame so localised motion can be reduced [62] [63] [64]. The displacement vector for every pixel in the DIC data is calculated. The TSA and DIC images are then image matched, and the closest four displacements to each pixel in the TSA data are combined using a bilinear interpolation, see Figure 2-5. This process creates a single vector to move the TSA pixel from frame to frame. The advantage over the first motion compensation technique is that it increases the accuracy of the motion compensation for complex, bidirectional loading. It also allows better resolution and motion tracking when there are sharp gradients or discontinuities in the displacement field. However, it is a very time and resource intensive approach and the careful set up requirements means it would not be feasible to use this technique in-situ as it currently is. The expected movement of pipes when the proposed plastic strain assessment approach is used onsite are large body movements with low gradients in the displacement field within each frame. Therefore, the first approach using

whole image vector displacements to correct for motion is the only alternative until the DIC approach can be combined in an efficient manner with the TSA.

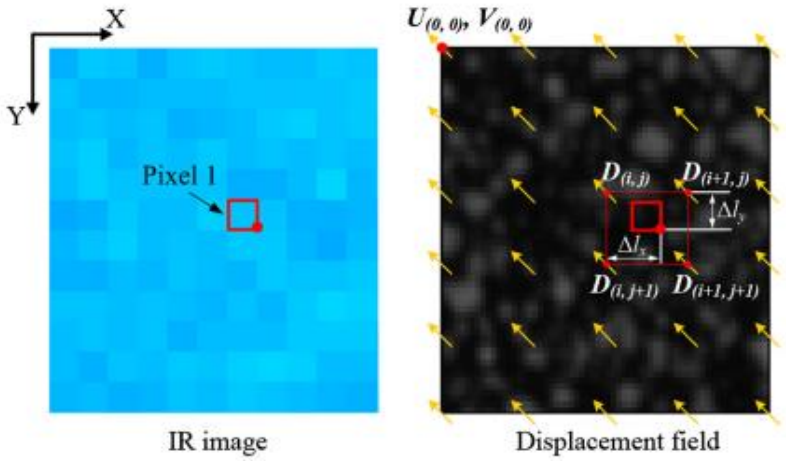

Figure 2-5 – A typical thermal image and the corresponding displacement field. The four vectors on the corners of the large red box in the displacement field are interpolated to provide the singe vector shift of the IR pixel (the smaller red box) [62].

With the decreasing cost of IR cameras, TSA is becoming a more widely used structural and material assessment tool. It has been used to examine cold expanded holes in aluminium plates [15], and to detect locations containing damage in structural components [65]. TSA has also been used in full-scale fatigue tests of aircraft structures, due to the full-field nature of the technique it is capable of showing stress concentrations at multiple points in a welded or riveted structure at once [66]. The present work is based on a small change in the thermoelastic constant caused by plastic straining of a material and an approach for obtaining the change in the thermoelastic constant resulting from the plastic straining must be devised. The effect of plastic strain of the material on the thermoelastic response is described in the next section.

2.5 Evaluation of the effect of plastic straining on the thermoelastic response

It was shown [10] that when plastic deformation is introduced, the thermoelastic constant is modified in steel, aluminium alloy, and EN1A mild steel. Specimens of each material were plastically yielded to between 1% and 8% strain. When plotting the K/K_0 against plastic strain the steel specimens were found to have a linear increase in K with plastic strain (~9% change in K when a plastic strain value of 8%). From this, it was suggested that the change in thermoelastic constant could be used to estimate the level of plastic strain within a

component. Since plastic straining can cause residual stress, it is considered that the residual stress within a component could be derived using TSA. It was shown by Rosenholtz et al. [67] that when steel specimens were exposed to compressive stress beyond the yield point there was a change in the coefficient of linear thermal expansion, α. The results showed that up to yield there is a small (~1%) increase in α and it is suggested that this effect is produced by the plastic deformation of a small number of steel crystals whilst the majority behave elastically. After yield, a very large increase in α was reported (~22%). When the specimen was unloaded the increase in α was still evident and of a similar magnitude to that of the loaded specimen. Work in [68] also showed there was a non-linear relationship between applied stress and the expansion coefficient beyond the yield point of the 1020 steel investigated. When plasticity has occurred, the expansion coefficient increases. In both [67] and [68], the change in α was a positive change when in both compression and tension. During the compression tests on mild steel in [67] there was a 22% increase in α whilst in [68] there was only a 5% increase in α observed during the tensile tests.

A further investigation into the literature has revealed the likely cause of the change in the thermoelastic constant, K. A caveat is that these changes have not been experimentally confirmed within the current PhD, and further investigations into these proposed changes of the material properties is recommended. The thermoelastic constant is calculated from three different components, the coefficient of thermal expansion, specific heat, and density. Density has been shown by other members of the RESIST consortium to be a constant at different plastic strain levels, and can therefore be discounted from further discussion. Figure 2-6 contains density values for two different set of 316L stainless steel specimens. The first set, “Large Dumbell specs”, are samples cut from a series of 316L stainless steel test specimens used in [17]. There is no discernible difference in density between test samples taken from specimens containing -10%, 0%, and +10% plastic strain. The second set, “Axisymmetric compression specs” are samples cut from the 316L stainless steel used in the current PhD. The uncertainty within the data cannot be plotted as it is unknown to the author so an assessment of the impact the difference in density has cannot be made; although there is a difference of 0.5% in density reading between the two sets of readings.

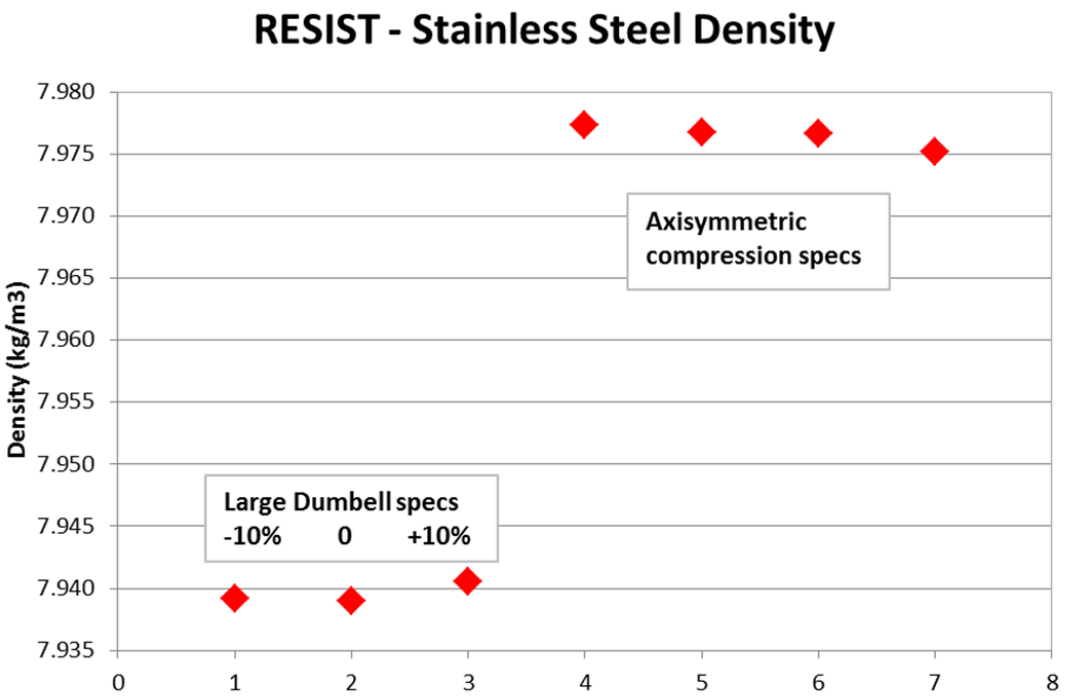

Figure 2-6 – Plot showing no relationship between plastic strain and density [69].

Following an extensive search of the literature, on the dependence of specific heat with plastic strain and temperature, there is no reference to the effect of plastic straining on specific heat and every source found agrees with [70] that at temperatures above cryogenic temperatures metals in general have a constant specific heat. The experiments described in the thesis were performed at room temperature, so specific heat can be considered a constant. Therefore, for a change in the thermoelastic constant to exist there must be a change in the coefficient of thermal expansion. In metals, the coefficient of thermal expansion can be described using the following relationship [71] :

$$\alpha = \frac{0.020}{M_p} \tag{2.2}$$

where M_p is the melting point of the solid form of the metal in degrees K [71].

If the melting point of the metal can be made to decrease there will be a corresponding increase in the coefficient of thermal expansion to maintain equilibrium. In a metal, deformations and strains can occur at the atomic level just as larger, macro-scale structures do. A change in the atomic distance within the crystalline structure away from equilibrium results in an increase in internal energy [72]. Therefore, the following causal relationship can be established: a change in engineering plastic strain causes an change in strain in the atomic spacing of the crystalline structure; the displacement of the atoms in the crystalline structure causes an increase in internal energy, and a decrease in the melting point of the metal; a

decrease in the melting point creates an increase in the coefficient of thermal expansion; and an increase in the coefficient of thermal expansion creates an increase in the value of thermoelastic constant.

An experiment to test for a change in the thermoelastic constant due to plastic deformation can be conducted by loading a specimen in uniaxial tensile loading. By taking the specimen material past its elastic limit, plastic deformation will be created; however, complete elastic relaxation will occur so there will be no residual stress within the specimen; any change in the thermoelastic response must purely be due to a change in a material property. Experiments in [10] used four steel (the grade of steel was not provided) specimens, one unstrained specimen and three plastically strained to 5%, 6%, and 8% tensile strain. The thermoelastic constant increased from 2.93 x 10^{-6} MPa^{-1} in the unstrained specimen to 3.19 x 10^{-6} MPa^{-1} in the 8% strain specimen. This change in thermoelastic constant, whilst small, was repeatable and also varied linearly with plastic strain. Further work was performed on curved bar specimens, one machined to a curved shape and stress relieved, the other machined straight and deformed to shape [13]. The thermoelastic response was measured across a section at the centre of the curve. Whilst the machined bar shows good correlation with the theoretical predictions, in the deformed bar there are significant deviations from that predicted from the thermoelastic equation. This departure was much larger in the compressive residual stress region, correlating with the observations in [68] that the change in is more significant in the compressive strain region than in the tensile region. [17] investigated the effect plastic strain had on the thermoelastic response of 316L stainless steel. Large 3D dogbone specimens were manufactured that could be deformed to contain high levels of either compressive or tensile plastic strain. A range of strain levels were investigated, from -10% to +15% plastic strain, and for each specimen the thermoelastic constant was calculated. When normalised against the thermoelastic constant of a unstrained reference specimen a linear relationship between tensile plastic strain and change in thermoelastic constant was observed. The observed change in thermoelastic constant is what led to the development of the approach described in the current PhD.

2.6 Novelty and definition of research questions

In the review it is clearly shown that there is a need for new approach to residual stress assessment and that TSA may be a means for achieving a non-contact, robust and portable means for residual stress assessment. The review has shown that TSA is a well-established technique and the methodology has been explained. Aspects such as the effects of paint coating have been explained and it is clear this affects the thermoelastic response. There is a

need to establish the effects of the surface of the material on the response and a means of establishing the surface emissivity, which are discussed in Chapter 4 of the thesis.

There are many examples of using TSA in conjunction with FEA as described above. However, none of them used FEA to provide a reference dataset for analysis purposes; they only used the FEA to confirm collected data was accurate. The approach laid out in Chapter 3 of the thesis, the development of a synthetic bitmap, is a completely new way of using FEA to provide data for analysis using TSA and establishes if it is possible to create an accurate FE model of the expected thermoelastic response from a structure.

In the current project, the difference in thermoelastic response is caused by plastic straining of the material and not the mean stress effect. The difference is established using a reference specimen. Unlike the mean stress effect it is not possible to directly derive the residual stress from the change in response due to plastic straining. Also a further calibration step is required to determine the relationship between the change in the thermoelastic response and the plastic strain experienced by the material. Then it will be necessary to adopt a modelling approach to back out the residual stresses from the plastic strain. This is a complicated procedure compared to that proposed in [9], but is selected here for further study as it has the advantages of (i) enabling studies in materials that are not sensitive to the mean stress effect and (ii) does not restrict studies to that of simple specimens that contain one dominant applied stress direction, as was the case in [9]. Using the technique proposed in the current project it will not be possible to identify the separate stress components but to identify a quantity related to $(\sigma_1 + \sigma_2)$, much the same as with ultrasound.

TSA has previously been used in a laboratory setting, and the experiments completed in the current PhD to develop the synthetic bitmap are also carried out in a laboratory. However, the RESIST project is developing TSA into an industrially relevant assessment technique. Therefore, the equipment needed to perform TSA must be taken onsite and assessed in-situ. Setup methodology and specimen preparation needs to be assessed for feasibility for onsite use and the loading, normally applied using a servo-hydraulic test machine in the laboratory, must be applied using portable equipment.

In summary the key research questions are:

1. Can a synthetic data set be established to reveal areas in a test specimen that have experienced plastic straining?
2. Is the plastic strain developed in the vicinity of welds sufficient to generate a measureable change in thermoelastic response?
3. Can the change in thermoelastic response generated by the plastic strain be calibrated and used to assess the level of plastic strain a component has experienced?

4. Is it possible to use TSA away from the laboratory environment?

In the following chapters of the thesis these four questions are addressed in turn and the possibilities of using TSA established alongside the limitations of the technique in such applications.

Chapter 3: Development of the synthetic reference bitmap

3.1 Introduction

An approach is developed that allows regions containing plastic strain in a component to be identified in the thermoelastic response without using a physical reference specimen. For laboratory studies, it is more convenient to manufacture a physical reference specimen of identical geometry to the component under investigation. However, it is more practical to produce simulated specimen by FE modelling. This requires accurate measurements of the component geometry and knowledge of the thermoelastic constant of the component material. The K value could be evaluated experimentally using strain gauges on the actual component which is common practice in TSA [14]. More importantly, if the approach developed in the thesis is to be taken into industry a physical reference specimen of actual industrial components would be required. A reference specimen of every weld investigated in industry would be difficult and costly to manufacture. Therefore, this chapter describes the development of a computer generated reference dataset, known as a 'synthetic reference bitmap'.

The approach for developing the synthetic reference bitmap is initially tested using a specimen with a known complex stress distribution, a configuration known as a 'hole-in-plate', which is a plate with a central circular hole, where the geometry of the plate is such that the plate can be considered to be infinite, and is loaded to give a stress state of uniaxial tension away from the influence of the hole. Here the specimen is constructed from AL2024 making use of the specimens and thermoelastic data available from previous work [15]. To provide inputs to the model alongside the geometry, accurate mechanical material properties are required as inputs to the FE model (i.e. Young's modulus, Poisson's ratio, yield behaviour) and as mentioned above the thermoelastic constant of the material is required to convert the stress data into the thermoelastic response. The material properties of AL2024 were provided by [15]. It is important to note that developing the approach for an aluminium component is relevant as the same approach can be adopted for other materials. An accurate knowledge of the applied load is necessary. In a laboratory setting with a test machine and specially designed rigs this is a relatively straightforward matter, but it should be considered that for onsite applications on in service components establishing the actual loading maybe more challenging.

Chapter 3

The present chapter focusses on developing the synthetic reference bitmap for a laboratory component of known dimensions and know applied load. An overview of the procedure is shown in Figure 3-1. For the synthetic bitmap an FE model of the stresses is produced and the component stresses from the surface of the model are extracted. The component stresses are summed to provide a stress value equal to $(\sigma_1 + \sigma_2)$ as given by Equation (1-1). Therefore, knowing the thermoelastic constant of the material it is possible to convert the sum of the principal stresses given by the FE model into values of $\frac{\Delta T}{T}$. The $\frac{\Delta T}{T}$ data derived from the finite element analysis (FEA) is referred to as $\left(\frac{\Delta T}{T}\right)_{FEA}$ or the synthetic reference bitmap. To convert the FEA data into the synthetic reference bitmap a Matlab routine was written. Likewise, the experimental TSA data is also converted using a specially developed Matlab script to give the experimental thermoelastic bitmap $\left(\frac{\Delta T}{T}\right)_{exp}$. It is important to note that the FE data is manipulated to the same resolution as the experimental data using a two directional linear interpolation. The final step is to subtract the synthetic bitmap from the experimental bitmap to give the resultant bitmap which reveals the regions containing plastic strain.

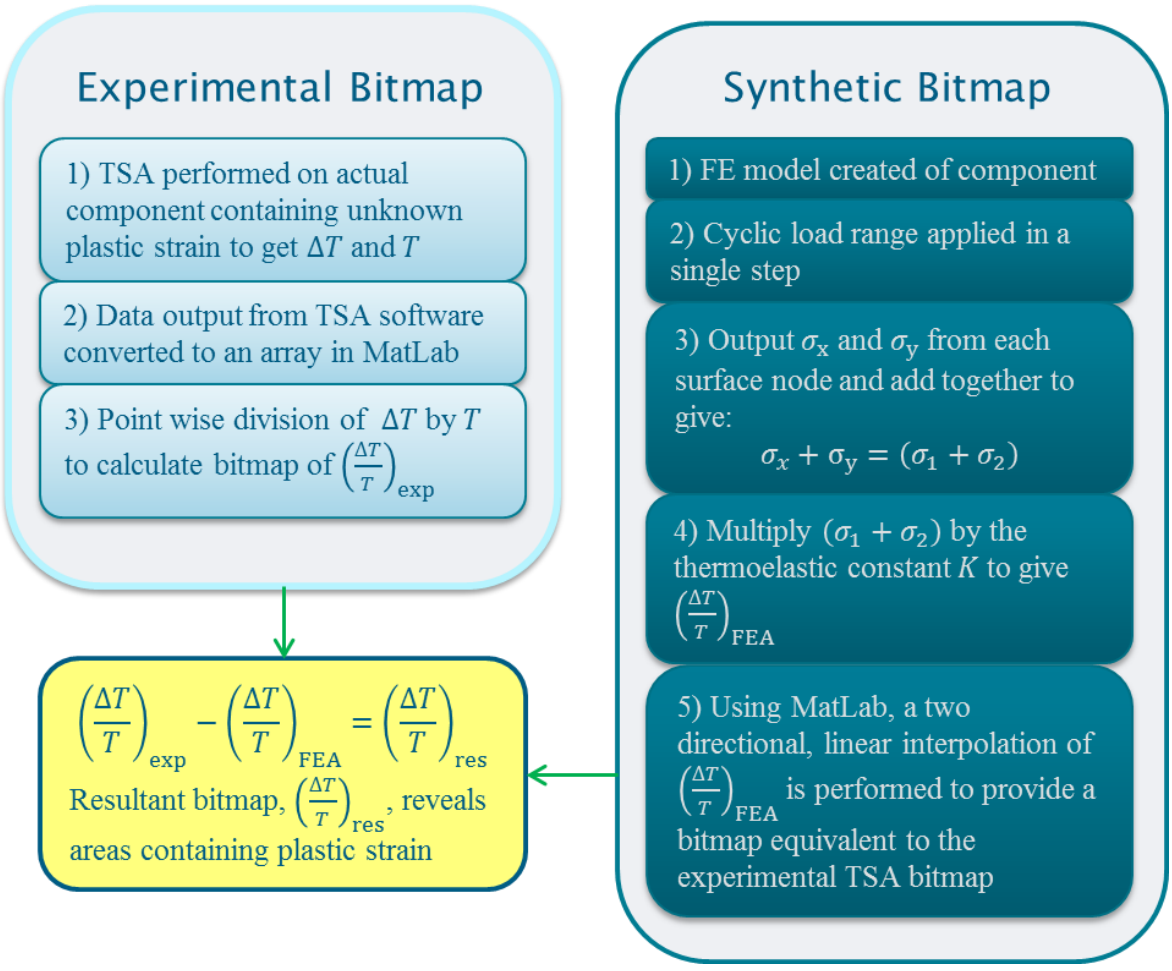

Figure 3-1 – Summary of the workflow used to validate the synthetic reference bitmap against the thermoelastic response from a physical reference specimen.

3.2 Summary of previous experimental work on aluminium alloy hole in plate specimens

The investigation in [15] used a set of three AL2024 hole in plate specimens manufactured to the dimensions in Figure 3-2; all had a thickness of 10 mm. In two of the specimens, a cold expansion procedure was applied to the hole in the centre of the plate to provide plastic strain levels of -2% and -4%. These specimens were used to investigate whether there was a difference in thermoelastic response due to plastic strain being present around the hole. The hole-in-plate specimens were cyclically loaded in a servo-hydraulic test machine as shown in Figure 3-2 with a load of 30 ± 25 kN (20 ± 16.67 MPa) at a loading frequency 10 Hz. The thermoelastic data was captured using a FLIR Silver 480M IR detector [15] and processed using the Altair proprietary software.

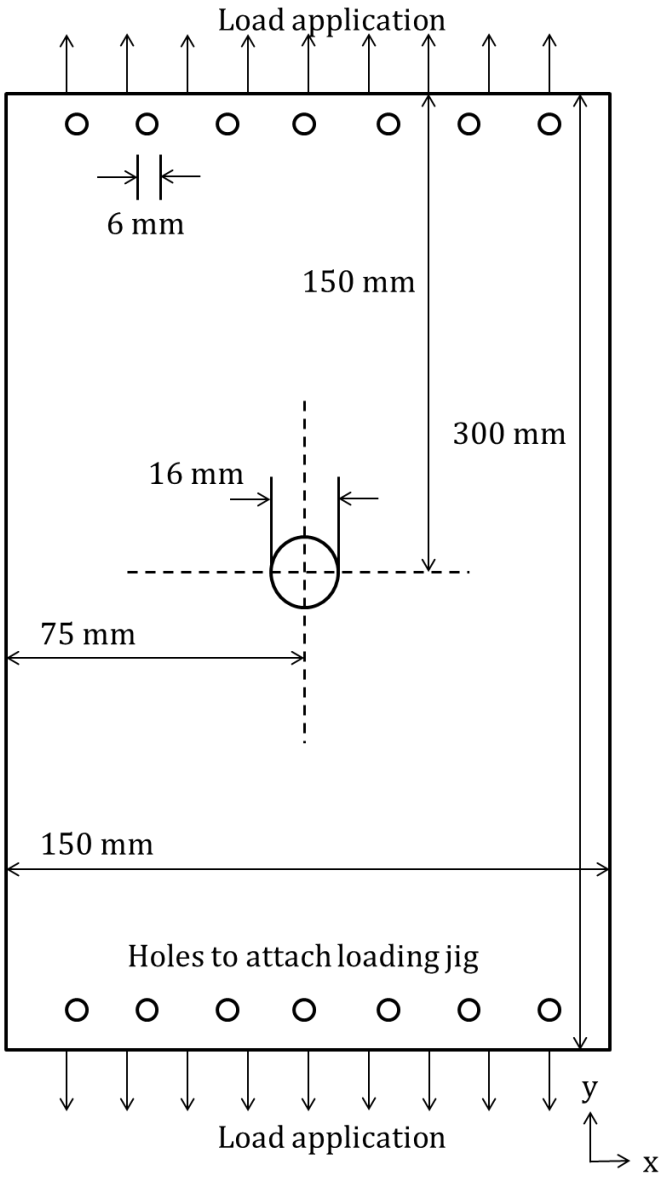

Figure 3-2 – Drawing of the hole-in-plate specimen [15] (specimen thickness is 10mm).

The thermoelastic response from a physical reference specimen was subtracted from the thermoelastic response of the specimens containing cold expansion around the central hole. The differences in thermoelastic response due to the change in plastic strain were revealed, shown in Figure 3-3. In [15] the data manipulation to produce Figure 3-3 was conducted using Microsoft Excel. The approach was cumbersome as it does not allow a straightforward application to datasets of different sizes or further manipulation without dealing with multiple spreadsheets. Furthermore, the data in Figure 2.3 are presented only in terms of ΔT and no attempt was made to include the surface temperature variation in the analysis. In the present work a routine will be developed that uses Matlab to process the image data and enable any variations in the surface temperature to be accounted for. The approach is detailed in the following sections of the chapter and uses the data collected during the work described in [15].

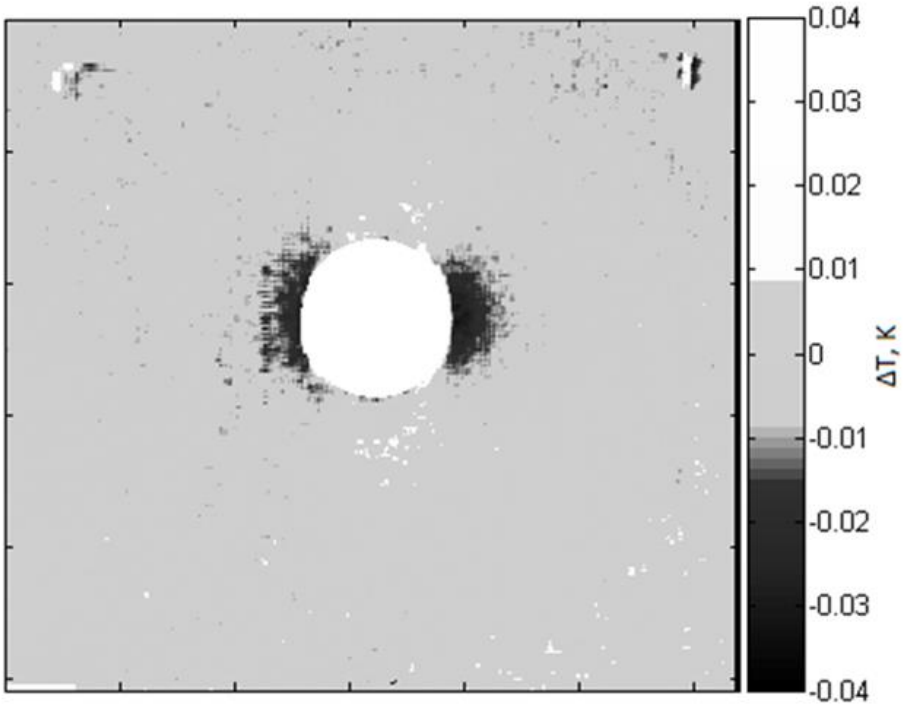

Figure 3-3 $-\Delta T_{4\%} - \Delta T_{0\%}$ of AL2024 hole-in-plate specimen. Change in thermoelastic response due to plastic strain shown around the sides of the hole [15].

The present work develops a synthetic reference bitmap for the hole-in-plate specimen. To create a simple linear elastic FE model it is necessary to know the elastic material properties of AL2024, Young's modulus, E, and Poisson's ratio, ν. These were obtained from tensile test performed on standard test coupons made from AL2024 as described in [17]. The thermoelastic constant, K, given in [17] is also used to generate the synthetic bit map. The properties obtained in [17] and used in the present work are summarised in Table 3.1.

Material property of AL2024	
Young's modulus, E	69 GPa
Poisson's ratio, ν	0.3
Thermoelastic constant, K	9.85×10^{-12} Pa^{-1}
Yield stress	275 MPa

Table 3-1 – Material properties of AL2024 used in the synthetic bitmap finite element model [17].

3.3 Creating the finite element model for the synthetic reference bitmap

The first stage of the synthetic bitmap process, shown in summary in Figure 3-1, is to create a finite element model of the component under investigation. The steps used to create a finite element model of the hole in plate specimen, as well as validation tests of the processes used to build the FE model, are described in the following section.

3.3.1 Finite element modelling

To perform the finite element modelling and analysis ABAQUS 6.13-3 was used. The finite element model for the synthetic bitmap of the hole-in-plate specimen, although relatively simple, provided the opportunity to perform mesh sensitivity studies, comparative studies of 2D vs 3D modelling, and also highlighted the necessity of using submodelling. The size of the specimen meant that to get a high enough mesh density around the hole, the region known to contain the largest stress gradient and plastic strain, it quickly became computationally inefficient to persist with a single model approach. The submodelling approach was chosen over other approaches, e.g. quarter-modelling using lines of symmetry, because for real industrial components it is submodelling of the welded junctions between pipes that will be required. Proving that submodelling worked with the hole-in-plate specimen allows the technique to be expanded further into other component geometries.

Geometry

The geometry of the finite element model was created from the design drawings in Figure 3-2 [15]. This was the original shape of the hole-in-plate specimens before cold expansion was performed and plastic strain put into the specimen. Therefore, it should be the same dimensions as the reference specimen. However, there may have been small differences that arose during the manufacturing of the hole-in-plate. This is important to note, as final

comparison of the bitmaps requires the surface geometry being compared to be exactly equal. Deviations in shape can result in regions being incorrectly identified as containing plastic strain.

The global model contains an interior boundary measuring 80.5 x 64.1 mm centred around the hole that provides the location of the outer boundary for the submodel. The interior boundary forces the generation of nodes along the boundary of the submodel. The interaction between the global model and the submodel is described using the displacements of nodes in the global model closest to the location of the submodel boundary; so driving the generation of nodes along the exact boundary increases the efficiency of the submodelling approach.

Having a model that exactly matches the geometry of the specimen under investigation is critical to ensure the stress outputs of the FE model accurately portray the real loading of the specimen under investigation. Alongside the accurate modelling of the boundary conditions and loads, having a correct geometry is the most critical part of the synthetic bitmap approach.

Material model

The material properties of the model were all taken from experiments conducted in [15]. These properties, shown in Table 3-1, are only the elastic material properties. This is due to the maximum applied stress being ~37 MPa, which even with a stress concentration effect due to the hole will only become a maximum of ~110 MPa. This value is below the yield stress of AL2024 (275MPa), so there will not be any effects of localised plasticity within the experimental results that need to be modelled. The same material model was applied to both the global FE model and the sub-model.

Boundary conditions and loads

To perform finite element analysis of a component tested using TSA, the experimental cyclic loading is applied in a single load step. This is because there is no need for averaging over a large number of loading cycles, nor does an adiabatic condition need to be created in the test specimen through cyclic loading. The range of the load cycle is used, and the output stresses from that single load step create the synthetic bitmap. The load is applied in tension in the y-direction.

The boundary conditions of the global model were set to match those of the experimental test conditions. The top boundary was restrained in the y-direction, and the top and bottom edges were all restrained from translating in the x- and z- directions. In the submodel, the boundary conditions were set to be driven by the output displacements of the global model at all points on the exterior of the submodel. Therefore, there was no independently applied load step,

just the output displacements from nodes in the global geometry after the load step was applied to that model.

Meshing

The global model only required a coarse mesh to be applied to it because it is only used to drive the displacements being applied to the submodel. The nodal spacing was 5 mm in the global mesh, giving a rough mesh size of 30 x 60 elements (w x h). The relative size of the submodel compared to the global model means the nodes used to generate the boundary conditions of the submodel are far from the hole and any steep gradients generated by the change in geometry. Around the hole a much higher mesh density is required to better calculate the relatively steep gradients in both displacement and stress fields. To find the best nodal spacing a sensitivity study was performed and is described in the element size convergence study. In both the global model and the submodel reduced integration quadratic solid elements (C3D20R) were used.

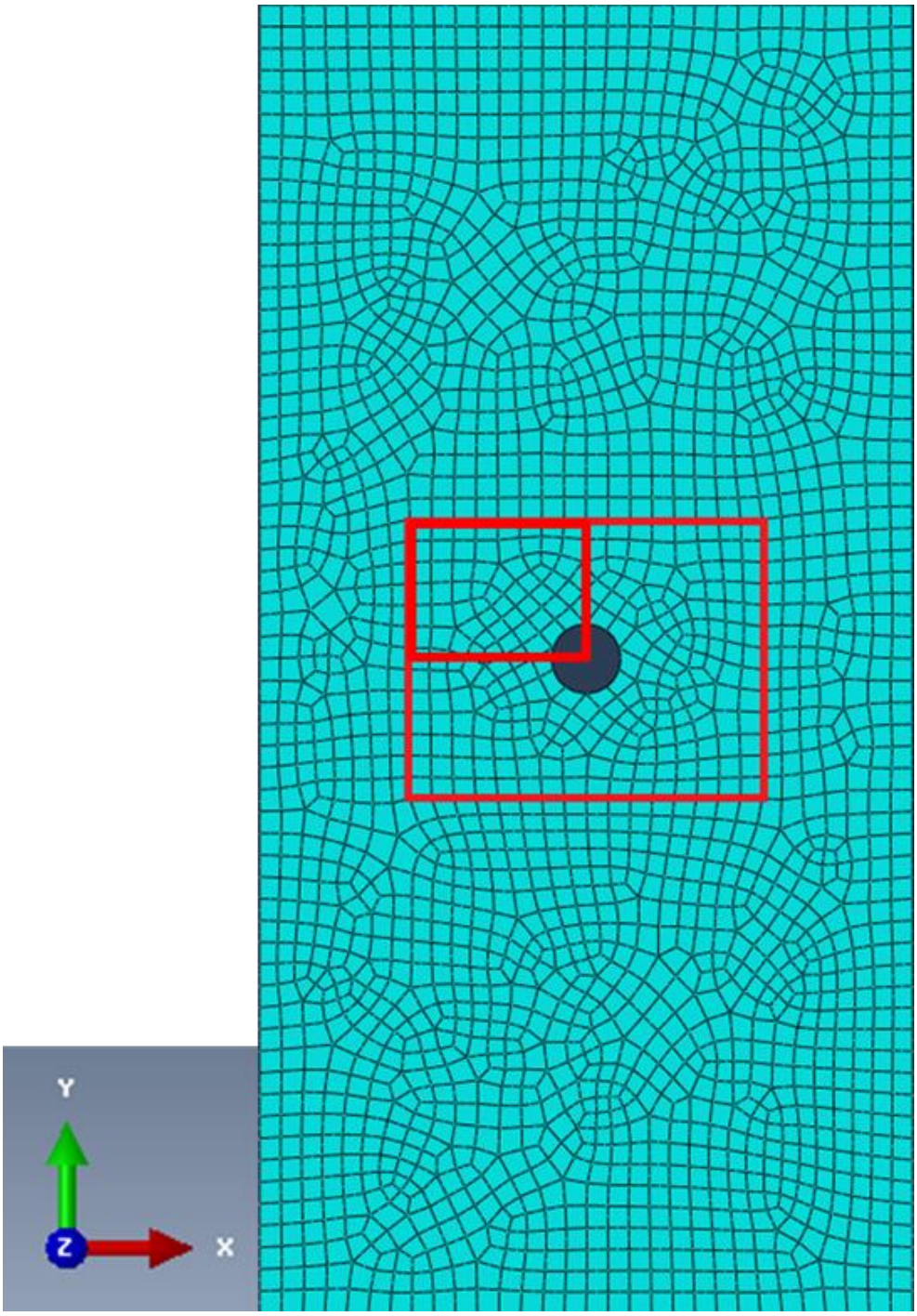

Figure 3-4 – Global model of hole-in-plate specimen with coarse mesh applied.

To decrease time taken for both mesh generation and analysis a “free” or unordered mesh was applied in the global model. However, in the submodel a controlled “structured” mesh was used, see Figure 3-5. A structured mesh provides regular element shapes that fit into a mesh evenly; it reduces the risk of distorted elements being present (which decrease the accuracy of the finite element analysis) but requires greater resources to complete an analysis. The submodel is the size of the large red rectangle in Figure 3-4, in Figure 3-5 an area ¼ the size of the submodel is shown.

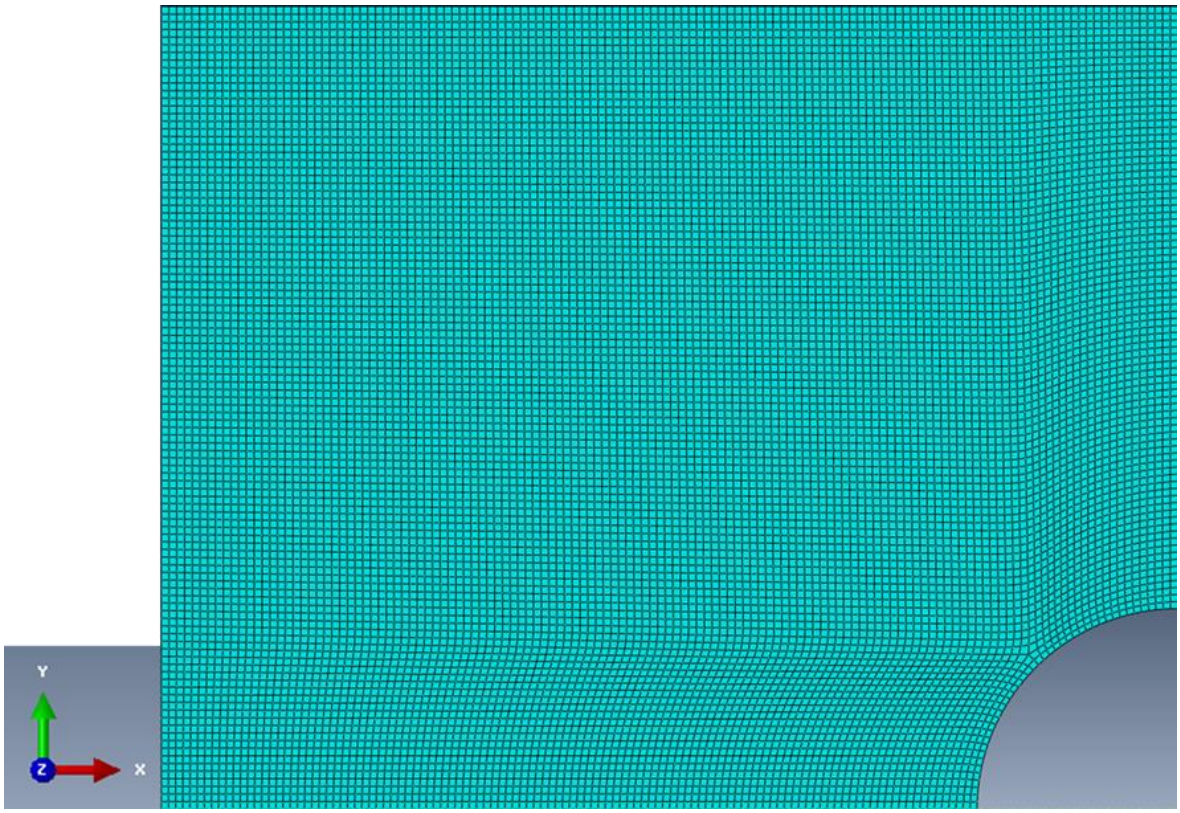

Figure 3-5 – 1/4 of the submodel geometry with fine mesh applied.

Validation of modelling approach

Element size convergence study

A sensitivity study was performed on a 2D model to assess how much effect decreasing the size of the elements used in the submodel mesh (and therefore increasing the number of elements) had on the output stress field. The parameter investigated was the maximum stress in the y-direction at the right-side of the hole. The target value for the study is calculated from the stress concentration factor (SCF = 3) and the applied stress in the y-direction, 33.33 MPa, giving a target maximum stress of 100 MPa. The percentage change in maximum y-stress between each decrease in element size was also calculated. It was decided that when a change of <1% occurred the model had converged. As shown in Table 3-2 elements of <0.3 mm resulted in <1% change in maximum y-stress; therefore, elements of size 0.3 mm were used for the submodel geometry.

Element size (mm)	Max. Stress (y-direction) (MPa)	Change in Max. Stress (%)	Time taken to run (s)	Number of elements
5	60.23	0	8	1860
2.5	78.97	31.11	8	4254
1	85.52	8.30	8	14562
0.8	89.60	4.78	8	18630
0.5	96.66	7.87	13	25400
0.3	98.28	1.68	15	45152
0.1	98.29	0.02	38	126234

Table 3-2 – Mesh convergence study of element size in submodel

2D vs 3D modelling study

A 3D model was used in the previous section. The added complexity of a 3D model greatly increases the computation time of the FE analysis. To potentially bring the computation requirements down, a study was undertaken to assess the effect of using only a 2D geometry rather than the 3D used previously. Two geometries were constructed that contained the same XY dimensions as Figure 3-2; the first was a 2D plane stress model with unit thickness. The second geometry was the 3D model with a thickness of 10 mm used to build the initial synthetic bitmap. Both models had x- and y-translation degrees of freedom constrained along the top edge of the y-direction of the geometry, and both had a tensile stress of 33 MPa applied at the bottom edge in the y-direction. Both models also had the same elastic material properties used previously. The stress in the y-direction was output after the FEA had been completed, and the stresses were plotted in Matlab and are shown in Figure 3-6. A sample of data through the horizontal centre line of the hole is plotted in Figure 3-7 to show the peak stress at the edge of the hole.

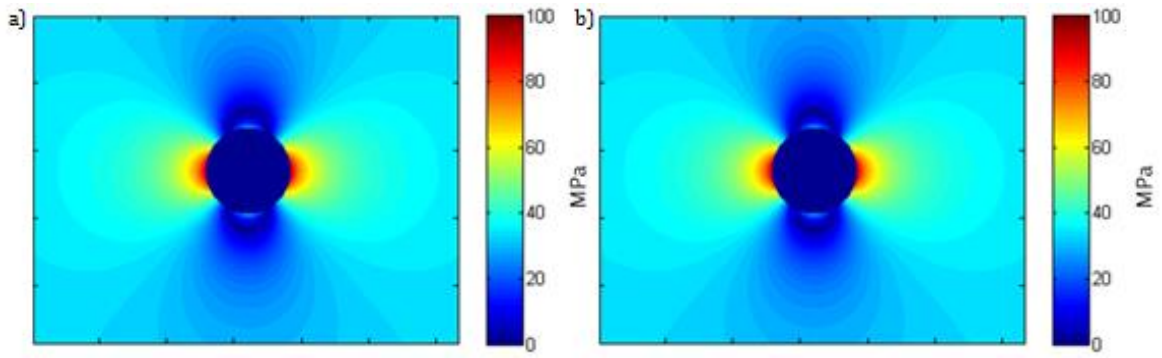

Figure 3-6 – a) y-direction stress map from the 2D geometry. b) y-direction stress map from the 3D geometry. Applied y-direction stress = 33 MPa in both models.

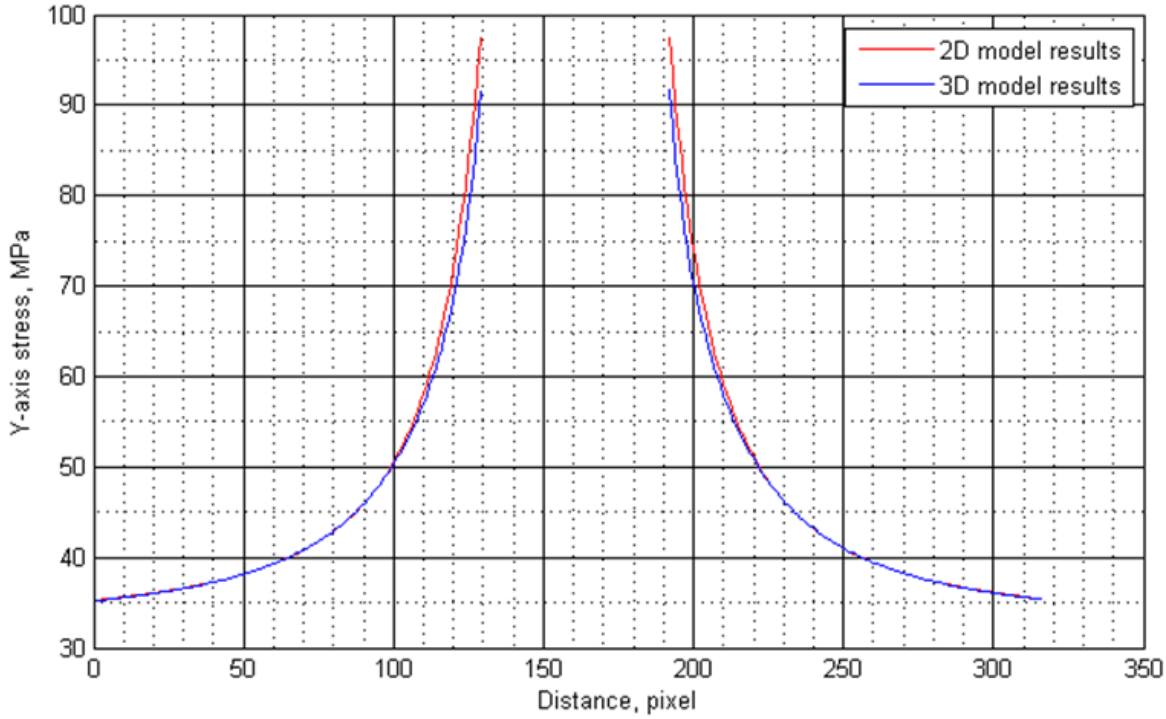

Figure 3-7 – Line plots from the horizontal centre of each stress map in Figure 3-6.

The line plot in Figure 3-7 shows that there is a greater stress concentrator effect in the 2D than in the 3D model when stresses are taken from the front face of the plate due to the plane stress assumption. In the 3D model, the stresses are at a peak halfway through the thickness and match the 2D assumption. This is expected from the theory, and in [15] it is calculated that for the 3D geometry of the hole-in-plate specimens the SCF would not be the theoretical infinite plate condition value, 3, but is 2.72 instead attributable to the finite thickness of the plate. When the calculated SCF [15] is used the peak y-stress at the hole edge should be 89.76 MPa, which the 3D model better estimates. Having accurate simulated stresses is the most important feature to allow the creation of a synthetic bitmap. Therefore, the conclusion to this study was that 3D models should be used for the generation of synthetic bitmaps in all future instances.

3.4 Realisation and validation of the synthetic bitmap

Having developed the finite element model it is now possible to extract the stress data from the FEA needed to realise the synthetic bitmap. Steps 2-5 in Figure 3-1 are detailed below:

- Step 2: FEA to simulate the cyclic loading used during TSA and output the principal stresses at each node in the mesh.
    - The load range of the experimental loading is applied to the global model as a single load step, which in turn drives the submodel.

    - From the submodel the principal stresses can be extracted after loading has been applied from the nodes, along with the nodal coordinates.
- Step 3: The principal stresses at each node are output with the node coordinates as a list format.
    - The script combines the stress outputs into a single stress value ($\sigma_1 + \sigma_2$).
- Step 4: The list of combined stress values is multiplied by the thermoelastic constant, K, converting the values into the thermoelastic response for each node of the submodel.
- Step 5: Finally the script sorts the data using a two directional, linear interpolation to provide a dataset that contains the same number of pixels and is the same shape as the TSA data from the IR detector.

The values of σ_x and σ_y for each node in the front face of the submodel were output from ABAQUS along with the original nodal coordinates. The stress values were summed together to provide a single value at each node equal to $(\sigma_1 + \sigma_2)$. The thermoelastic constant, K, was used to convert the summed stresses into values of $\frac{\Delta T}{T}$.

The values of $\frac{\Delta T}{T}$, with the attached node coordinates for each value, were read into the Matlab script in the Appendix. The script generates a matrix of size equal to the pixels in the experimentally acquired TSA data. Then, using the coordinate data attached to the $\frac{\Delta T}{T}$ data the script uses a linear interpolation of the closest four data points to populate the matrix with $\frac{\Delta T}{T}$ data generated by the FE analysis. The script increases the size of the FEA dataset to match the larger TSA dataset, rather than reduce the TSA data.

It is now possible to compare the reference datasets against one another. The two bitmaps are shown together in Figure 3-8. In the experimental bitmap there is a lot of noise, this is to be expected and highlights one of the potential benefits of using FEA and the synthetic bitmap approach. There will only be one source of experimental noise in the data used for the comparison, not two.

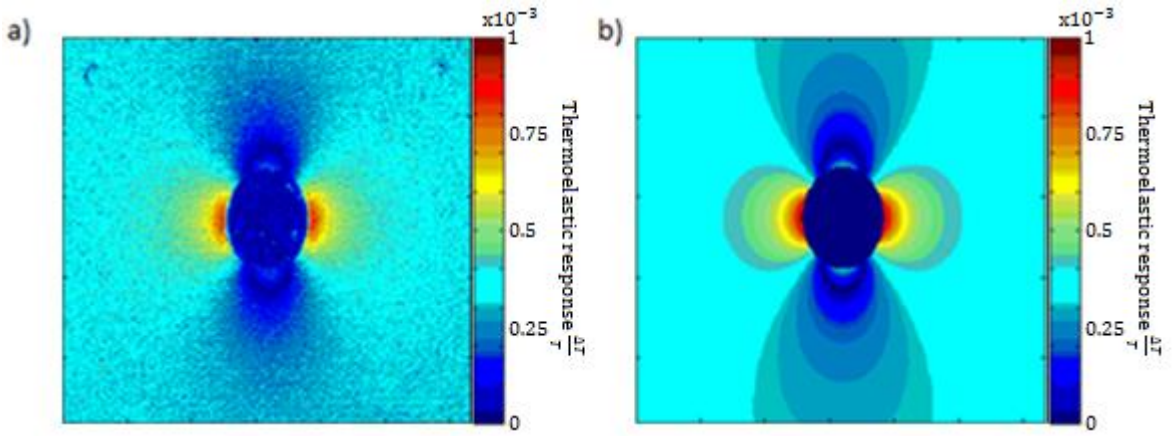

Figure 3-8 – a) $\Delta T/T$ bitmap of the experimental reference data. b) $\Delta T/T$ bitmap of the synthetic bitmap generated by the FEA.

To confirm the synthetic bitmap provides the same thermoelastic response as the experimental reference specimen the synthetic bitmap was subtracted from the experimental data bitmap. This is shown in Figure 3-9 alongside a line plot of the far field data. A visual inspection of the data shows there is a lot of noise in the data but no obvious bias away from the zero point, except for around the hole. This comes from the image matching used to line the geometries of the two datasets up against one another. The discrepancy arises from the fact that an assumed geometry was used for the initial FE model, the final manufactured specimen may not have matched the design drawings accurately enough. The model was also only an elastic model, without any localised plastic effects being included around the edge of the hole. In the further development of the synthetic bitmap technique, presented in Chapter 5, this was taken into account with greater accuracy used in the reproduction of the FE model.

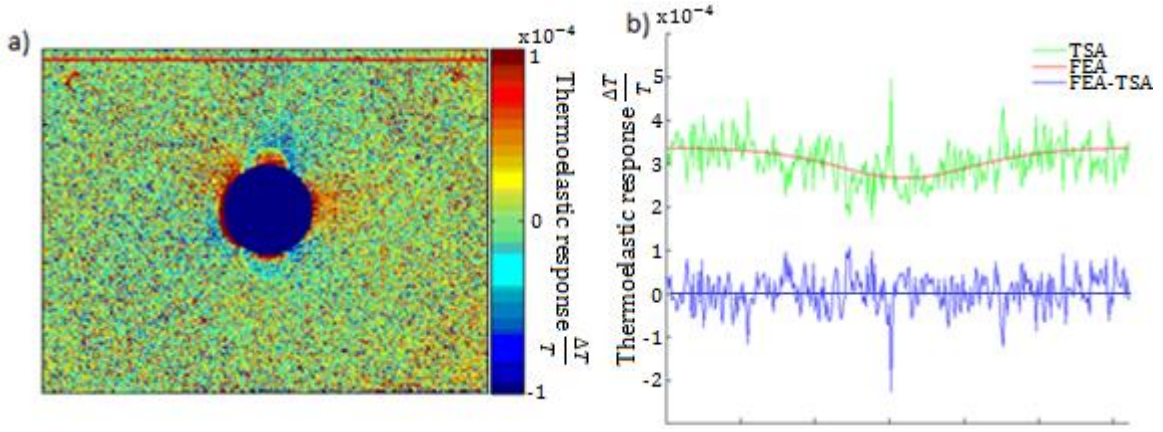

Figure 3-9 – a) Resultant bitmap $(\Delta T/T)_{TSA} - (\Delta T/T)_{FEA}$ b) Thermoelastic response at the top of a)

The line plot in Figure 3-9b is data taken far from the hole and provides a measure of the noise, the same line of $\frac{\Delta T}{T}$ data was taken in the experimental reference, the synthetic reference, and the resultant bitmaps. In both the reference bitmaps the thermoelastic response was of the order 10^{-4}, however, in the resultant bitmap, the thermoelastic response that was left, the noise was centred around zero and of the order 10^{-5}. Most of the scatter in the data is between -1x10^{-4} and 1x10^{4} so a filtering approach might be considered, which further removes the background scatter from the data and may aid in revealing changes in thermoelastic response due to plastic strain. A large sample of data was taken from the far field noise in the resultant bitmap and the average noise and standard deviation were calculated. The mean average noise value was 1.12×10^{-6} and the standard deviation was 2.04×10^{-5}. This confirms that the synthetic bitmap is accurately simulating the experimental reference.

3.5 Summary

A simulated reference bitmap, the synthetic bitmap, has been successfully created and has been shown to be reasonably accurate when compared against the thermoelastic response of a physical reference specimen. The synthetic bitmap has a number of limitations that need to be fully understood by the user to create an accurate reference bitmap. The geometry used to build the FE model has to accurately portray the specimen under investigation; slight deviations from the actual geometry can have large effects in the final stress map used to build the synthetic bitmap. The meshing of the model needs to be of sufficient density to capture the stress gradients within the FE model. The alignment of the synthetic bitmap to the thermoelastic data recorded by the IR camera needs to be perfect so that gradients in the thermoelastic response are accurately calculated in the resultant bitmap. The synthetic bitmap approach is next used to assess the plastic strain distribution around a typical weld in 316L stainless steel. Before that work is completed, a series of sensitivity studies has to be carried out. This is because as shown in the results in Figure 3-9 and the results in [15] the final resultant value of thermoelastic response is a very small value. Therefore, it is necessary to try and reduce the sources of noise in the final dataset through careful examination of test parameters, such as surface preparation before painting, a further investigation into the paint coating, and the use of motion compensation techniques. These are described in Chapter 4.

Chapter 4: Investigations into sources of error in the thermoelastic response

4.1 Introduction

It was noted in [17] that the change in thermoelastic constant due to the plastic strain was a very small quantity. It is small enough that without careful specimen preparation and experimental procedure, the change in K could be masked in the experimental data by experimental inaccuracies. Inaccuracies are introduced in thermoelastic stress analysis because of the following

- Test machine alignment – the test machine is designed to apply the load along the axis of the machine. Over time the grips of the test machine require realignment to ensure the application of load stays through the axis of the machine.
- The rigid body motion of the surface – the specimen is cyclically loaded and if the motion is greater than the projected area of the elements in the detector array blurring of the image occurs, which can be resolved by utilising 'motion compensation' approaches [62] [61] as described in Chapter 2.
- Reflections from the surroundings, even though a black cloth shrouds the entire experimental set-up, as discussed in Chapter 2, there are reflection sources such as the hydraulic hoses from the test machine and the cold detector. In the present work the quantity $\frac{\Delta T}{T}$ is obtained. The surface temperature measure is particularly susceptible to the effect of reflections as it is an absolute measure, whereas ΔT is simply a measure of the change in the surface temperature as a result of the cyclic loading.
- The surface condition both in terms of roughness and oxidisation of the surface; both are known to affect the thermoelastic response with rough surfaces magnifying the effect of motion as the roughness can either pick-up reflections from the cold detector and the room temperature surroundings [62].
- The paint coating is a known cause of attenuation of the response [18] as discussed in Chapter 2.

Even though much of the above has been examined previously it was decided that another examination of the effect of the all the above was necessary, to ensure that any inaccuracies arising from the above are known and can be eliminated or accounted for in the analysis. Therefore, before the investigation into plastic strains induced by the welding process in 316L stainless steel specimens took place, it was decided to re-establish the effects of each of

the above on the thermoelastic response so as to have better confidence in the results. The knowledge gained through the investigations of this chapter will be used to enhance the test methodology of the subsequent TSA tests carried out. As noted, the change in thermoelastic response being investigated is very small and each source of error in the measurement could be sufficiently large to hide the change in thermoelastic response, so understanding the magnitude of the sources of error is critical.

4.2 Test set up and loading conditions

4.2.1 Test machine alignment

In TSA it is essential for a cyclic load to be applied and the common means of doing this is to use a servo-hydraulic test machine as described in Chapter 2. The test specimen is mounted in hydraulic grips which are designed to be in alignment with the test machine axis, so that the line of action of the applied load is along the midline of the specimen. However, the grips can become misaligned due to movements in the test machine. It is usual to use fixtures that eliminate the misalignment but for much of the work described in the thesis the specimens were such that they needed to be gripped directly in the test machine grips. To evaluate the thermoelastic response from the specimens accurately it was necessary to produce a simple uniaxial loading along the axis of the test specimens to create a known nominal stress state (i.e. away from any feature) so that in equation (1-1) only σ_1 is non-zero. This means that the grips must provide an even pressure over the test specimen ends to avoid any in-plane bending and that they must be aligned to prevent any out of-plane bending.

The test machine used in most of the work described in the thesis is an Instron 8800 servo-hydraulic test machine. To investigate if the machine was aligned a 316L stainless steel strip specimen of dimensions 30 x 2 x 360 mm was mounted in the test machine and loaded as given in Table 4-1. A combination of mean loads and load ranges was used to provide a large number of datasets to remove the possibility of loading irregularities at a particular load step skewing the data.

Test Number	Frequency (Hz)	Mean Load (kN)	Load Amplitude (kN)
1	10	2600	2000
2	10	3500	2000
3	10	3500	3000
4	10	4400	2000
5	10	4400	3000
6	10	4400	4000
7	10	4400	2000
8	10	4900	3000
9	10	4900	4000
10	10	5900	2000
11	10	5900	3000
12	10	5900	4000

Table 4-1 – Testing load plan for alignment tests.

TSA data was collected from the front face of the specimen and then without removing the specimen from the test machine, thereby preserving the boundary conditions, the IR camera was positioned to capture the back of the specimen and a second set of TSA data was taken. This gave 24 data sets in total, from which the thermoelastic constant of the material was calculated; the results are shown in Figure 4-1 with the first standard deviation shown by error bars on the data. The results from the front and back faces of the specimen show an average difference of 0.68×10^{-12} Pa^{-1} in the thermoelastic constant. When the data is averaged front to back, the value of K matches experimental values of K captured using the same equipment and 316L specimen before grip misalignment had taken place. Now that the test machine misalignment is known it has been realigned by an Instron engineer so this cause of error has been removed from future results.

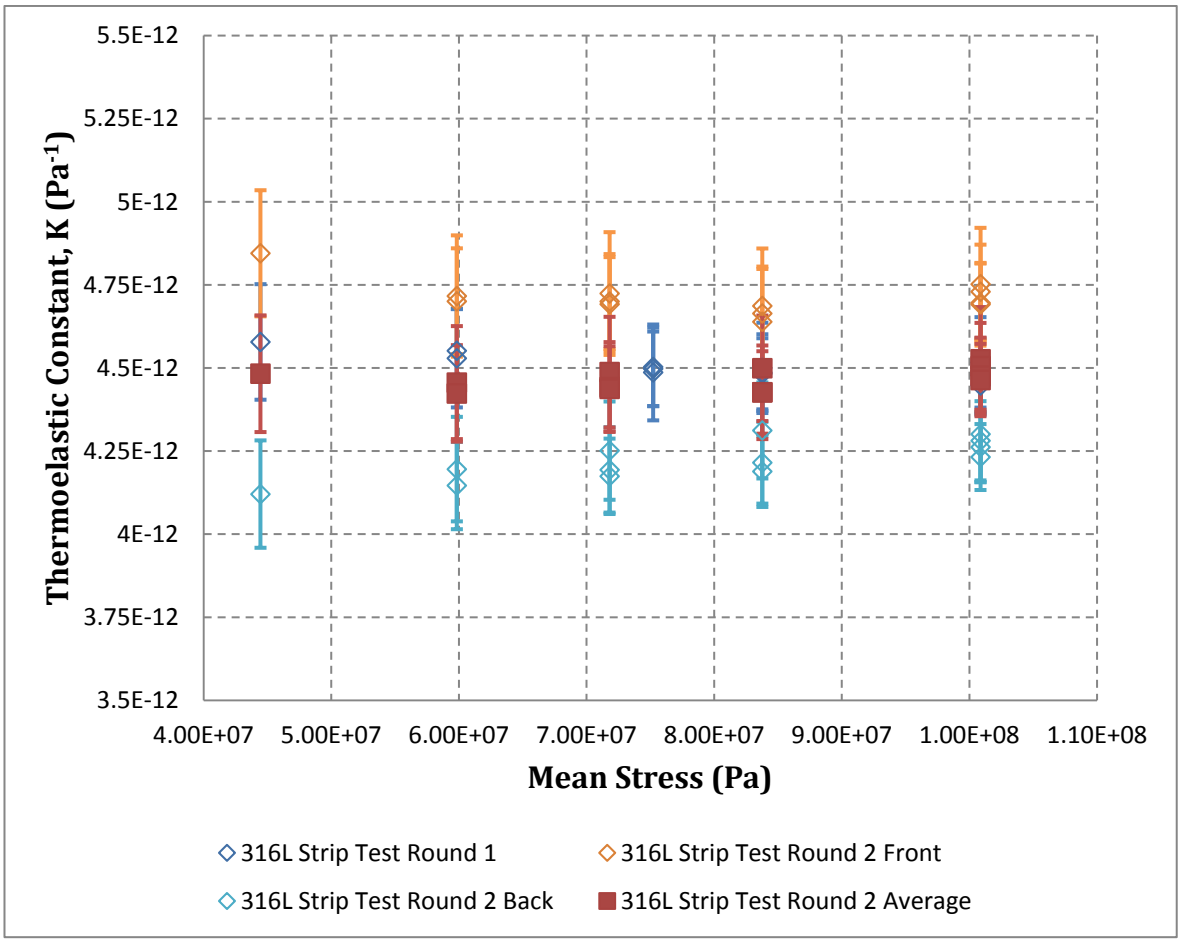

Figure 4-1 – Results of thermoelastic constant from a 30 x 2 x 360 mm strip specimen made from 316L stainless steel.

The design of the Instron servo-hydraulic test machines is such that the actuator that applies the load is able to rotate around the central axis. This allows the grip faces to align themselves along the central axis of a test specimen placed into the test machine. However, on slender specimen with low torsional resistance (e.g. specimens such as the 316L strips used previously) the free rotation of the actuator can place a small torsional load through the specimen as it loads over a loading cycle. To prevent this from changing the stress state being applied to the specimens that are undergoing TSA an anti-rotation collar is used, see Figure 4-2. The collar tightens around the actuator to clamp it in place thereby preventing any natural rotation that may be applied by the test machine. With this device in place and with the realignment performed by the Instron engineer the errors that arise due to test machine misalignment have been reduced in future tests.

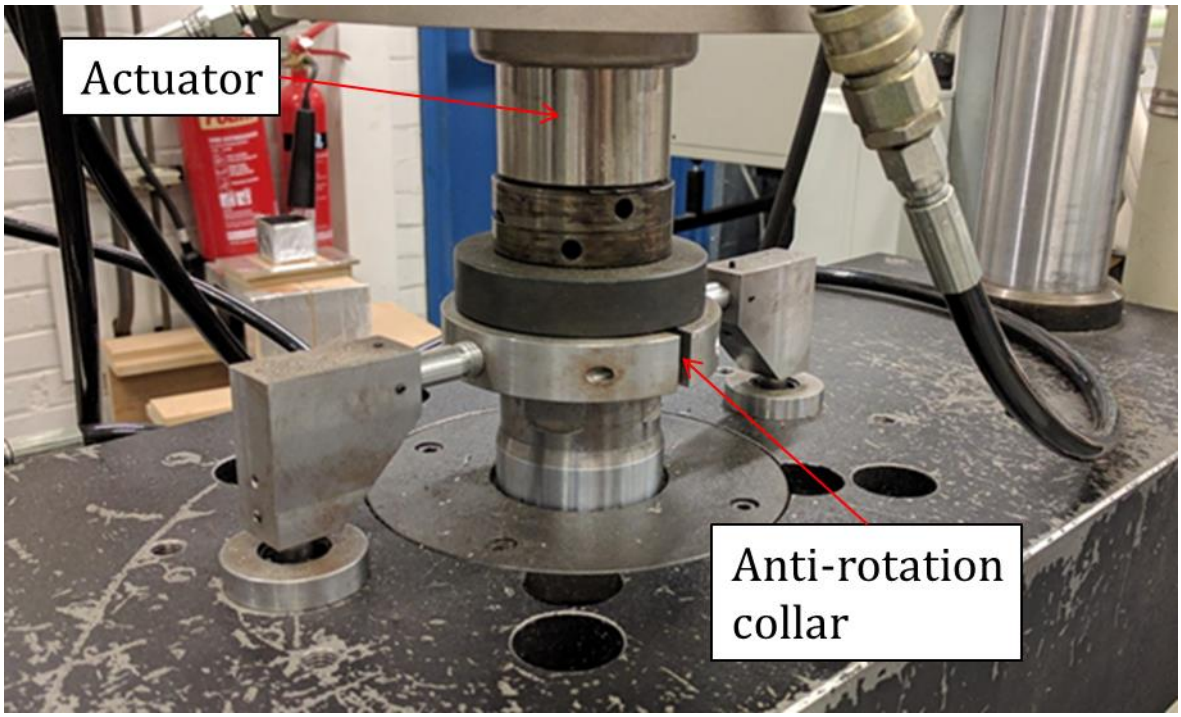

Figure 4-2 – Image of the anti-rotation collar on the Instron 8800 servo-hydraulic test machine.

4.2.2 Rigid body motion

Relative motion between a test specimen cyclically loaded for TSA testing and the IR camera causes a blurring effect in the captured images. The magnitude of scatter that this puts into the data is related to the stand-off distance of the camera and therefore the size of the movement of the specimen relative to the pixel size in the IR data. If the size of the motion is large, e.g. greater than the projected area of one detector element, then marks can be made on the surface of the specimen and the displacement of these marks is tracked frame by frame through the captured video [61]; this procedure is described in Section 2.4.1. However, if the size of the motion is small, e.g. less than a pixel, or there are very large stress gradients, e.g. around a crack tip opening, a more complex approach is required. This approach uses a DIC system to track the displacement vector field of the whole surface; this procedure is also described in Section 2.4.1.

The movement in the TSA tests performed in the current PhD are uniform, whole body movements that can be compensated for with a single vector shift frame-by-frame. Therefore, the approach using two markers and the Random Motion software has been used to reduce the scatter arising from relative motion in the TSA. Random Motion functions by using two marker points that are distinct in the thermal data recorded. These marker points are tracked through each frame of the thermal video recorded and their displacement and rotation vectors are calculated frame-by-frame. These vectors are used to correct the orientation of

each frame relative to the first frame, such that the relative motion of each pixel is removed. A further description is provided in Chapter 2.

4.2.3 Reflections

The IR camera used to record the data for TSA testing is extremely sensitive to changes in temperature, capable of measuring changes in temperature to around 20 mK. Therefore, sources of heat in the environment around the test may create an erroneous reading in the mean temperature data, *T*, if reflected onto the specimen and correlated into the response. To remove the influence of unwanted IR sources, the test environment is surrounded by a heavy black curtain that prevents radiation from the surroundings. However, there are still hot and cold sources located within the curtain that cannot be removed by necessity. The hydraulic test machine contains hydraulic fluid that is warmer than room temperature, ~ 40-50°C. The IR camera itself contains heat sources that can influence the TSA data taken. The sensor is kept very cold at 73K and the reflection of this in the surface from where TSA data is being gathered can be an influence in the *T* dataset. The body of the camera itself is the radiator for the sterling heat engine used to cool the sensor. The heat from camera housing can also be correlated into the *T* data.

Due to the heat of the hydraulic fluid used by the test machine, a thermal gradient of hot to cold from the bottom to the top of a test specimen is not uncommon; however, in Figure 4-3 the thermal gradient is reversed. The colder region, black and blue, is at the bottom of a painted section on a 316L stainless steel strip specimen and the warmer region, red and pink, is at the top. In the space below the painted section being measured there is a cold spot reflection in the metal surface. This is the IR detector and is the cause of the thermal gradient being driven in from the cold section in the bottom left corner of the image.

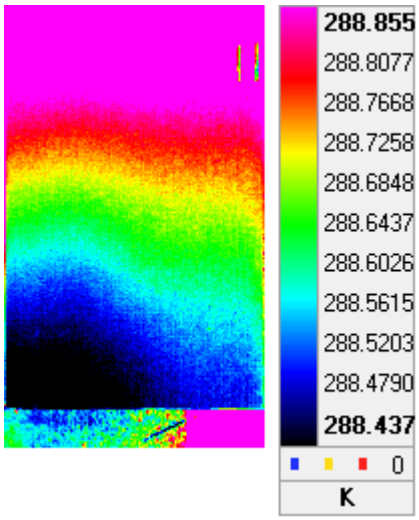

Figure 4-3 – Mean temperature data, *T*, from a 316L stainless steel strip specimen.

As with any surface, the smoother it is the more reflective it becomes. In the test specimens used in Chapter 5 there was a thin layer on the surface of the 316L that was formed during the cutting of the specimens via electro-discharge machining. This surface had to be abraded using silicon carbide (SiC) paper, and this reduced the surface roughness of the specimens so the danger of influence by reflections was increased. To reduce the effect of reflections in the calculated $\frac{\Delta T}{T}$ bitmaps when there is a large peak in the T data, a mean value for T is calculated for each dataset. The averaged value of T is used to perform the pixel by pixel analysis when constructing the bitmaps.

4.3 Paint coating

4.3.1 Paint coating quality

When performing TSA it is required that the surface under investigation has a high thermal emissivity. For metals this requires the application of a black, non-reflective coating. The requirements for the coating were defined in Chapter 2, and from the work completed in [18] a specification of a good paint coating was defined:

- A paint thickness of 15-25 μm is thick enough to prevent reflections from the metal surface being present in the TSA data gathered but not so thick that thermal lag becomes an error source in the data.
- Good contact with the surface to ensure the thermoelastic response of the metal is transferred through the paint.
- High, consistent emissivity and non-reflective finish. The constant emissivity prevents variations in the temperature change from being recorded as variations in the stress field and the non-reflective finish, as mentioned in the previous section, helps prevent external sources of IR radiation from being falsely recorded from the surface.

In addition to the conclusions of [18] it is also beneficial for the painted surface to be durable so that careful handling of the specimen does not damage the surface coating. In [18] a large number of different black spray paints were tested for the effect on the thermoelastic response of an aluminium specimen and a steel specimen. The conclusion of these tests was that a matt black spray paint from RS components, here known as RS matt black, should be used to provide the emissive surface in TSA tests. However, in the time since the study was published there has been a change in the formulation of RS matt black so a second study is required to assess if the new formulation still provides the best surface preparation for TSA.

The first assessment carried out was a qualitative study on how a range of black spray paints sprayed onto the surface of an aluminium test specimen. The exact grade of aluminium is

unknown but it is not important for these particular tests. The test piece was chosen because it was still in an as received condition, with a protective plastic layer covering the surface providing the same condition of surface for each paint to be applied to. Every paint can was prepared with two minutes of vigorous shaking as suggested by the manufacturer. Table 4-2 shows the observations of each paint in three stages; the first is how the paint flowed from the spray can. The second is a visual inspection of the painted surface whilst the paint was still wet. The final is a visual inspection of the dried surface of each painted section. Figure 4-4 shows the final, dried surface of each paint.

Paint type	Spray type	Wet surface	Dry surface
New formula RS matt black	Clean, even spray. Very fine	Smooth, no pooling	Good, matt finish. Very smooth
Krylon 1602 Ultra-flat	Large coverage spray	Some pooling Spread to edges	Matt finish, lumpy surface
Ambersil Black Matt	Quick, heavy flow	Heavy, splattered look	Very spotted look. Shiny
Electrolube Black Matt	Fine spray	Thin covering, even after multiple coats	Thin in areas, thick in others. Spotted
Electrolube EMBP400	Clean, fine spray.	Smooth, no pooling	Good, matt finish. Very smooth

Table 4-2 – Comments of the quality on different spray paint coatings after visual inspections.

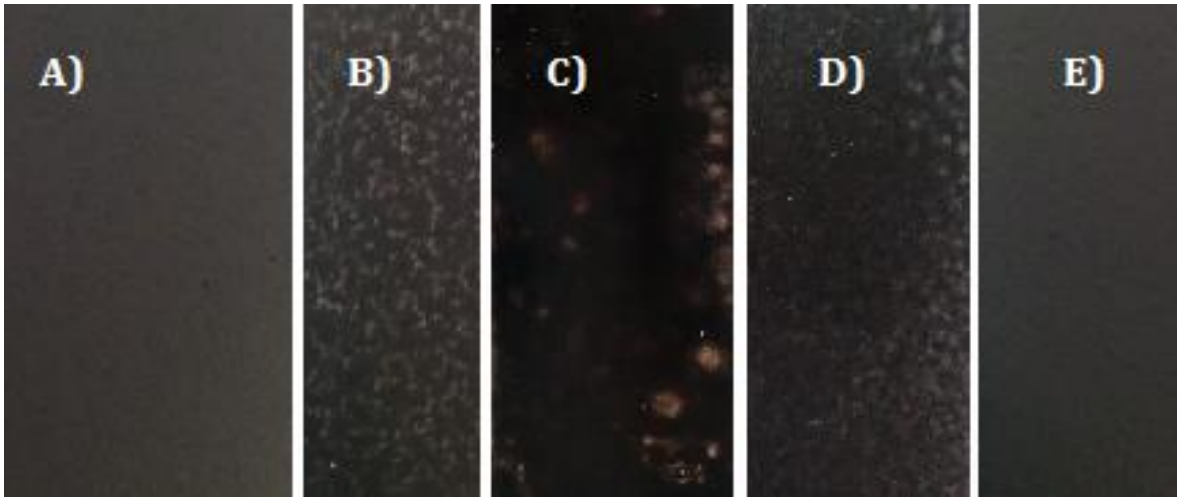

Figure 4-4 – Images of the dried surfaces from each paint in Table 4-2. A) New formula RS matt black. B) Krylon 1602 Ultra-flat. C) Ambersil Black Matt. D) Electrolube Black Matt. E) Electrolube EMBP400.

The conclusion of this test was that the new formula RS matt black and Electrolube EMBP400, referred to as Electrolube, would be taken forward for future tests. The tests described in the next two sections investigated two properties. The emissivity of different thicknesses of both paints is calculated through comparison with a blackbody heat source in a non-loaded, static

test. The thermoelastic response of a 316L stainless steel test specimen is calculated for different thickness of each paint type.

During repeats of the tests of the five spray paints flaking of the paints from the surface after one day was noticed. It was suggested that this could be due to a thin residual layer of acetone on the surface of the specimen after the previous paint layer was cleaned from the specimen. To check, the specimen was cleaned using acetone and one half was cleaned with water to remove any residue. Four sections on each half were masked out and then the specimen was sprayed with a thin coating of Electrolube paint. After drying for two hours a wooden stirring stick was scraped across the surface to attempt to dislodge the paint. Images of each painted section are shown in Figure 4-5.

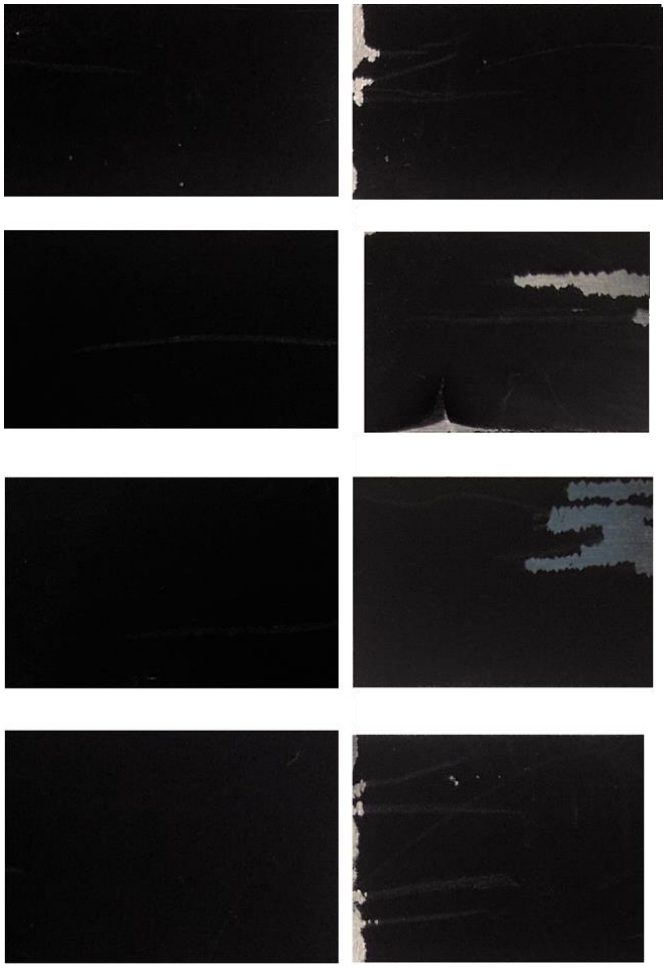

Figure 4-5 – Eight sections on the aluminium specimen painted with Electrolube matt black paint.

The non-rinsed sections, shown on the right of Figure 4-5, show some signs of flaking and are more easily removed with the wooden stirrer. The painted sections that were rinsed, on the left of Figure 4-5, were a lot more durable and resistant to handling. Therefore, it is suggested that all future specimens have the residual acetone rinsed from their surface to increase the durability of the paint coating.

4.3.2 Paint emissivity

To establish the relative emissivity of both the RS matt black and the Electrolube paints, a blackbody was used to provide a reference value of emissivity; the blackbody had been recently calibrated and had a surface emissivity of very close to 1. The specimen used for the emissivity tests is the same specimen that will be used in the thermoelastic response tests, therefore the exact material had to be known; unlike in the previous paint coating quality tests. The new specimen is the 316L stainless steel strip specimen used in the test machine alignment tests. Two specimens were made that measured 30 x 2 x 360 mm, and each was divided into six sections that were painted. The sections were painted such that the first section on a specimen had a single pass of paint and the sixth section had six passes of paint applied. To increase the number of datasets the specimens were painted twice, providing two painted sections for each pass number. An image of the Electrolube painted specimen is shown in Figure 4-6. As noted by [18] a pass of paint is heavily dependent on the user applying the paint, so the thickness of each section was measured using an Elcometer 456 FNF Model B Separate DFT Gauge using an NF-Standard Probe. The results of the thickness tests are shown in Table 4-3. The standard deviation of each section was also recorded and the variation in thickness was calculated, the results show that Electrolube provides a more uneven surface than RS matt black and as already mentioned a smooth coating surface is desirable.

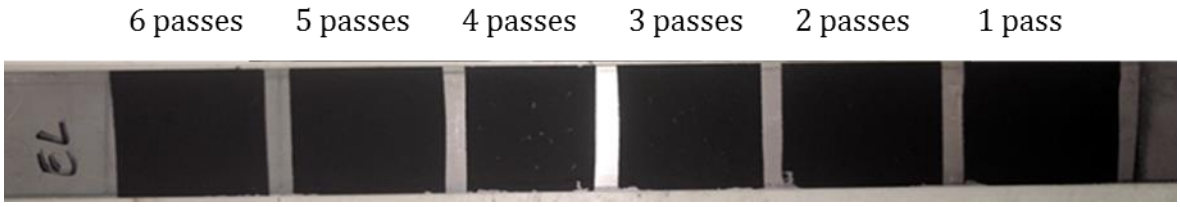

Figure 4-6 – Electrolube painted 316L stainless steel strip specimen.

Specimen	Layer no.	Thickness (µm)	Standard Deviation	Coefficient of Variation
RS - 1	1	8.01	0.72	8.9%
RS - 1	2	10.5	1.37	13.0%
RS - 1	3	13.31	1.25	9.4%
RS - 1	4	19.28	0.85	4.4%
RS - 1	5	25.88	1.31	5.1%
RS - 1	6	28.86	1.11	3.8%
RS - 2	1	6.77	0.46	6.8%
RS - 2	2	14.6	0.87	5.9%
RS - 2	3	18.36	1.27	6.9%
RS - 2	4	18.56	0.73	3.9%
RS - 2	5	23.35	0.91	3.9%
RS - 2	6	27.05	1.29	4.8%
EL - 1	1	18.08	1.52	8.4%
EL - 1	2	21.51	2.43	11.3%
EL - 1	3	23.33	1.98	8.5%
EL - 1	4	27.32	1.68	6.2%
EL - 1	5	32.22	1.99	6.2%
EL - 1	6	37.15	2.11	5.7%
EL - 2	1	17.35	2.72	15.7%
EL - 2	2	23.36	2.61	11.2%
EL - 2	3	25.35	2.32	9.1%
EL - 2	4	30.89	1.67	5.4%
EL - 2	5	34.02	2.73	8.0%
EL - 2	6	36.06	2.77	7.7%

Table 4-3 – Thickness of each painted section. Highlighted are the painted sections that contain a thickness of 15-25 µm.

To assess the emissivity of either paint the thermal signature emitted from the surface has to be normalised against the thermal signature of a reference source. This is performed by dividing the raw IR reading from the painted section by an IR reading from a blackbody with an emissivity value of 1. The blackbody needs to be set to the same temperature as the painted section, and then the following equation can be used:

$$\frac{DL_{\text{paint}}}{DL_{\text{blackbody}}} = \frac{T \text{ x } e_{\text{paint}}}{T \text{ x } e_{\text{blackbody}}} = \frac{e_{\text{paint}}}{e_{\text{blackbody}}} \tag{4-1}$$

where *DL* is the digital level recorded by the IR camera, *T* is the temperature of the object being recorded, *e* is the emissivity value of the surface.

It was decided to use *DL* instead of the *T* readings as this eliminates any inaccuracies brought about by the IR camera calibration. This way by taking readings from both the painted sections and the blackbody the emissivity of the paint on each section can be calculated if the emissivity of the blackbody is known. The blackbody emissivity is 0.96±0.02.

To ensure the blackbody and the painted specimen are at the same temperature when the *DL* data is taken thermocouples have been used. Two thermocouples were attached to the

reverse of the thin strip specimen behind the painted section. Two thermocouples were attached to the surface of the blackbody, one in the centre and one at the edge to check the whole surface of the blackbody was heated evenly. Getting all four thermocouples to the same reading guaranteed the *DL* data was taken at the same temperature. Using equation (4-1) a value of emissivity was calculated for every painted section, the results of those sections that are between 15 – 25 μm is shown in Figure 4-7. The coefficient of variation was calculated for each section as well to provide a measure of the noise for each thickness of paint; these results are shown in the error bars in Figure 4-7. There are error bars on the RS Matt Black, but they are so small (the largest is scatter is a 0.1% coefficient of variation) that they are not visible in the figure. From the results of the blackbody tests, Electrolube has a mean emissivity of 0.92 when compared to the blackbody and RS matt black has a mean emissivity of 0.91; Electrolube is a slightly more emissive paint coating. However, the scatter in the Electrolube emissivity results, as well as in the thickness measurements of paint coating itself, suggest that RS matt black will provide a more reliable and repeatable measurement of the thermoelastic response.

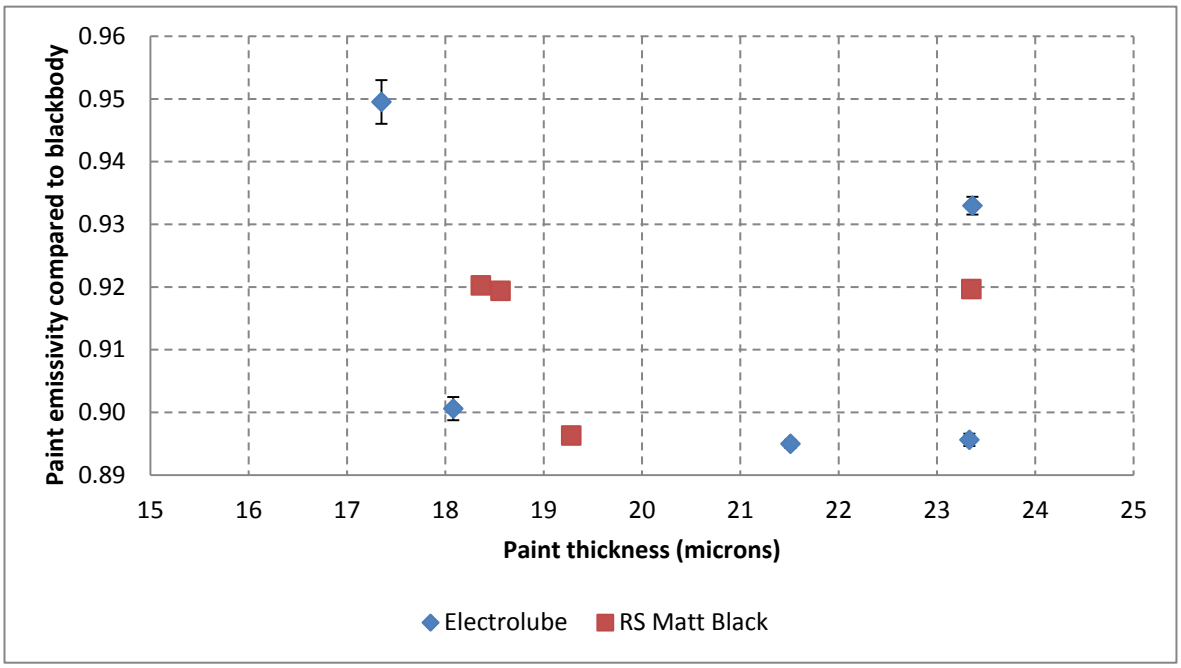

Figure 4-7 – The emissivity results when each painted section was divided through by the reference IR data taken using the blackbody.

4.3.3 Thermoelastic response

The 316L stainless steel strip specimens used in the previous test are used in the tests to assess the thermoelastic response recorded from each paint type. The TSA tests were performed using an Instron 8800 servo-hydraulic test machine with the specimens loaded directly via the grips. To accommodate the section of the specimen that needed to be gripped

at either end of the test specimen, the six painted sections shown in Figure 4-6 had to be removed and five painted sections could be fitted onto each test specimen. The layout of the painted sections is shown in Figure 4-8. The specimens were painted using passes of paint, 1 to 5 passes this time, and the thickness of the paint was recorded after the TSA tests had been carried out. This is because the paint thickness probe can cause small marks in the surface of the paint due to the hard tip of the probe, to avoid damaging the surface thickness measurements should be made after the test has been completed if possible.

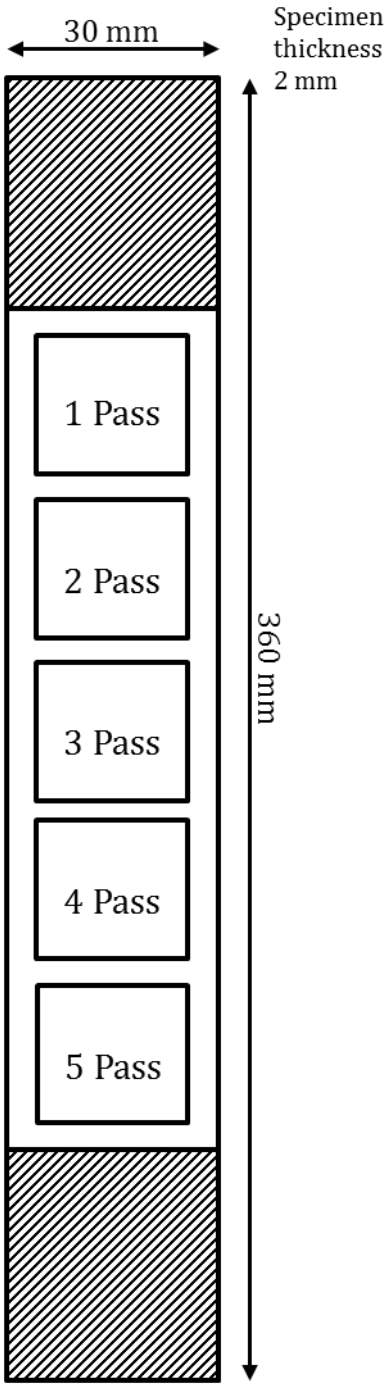

Figure 4-8 – Painted 316L stainless steel strip specimen.

The specimen was loaded cyclically with a load of 4±3 kN at a frequency of 10 Hz. This load range provided an applied tensile stress of 98.7 MPa to each specimen. The value of thermoelastic constant was calculated for each painted section, and the results of the test for all sections that are within 15-25 μm is shown in Figure 4-9. For reference, the value of the thermoelastic constant for 316L stainless steel (4.63×10^{-12} Pa^{-1}) as calculated in [17] is shown by the black line. The RS matt black paint provides a reading of thermoelastic constant for 316L much closer to the literature value than the Electrolube paint. The coefficient of variation from each painted section was calculated as well and is shown as the error bars on Figure 4-9. The scatter in the results of the RS matt black are smaller than the Electrolube as well. Therefore, RS matt black will be used with future TSA tests and the paint coating thickness will be checked before each TSA test.

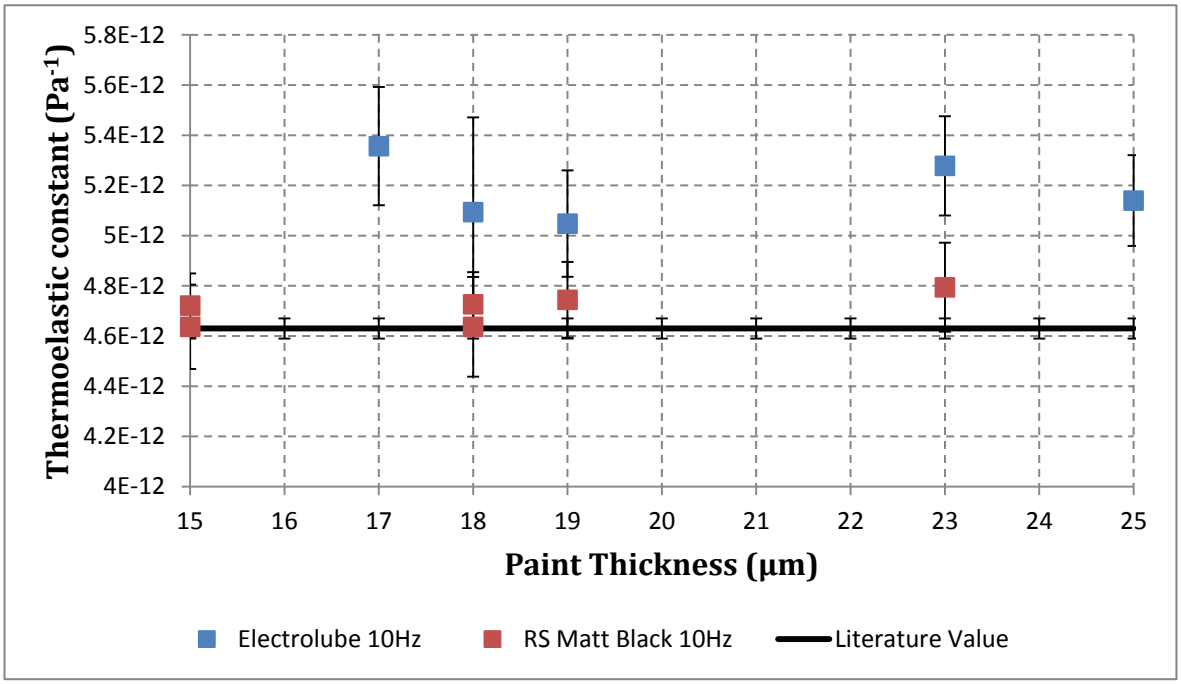

Figure 4-9 – Thermoelastic response of both the Electrolube and the RS matt black paint plotted against the thickness of the paint applied.

4.4 Summary

The change in thermoelastic constant driven by the change in plastic strain is very small, so it is necessary to reduce the error in the experimental technique when applying TSA to a specimen. The misalignment in the test machine grips has been investigated and the bending moment this was applying to specimens has been corrected by an Instron engineer. The rotation of the lower actuator, and the torsion this applied through the length of the specimen, has also been corrected through the use of a collar that clamps the actuator into a fixed location. The influence of reflections has been considered in the thermoelastic data, in

future TSA tests this will be corrected for when calculating $\frac{\Delta T}{T}$ and K by using an averaged value of T if reflection is putting an error in the data.

The requirements of the paint coating have been described, and after a change in formulation of the previously recommended paint for TSA a series of studies were carried out. These studies investigated the surface finish of different paints, the effect of acetone residual remaining on the surface after cleaning, and also the emissivity and behaviour of the paint during TSA. The conclusion of the studies is that the new formula RS matt black is still the most effective paint for use with TSA and should be used where available.

Chapter 5: Demonstration of synthetic bitmap on a welded mock-up

5.1 Introduction

When using TSA to assess the amount of plastic strain a component has experiencd it is necessary for a reference dataset of thermoelastic response from a component containing no plastic strain to be available. For a laboratory specimen this is something that can be generated from a physical reference specimen alongside the specimen being assessed. For a component from industry, however, a physical reference specimen will not be available. In Chapter 3 it was shown that it is possible to generate a synthetic bitmap of a hole-in-plate specimen that provides a reference dataset similar to that acquired experimentally. The process of synthetic reference bitmap generation is used to create a reference bitmap for a welded mock-up cut from a double bead-on-plate specimen.

The aim of creating the synthetic reference bitmap is to use it to find the regions that have undergone plastic strain in the welded mock-up. The TSA data generated by a synthetic bitmap is subtracted from a bitmap of actual TSA data to identify the regions that have experienced plastic straining. The process for applying the synthetic bit map is provided in Figure 3-1. The experimental thermoelastic response $\left(\frac{\Delta T}{T}\right)_{exp}$ is obtained from the IR data during the experiment and stored as a bitmap. The synthetic reference thermoelastic response $\left(\frac{\Delta T}{T}\right)_{FEA}$ is created from a FE model that does not contain any effects from the welding process, using the process explained in chapter 3. The resultant bitmap should show a zero response except where there is plastic strain causing a change in the thermoelastic constant.

The shape of the welded mock-up was obtained using a camera with a macro lens, which provided a high resolution image of its geometry. The macro image was digitised to provide an accurate FE model, from which the synthetic bitmap could be created. To aid in validating the use of a synthetic bitmap, a physical reference specimen of the digitised welded mock-up geometry was manufactured using water-jet cutting.

The chapter describes the design and validation of the Mock-up A specimen. This mock-up was designed to have simple weld geometry with no deformation of the bulk material due to the differential cooling effects after welding. The welding and cutting processes have been modelled by Elise Chevallier in a parallel PhD project to provide the predicted plastic strain generated by the welding process. TSA data has been taken from the welded Mock-up A, and

the design process of the synthetic bitmap to provide a reference dataset is described. The resultant bitmap is compared to the plastic strain predictions from the FE model.

5.2 Design and manufacture of Mock-Up A

5.2.1 Definition of welded mock-up

The first step of the process for the utilisation of a synthetic bitmap as a reference bitmap is to create a welded specimen with sufficient plastic strain for which there is a detectable difference in thermoelastic response due to the plastic straining. To create this welded specimen it was decided to use a "mock-up" approach similar to that used by industry when validating FE models. Industry uses mock-ups because it is not always possible to obtain measurements from the components being assessed, so samples of welds and other components are made that can be analysed in a laboratory. The part of the structure being assessed is created to scale (sometimes 1:1) and measurements are conducted on the mock-up to provide information, e.g. calibration information, to validate the results from an FE model.

The mock-up described in this chapter is the first of a series of mock-up specimens, designed for the RESIST project, that have an increase in the complexity of their base geometry, and also the weld type and weld geometry. The first mock-up, known as Mock-Up A (MU-A), was designed to fit the following criteria:

- Have a clear HAZ through the cross-section of the specimen.
- Not suffer from macroscale deformation as a consequence of the heating and cutting process.
- Be of a geometry that can be cyclically loaded in a servo-hydraulic test machine and has the welded section that can be seen in the field of view of an IR detector so TSA can be performed on the welded section.

5.2.2 Manufacture of MU-A

To meet these criteria it was decided that MU-A would be manufactured from a plate of 316L stainless steel. On this plate, two weld beads were produced using manual metal arc welded at the same time and positioned on opposing faces of the plate. Three MU-A specimens were then machined from the middle of the plate using EDM so the HAZ through the cross section of the plate could be assessed using TSA. The general design of the bead-on-plate and MU-A specimens can be seen in Figure 5-1 and Figure 5-2.

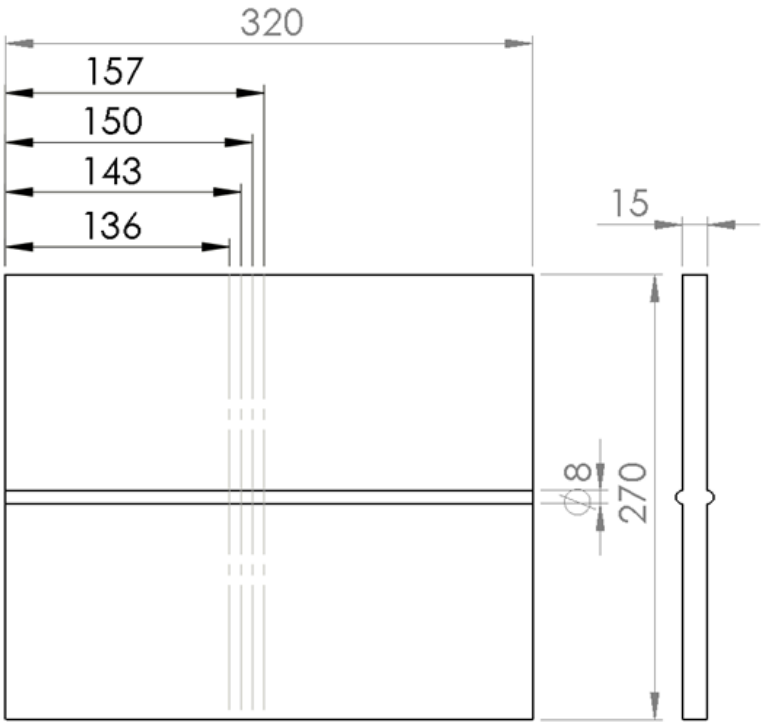

Figure 5-1 – 320 x 270 mm plate of 316L stainless steel with double weld bead across the horizontal midline of the plate. The broken likes denote the locations from which MU-A was cut.

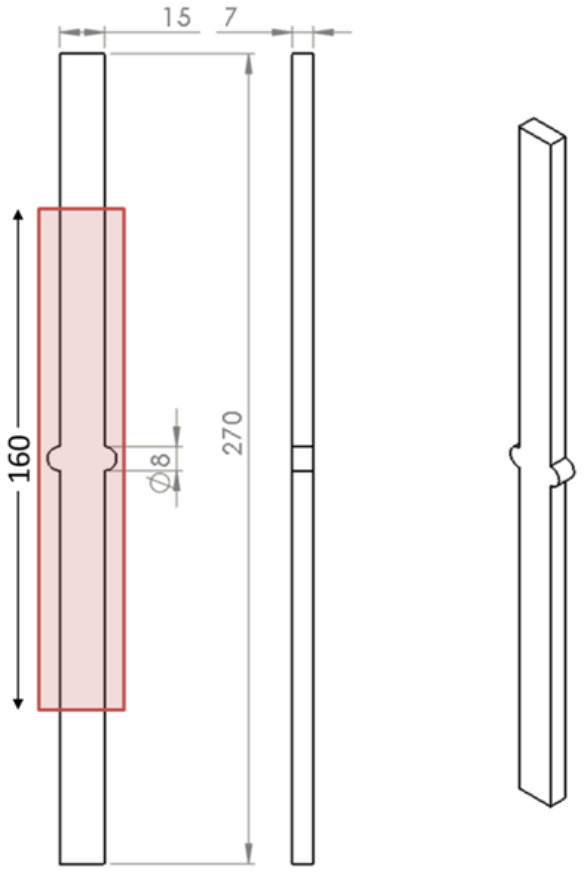

Figure 5-2 – MU-A design drawings with assumed weld bead shape. The red shaded section highlights the initial area recorded with the IR detector for TSA.

Figure 5-2 shows the design of MU-A, it is a strip of 316L stainless steel of dimensions 270 x 15 x 7 mm with a welded section at its centre. MU-A has been cut from a larger plate, shown in Figure 5-1, so that the cross section of the weld and the weld penetration can be imaged with both white light imaging and IR imaging. To perform TSA, MU-A has to be cyclically loaded to provide a stress input for the TSA equation. This will be done through gripping either end of the specimen and pulling to apply a tensile load. To ensure the stress field being applied to the specimen is uniform the specimens were designed to be as thin as possible, 7 mm provided a sufficient thickness so no deformation occurred due to the EDM cutting.

To avoid distortion due to the differential cooling rates after the welding process it was decided that a large plate with weldment on either side would be manufactured and from this MU-A would be machined. Figure 5-1 shows the single plate of 316L stainless steel with a double weld bead put on to the opposing surfaces. By using a single plate the complex relationship of joining two pieces of metal could be avoided, whilst at the same time allowing a replication of the temperature fields that cause plastic straining in an actual weld. Both welds were created at the same time and in the same direction; this allowed a symmetrical temperature field to be created and avoided distortion due to the heat source only being applied to a single surface. After welding the plate was cut along the lines as shown in Figure 5-1, a process that could cause residual stress to be relaxed and thereby create deformations in the MU-A specimens. Modelling of the cutting process (using a technique devised by RESIST project partners TWI) informed that a thickness of 6 mm would be sufficient to prevent stress relaxation deformation from taking place. Therefore, an initial trial specimen of 6 mm thickness was cut, but suffered deformation due to stress relaxation so a second trial was cut with a thickness of 7 mm which suffered no deformation.

The bead-on-plate specimen was manufactured under the supervision of Elise Chevallier at TWI Ltd. It was made from a plate of 316L stainless steel with the weld bead material being 308 stainless steel. The plate dimensions were 320 x 270 x 15 mm as shown in Figure 5-1. The welding was performed via manual metal arc welding by two technicians at TWI.

Once the welds had cooled to room temperature the three MU-A specimens were cut from the centre of the plate using EDM cutting. The centre was chosen as this was away from any boundary effects that might influence the cooling rate of the surrounding metal after the weld pass. EDM was chosen as the cutting technique because it allowed for a slow removal of material during cutting without the need to introduce a cutting tool that would influence the stress state of the surface of the MU-A specimens. The cut weld bead surface of the MU-A specimen was imaged using two different techniques. A micrograph image was taken that shows the depth of weld penetration into the surface of the 316L stainless steel plate, see

Figure 5-3. The specimens did not contain any out of plane distortion as a result of the cutting process.

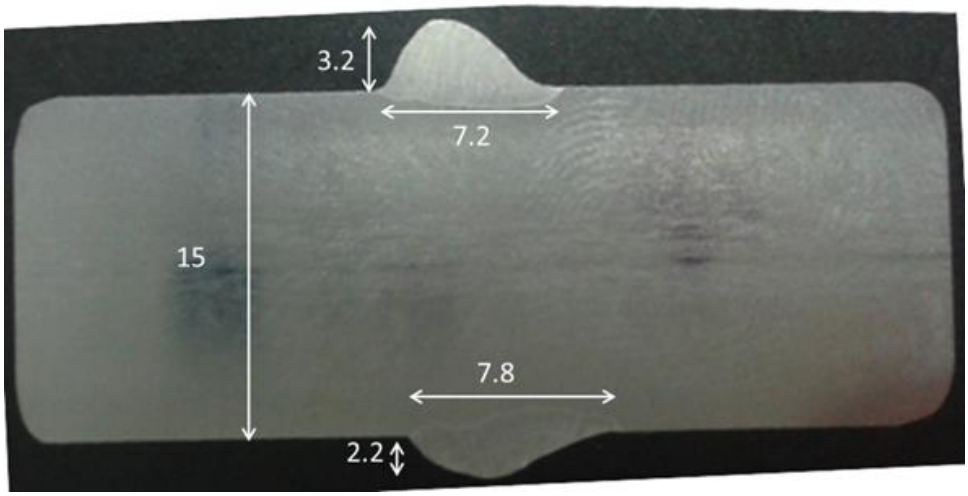

Figure 5-3 – Micrograph of the weld bead cross section taken by Elise Chevallier. The small level of weld penetration into the parent material is visible under both weld beads.

5.2.3 Modelling of Mock-Up A

To evaluate the plastic strain caused by the different cooling rates after welding, and the effects of EDM on any potential relaxation of those strains, it was necessary to model the behaviour of the 316L stainless steel plate during welding and cutting. This was performed by Elise Chevallier, and a summary of the results are presented here for completeness. This demonstrates the necessity for the weld modelling in this approach to estimate the level of plastic strain from the model. A summary of the modelling of the EDM cutting is also provided which shows that the distortion due to cutting was minimal and that the plastic strain was not significantly affected by the cutting.

Evaluating plastic strains from a thermal model

As the weld torch moves across the surface of the plate, the heat source creates a very high thermal gradient within the immediate vicinity of the weld bead. The heat dissipation takes place at various different rates dependent on the location from the heat source as it moves. This difference in heat dissipation will create an amount of plastic strain as the material expands and contracts at different rates. A prediction of this change in plastic strain was required to check that the mock-ups created would contain regions with a measurable difference in thermoelastic response. From the work of Robinson [17] it has been shown that with a small amount of plastic strain, <2%, there is a measurable difference in the

thermoelastic response of 316L stainless steel. Therefore, if the strain prediction is around this level or greater the difference in plastic strain will be observable using TSA.

A model was created in Abaqus of the whole bead-on-plate component shown in Figure 5-1. The material and thermal properties for this came from the work of Bate et al. [73]. This was an elastic-plastic model with the non-linear response modelled using an isotropic hardening model. The thermal model was calibrated for size and intensity using the micrograph in Figure 5-3 for the heat source geometry, and data taken from thermocouples attached to the plate during the welding process to measure the temperature at points along the weld line and at different distances perpendicular to the weld line. An example of the thermal model from near the end of the welding simulation is shown in Figure 5-4. In this figure the heat source can be seen at the off-scale grey section near the front of the plate, with the heat 'wake' behind it as the plate cools.

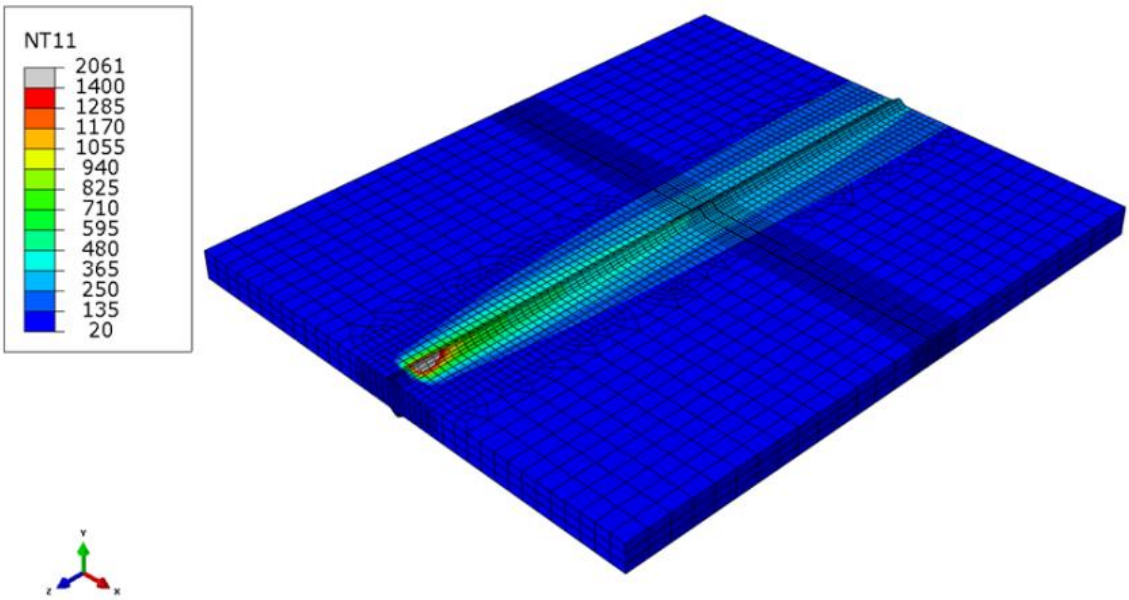

Figure 5-4 – Thermal model created in Abaqus showing the progression of the weld torch in the positive z-direction. Cooling is already taking place at the far end of the plate after the weld torch has moved on [74].

After the model had sufficient time to allow cooling to the initial temperature of 20˚C a cross section was taken from the centre of the plate in a location approximate to where MU-A has been cut from. The Equivalent Plastic Strain (PEEQ) can be extracted from this section and from the results shown in Figure 5-5 it can be seen that beneath the weld beads, in the centre of the cross section there is a small amount of plastic strain within the HAZ. PEEQ is used as this is a scalar measure of the accumulated plastic strain, similar to Von Mises stresses being a combination of the principal stresses, and is calculated using equation (5-1). Figure 1-10 shows that the maximum plastic strain occurs within the solidifying metal of weld bead as

expected. There is also a clear region in the HAZ between the weld beads where a region of plastic strain is clearly defined. The scale in Figure 5-5 is in % strain and it can be seen under the weld bead that strain is well above the 2% strain detection threshold as defined by the previous work [17].

$$\text{PEEQ} = \sqrt{\frac{2}{3}\varepsilon_{p_{ij}}\varepsilon_{p_{ij}}} \tag{5-1}$$

When modelling of the cutting was performed by Elise Chevallier, it was found that there was no influence on the plastic strain distribution, only the residual stress within the specimen. Therefore, the additional modelling step was not performed, just the thermomechanical model of the welding process. The model used to generate Figure 5-5 did not include the annealing effects that the welding would have on the material. Therefore, an updated model, shown in Figure 5-6, was constructed that did include the effects of annealing on the material.

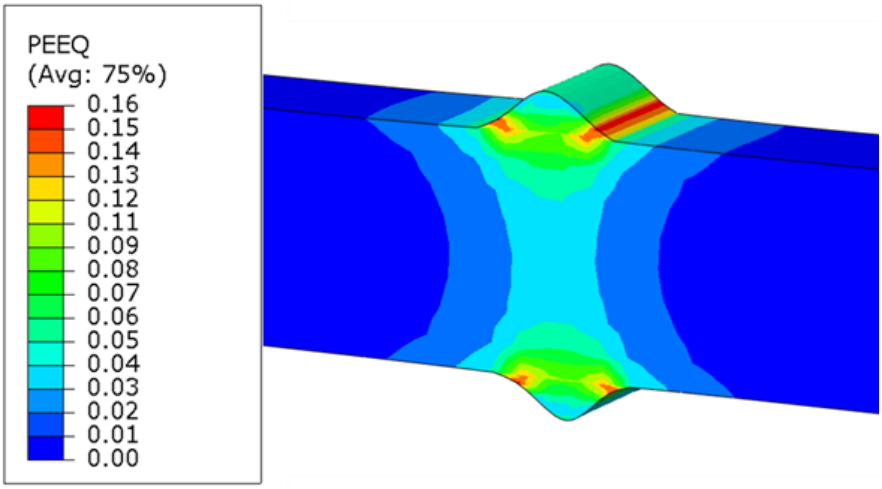

Figure 5-5 – Plastic strain results after the thermal model had simulated the welding process [74].

With the annealing effects included in Figure 5-6, there is a reduction in the predicted amount of plastic strain through the cross section of the welded plate. In the centre of MU-A, the predicted plastic strain is above the 2% threshold of detectability so there is the potential to observe a change in the thermoelastic response across the centre section. In the regions directly below the weld beads, there are strain predictions of between 4% - 6% plastic strain; therefore, when the resultant thermoelastic bitmap is calculated, this should show a larger difference in thermoelastic response than the centre section. At either edge of the weld toes, At the edge of the weld bead there is about 8% plastic strain predicted by the model, so large differences in the resultant thermoelastic bitmap should be visible at these locations.

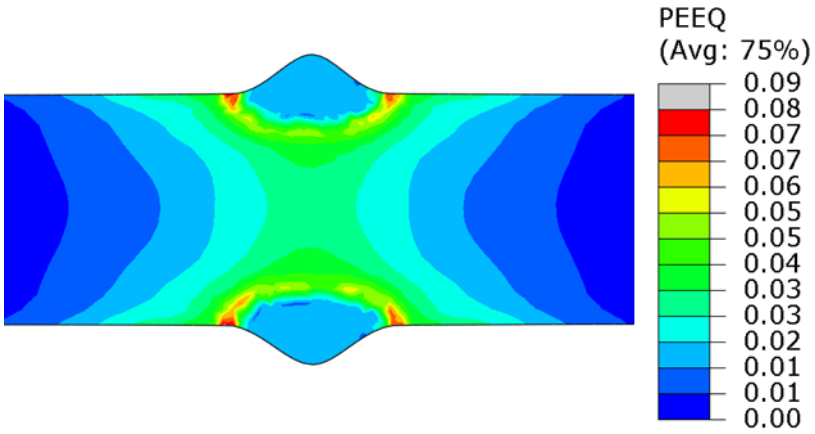

Figure 5-6 – Plastic strain prediction with annealing effects included [74].

5.3 Synthetic bitmap of MU-A

The next step in the process is to produce a synthetic bitmap of MU-A as described in Chapter 3. Although MU-A has a simple geometry compared to the hole-in-plate specimen, the weld beads are geometrically complex and so a submodel has been used to model the weld beads effectively and minimise computational expense. In producing the synthetic bitmap the weld beads were not included so that MU-A was reduced to a simple rectangular shape for the purposes of mapping into Matlab; a similar treatment was applied to the actual thermoelastic data described later in the chapter.

In Figure 5-2 it can be seen that the weld geometry has been idealised to a simple semi-circular geometry and is clear that the geometry of MU-A is more complex. Here it is shown that making this assumption in the modelling causes error and it is necessary to use the actual measured geometry of MU-A to produce the FE model. Solidworks was used to convert the measurements into a manufacturing drawing for the physical reference specimen (shown in Figure 5-7) and this was used eventually to create the FE model used for the synthetic bitmap. A comparison will be made between the data from the physical reference specimen and that generated from the synthetic bitmap to provide the validation of the synthetic bitmap. Both the synthetic bitmap and the physical reference specimen will then be used as the reference dataset for mapping the regions containing plastic strain, such that a comparison of the two can be performed.

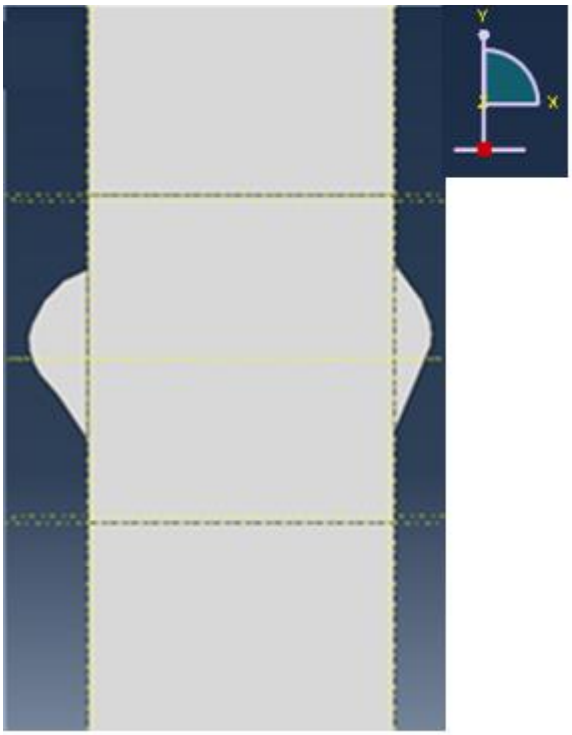

Figure 5-7 – MU-A actual weld geometry converted into a Solidworks model.

5.3.1 Evolution of the finite element model

The final FE model of MU-A used for the synthetic bitmap is an elastic-plastic model containing a multi-node spline that replicates the actual weld geometry. However, to assess if there was a more computationally efficient approach the first FE model contained a much simpler representation of the weld bead and considered only elastic material properties. The material properties, E = 197 GPa and ν = 0.3, for 316L were calculated using the stress/strain curve in Figure 5-8 [17]. For all FE models a mesh was assigned to the geometry containing reduced integration quadratic solid elements (C3D20R). In the far field sections of the model the node spacing in the mesh was 3 mm to reduce the computation time of the FEA. In the section of the model close to the weld node spacing of 0.3 mm was used because a greater mesh density was needed to capture the stress gradients around the change in geometry and was informed by the results of the mesh sensitivity study in Chapter 3. Along the top of the FE models the nodes were all fixed in the x-, y-, and z-directions to simulate the gripping of the servo-hydraulic test machine that was used in the TSA tests to apply loading to the specimen. The nodes along the bottom of the finite element model were restrained in the x-, and z-directions. A tensile stress of 124.64 MPa was applied in the y-direction to the bottom surface of the finite element model. This is the stress range applied to MU-A during TSA testing and is about 50% of the yield stress of the material.

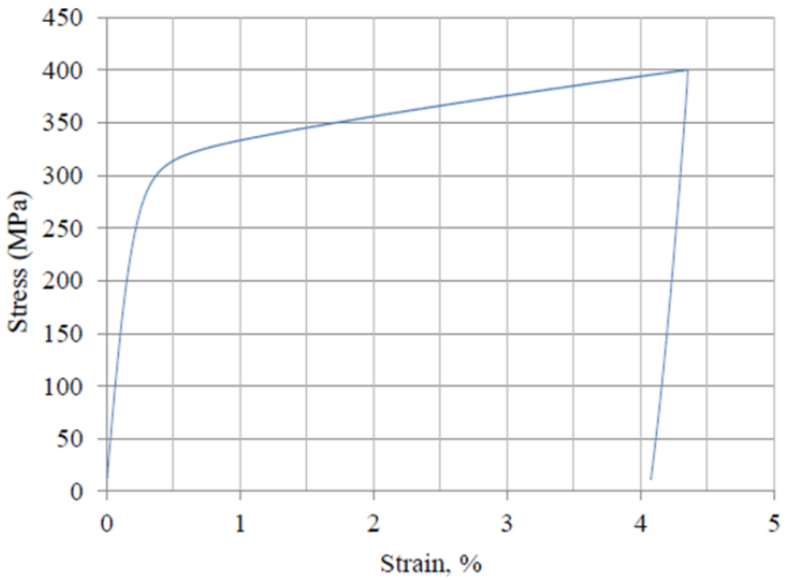

Figure 5-8 – Stress/strain curve for 316L stainless steel from [17].

Two alternative weld bead shapes were modelled that were approximations of the real weld geometry. The first used a semi-circular assumption for the weld bead geometry, shown in Figure 5-9. However, the toe of the weld bead geometry being a different shape to the actual weld geometry meant the stress concentration factor was too large. The peak σ_y at the corner of a semi-circle weld shape is 259.3 MPa. 316L stainless steel has a yield stress of 250MPa, meaning the summed resultant stress from the assumed geometry in Figure 5-9 was large enough to be causing localised plasticity effects. In the bulk of the FE model σ_y is the same as the applied stress, 124.64 MPa. There is a combination of assumptions causing the model to wrong, the linear material properties assumption and the weld bead geometry. Therefore, a second generation model was created, one that better matched the weld bead geometry.

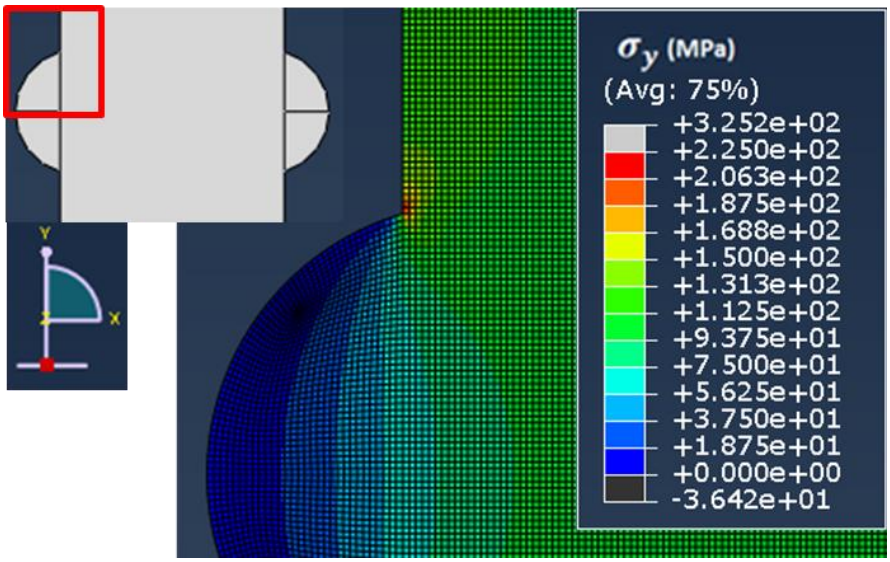

Figure 5-9 – The first FE model.

The second assumed geometry still used the semi-circle to assume the weld bead on the left side of MU-A, however, on the right a triangle with the corners smoothed using a filleting tool has been used to simulate the weld geometry on the right hand side, see Figure 5-10. Peak σ_y under the edge of the semi-circular weld bead is still 259.3 MPa but under the edge of the smoothed triangle geometry peak σ_y is 231.8 MPa. The FE model still reported a value of σ_y away from the weld as being 124.64 MPa. Instead of trialling further assumed geometries the third FE model used the real geometry of the weld bead.

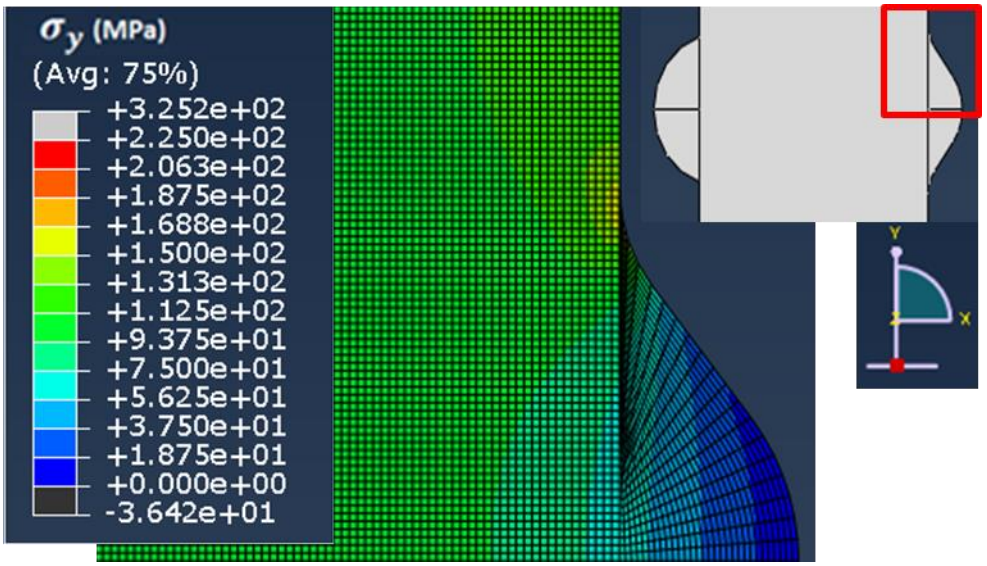

Figure 5-10 – The second FE model.

A third FE model was created in Abaqus that used the Young's modulus derived from Figure 5-8, Poisson's ratio is the same as reported in [17]. This model included the exact weld bead geometry so any geometric effects on stress, e.g. stress concentration effects, would be precisely modelled in the FE model. A macro image of the weld bead, shown in Figure 5-11, was imported into Solidworks 2013 and a multi-nodal spline applied to the boundary of the weld bead. From this, the bulk length of the specimen was then modelled giving an FE model of nominal dimensions 207 x 15 x 7 mm and containing an accurate representation of the weld geometry, see Figure 5-12.

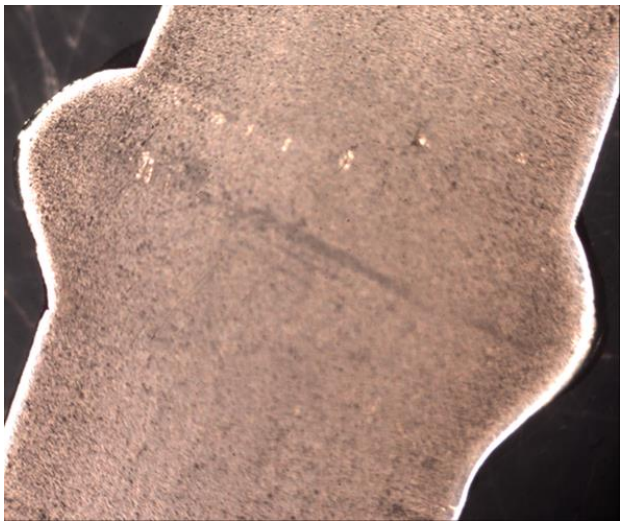

Figure 5-11 – Macro image of the welded cross section.

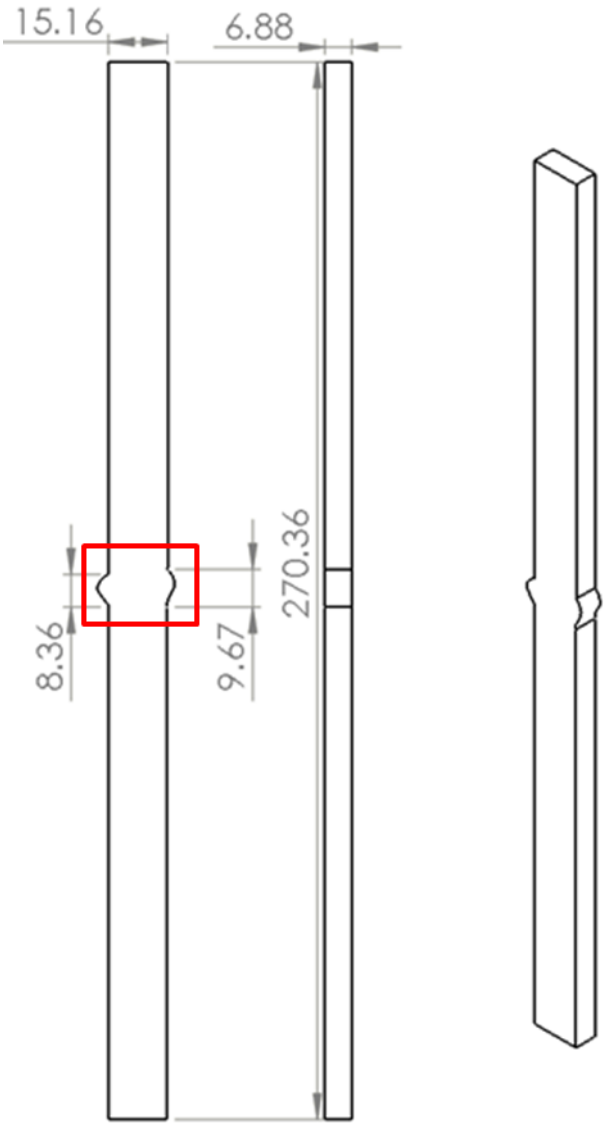

Figure 5-12 – Design drawing of the FE model containing the real bead geometry.

In an attempt to increase the computational efficiency of the FE model a submodelling approach, similar to that in Chapter 3, was used. A submodel of the central section of MU-A (highlighted by the red box in Figure 5-12) is used such that a greater mesh density can be used within the submodel. The mesh of the global model has an element size of only 1mm (see Figure 5-13) and the submodel has an element size of 0.3mm. The global model could be run using an element size of 0.3mm but it took significantly longer to solve (~12 hours to solve global model); the submodel approach took only 45 minutes to solve. The global model in Figure 5-13 shows the stress concentrations at the edge of either weld bead; however, the stress gradient is contained within a single element meaning it cannot be identified using the coarse mesh. The submodel of FE model 3 with the real geometry is shown in Figure 5-14 alongside a contour plot of σ_y. The peak value of σ_y at the edge of a weld bead in FE model 3 is 258.0 MPa. 316L has been calculated to have a yield stress of 250 MPa, therefore despite the reduction in peak stresses at three of the weld bead toes, an elastic-plastic model is required to fully model the localised plastic effects at the regions containing stresses above the yield stress.

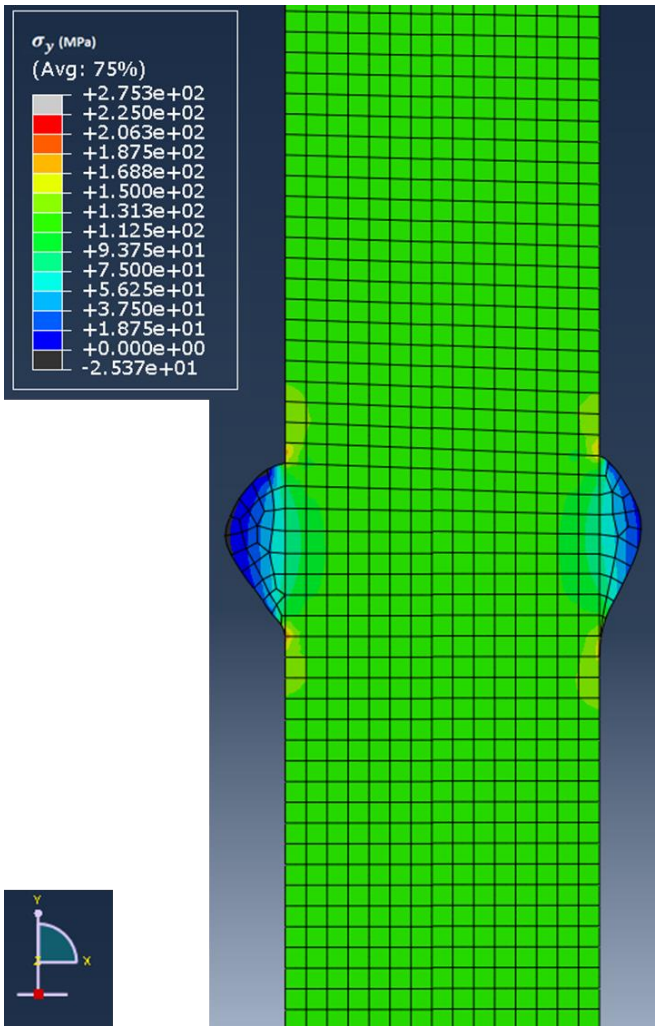

Figure 5-13 – Global model used to generate displacement boundary conditions for the submodel in Figure 5-14

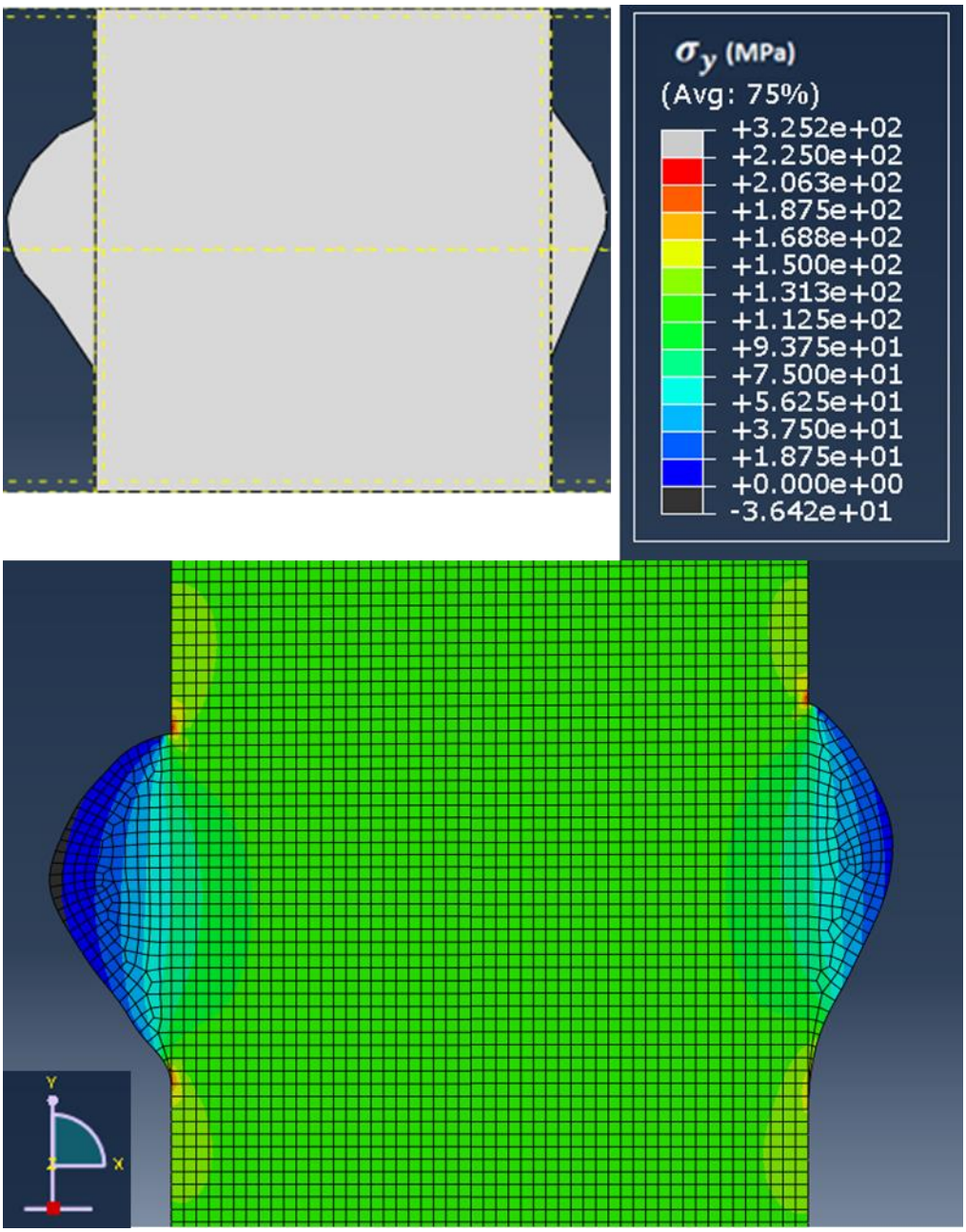

Figure 5-14 – The third FE model.

The evolution of the three linear models and their synthetic bitmaps is shown in Figure 5-15. From left to right is a) Model 1, b) Model 2, and c) Model 3. As expected, they all show the same value of $\frac{\Delta T}{T}$ in the regions away from the weld beads. The decreasing stress concentration effect at the edge of the weld beads can be seen between each bitmap.

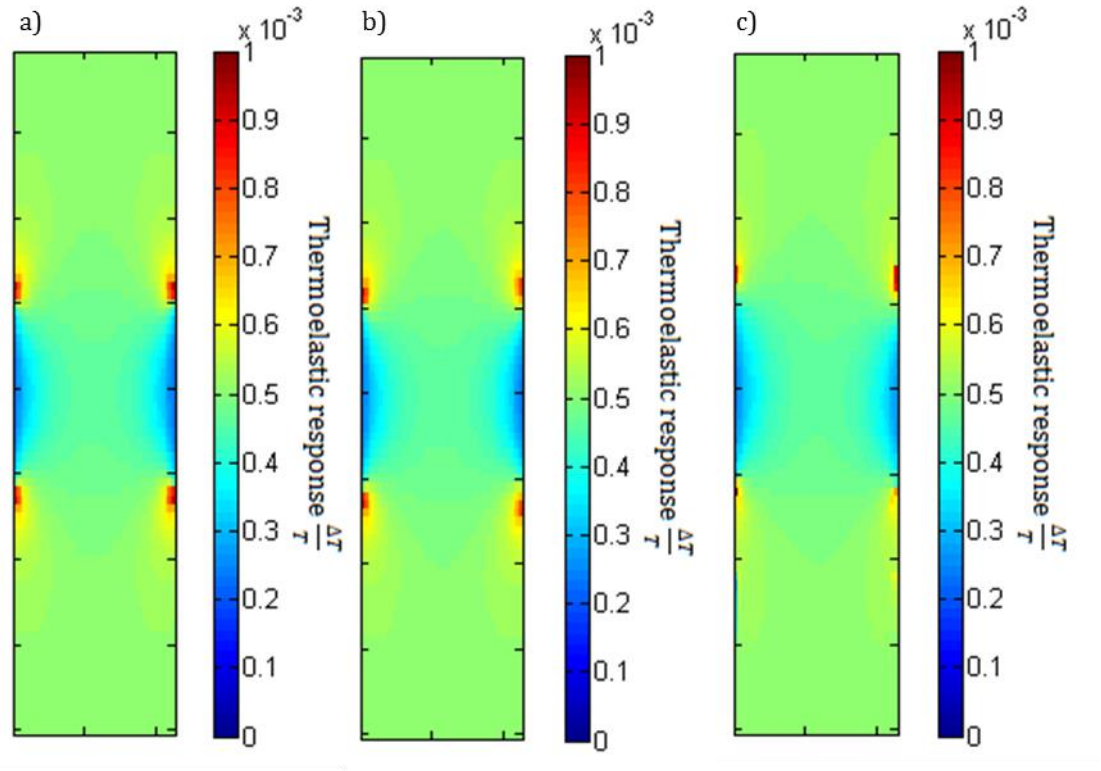

Figure 5-15 – Thermoelastic bitmaps constructed using the stresses in the FE models 1-3. a) FE model 1, b)FE model 2, c) FE model 3

The FE model containing the real weld contours was next used to construct a synthetic bitmap using elastic-plastic material properties. The stress/strain plot in Figure 5-8 was used to calculate the material properties reported in Table 5-1.

Elastic-plastic material properties of 316L stainless steel	
Young's modulus, E	197 GPa
Poisson's ratio, ν	0.3
Yield stress, σ_Y	250 MPa

Table 5-1 – Elastic-plastic material properties of 316L stainless steel [17].

As with the first synthetic bitmap the principal stress data needs to be output from the finite element model. Contour maps of both σ_y and σ_x directly from the global model are shown in Figure 5-16 so the weld bead geometry and the effects on the stress fields can be visualised. The weld bead geometries have been removed with a submodel from the final datasets, but the influence of the change in geometry can be seen in the output stresses from the finite element model. As noted in the previous models the weld bead is carrying very little stress and as expected σ_x is very small away from the weld as the specimen is dominated by the y-direction stress. In the vicinity of the weld σ_x is negative and large (around 40% of the applied stress) because of the constraining effect of the weld bead. However, it should be

noted that there is a stress concentration above the weld bead of 224.34 MPa and below the weld bead of 204.27 MPa. When the σ_y stress in the bulk of the FE model is interrogated the reading is 124.64 MPa, the same as the stress applied to the FE model. At the edge of the weld bead, there is a localised area containing shear stress, 76 MPa at the top edge and -65MPa at the bottom edge. The region containing shear stress is localised to the weld toes, and reduces to zero away from the change in geometry causing a stress concentration.

The σ_x and σ_y stress outputs were summed to give a value identical to $(\sigma_1 + \sigma_2)$ for every node output from the finite element model. The nodal values are arranged using the Matlab code in the Appendix into a matrix of equal size to TSA data taken from MU-A; see section 5.4. Once in the final size and shape for comparison with the TSA data, the synthetic bitmap needs to be converted into values of $\frac{\Delta T}{T}$. The value of thermoelastic constant used to perform the conversion is one that was experimentally derived in [17] as $K = 4.63\text{x}10^{-12}$ Pa^{-12}. The final synthetic bitmap of MU-A is shown in Figure 5-17. The stress concentration effects at the top and bottom of the weld bead can be seen on either side of the specimen.

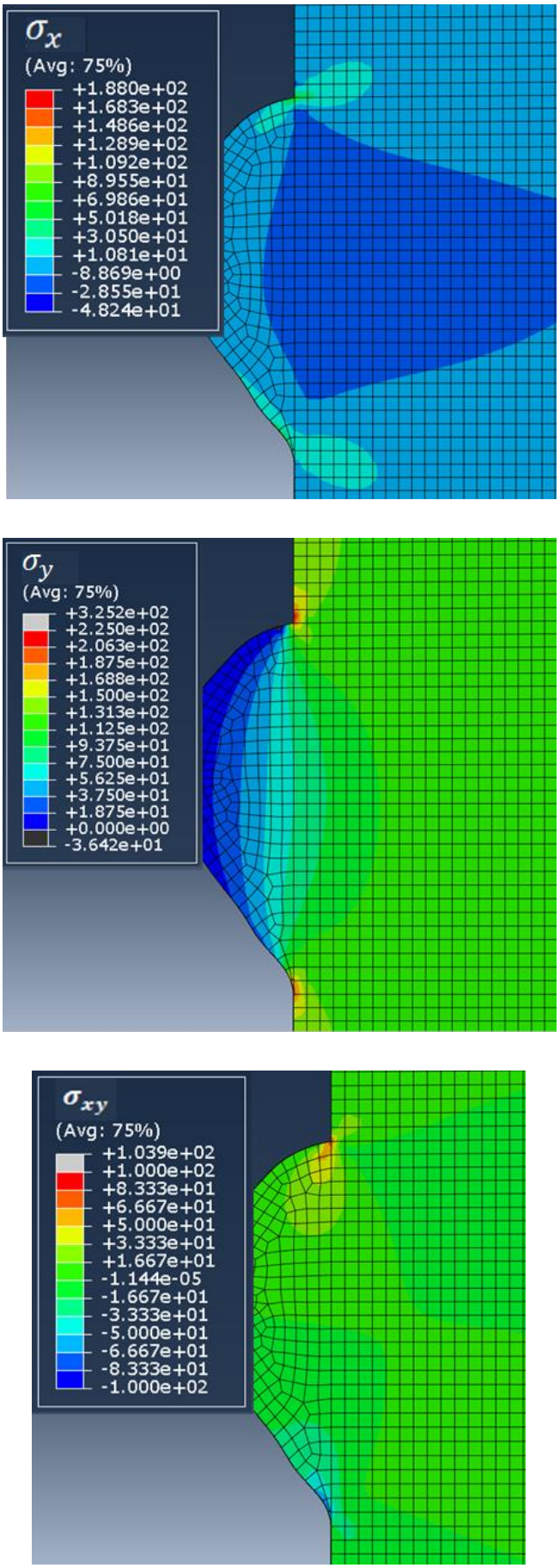

Figure 5-16 – Stress contour maps from the left hand weld bead of the MU-A finite element model.

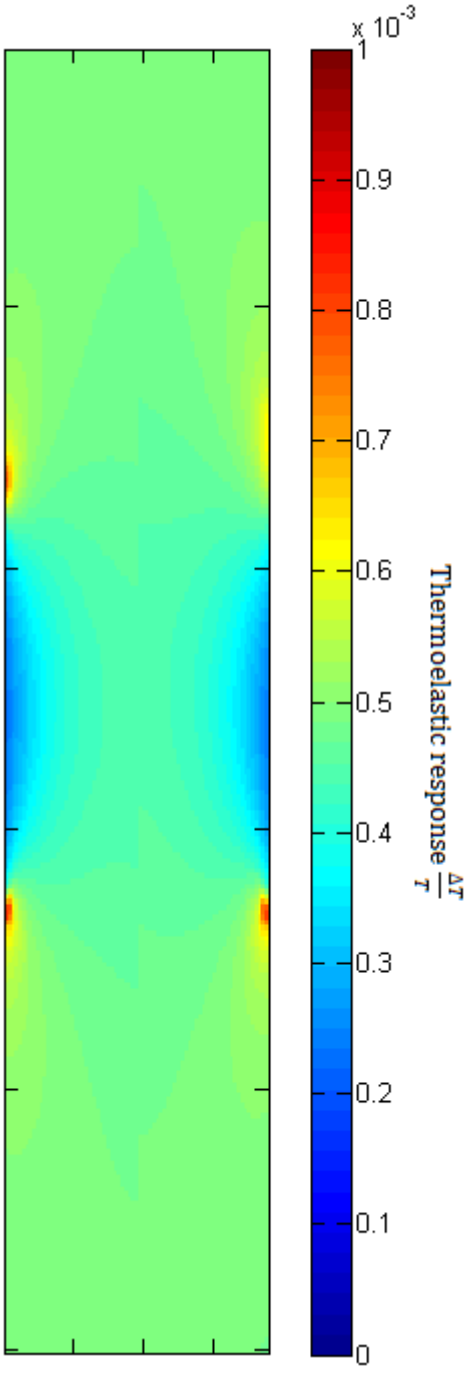

Figure 5-17 – Synthetic bitmap of MU-A using the actual geometry of the weld bead.

5.3.2 Physical reference specimen

To validate the synthetic bitmap it was decided that a physical reference specimen would be manufactured. A design drawing was created using the Solidworks model used to create FE model 3 in the development of the synthetic bitmap, Figure 5-12. This geometry was converted into a .dxf file, which is a format used by computer controlled manufacturing, that was used to manufacture by water-jet cutting a reference specimen from 316L stainless steel. The reference specimen contains identical weld bead geometry to MU-A, but without any

welding or heating effects. The reference specimen was cut from cold-rolled 316L stainless steel. Water-jet was used to manufacture the reference specimen because it provides an ability to accurately follow a complex geometry without any heating of the metal. MU-A and the reference specimen can be seen in Figure 5-18.

Figure 5-18 – A photo of both MU-A (top) and the physical reference specimen (bottom). The weld geometries of both have been enlarged in the red boxes to the right.

5.4 TSA and comparison to plastic strain predictions

Two rounds of testing were undertaken to use the synthetic bitmap as the reference dataset for the proposed plastic strain mapping using TSA approach. The first tests had a large proportion of MU-A prepared with black paint and TSA data was taken of a large region. However, the results did not show the HAZ in a great amount of detail. Therefore, a second set of data was recorded which shows the HAZ in much greater detail. This second set of data allowed for a much closer examination of the region under the weld toes, and a comparison to the plastic strain predictions was made using this set of data.

5.4.1 Experimental methodology

TSA was performed on the MU-A and physical reference specimens to provide the $\left(\frac{\Delta T}{T}\right)_{exp}$ dataset that is used with the synthetic reference bitmap to find the resultant bitmap of the differences between the two. With the knowledge acquired during the experiments in Chapter 4 the test specimens were prepared with a light abrasion using 400 grit SiC paper before cleaning with acetone and rinsing with water. The specimens were then prepared with a thin coating of RS matt black paint, paint thickness measurements are provided in Table 5-2. After the surface preparation, the specimens were mounted in an Instron 8800 100 kN servo-hydraulic test machine and loaded to 7.5 ± 6.5 kN (71.9 ± 62.3 MPa) at a frequency of 10 Hz. This loading provided a tensile stress range of 124.6 MPa away from the weld in MU-A. A Cedip Silver 480M IR detector was used to record the thermoelastic response of the specimen surface under loading.

Specimen	Number of measurements	Mean (μm)	Standard Deviation (μm)	Coefficient of Variation
MU-A	16	20.14	0.286	1.42%
Reference	16	22.13	0.708	3.20%

Table 5-2 – RS matt black paint thickness measurements over the MU-A and Reference specimens.

After recording the thermal response, the data has to be processed to provide an array the same size and units as that from the synthetic bitmap work described in Section 3.4. This was performed using Altair LI which utilises a lock-in approach that matches the temperature change to the loading cycle applied to the specimen. This provides three sets of data; T, ΔT, and the phase data as described in Chapter 2. The T and ΔT datasets were input as 255x320 matrices into Matlab. In Matlab the datasets had the background data cut along with the weld beads to provide rectangular datasets that are more easily matched to the synthetic bitmap generated by the FE model. In Matlab the datasets have been divided by each other to create the $\left(\frac{\Delta T}{T}\right)_{exp}$ dataset. With the data in this format it is possible to compare against the synthetic bitmap data created in Section 5.3. The ΔT and T datasets in their raw form are shown in Figure 5-19, whilst the combined $\frac{\Delta T}{T}$ datasets from Matlab that are used with the synthetic bitmap is displayed in Figure 5-20. Figure 5-20a) shows the $\frac{\Delta T}{T}$ bitmap from the reference specimen, and at the top and bottom edge of the weld bead are stress concentrations that match the stress concentrations estimated by the FE model used to construct the synthetic bitmap. The stress concentrations are not present in the MU-A bitmap in Figure 5-20b) and so the heating during the welding process must be producing a complementary residual stress in that region which is not present in either the synthetic reference of the physical reference bitmaps. In the T raw dataset there is a slight heat bias, with the bottom of MU-A being slightly hotter than the top. This bias was accounted for in the calculation of $\frac{\Delta T}{T}$ by using an average value of T calculated using the whole surface of MU-A.

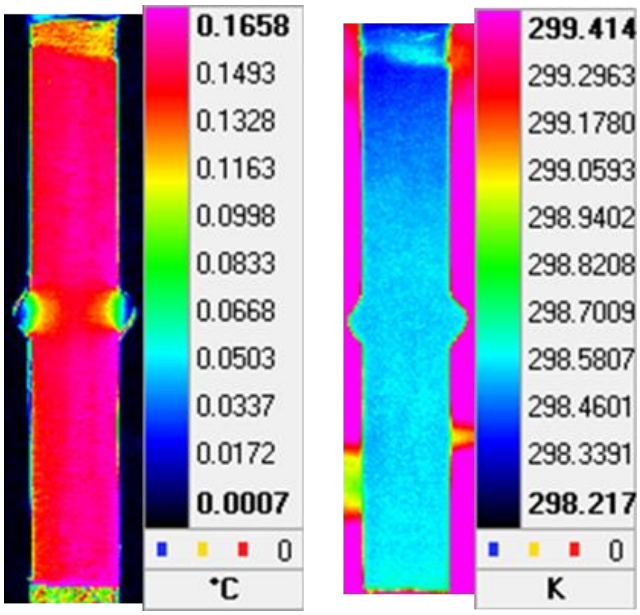

Figure 5-19 – The ΔT (left) and T (right) images of MU-A after processing through Altair LI displayed using the Altair software

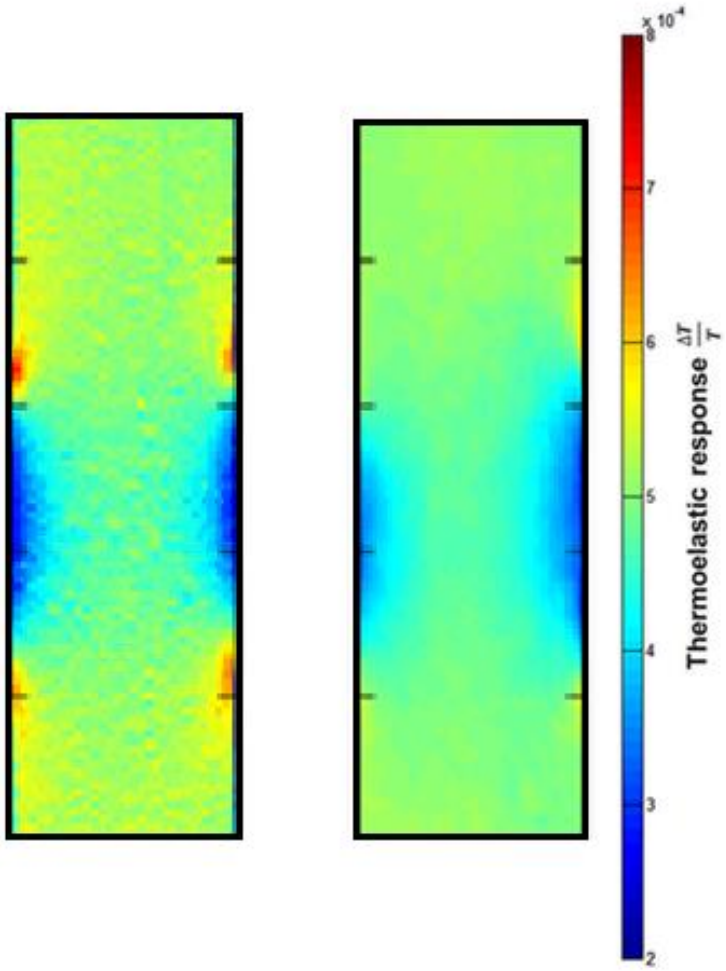

Figure 5-20 – $\Delta T/T$ dataset of a) Physical reference specimen, and b) MU-A displayed using Matlab.

5.5 Results from initial experimental investigation

Experiment results

The TSA bitmaps of MU-A and the physical reference specimen are shown in Figure 5-20. The average thermoelastic response of the specimen away from the effects of the welded region, or weld geometry in the reference specimen, has been calculated from all data points in the regions above and below the welded sections. The thermoelastic response of MU-A is 5.11×10^{-4} with a coefficient of variation of 1.36% and the thermoelastic response of the reference specimen is 5.13×10^{-4} with a coefficient of variation of 3.06%. The difference in the coefficient of variation between MU-A and the reference follows the difference in the coefficient of variation between the paint coating on each specimen.

To provide a verification of the synthetic bitmap, the synthetic reference $\frac{\Delta T}{T}$ bitmap was subtracted from the physical reference TSA data; the resultant bitmap is shown in Figure 5-21. If the synthetic bitmap has faithfully recreated the reference TSA data it should provide a resultant bitmap of near zero with a very small standard deviation. The mean $\frac{\Delta T}{T}$ value across the whole bitmap is 9.61×10^{-7}, a factor of 10^3 smaller than the thermoelastic response of the reference or welded specimen. The standard deviation of the resultant bitmap in Figure 5-21 is 6.82×10^{-6}, which is around 100 times smaller than the mean response. Deviations from the mean response have been shown in Figure 5-23 to be as large as 6×10^{-4}, therefore the change in thermoelastic response caused by welding is above the standard deviation of the reference bitmaps.

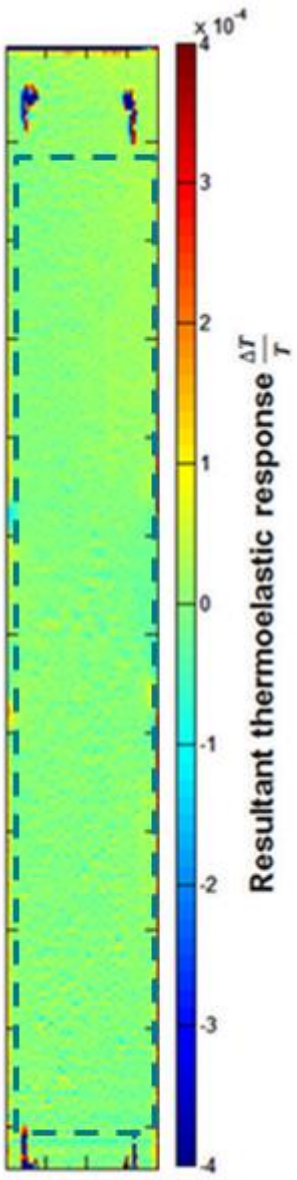

Figure 5-21 – Validation of the synthetic bitmap by subtracting it from the physical reference bitmap.

Figure 5-22a) is the welded TSA data minus the physical reference TSA data and Figure 5-22b) is the welded TSA data minus the synthetic reference bitmap. Line plots were taken from both of the resultant bitmaps and the results are plotted in Figure 5-23. The blue and the black lines are data taken from the far field of the resultant maps and are of the same order as the mean $\frac{\Delta T}{T}$ values in the first resultant bitmap. The red and green lines are from lines plotted across the specimen between the weld beads. Both datasets match closely to each other; the resultant bitmap generated using the synthetic bitmap contains a lot less noise than when the physical reference specimen is used. The same trend was seen earlier, and is because there is only one set of experimental noise in the resultant bitmap rather than the combination the noise generated in the two experimental data sets.

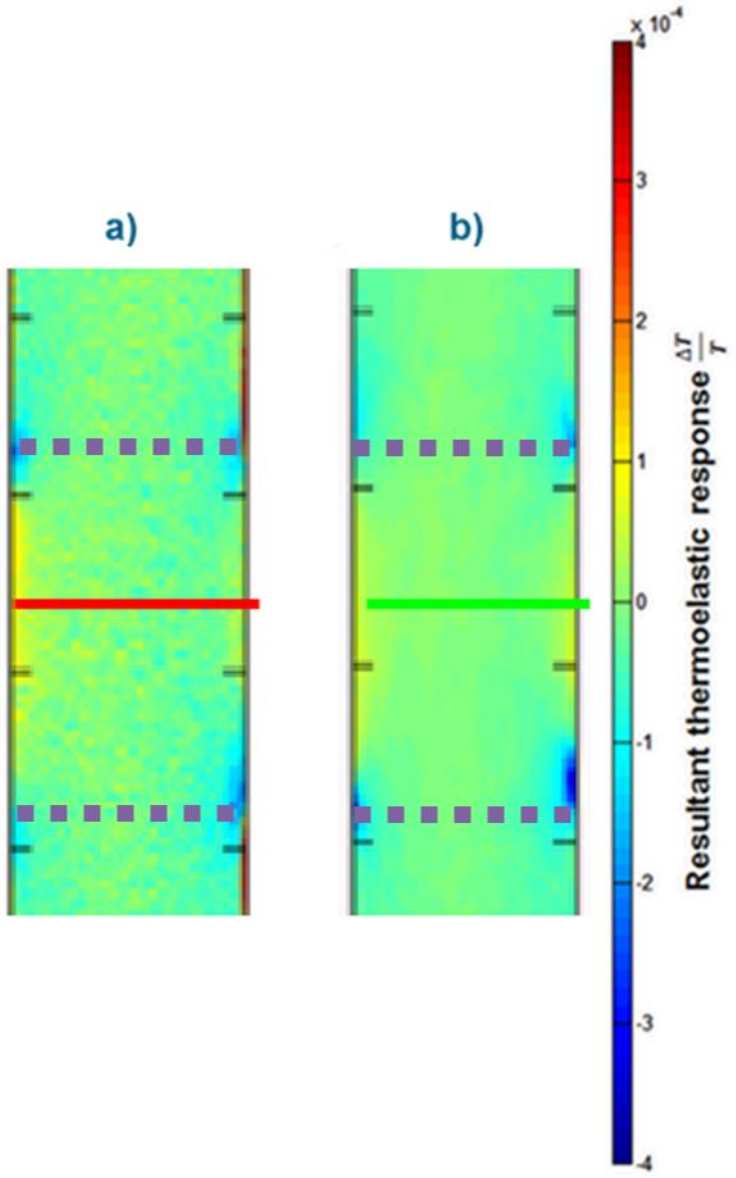

Figure 5-22 – Resultant thermoelastic bitmaps. a) Welded bitmap – physical reference bitmap. b) Welded bitmap – synthetic bitmap.

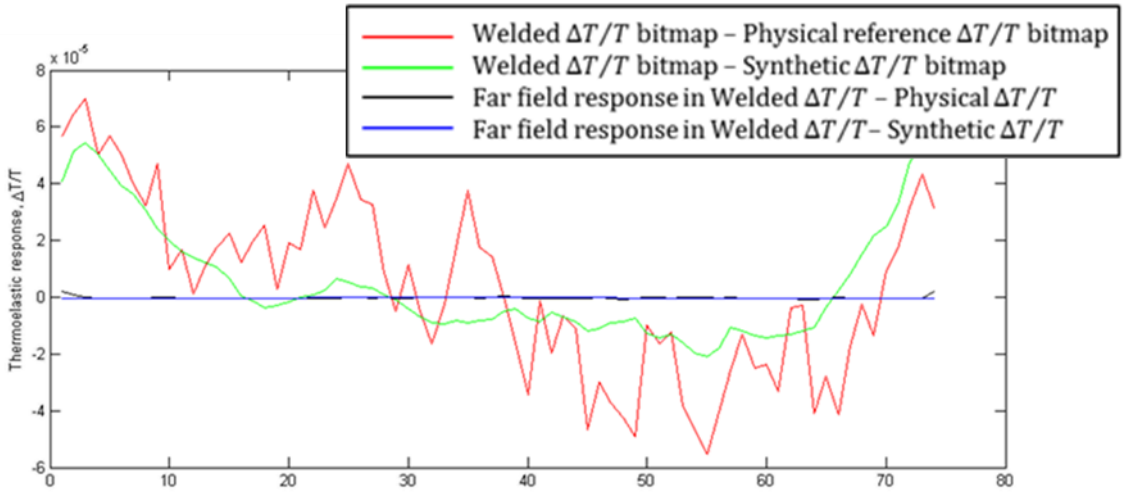

Figure 5-23 – Line plot from the location of each coloured line in Figure 5-22.

The thermoelastic data in the resultant bitmaps created using the TSA data of the welded specimen can now be compared with the plastic strain predictions in the thermomechanical model constructed by Elise Chevallier in Section 5.2.3. To facilitate the comparison of the resultant bitmaps and the plastic strain a line plot is taken across the centre of cross section between the welds. This line is then normalised against the value in the centre of the cross section, i.e. the smallest value of either strain or thermoelastic response. When the datasets are normalised in this fashion they can be plotted together and directly compared, see Figure 5-24. Across the centre of the section, where the HAZ has seen minimal plastic strain, there is a match between the resultant thermoelastic data and the plastic strain predictions. However, under one of the weld beads at the left end of the line plot, the difference between the plastic strain and the resultant plots gets much larger. This is believed to be caused by the small inclusion of melt zone under each weld toe, seen in Figure 5-3. The melted section under each weld toe will have different material properties than the parent metal as the weld metal used was 308 stainless steel, and it has undergone recrystallisation upon solidification from the molten state. These changes in material property mean the thermoelastic response of the welded specimen in those regions will not behave as expected and will not be accounted for in either the physical reference specimen or the synthetic bitmap. Therefore, the data at the two ends of the line plot, marked by the vertical green lines in Figure 5-24, should be ignored. After doing so the resultant bitmap constructed from the synthetic bitmap matches relatively closely to the plastic strain prediction. However, there is still significant scatter within the data and drawing a firm conclusion is difficult. The agreement between the blue line and the red line in Figure 5-24 is encouraging and suggests that it is possible to use TSA data of a welded component and a synthetic reference bitmap to map the regions that have undergone plastic strain.

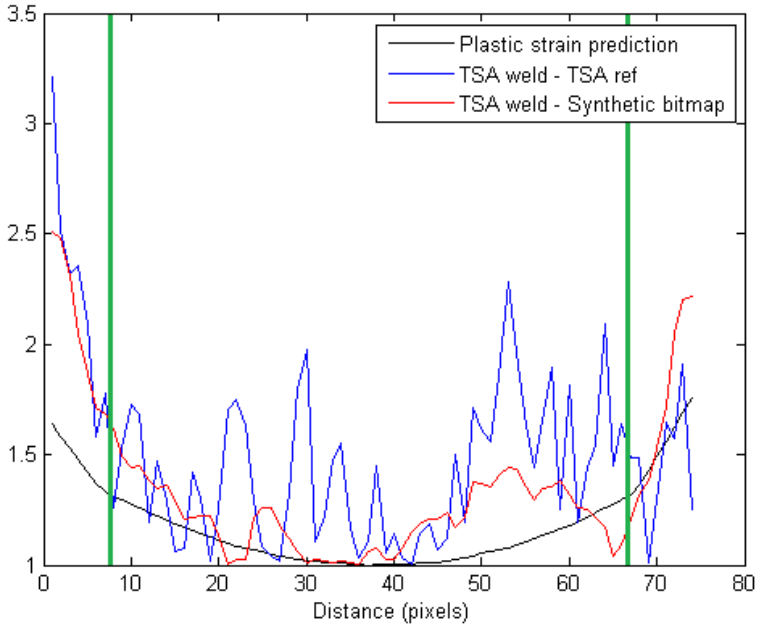

Figure 5-24 – Line plot of the normalised plastic strain and resultant thermoelastic response from between the weld beads.

In addition to the profile between the weld beads, profiles were taken above and below the weld beads as shown in Figure 5-22 by the broken purple lines. The line of resultant thermoelastic response was normalised using the value at the centre of MU-A for each line. The normalised results are shown plotted with the normalised plastic strain prediction in Figure 5-25. It should be noted that because of the symmetry in the thermomechanical model the strain prediction is the same above the weld as it is below the weld.

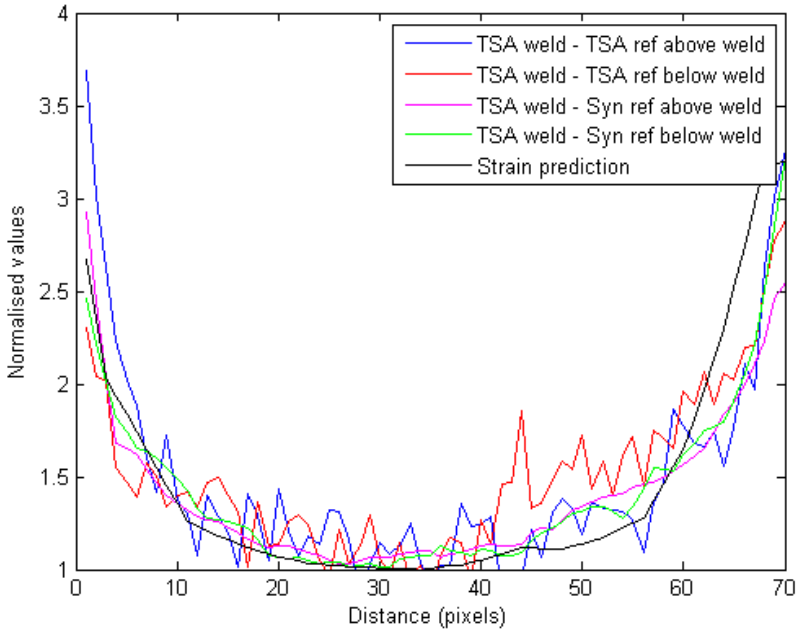

Figure 5-25 – Normalised thermoelastic response and normalised plastic strain above and below the weld bead.

There is correlation across the width of the specimen in all profiles taken, except the right hand side of the line from below the weld in the $\left(\frac{\Delta T}{T}\right)_{Weld} - \left(\frac{\Delta T}{T}\right)_{Physical}$, to the plastic strain prediction. As found in Figure 5-24, there is more scatter in the results when the physical reference specimen has been used rather than the synthetic bitmap, making a correlation harder to define. There appears to be good correlation between the results of both resultant bitmaps at the left side of the specimen. To reduce the scatter in the data and allow a clearer correlation to be drawn, further study into appropriate motion compensation should be performed.

5.6 Summary

Following from the work in Chapter 3 that showed the process required to construct a synthetic reference bitmap; a welded specimen, MU-A, has been designed and manufactured to include a HAZ within the cross section that contains varying levels of plastic strain. The plastic strain within the HAZ has been predicted by a thermomechanical model created by Elise Chevallier and was sufficiently large that it should drive a change in thermoelastic response. A synthetic bitmap was created of MU-A as well as a physical reference specimen. Both have been used as the reference data to generate a resultant thermoelastic bitmap; the resultant bitmap for both was then compared to the plastic strain predictions and it was found that there whilst a weak correlation between the plastic strain prediction and the resultant bitmaps can be drawn there are too many variables still having an influence in the final dataset. The alignment of the synthetic bitmap, mentioned in Chapter 3 has a large influence on the quality of the final resultant bitmap. This is improved, but still potentially causes a bias within the final dataset. Although every effort was made to eliminate the potential sources of error in the experimental setup, investigated in Chapter 4, these may still have an effect in the final resultant bitmaps. Motion compensation has not removed all of the effects of motion. Also, the paint is applied by manual spray painting, a more automated system providing a more uniform thickness could produce a more uniform thermoelastic response.

The next process required is to try and determine the detectable threshold of plastic strain using TSA and to derive a constant of calibration for the change in thermoelastic constant, *K*, and plastic strain in 316L stainless steel. The work is described in Chapter 6.

Chapter 6: Determining the relationship between thermoelastic response and plastic strain

6.1 Introduction

In Chapter 5 the region that contained plastic strain as a result of the welding process was shown to be detectable using TSA and a synthetic reference bitmap of the welded test specimen. It is now required to define the threshold of detectability of plastic strain when using the proposed TSA based plastic strain detection approach, and also to derive the relationship between the change in thermoelastic response and plastic strain. The thermoelastic constant is unique for each material; therefore, the relationship derived in this chapter will only be applicable for components manufactured from 316L stainless steel.

Work described in [17] derived a relationship between the change in thermoelastic constant and plastic strain using large, dumbbell specimens manufactured from 316L stainless steel. The results showed there appeared to be a linear relationship when tensile plastic strain was in the specimen; and a second, different linear relationship when the plastic strain was compressive. At the start of the present PhD work was repeated on the specimens made for [17]. However, some anomalous readings were obtained and it was not possible to repeat the work reported in [17]. The reasons for this was speculated to be possible strain relaxation over the 2 year time period and/or deformations caused by non-uniaxial loading. The deformation of the specimens was not done systematically and the deformation and the thermoelastic work took place at different locations (described in section 6.2). Therefore, it was decided to repeat the work with new specimens with improvements made to the test methodology to attempt to better validate the findings and understand the sources of error. The error sources proved difficult to eliminate, so a different specimen was designed, that was tapered in form and contained a gradient of plastic strain rather than a single constant plastic strain. The tapered specimen only contains tensile plastic strain, but the simpler specimen and test design allows the relationship between plastic strain and thermoelastic constant to be more easily defined using one test specimen and one test set-up.

6.2 Review of previous work and definition of improved methodology

Previous work [17] used large, dumbbell shaped specimens that were capable of containing either large compressive plastic strain or large tensile plastic strain (-10% to +15% plastic strain), see Figure 6-1. The dumbbell specimens were used to obtain the thermoelastic constant data for compressive plastic strain as well as tensile plastic strain; they had been designed to resist buckling under high, compressive loads. The thermoelastic response from each plastically deformed specimen is recorded and the change in thermoelastic constant is calculated by normalising against the thermoelastic constant, *K,* of a reference specimen, without plastic deformation.

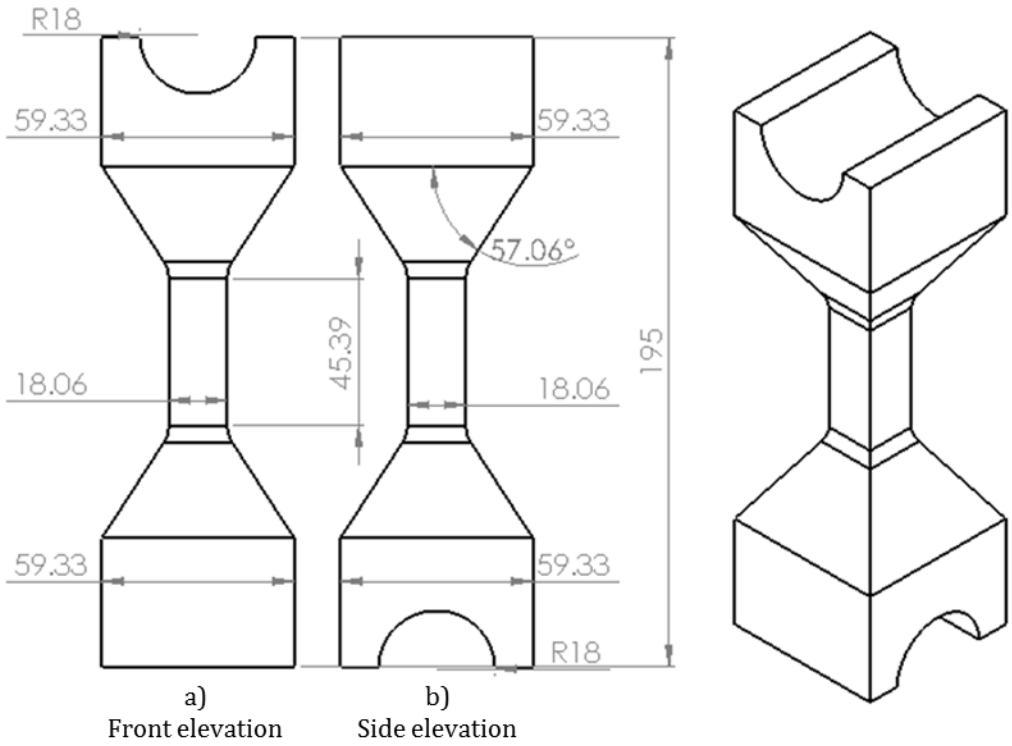

Figure 6-1 – Design of 316L stainless steel dumbbell specimens used in [17] and later the present work. All dimensions in mm.

6.2.1 Dumbbell specimen design

The dumbbell specimens were manufactured out of individual billets of 316L stainless steel. Each billet was cold rolled and the dumbbells were cut in the same orientation from every billet of steel. The design of the dumbbell specimen is shown in Figure 6-1, with the key dimensions added to the design drawing. The shape and dimensions of the dumbbells were designed to fit the following criteria:

- Be able to contain tensile plastic strain without necking.
- Contain compressive plastic strain without buckling.
- Have a single geometry that can be loaded in either compression or tension.

The loading of the dumbbell specimens was conducted in a specially designed rig which was mounted in the test machine grips, shown in Figure 6-2 and Figure 6-3. The tensile load was imparted through the angled sections in the grip and the specimens. The compressive load was imparted through a roller positioned in the groove at either end of the specimen and in the grips. It should also be noted that the grips are different with the section that is gripped by the machine orientated at 90° to each other; this was done to ensure a uniform loading to be imparted into the specimens.

These design criteria were satisfied by the following solutions:

- The relatively thick central section, nominally 18 mm in each direction, provides resistance to buckling when compressive loading (≈ -130 kN (≈ -400 MPa) for -10% strain specimen) is applied through the centroid of the test specimen.
- The filleting of the edge between the angled surface and the straight, central section reduces the stress concentration to ensure the plastic deformation occurs evenly through the central section of the specimen under tensile loading.
- The angled sections were cut to be matched with the angled surfaces of the loading rig shown in Figure 6-2 and Figure 6-3. This allows tensile loading of the specimen from the test machine.
- The semi-circular section at the top and bottom of the specimen allowed compressive loading to be applied. A pair of rollers was used at 90° to each other; this perpendicular arrangement had the rollers crossing through the centroid of the specimen. Therefore, the compressive load would be applied directly through the centre of the specimen and a moment would not be applied through the dumbbell specimen.

After the dumbbell specimens had been manufactured using EDM cutting the material needed to be stress relieved to remove all residual stresses caused by the rolling of the billets and the cutting of the geometry. This was completed in a vacuum furnace at a temperature of 900°C for one hour. The dumbbells were then left to air cool. After investigations into phase transformations in 316L stainless steel, the 900°C used for stress relieving the dumbbell specimens is considered not to be high enough, to achieve recrystallisation. Therefore, in the new methodology described in Section 6.2.3 the stress relieving is carried out at 1050°C for a 2 hour soak time as recommended by the British Stainless Steel Association [75].

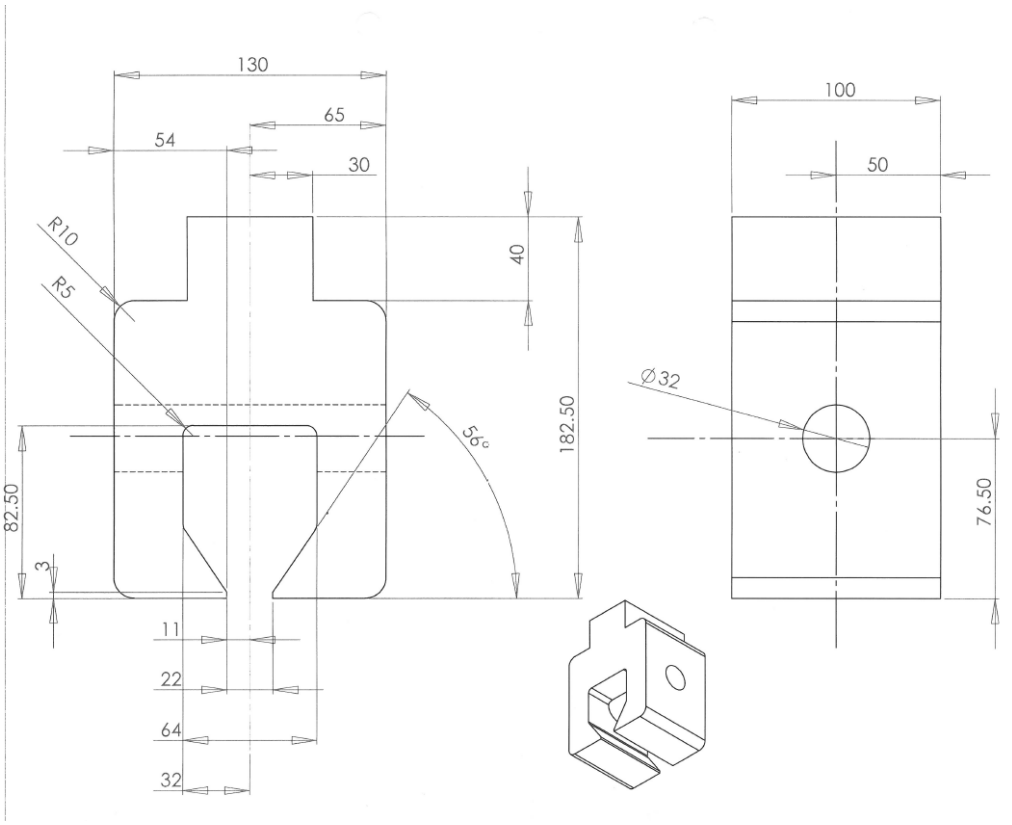

Figure 6-2 – Design drawing of one of the grip fixtures for use with the dumbbells [17]. All dimensions in mm.

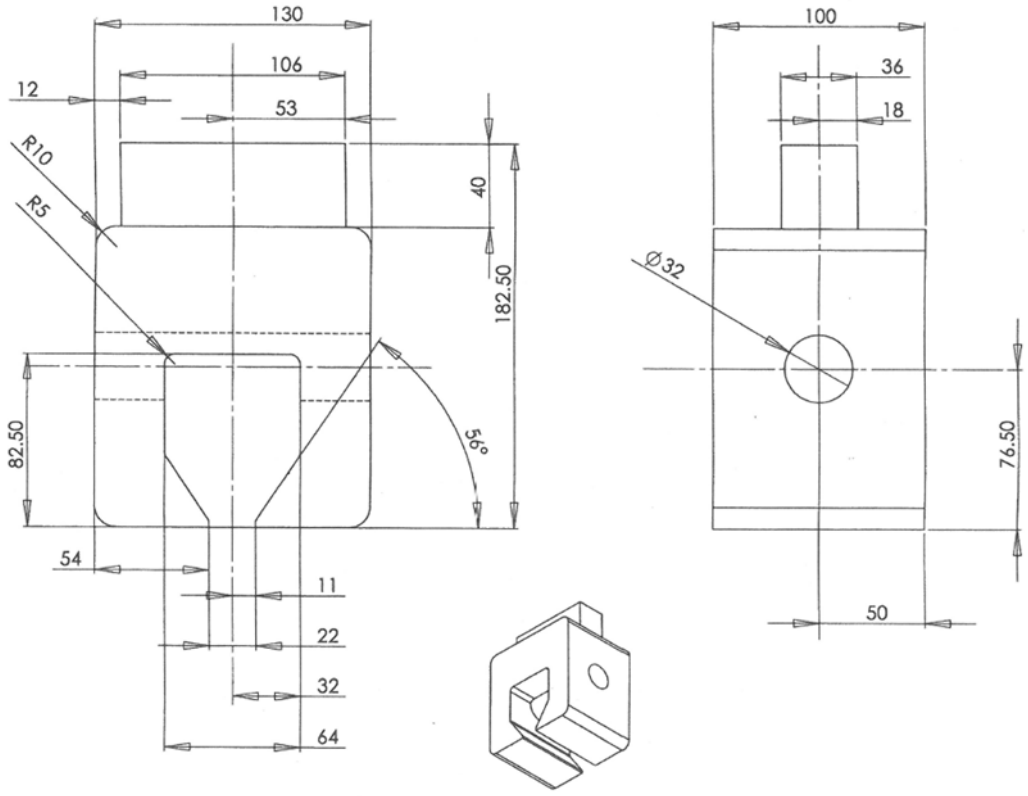

Figure 6-3 – Design drawing of one of the grip fixtures for use with the dumbbells [17]. All dimensions in mm.

At the time the work in [17] was performed the University of Southampton did not have a test machine with adequate loading capacity. The plastic deformation and TSA of the specimens was therefore planned to take place in laboratory facilities at Airbus in Bristol (the sponsors of the research). However, the TSA work could not be completed at the same facility; this was done at Lloyds Register failure analysis facilities, which at the time were located in Croydon, London. The reason for this was, as described in Chapter 2, TSA requires an analogue signal of the load input from the test machine to allow the analysis to be undertaken. The Airbus test machine did not have analogue output ports, so the load input signal could not be taken from the test machine and processed with the images from the IR detector; therefore, it was necessary to perform the TSA elsewhere using a test machine with the necessary connections and loading capacity. The test specimen orientation and grip orientation were not recorded or labelled so it was impossible to ensure that the test configuration was the same at Airbus and Lloyds Register. This is a potential source of error in the methodology described in [17] because each removal of the test specimen from the test machine increases the likelihood of a misalignment within the load path; therefore, there is a greater chance the loading will not be exactly uniaxial.

In [17] the thermoelastic response of both the dumbbell specimens (labelled as "3D Dogbone #1 and #2") and some preliminary measurements using dogbone test coupons manufactured for 316L stainless steel [17] were measured. From the thermoelastic response the values of thermoelastic constant were calculated. These results were normalised against the reference specimen (0% plastic strain) from each set of test results. This allowed changes in the thermoelastic constant to be clearly identified; the results are shown in Figure 6-4.

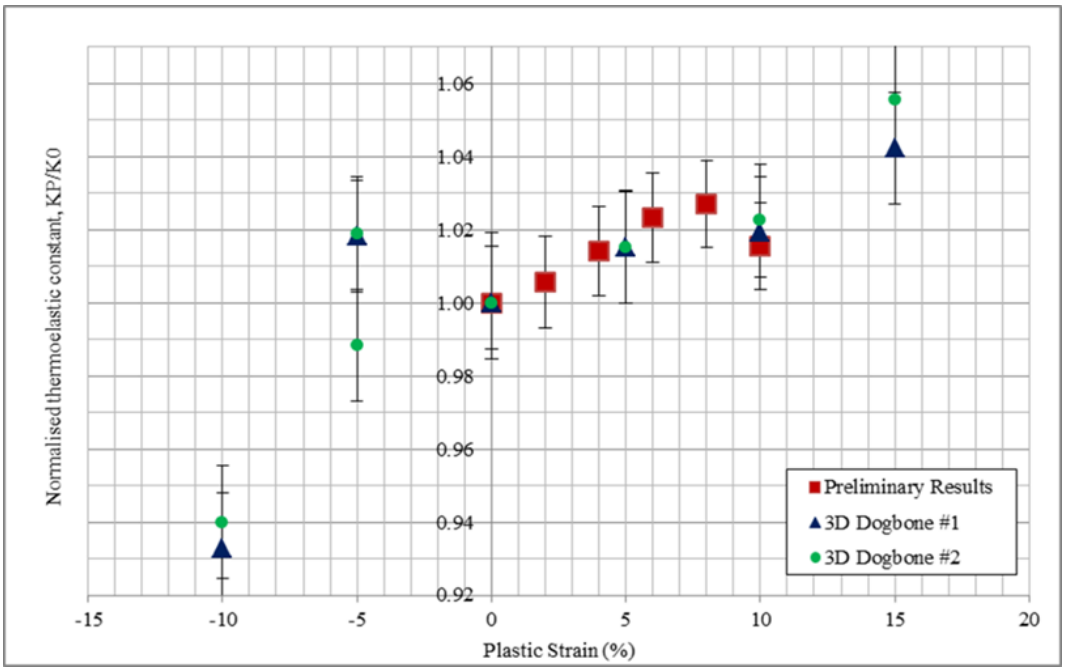

Figure 6-4 – Results from the dumbbell tests in [17] labelled as Dogbone #1 and Dogbone #2.

The results from the coupon tests show a linearly increasing change in thermoelastic constant up to 8%, however, there is then a drop in the 10% specimen. This drop is also seen in the 10% specimen from the dumbbell results. The dumbbell tests had a specimen that contained a higher amount of plastic strain, 15%, than the dogbone coupons, and this result continued the linearly increasing trend shown in the 2% - 8% results from the coupon tests. The negative plastic strain results also show a deviation from a linear trend. The difference in thermoelastic constant for the -10% plastic strain specimen is around 3 times greater than the difference for the +10% specimen. A further discrepancy are the results for the -5% specimen. Three results were taken from this specimen, and two showed an increase in thermoelastic constant rather than the expected decrease. The difficulty in measuring a consistent thermoelastic response for the compressive plastically deformed dumbbell specimens contributed to the decision to manufacture the tapered specimens described later that only included tensile plastic strain.

The original dumbbells were tested in the current project before new dumbbell specimens were manufactured. Due to degradation between the original paint coating and the surface of the dumbbell specimens the paint was cleaned use acetone, as described in Chapter 4. A new coating of RS matt black paint was applied. Careful masking of each face was required to ensure paint was only applied to each face once. The cyclic load used for the TSA test was the same as that used in [17], 20 ± 16 kN (61.7 ± 49.4 MPa) at 10 Hz. During the experiment, the specimen was removed from the grips and rotated to present each of the four faces to the IR camera. In this way, the average thermoelastic response of each differently strained specimen was obtained. The normalised thermoelastic constant results can be seen in Figure 6-5 compared against the TSA results from the original work. Two conclusions can be drawn from these results.

1. The noise in the new data is a lot more than the old; this could be masking part of the relationship between normalised thermoelastic and plastic strain.
2. There is an increase in thermoelastic constant when plastic strain is positive, and there is a decrease in thermoelastic constant when plastic strain is negative.

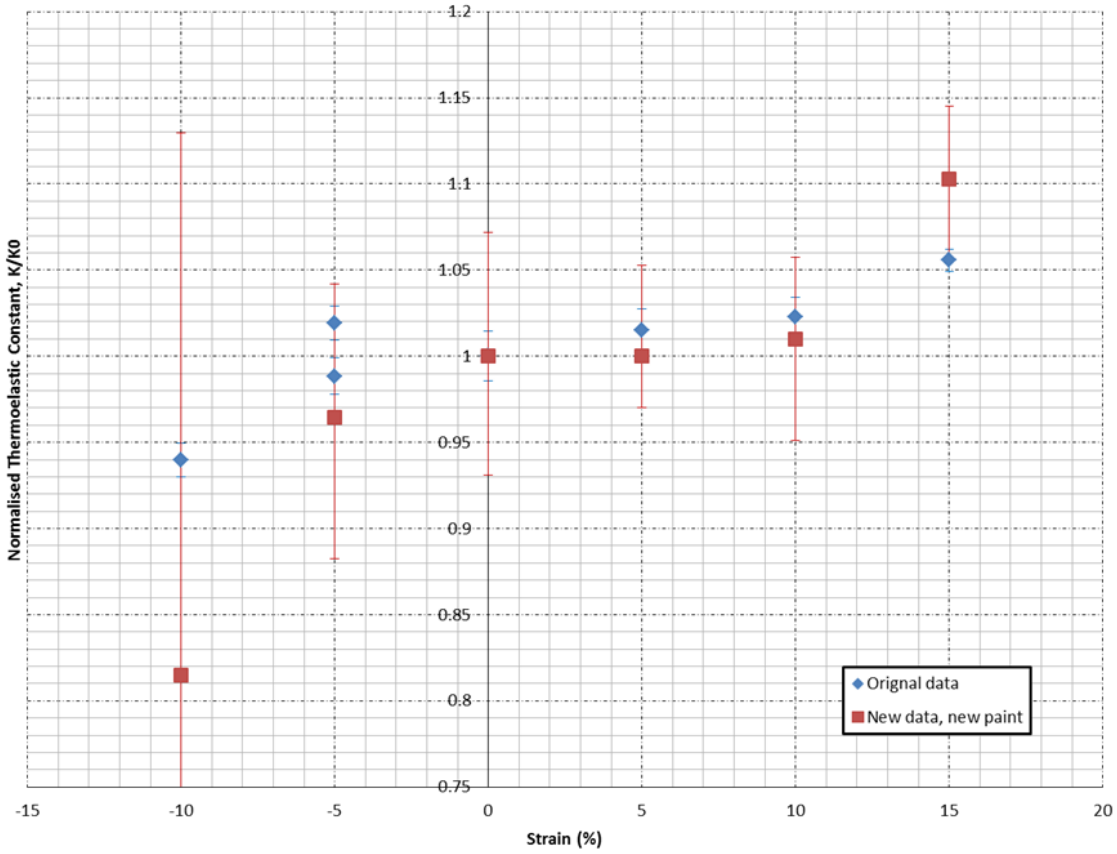

Figure 6-5 – Plot of repeat tests performed on the dumbbell specimens by the present work. Data from [17] shown as "Original data".

In the data shown in Figure 6-5 there are significant error bars on all the data points. The data is the average of the four surfaces of each specimen and it cannot be ensured that the specimens were put into the test machine with perfectly uniaxial loading through the centreline of the specimen. To eliminate and evaluate this potential major source of error there are three improvements that can be made to the methodology.

1. Use the same test machine to perform the plastic straining and to perform the cyclic loading for TSA. This will reduce any errors associated with an inconsistency within the test machine as this will be common to all loads applied by the test machine, whether that is during deformation or the elastic load cycles. It should be noted that the test machine used a Lloyds register has relocated to the laboratories at the University of Southampton.
2. Do not remove the loading rig, and if possible the specimen, from the test machine between tests. By keeping the load rig and specimen in the test machine the same loading path will be used in both sets of tests. This will reduce the chance of misalignment being a source of error.
3. Track the movement within the surface of the test specimen in some fashion and remove this as a source of noise. The noise caused by movement of the specimen during

cyclic loading relative to the IR detector position has been explained in Chapter 4. The same noise source is likely present in the results in Figure 6-4; it is unclear if any motion compensation was undertaken. Introducing motion compensation into the recorded IR data will allow a better measure of the thermoelastic response to be calculated, and so any changes in the thermoelastic constant will also be easier to discern.

6.2.2 Evaluation of loading rig

A new set of 6 dumbbell specimens were manufactured and heat treated to 1050°C as it was determined that full stress relief in 316L stainless steel could only be obtained at this temperature [75]. As the same loading rig used in [17] was to be used for the new experiments, prior to loading and plastically deforming these specimens it was decided to conduct a full validation of the loading rig. Therefore, an additional specimen that could be used as a dummy was manufactured. A detailed study was conducted to evaluate the loading rig and the roller choice for the compression tests. There are 32 different combinations of loading rig and test specimen orientation so a series of test were conducted on the dummy to identify the effect the different combinations had on the loading of the test specimen.

Uniaxial test methodology

The dummy specimen had tri-axial strain gauge rosettes adhered in the centre of each face of the centre section. The rosettes were applied so the gauges were at nominally 0°, 45°, and 90° orientation, where 0° is the vertical axis of the dumbbell specimen. The two halves of the loading rig were labelled X and Z, the two rollers were labelled 1 and 2, and each face was labelled A, B, C, and D in series around the dumbbell. This labelling system allowed a series of 32 elastic loading tests in both tension and compression to be carried out, see Table 6-1. The strains were obtained using a StrainSmart 8000 system. The test machine used was a Schenk 630 kN servo-hydraulic test machine and the specimen was loaded with 40 kN (122.6 MPa) tensile and compressive load. The load level was chosen because the yield stress of 316L is 250 MPa [17], therefore, the load would not go beyond the yield point but would provide a large dataset to construct the elastic stress/strain curves. Each row in Table 6-1 is a pair of tests for a single combination of loading rig, compression roller, and specimen orientation. A pre-test load of ±2 kN was applied to the specimen before each test was performed to hold the specimen at a constant, controllable level whilst final test set up was performed. A tensile load of 40 kN was initially applied via a ramp loading rate of 40 kN/min. The loading rate was chosen to allow a close level of control over the loading of the specimen. The specimen was then unloaded through the zero point and a compressive load of -40kN was applied, again at a loading rate of 40 kN/min. After each pair of tension/compression tests for a single

configuration was completed, the lower loading rig was ungripped and the specimen rotated 90° for the next configuration. After the first 16 tests, the loading rig was reversed to have grip 'X' be in the top position rather than 'Z'. Another 8 pairs of tests (16 in total) were performed.

Tension							Compression						
Test Number	**Top Grip**	**Top Roller**	**Bottom Grip**	**Bottom Roller**	**Face**	**Orientation**	**Test Number**	**Top Grip**	**Top Roller**	**Bottom Grip**	**Bottom Roller**	**Face**	**Orientation**
1	Z	1	X	2	A	Up	**2**	Z	1	X	2	A	Up
3	Z	1	X	2	B	Down	**4**	Z	1	X	2	B	Down
5	Z	1	X	2	C	Up	**6**	Z	1	X	2	C	Up
7	Z	1	X	2	D	Down	**8**	Z	1	X	2	D	Down
9	Z	2	X	1	A	Up	**10**	Z	2	X	1	A	Up
11	Z	2	X	1	B	Down	**12**	Z	2	X	1	B	Down
13	Z	2	X	1	C	Up	**14**	Z	2	X	1	C	Up
15	Z	2	X	1	D	Down	**16**	Z	2	X	1	D	Down
17	X	1	Z	2	A	Up	**18**	X	1	Z	2	A	Up
19	X	1	Z	2	B	Down	**20**	X	1	Z	2	B	Down
21	X	1	Z	2	C	Up	**22**	X	1	Z	2	C	Up
23	X	1	Z	2	D	Down	**24**	X	1	Z	2	D	Down
25	X	2	Z	1	A	Up	**26**	X	2	Z	1	A	Up
27	X	2	Z	1	B	Down	**28**	X	2	Z	1	B	Down
29	X	2	Z	1	C	Up	**30**	X	2	Z	1	C	Up
31	X	2	Z	1	D	Down	**32**	X	2	Z	1	D	Down

Table 6-1 – Full test plan of the grip orientation tests.

Uniaxial test results and conclusions

As the test is nominally uniaxial and the gauges are aligned parallel and transverse to the line of action of the load, the longitudinal strain should be equivalent to the principal strain, ε_1, in the specimens. Calculating the principal strains from the coordinate strains given by the strain gauges is a good check to ascertain if the loading generated by the rig is uniaxial. This was done for all tests and the difference between the longitudinal and principal strain was of the order of a few microstrain. Therefore, to obtain Young's modulus, it is valid to plot the

stress against the maximum principal strain. Results for a typical test is shown in Figure 6-6 and the Young's modulus is given in Table 6-2. Although only a single of pair of test, the results are representative of the whole test program; both the tensile and compressive tests show consistent elastic loading and unloading in both tension and compression. The Young's modulus of every face and every test combination was calculated and the mean average was 195.42 GPa with a coefficient of variation of 0.28%. The tests conclusively show that that there is very little effect from different combinations of loading rig, compression roller, and specimen orientation. This is a very valuable finding that suggests it is very unlikely that the original specimens tested in [17] were subject to loading differences that could be attributed to the specimens having different combinations of the loading rigs. It should be noted that this series of experiments cannot show any effects that may occur post yielding, so the strain applied during each of the plastic straining operations will be monitored separately. However, the result is encouraging especially as it will be necessary to remove the test specimen from the rig to obtain the thermoelastic response from each face.

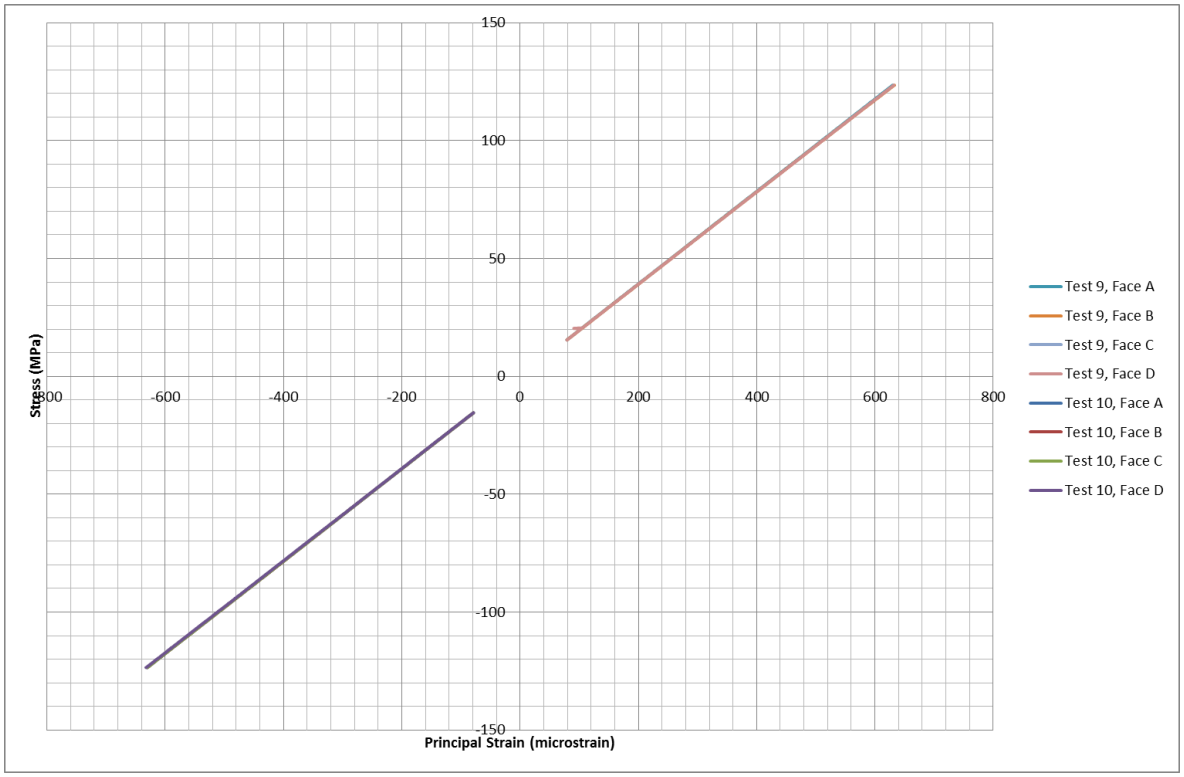

Figure 6-6 – Elastic loading and unloading test results of one pair of grip orientation tests. Data from all four faces is shown; however, the lines sit almost directly over each other making it difficult to discern the individual data.

Test	Young's modulus (GPa)

Test 9, Face A	196.08
Test 9, Face B	195.42
Test 9, Face C	195.80
Test 9, Face D	195.55
Test 10, Face A	195.95
Test 10, Face B	195.92
Test 10, Face C	195.97
Test 10, Face D	195.36
Average	**195.76**

Table 6-2 – Calculated Young's Modulus values from test results of Figure 6-6

A key consideration is the removal of the clamps from the test machine. Figure 6-7 shows stress-strain data from one test that was not loading uniaxially. A relatively large amount of bending took place when loading in this test and around a 0.02% difference in strain (around 1/3 of the total strain recorded during the test) was recorded from two strain gauges on opposing faces. This test configuration was set up a second time and the errant negative strain reading during a settling period was not repeated, see Figure 6-8. The improvement was as a result of the loading rig being gripped by the test machine actuator in a different manner. As well as principal strain values, the principal strain angle calculated from the strain gauge rosette data. This revealed that after an initial settling period during the first 5-10 MPa of elastic loading the angle was aligned with the loading direction and did not change during the remainder of the elastic loading. The small amount of settling at the beginning of the test led to the conclusion that the greatest influence on the direction of the applied load relative to the specimen geometry is the clamping of the loading rig by the actuator. If the loading rig does not sit flush with actuator and static grip of the test machine, the perpendicular loading axis from each half of the rig will not align down the centre of the specimen. The combination of rig, compression roller, and specimen orientation is largely unimportant compared to the gripping of the loading rig.

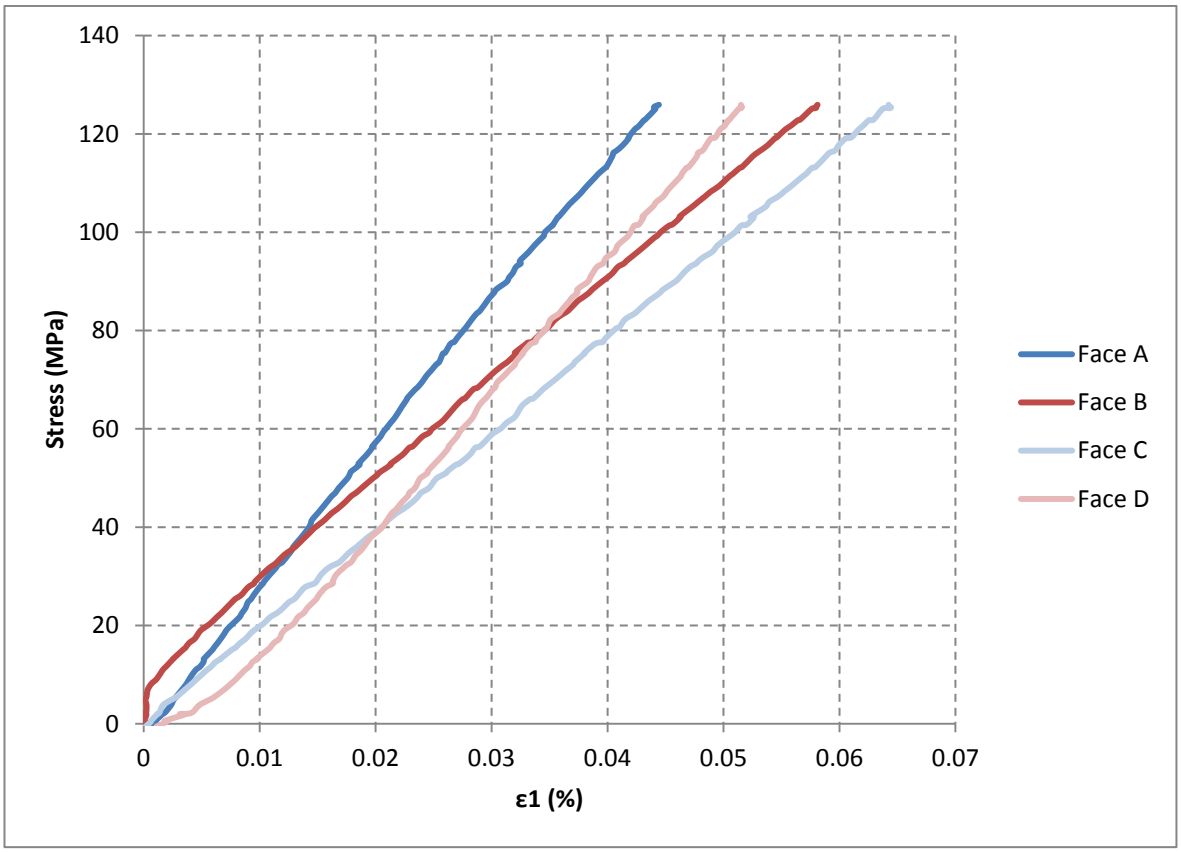

Figure 6-7 – Misalignment in the grips put a bending moment through the specimen. Similar colours are paired opposite faces.

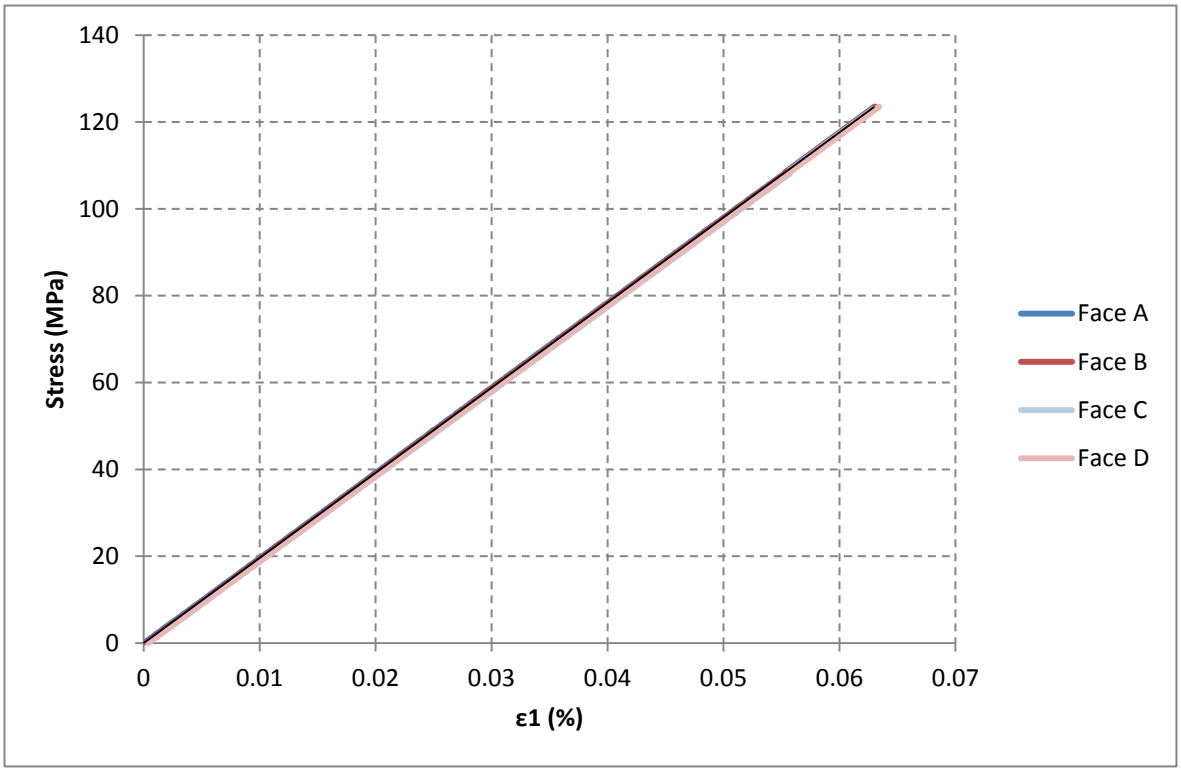

Figure 6-8 – After adjustment of the loading rig in the grips of the test machine the elastic extension was performed again and no misalignment is evident in the data.

6.2.3 Application of plastic deformation

A new plastic straining and TSA methodology was developed based on the results of the alignment and orientation tests to ensure a more systematic approach to the plastic straining than that defined in [17]. Although there were six specimens in total to be tested; the reference specimen has no plastic deformation applied to it. This is only elastically loaded for the TSA testing. The five remaining specimens were plastically deformed to -10%, -5%, +5%, +10%, and +15% strain respectively. It should be noted that during the deformation of the +15% strain the strain gauge debonded and no data could be collected for this specimen.

Specimen preparation

The key difference between the work presented here and that performed previously is the stress relaxation that was performed on the dumbbell specimens. The dumbbell specimens were stress relieved at a temperature of 900°C in the previous work, which further investigation has revealed to not be sufficient to achieve full recrystallisation of the material. The new dumbbells were stress relieved at 1050°C in a vacuum furnace and held at this temperature for 2 hours. A vacuum furnace large enough to heat treat the dumbbell specimens was not available at the University of Southampton, therefore, the RESIST partner TWI was asked to perform the heat treatment.

After stress relieving, each face on the dumbbell specimens was marked, e.g. “Face A” was from the same face in the billet of 316L stainless steel for all specimens. The marking of the specimens will allow comparisons between named faces on separate specimens to be made if required. The marking also allowed specimen during cyclic loading during TSA to be rotated the same way when recording all four faces of the centre section. Uniaxial strain gauges were applied to faces B and D of each specimen and adhered using high strain resistant adhesive. From these strain gauges the live-strain during the test can be monitored and used to control the deformation of the test.

Face A was spray painted with a speckle pattern which allowed DIC to be performed during the deformation and acted as a third set of strain readings both to check the evolution of strain during the loading and also to check the final strain in the specimen. The speckle pattern and strain gauge placement is shown in Figure 6-9.

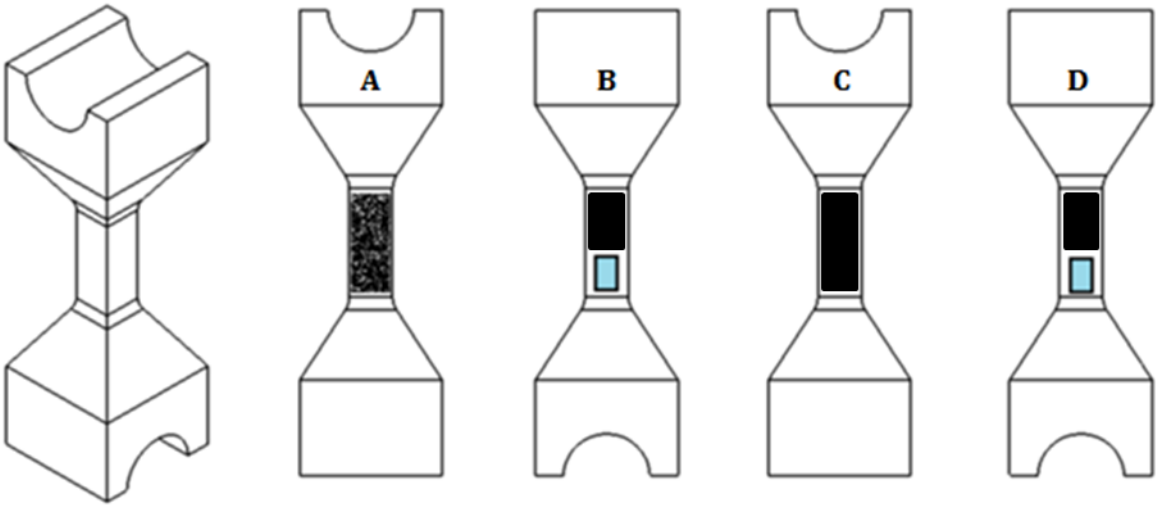

Figure 6-9 – Specimen preparation of each face, the blue sections denote strain gauge location. Face A – speckle pattern for DIC; Face B – strain gauge and matt black paint; Face C – matt black paint; Face D – strain gauge and matt black paint. Faces are opposites with A-C paired, and B-D paired.

Methodology

A test plan was devised for the plastic straining, and elastic cyclic loading for the TSA, that keeps the top section of the loading rig in the same position for every test. Only the specimen and bottom loading rig are moved in and out. This is unavoidable, so careful attention was paid to the gripping of the loading rig; this was most important with the plastic straining as the forces involved, especially in the compression specimens, meant any effect of non-uniaxially loading would be amplified. An overview of the test plan is given in Table 6-3 which shows each step in the plastic strain and cyclic loading experiment. It can be seen that between step 4 and 9 each specimen stays gripped in the test machine so the first set of TSA data is recorded without introducing possible errors from ungripping and regripping the lower half of the loading rig.

Dumbbell Test Plan	
Step	**Activity**
1	Manufacture via EDM the six dumbbells.
2	Stress relieve at 1050°C all six dumbbells.
3	Apply strain gauges to dumbbell faces B and D. Spray speckle for DIC onto face A. Spray matt black coating for TSA onto faces B, C, and D.
4	Install specimen into test machine and rig.
5	Plastically deform to required strain value using displacement controlled test (0.5 mm/min – rate chosen to allow careful control of the test).
6	Relax to zero load and check final strain values reported by strain gauges.
7	Process strain data to check twisting and bending. Specimen kept in test rig.
8	Set up IR camera and apply cycling loading for TSA.
9	Perform TSA on first pair of faces (A and C) by moving camera to rear of test machine.
10	Remove specimen from the test machine and place back in with face B forward.
11	Perform TSA on second pair of faces (B and D).
12	Remove specimen from test machine.
13	Repeat steps 4-12 with all dumbbell specimens
14	Process TSA data and normalise $\frac{\Delta T}{T}$ for each specimen against the $\frac{\Delta T}{T}$ of the 0% reference specimen.

Table 6-3 – Methodology of new dumbbell test plan.

In step 3 each dumbbell specimen had a uniaxial strain gauge applied in nominally the 0^{o} direction (i.e. aligned with the loading direction) on opposing faces; these faces were to the left and the right of the front face. By having the gauges on opposing faces any bending of the specimen in that plane would be shown by one gauge displaying a compression strain reading and the other a tensile strain reading or vice-versa. On the front face there was a speckle pattern applied, matt white dots on a matt black background. DIC data was taken during the deformation to allow a third set of strain data to be taken and processed if required due to a large discrepancy between the strain values reported by the strain gauges.

Every face apart from the speckled face has a coating of matt black paint applied to it. This meant that TSA data could be taken without removing the specimen from the test machine after plastic straining for the first two faces so the boundary conditions during the straining would be preserved. TSA data could also be taken from the speckled face because the IR emissivity of the matt white used for the speckles is approximately the same as the matt black and the speckles cannot be seen in the IR images [62] .

Results

In Figure 6-10 the full stress/strain curves for the -10%, -5%, +5%, and +10% specimens are shown. During plastic extension of the +15% specimen the strain gauge debonded from the surface of the specimen as around 4-4.5% strain. From the displacement reading of the test machine it was thought possible to continue the deformation with some degree of confidence; however, when unloaded back to zero load it was found that the final deformation was only slightly more than the +10% specimen when the DIC data was processed. For this reason it has not been included in the summary of results here.

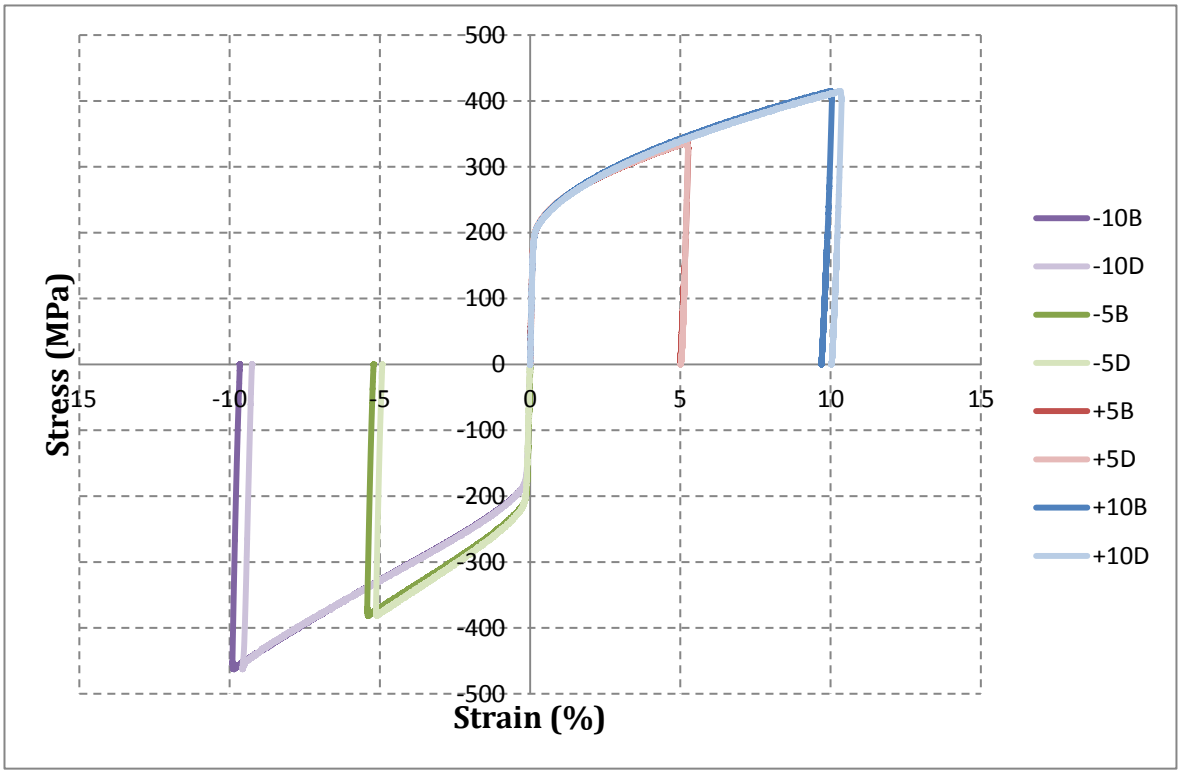

Figure 6-10 – Loading and unloading paths of each plastic deformation test.

The final strain readings for the nominally +5% strain specimen were the most consistent between the two strain gauges. The values from the strain gauges on the other dumbbell specimens all deviated from each other; -5% specimen by 0.08% strain, -10% specimen by 0.41% strain, and +10% specimens by 0.32% strain. During the elastic loading phase there was no difference between the gauges, the small moment was only applied during the plastic deformation part of the test. All the strain gauges on the four specimens in Figure 6-10 gave close to expected results however, so a final plastic strain value was determined for each specimen by averaging the two strain gauge readings; these results are shown in Table 6-4. In the rest of the chapter these specimens will be referred to by their nominal strain values, e.g. -10%, -5%, +5%, and +10%.

	Final Strain Value		
Specimen	**B**	**D**	**Average**
-10%	-9.66	-9.25	-9.45%
-5%	-5.20	-4.92	-5.06%
5%	5.01	5.01	5.01%
10%	9.70	10.02	9.86%

Table 6-4 – Final plastic strain values of each strain gauge.

6.2.4 Thermoelastic stress analysis of dumbbell specimens

Each dumbbell specimen had an initial set of TSA tests performed on all four faces directly after the plastic deformation had taken place. The results contained noisy data that did not allow the calculation of a thermoelastic constant. It is thought that this was due in part to the paint not having a good bond to the surface because of the large plastic deformation. To attempt to avoid this, the paint was still wet when the specimen was loaded into the test machine. Painted specimens are normally allowed to rest with the surface horizontal to let the paint dry, mounting the specimens vertically in the test machine affected the quality of the final paint coating. The thickness of the paint could not be checked before deformation, and after the TSA tests had been performed thickness tests showed the paint coatings had coefficients of variation >30%.

A second set of TSA data were taken after all the plastic deformation tests had been completed. The strain gauges were removed from each face; the speckle pattern was removed from the front face. Each face was painted with a thin layer and the thickness of each painted rectangle was measured using a thickness gauge (Elcometer 456 FNF Model B Separate DFT Gauge, with a NF1 Standard Probe). The thickness results for each specimen and face are shown in Table 6-5.

Specimen	A [mean, µm (%var)]	B[mean, µm (%var)]	C[mean, µm (%var)]	D[mean, µm (%var)]
-10%	17.56 (4.02%)	16.54 (5.68%)	28.40 (3.44%)	16.05 (6.25%)
-5%	23.12 (5.52%)	19.38 (4.87%)	25.12 (4.25%)	18.98 (8.09%)
0%	16.53 (8.14%)	9.11 (12.54%)	28.67 (4.22%)	16.47 (2.67%)
5%	22.21 (3.27%)	22.67 (6.38%)	22.33 (6.28%)	15.56 (2.12%)
10%	14.87 (7.54%)	27.93 (5.89%)	18.27 (7.21%)	26.79 (5.34%)

Table 6-5 – Paint thickness on each face when the dumbbell specimens were prepared for a second batch of TSA testing.

The second set of tests were performed whilst the top half of the loading rig was still clamped in the test machine. This controlled the major source of error from the loading, and the measurement of the paint layer allowed the error from the paint layer in the TSA to be accounted for.

Thermoelastic stress analysis results

From the measurements recorded by the IR detector the change in temperature over the loading cycle, ΔT, and the average surface temperature during the loading cycle, T, can be extracted for each face. This information was taken from a rectangle at the centre of each face measuring approximately 30 x 60 pixels. A point by point analysis was performed on the pixel data from each section to find a matrix of $\frac{\Delta T}{T}$ for each face that measured 30 x 60 data points. An average $\frac{\Delta T}{T}$ value from each face was calculated along with the standard deviation of the sample data. The results of this are shown in Table 6-6. To assess the noise in the thermoelastic data the coefficient of variation was also calculated; half the data had a coefficient greater than 10%. The results of the coefficient of variation were particularly high for the +10% dumbbell specimen.

Specimen	$\frac{\Delta T}{T}$						
	A, $\bar{x}$	**A, SD**	**A, %var**	**B, $\bar{x}$**	**B, SD**	**B, %var**	**Avg.**
-10%	4.58×10^{-4}	1.1×10^{-5}	2.51	4.06×10^{-4}	3.0×10^{-5}	7.42	3.95×10^{-4}
-5%	3.93×10^{-4}	5.0×10^{-5}	12.84	3.79×10^{-4}	7.1×10^{-5}	18.70	3.89×10^{-4}
0%	4.21×10^{-4}	2.5×10^{-5}	5.84	3.99×10^{-4}	10.9×10^{-5}	27.30	4.20×10^{-4}
5%	4.63×10^{-4}	4.3×10^{-5}	9.37	4.20×10^{-4}	5.0×10^{-5}	11.97	4.39×10^{-4}
10%	4.94×10^{-4}	6.3×10^{-5}	12.78	4.47×10^{-4}	12.4×10^{-5}	27.69	4.62×10^{-4}
	C, $\bar{x}$	**C, SD**	**C, %var**	**D, $\bar{x}$**	**D, SD**	**D, %var**	
-10%	3.80×10^{-4}	8.2×10^{-5}	21.55	3.38×10^{-4}	2.3×10^{-5}	6.80	
-5%	4.04×10^{-4}	3.5×10^{-5}	8.72	3.80×10^{-4}	3.3×10^{-5}	8.63	
0%	4.43×10^{-4}	3.1×10^{-5}	7.10	4.18×10^{-4}	3.5×10^{-5}	8.42	
5%	4.29×10^{-4}	9.0×10^{-5}	20.96	4.46×10^{-4}	7.6×10^{-5}	17.07	
10%	4.72×10^{-4}	13.4×10^{-5}	28.36	4.35×10^{-4}	4.7×10^{-5}	10.91	

Table 6-6 – $\Delta T/T$ response of each face of every specimen. The average column is the average for every face on each specimen.

The $\frac{\Delta T}{T}$ data contains a high level of variance and this is carried through the calculations to find the values of thermoelastic constant, K, and the normalisation of those values to plot $\frac{K}{K_0}$. Table 6-7 shows the results of the thermoelastic constant calculations. The reason for the

large scatter in the data is combining the noise from the T values with the noise in the ΔT values. This is highlighted further in the information in Table 6-8 and Figure 6-11, where the normalised results show no trend between the values of plastic strain and the calculated normalised thermoelastic constant.

Specimen	Stress Range (MPa)	K (Pa^{-1})							
		A, $\bar{x}$	A, CoV	B, $\bar{x}$	B, CoV	C, $\bar{x}$	C, CoV	D, $\bar{x}$	D, CoV
-10%	88.0	5.21x10^{-12}	2.51	4.61x10^{-12}	9.41	4.31x10^{-12}	21.55	3.84x10^{-12}	6.8
-5%	93.3	4.21x10^{-12}	12.83	4.07x10^{-12}	18.67	4.33x10^{-12}	8.73	4.07x10^{-12}	8.62
0%	98.6	4.27x10^{-12}	5.83	4.05x10^{-12}	2.78	4.50x10^{-12}	7.09	4.24x10^{-12}	8.49
5%	103.6	4.48x10^{-12}	9.38	4.06x10^{-12}	11.97	4.15x10^{-12}	20.94	4.31x10^{-12}	17.08
10%	107.3	4.60x10^{-12}	12.78	4.16x10^{-12}	2.76	4.40x10^{-12}	2.84	4.05x10^{-12}	10.91

Table 6-7 – Thermoelastic constant of each face from TSA tests on the dumbbell specimens.

Specimen	Stress (MPa)	$\frac{K}{K_0}$				
		A	B	C	D	Avg.
-10%	88.0	1.219	1.141	0.959	0.904	1.054
-5%	93.3	0.985	1.005	0.962	0.959	0.977
0%	98.6	1.000	1.000	1.000	1.000	1.000
5%	103.6	1.049	1.004	0.922	1.016	0.997
10%	107.3	1.078	1.028	0.978	0.955	1.009

Table 6-8 – Normalised thermoelastic response, values normalised against K for the 0% strain specimen.

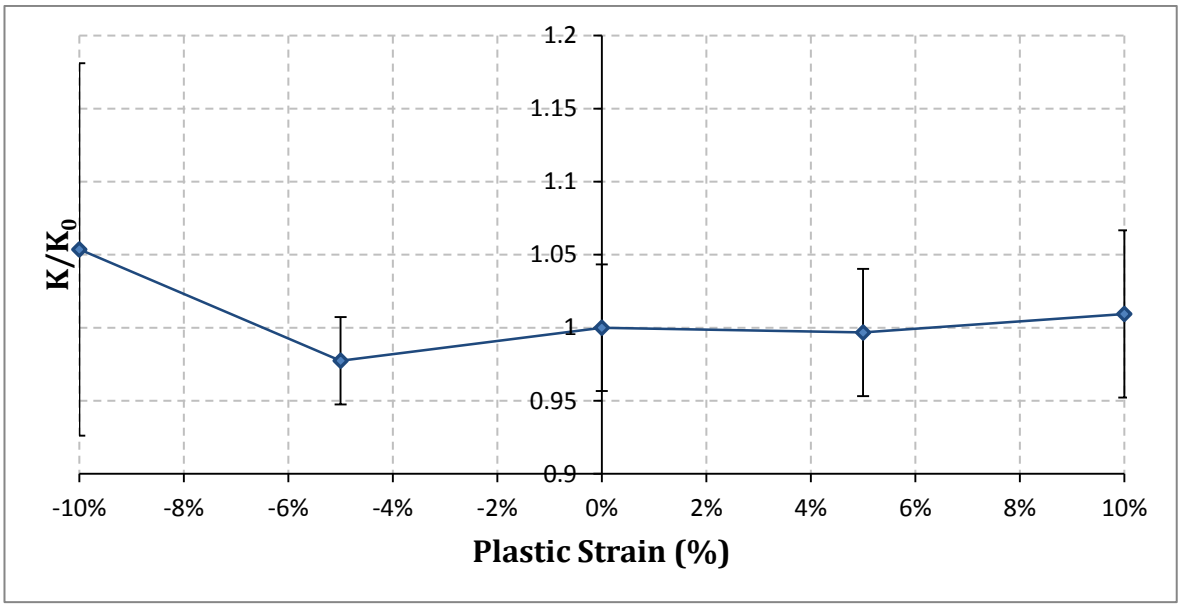

Figure 6-11 – Thermoelastic constant for each specimen normalised against the 0% strain specimen.

Figure 6-11 shows the averaged, normalised thermoelastic constant for each specimen plotted against plastic strain and there is no recognisable trend in the data. The large amounts of noise in each dataset make drawing conclusions from the data impossible. The different mean average response of each face for a single specimen suggests that some bending may have taken place despite the precautions taken. The results in Table 6-7 show there is a high coefficient of variation in the thermoelastic response of half the faces measured. A rectangle of data covering the length of each face on each specimen was taken. The average of each row was calculated such that K could be plotted along the vertical distance of each face, see Figure 6-12. The scales on each plot are the same and it would be expected that a trend be seen in the horizontal grouping of the data from plot to plot; however, there is no discernible trend in the plots.

-10%

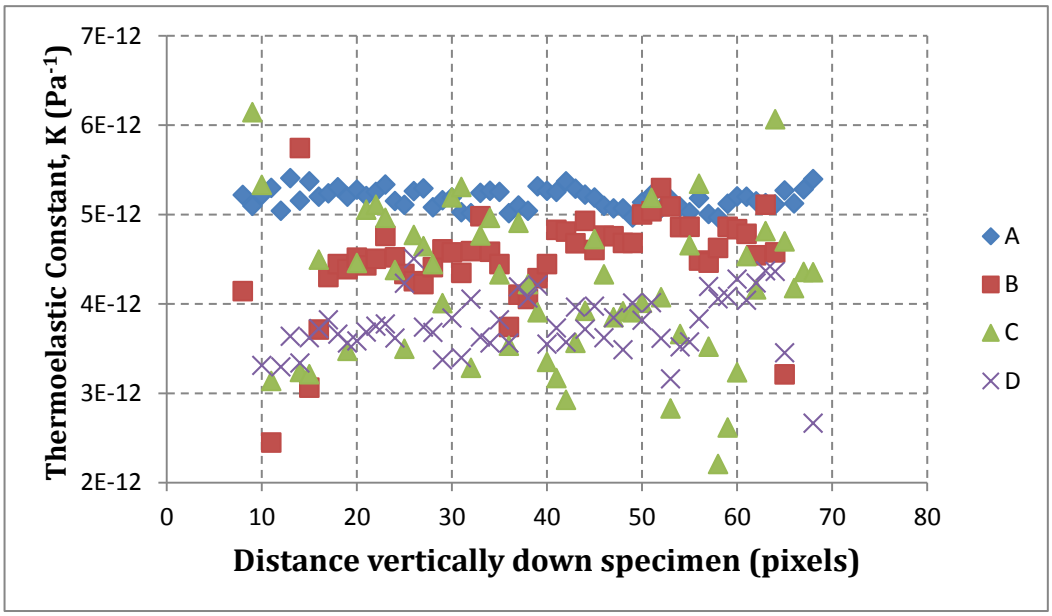
Thermoelastic Constant, K (Pa-1)
7E-12
6E-12
5E-12
4E-12
3E-12
2E-12
0
10
20
30
40
50
60
70
80
Distance vertically down specimen (pixels)
A
B
C
D

-5%

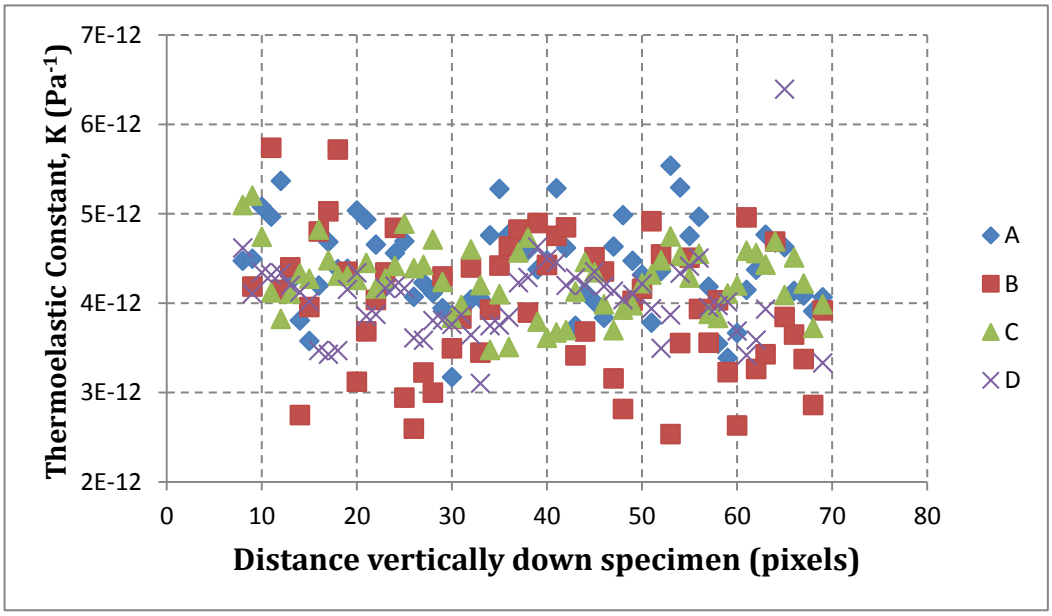
Thermoelastic Constant, K (Pa-1)
7E-12
6E-12
5E-12
4E-12
3E-12
2E-12
0
10
20
30
40
50
60
70
80
Distance vertically down specimen (pixels)
A
B
C
D

0%

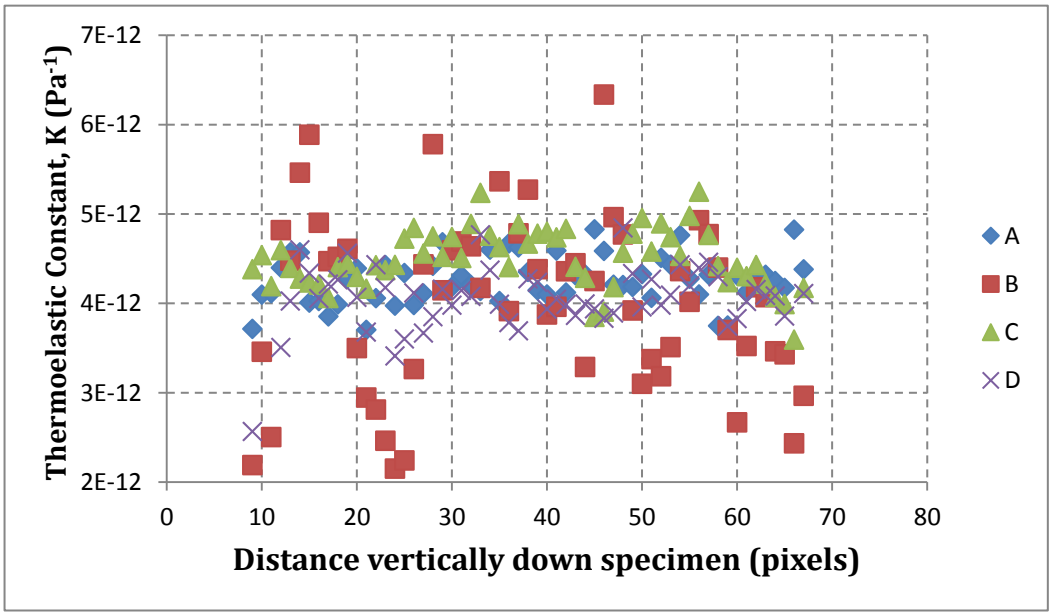
Thermoelastic Constant, K (Pa-1)
7E-12
6E-12
5E-12
4E-12
3E-12
2E-12
0
10
20
30
40
50
60
70
80
Distance vertically down specimen (pixels)
A
B
C
D

5%

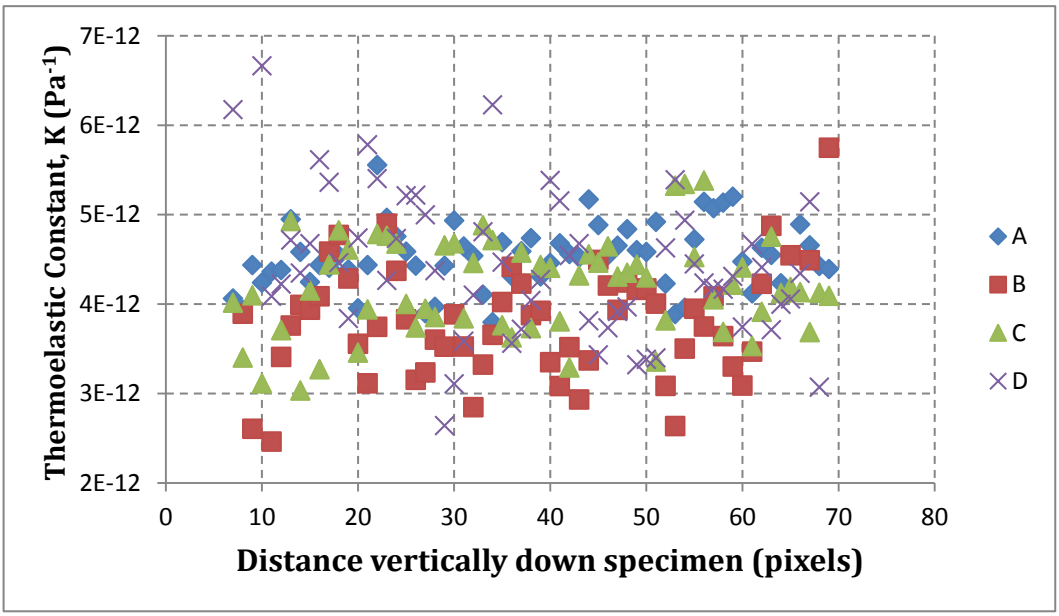

10%

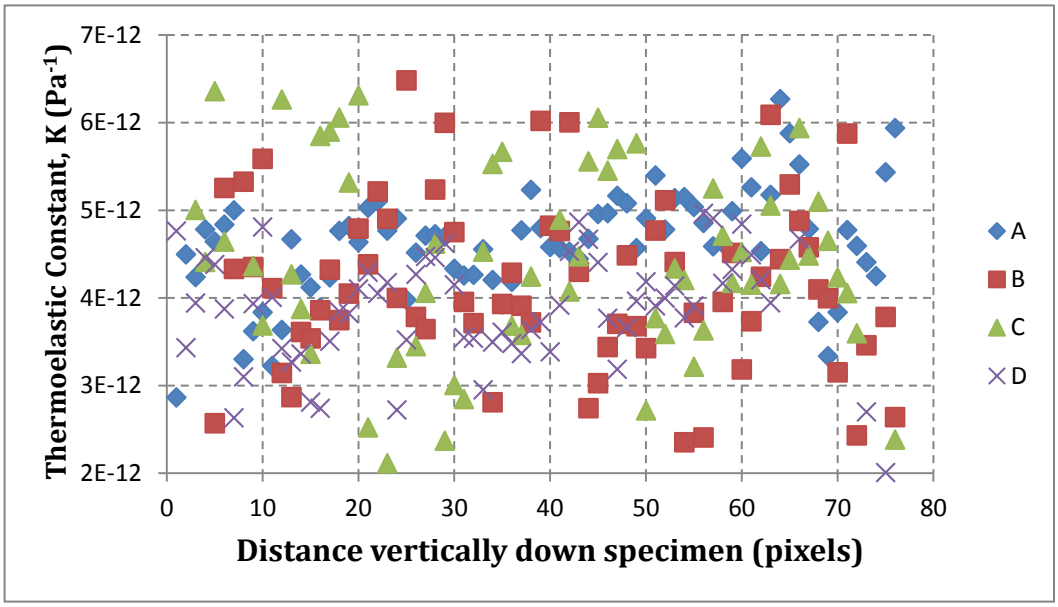

Figure 6-12 – Thermoelastic constant plotted along the centreline of each face for every specimen.

6.2.5 Summary

This chapter started with a review of the work in [17] that investigated the relationship between plastic strain in 316L stainless steel and changes in the thermoelastic constant. The results of that work suggested that there might be a relationship between plastic strain and changes in thermoelastic constant, however, there were significant sources of error found within the methodology of the study so an improved methodology was devised and the experiments were completed a second time using newly manufactured specimens.

The new investigation used the same test machine to perform the plastic deformation and the cyclic loading for TSA. Before the plastic deformation took place a study was conducted into potential causes of non-uniaxial loading through the specimen. From this study it was concluded that the combination of loading rig, compression rollers, and specimen orientation did not make a significant difference to the uniaxial loading. Instead it was the gripping of the loading rig by the test machine that had the greatest effect; therefore, the loading rig was left gripped by the test machine as much as possible during the plastic deformation experiments to avoid this source of error.

The deformation of the dumbbell specimens was performed and two sets of TSA data recorded. The first set contained significant sources of noise thought to arise from a lack of good contact between the paint and the specimen; there was also a high level of variation in paint thickness, only found after the TSA tests had been performed. The second set of TSA data had more even thickness of paint on each face; however, the $\frac{\Delta T}{T}$ and $\frac{K}{K_0}$ results contained high levels of scatter in the sample sets used to calculate the thermoelastic constant. It was concluded that the complicated loading path through the rig into the dumbbell specimens meant it was very difficult to remove all possibility of bending from the specimens during plastic deformation. A new type of test specimen was designed, a test specimen that would contain a gradient of plastic strain along the length of the specimen rather than separate test specimens for each value of plastic strain. It should also be noted that the heat treatment of the dumbbell specimens was different to that carried out in [1], so in the next part of the work the effect of different heat treatments is also studied.

6.3 New design of 316L stainless steel specimen containing plastic strain gradient

Due to the uncertainty in the TSA data taken using the dumbbell specimens, a new type of test specimen was designed based upon a test specimen used by [76]. The tapered shape on the test specimen allows a continuous gradient of plastic strain to be set up within a single specimen. This allows the change in thermoelastic response to be measured on a single test specimen, removing the potential source of error that comes from comparing different test specimens.

The final design of the test specimen deviated from the specimen shape of [76] in two important ways. The angled shape of the specimen sides is a constant angle instead of a curve. This lead to a linearly increasing cross section along the length of the specimen so final calculations of applied stress at a point on the specimen could be more easily calculated. The second change is the addition of a straight section at the specimen's narrowest point. The

constant cross section at this point creates a region which undergoes peak plastic strain across a length rather than a single point so the largest change in thermoelastic response can be captured from a larger area. The final design is shown in Figure 6-13 and contains all the key dimensions. The tapered specimens were waterjet cut from a sheet of 6 mm thick 316L stainless steel with the major dimension in the rolling direction of the plate. Waterjet cutting was used to remove the possibility of thermally induced surface stresses that can be found during electro-discharge machining. Keeping all the specimens aligned with the rolling direction removes any possibility of differences in thermoelastic response and yield point due to the grain orientation. At the narrow neck section of the specimen, the thickness becomes larger than the width (6 mm thickness to 5.2 mm width) therefore the plane stress assumption can no longer be considered valid and the results from this part of the specimen should be ignored until further investigation is conducted.

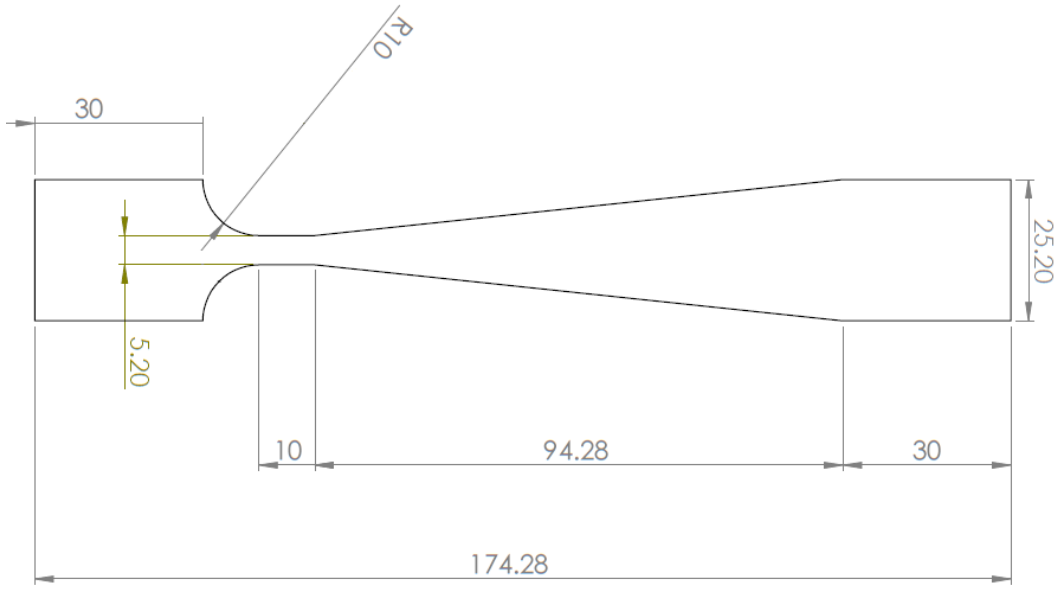

Figure 6-13 – Design drawing of tapered specimen. All dimensions in mm.

To provide values of thermoelastic constant for a non-plastically deformed specimen dogbone test coupons were cut from the same sheet of 316L; with the major dimension again aligned with the rolling direction. The design of these specimens is shown in Figure 6-14. The dogbone specimens were also plastically deformed. The load and strain applied to the dogbone specimens were recorded and the elastic-plastic behaviour was used as the material properties in a finite element model of the tapered specimens. The material properties were required because the deformed shape of the tapered specimen needed to be recreated in a finite element model to allow a synthetic bitmap of the tapered specimen to be created. The synthetic bitmap is used to calculate the resultant thermoelastic response of the plastically deformed tapered specimen so it can be plotted against the plastic strain gradient in the tapered specimen.

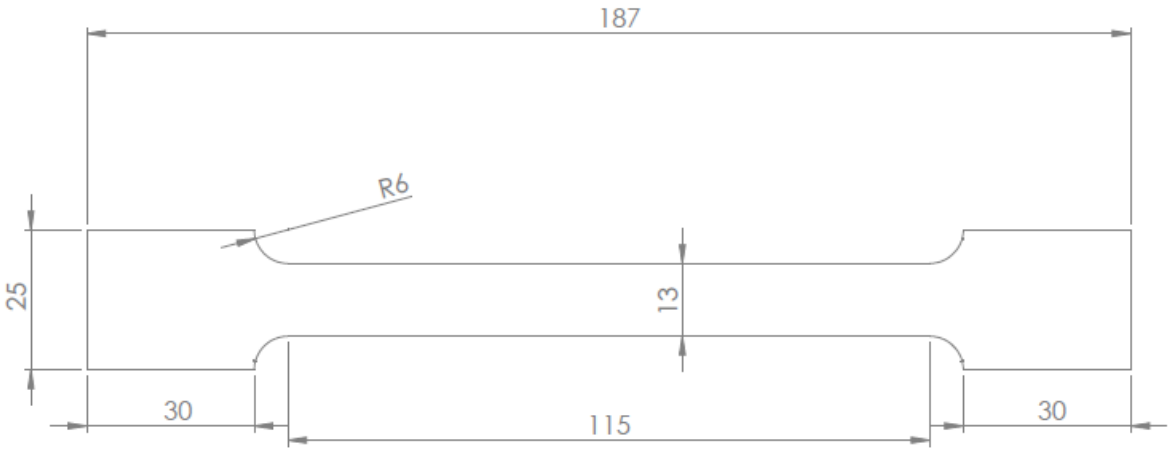

Figure 6-14 – Design drawing of dogbone specimen. All dimensions in mm.

A second, parallel study was undertaken using the tapered and dogbone specimens. Three sets of tapered and dogbone specimens were manufactured and three different heat treatments applied to the specimens. The first set was left non-heat treated to act as a control set of specimens. The second set was heat treated in a vacuum furnace at 900°C, just as the 316L stainless steel specimens in [17] were. The final set was heat treated at 1050°C as the second set of dumbbells was and as recommended in [75]. Any difference in the yield stress due to different heat treatments can be assessed, as well as any differences in thermoelastic response as a result of the different heat treatments.

6.3.1 Specimen preparation

Before testing the specimens, a series of heat treatments had to be applied. The test specimens were separated into three groups with each group containing one tapered specimen and two dogbone specimens. All three specimens in each group heat treated together. The first group were left in the as received condition. This allows the effects of any stress relaxation that occurred as a consequence of heat treatment to be revealed. The second group were heat treated to 900°C, all three specimens were placed inside a vacuum furnace such that the same exact heat treatment was performed on all three specimens at the same time. The third group were heat treated to 1050°C, and again all three specimens were heat treated in the same thermal cycle. A summary of this is shown in Table 6-9. The heating within the furnace was performed at 200°C/hr to the target temperature and then held for one hour. The cooling rate was controlled at 100°C/hr back to room temperature. The cooling rate was chosen to prevent precipitate formation around the grains, which is known about due to tests into different cooling rates of 316L stainless steel performed by Elise Chevallier.

Specimens	Heat Treatment	Heating Ramp Rate (°C/hr)	Heating Time (hrs)	Hold Temp (°C)	Hold Time (hrs)	Cooling Ramp Rate (°C/hr)	Cooling Time (hrs)	Total Time (hrs)
1 x Tapered 2 x Dogbone	As received	-	-	-	-	-	-	-
1 x Tapered 2 x Dogbone	900°C heat treatment	200	4.5	900	1	100	9	14.5
1 x Tapered 2 x Dogbone	1050°C heat treatment	200	5.25	1050	1	100	10.5	16.75

Table 6-9 – Heat treatment performed using a vacuum furnace on tapered and dogbone specimens.

After heat treatment had been performed a small amount of surface cleaning was required. This was due to the vacuum tubes being used previously for powdered samples and there was some residue left in the tubes during the thermal cycles applied presently. The specimen surfaces were abraded using 800 grit SiC paper until the bare metal surface was revealed, then cleaning was performed with acetone and the residue was rinsed off as per the results of Chapter 4.

The dogbone specimens were coated with a thin layer of RS matt black paint to allow TSA data to be recorded, see Table 6-10. From the TSA tests the thermoelastic constant, *K,* of each heat treatment of 316L will allow the synthetic bitmap for each tapered specimen with a different heat treatment to be generated. The tapered specimens were prepared for plastic deformation with a black on white speckle pattern. This is so that DIC data can be taken during the plastic extension and the plastic strain within the specimen obtained experimentally.

6.3.2 Thermoelastic constant of each heat treatment

The dogbone specimens, prepared with a thin layer of RS matt black spray paint, see Table 6-10, were loaded using an Instron 8800 servo-hydraulic test machine. Each specimen was loaded with 4 ± 3 kN (51.49 ± 38.62 MPa) at a loading frequency of 10 Hz. The load was chosen so that each specimen has 77.24 MPa of applied stress with a maximum stress of 90.11 MPa. The heat treatments will lower the yield stress of 316L stainless steel from 250 MPa by an unknown amount, but the selected applied load is well below the yield point of 316L. The full test plan alongside the results of the TSA testing is shown in Table 6-11.

Specimen	Number of measurements	Mean (μm)	Standard deviation (μm)	Coefficient of variation
As received 1	18	21.22	0.8976	4.23%
As received 2	18	20.89	0.2632	1.26%
Heat treat 900 1	18	23.20	0.5220	2.25%
Heat treat 900 2	18	20.12	0.7163	3.56%
Heat treat 1050 1	18	22.42	1.078	4.81%
Heat treat 1050 2	18	23.55	0.4663	1.98%

Table 6-10 – RS matt black paint coating information for each dogbone specimen.

Specimen	Area (mm^2)	Load (kN)	Stress (MPa)	Mean $\frac{\Delta T}{T}$	St. Dev	Mean K (Pa^{-1})	St. Dev (Pa^{-1})	%Var
AR	77.68	6	77.24	3.69×10^{-4}	8.40×10^{-6}	4.78×10^{-12}	1.09×10^{-13}	2.28%
AR 2	77.68	6	77.24	3.70×10^{-4}	8.70×10^{-6}	4.79×10^{-12}	1.13×10^{-13}	2.35%
HT 900	77.53	6	77.39	3.63×10^{-4}	9.30×10^{-6}	4.69×10^{-12}	1.20×10^{-13}	2.56%
HT 900 2	77.35	6	77.60	3.63×10^{-4}	6.20×10^{-6}	4.68×10^{-12}	0.80×10^{-13}	1.71%
HT 1050	77.11	6	77.81	3.59×10^{-4}	7.70×10^{-6}	4.61×10^{-12}	0.99×10^{-13}	2.14%
HT 1050 2	77.61	6	77.31	3.58×10^{-4}	8.90×10^{-6}	4.63×10^{-12}	1.15×10^{-13}	2.49%

Table 6-11 – Loading conditions and results of the dogbone TSA tests.

The TSA data, shown for one test in Figure 6-15, shows the small heating effects from the warmer, lower actuator in the T dataset. Although there is no trace of the IR detector reflection a single mean value of T was calculated for each specimen as suggested by Chapter 4. A graph showing the K values for each specimen, and the noise, is shown in Figure 6-16. The results display a small trend suggesting thermoelastic constant is slightly reduced with recrystalisation. However, the standard deviation, shown in the error bars on the plot, potentially masks any actual trend. Numerical values of the data shown in Figure 6-16 are shown in Table 6-12 alongside an average value of K for each heat treatment that is used later to generate the required synthetic bitmaps.

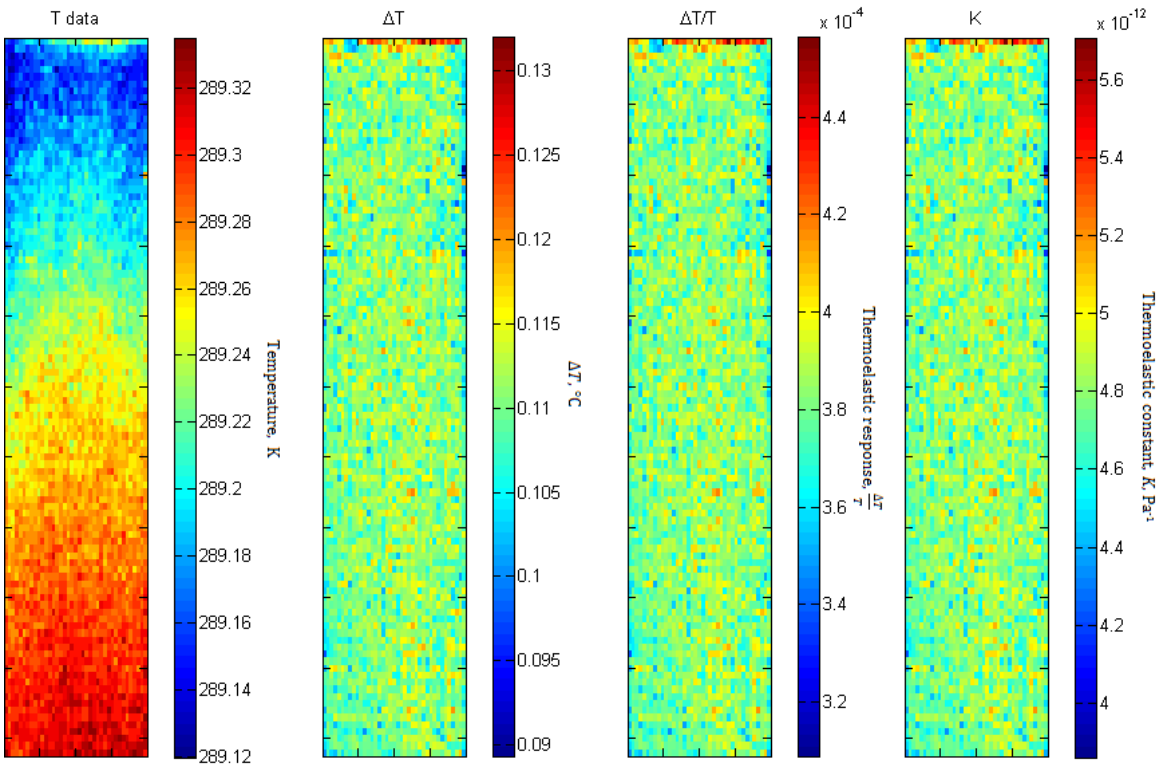

Figure 6-15 – TSA results from the dogbone specimen. Shown is the data from specimen AR 2 and is typical of all the dogbone tests.

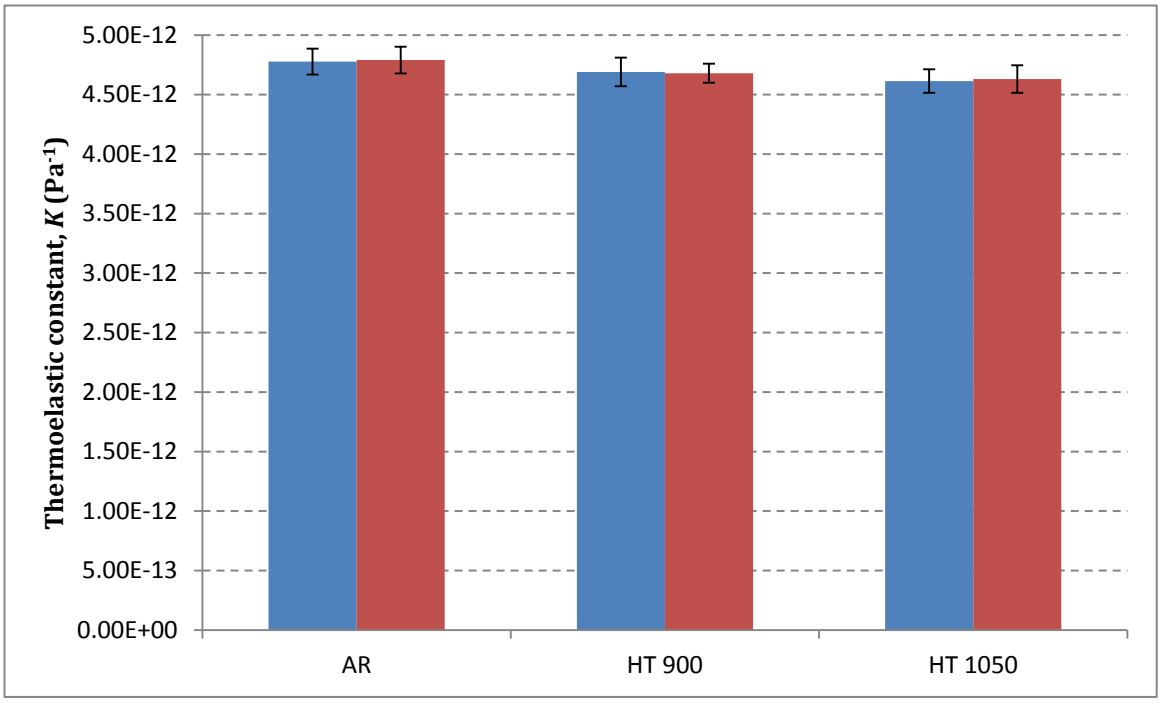

Figure 6-16 – Thermoelastic constant results for each heat treatment. Blue and Red are used to denote specimen 1 and specimen 2 for each heat treatment.

	Thermoelastic constant, *K*						
	1 (Blue)		2 (Red)		Average		
Heat Treatment	**Mean (Pa^{-1})**	**St. Dev. (Pa^{-1})**	**Mean (Pa^{-1})**	**St. Dev. (Pa^{-1})**	**Mean (Pa^{-1})**	**St. Dev. (Pa^{-1})**	**Coefficient Of Variation**
AR	4.78×10^{-12}	1.09×10^{-13}	4.79×10^{-12}	1.13×10^{-13}	**4.78×10^{-12}**	1.11×10^{-13}	2.31%
HT 900	4.69×10^{-12}	1.20×10^{-13}	4.68×10^{-12}	0.80×10^{-13}	**4.69×10^{-12}**	1.00×10^{-13}	2.14%
HT 1050	4.61×10^{-12}	0.99×10^{-13}	4.63×10^{-12}	1.15×10^{-13}	**4.62×10^{-12}**	1.07×10^{-13}	2.32%

Table 6-12 – Numerical results of the thermoelastic constants calculated from the dogbone specimens.

6.3.3 Plastic strain prediction

To determine the amount of deformation that should be applied to tapered specimens such that a large amount of plastic strain would be put into the specimen, elastic-plastic finite element modelling was used to make plastic strain predictions for different applied displacements. To create an accurate model of each heat treated tapered specimen the dogbone specimens were used to generate stress strain curves of the elastic-plastic behaviour. This can then be input into the finite element models, which allows for two things. Firstly, the required plastic strain predictions to inform the test methodology. Secondly, the deformed output geometry which forms the basis of the synthetic bitmap that will be used later on in this chapter to calculate the change in thermoelastic response along the tapered specimens.

Determining the plastic behaviour of 316L stainless steel

The dogbone specimens were cleaned of the black paint used for the TSA in 6.3.2 and had a new coating of matt white spray paint applied; to this a black speckle pattern was added for DIC. The dogbone specimens were plastically deformed using an Instron 8800 in displacement control. The test was performed using a rate of 0.5 mm/min for the first 2 mm of displacement; this took the specimen through the yield point and into the start of plastic behaviour. At 2 mm the rate increased to 5 mm/min until 18 mm had been reached where the specimen was then unloaded at 5 mm/min until the applied load reading of the test machine was zero. The test data was recorded using an E-Lite 5M camera from LaVision (Resolution 2448 x 2050, pixel size 3.45 x 3.45 μm^2, spectral range 400 – 850 nm, and a dynamic range of 8.5 bit) with a 50mm Nikkon lens attached to a computer running DaVis DIC software, DIC data for four of the specimens is shown in Figure 6-17. During the first test load data for

specimen AR1 was not recorded by the DaVis software, and for specimen HT 1050 there was a discrepancy in the strain field after the data was processed which suggested a strain gradient was present in the specimen. For these reasons both of these datasets have been excluded from the further steps in this study. In Figure 6-17 includes an image of a dataset showing the strain field with an adjusted scale, and it can be seen that the centre of the specimen is the region that experiences the most plastic strain. A virtual strain gauge was applied through the DaVis software to each specimen so that stress/strain curves could be constructed for each heat treatment. The results of the plastic deformation tests are shown in Figure 6-18 and there is a clear difference in the yield behaviour of the 900°C heat treatment and the 1050°C heat treatment. When this region of the graph is expanded, Figure 6-19, the difference between the yield behaviour of all three heat treatments is revealed. In all the plots in Figure 6-17 and Figure 6-18, there is a step change in the stress/strain curves, this corresponded to the test machine changing from an initial rate of displacement of 0.5 mm/min for the initial loading through the yield point, to a rate of 5 mm/min for the plastic deformation. This stress/strain curves are used in the finite element models of the tapered specimens built in Abaqus to calculate plastic strain predictions.

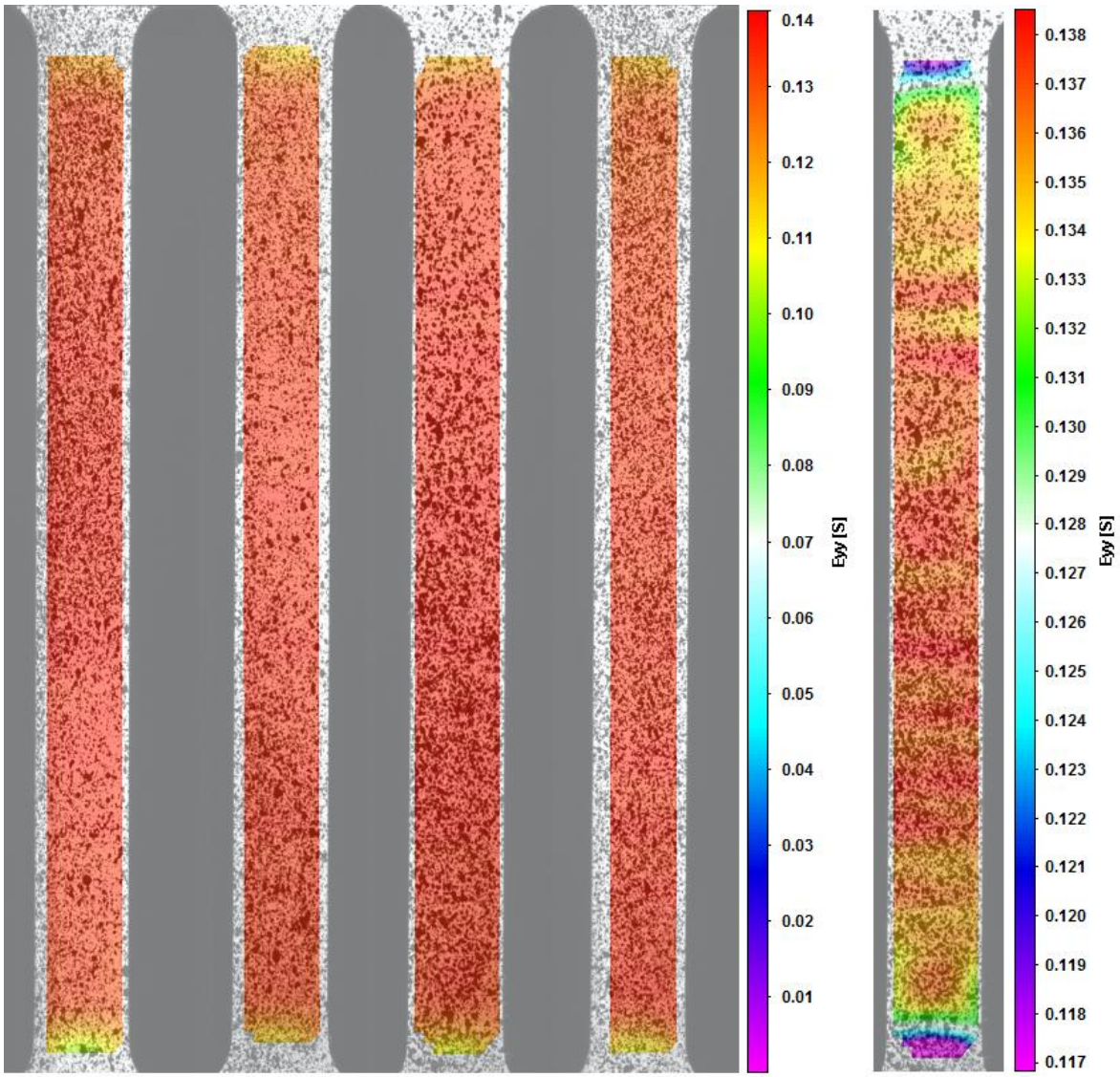

Figure 6-17 – DIC results of (L-R) AR-2, 900-1, 900-2, 1050-2. The far right image shows a slight striping in the calculated strain field and that the plastic strain is symmetrical about the centre.

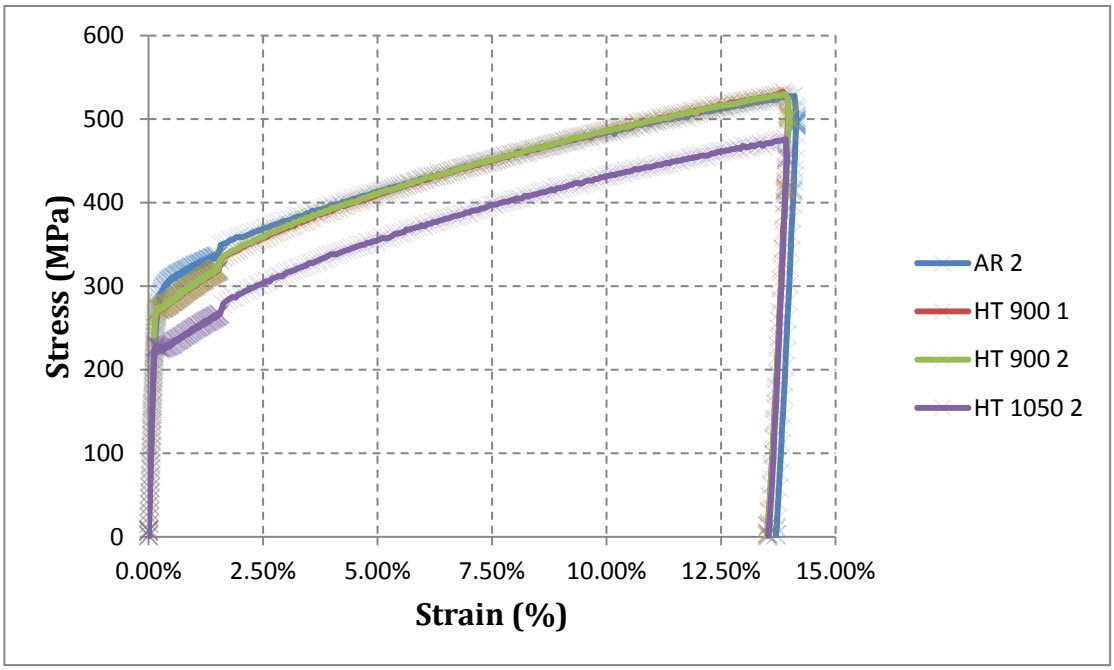

Figure 6-18 – Stress/strain curves for each dogbone specimen. The step is the point where the rate of displacement changes from 2 mm/min to 5 mm/min and is just an inertial effect of the test machine.

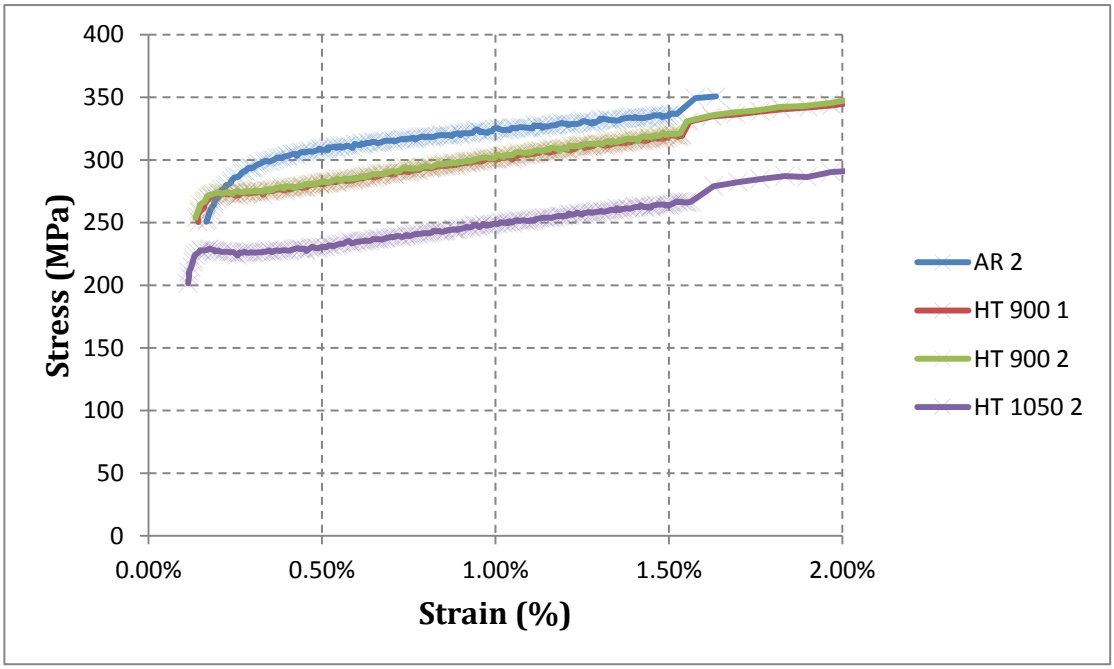

Figure 6-19 – Stress/strain curves that focus on the yield point and the initial plastic behaviour.

Plastic predictions of the tapered specimens using FEA

A 3 dimensional Solidworks geometry was created to the dimensions given in Figure 6-13. This geometry is the same shape as provided for the waterjet cutting of the tapered

specimens. The geometry was converted into an Abaqus assembly using the Abaqus Unified FEA-CAD Interface. This software allows exact CAD geometries to be imported into the Abaqus FEA environment, and also sets up an auto update of the geometry if any alterations are made to the original CAD design. Elastic and plastic material properties of each heat treatment of 316L were calculated using the engineering stress/strain curves in Figure 6-18. An isotropic hardening model was used in Abaqus through the definition of the plastic behaviour assuming small deformations. Abaqus uses a Von Mises stress criterion that uses a defined stress/strain curve to calculate the behaviour of the material. If the maximum stress on the curve is smaller than the maximum stress in the FEA, an assumption of perfectly plastic behaviour is used. True stress and plastic strain values of the plastic behaviour were calculated and are shown in Table 6-13.

		Specimens					
		As received		**900°C H/T**		**1050°C H/T**	
Young's modulus (MPa)		197,000		197,000		197,000	
Poisson's ratio		0.3		0.3		0.3	
Yield stress (MPa)		280		267		226	
σ_{true} **(MPa)**	ε_P $\left(\frac{\%}{\mathbf{100}}\right)$	280.82	0	267.5952	0	226.2057	0
		301.59	0.0014	281.61	0.0031	241.84	0.0060
		323.54	0.0065	303.29	0.0080	263.56	0.0118
		341.73	0.0128	324.2095	0.013596	286.97	0.0154
		367.87	0.0187	346.61	0.0164	308.08	0.0221
		391.25	0.0282	370.66	0.0245	331.29	0.0305
		417.76	0.0394	394.20	0.0331	354.01	0.0396
		442.43	0.0510	419.30	0.0428	378.30	0.0502
		468.97	0.0629	442.67	0.0530	404.58	0.0614
		496.19	0.0751	469.78	0.0642	431.17	0.0734
		524.04	0.0894	496.21	0.0768	457.68	0.0864
		554.04	0.1060	525.02	0.0906	484.83	0.0995
		585.24	0.1218	554.47	0.1042	514.38	0.1156
				583.27	0.1192	537.81	0.1289

Table 6-13 – Material properties for each tapered specimen model

Boundary conditions were applied to the model so that the upper end block of each specimen was restrained from moving in all three principal directions. The lower end block had movement restrained in the x- and z- directions (e.g. no movement in the horizontal plane) and had the displacement boundary condition applied to the bottom face, simulating a fixed displacement using a test machine.

To determine a suitable element size a sensitivity study similar to that carried out in Chapter 3 was performed. The target parameter was the output stress in the y-direction in the straight, narrow section when a given load was applied. A load of 4 kN was applied to the bottom face of the model. The % difference between the output stress and the expected stress (calculated from the cross-sectional area of the narrow section and the applied load) was recorded. Once the difference between the two values was less than 1% the element size was deemed appropriate to use in the future models. An element size of 0.5 mm was found to be the optimal size for the tapered model. An additional model was run however, this took nearly six times as long to calculate and the improvement was only 0.04% over the 0.5 mm element size. The results are shown in Table 6-14.

Element size (mm)	**Applied Load (N)**	**Area (mm^2)**	**Time taken (s)**	**Output stress (MPa)**	**Target stress (MPa)**	**% difference**
2.0	4000	31.2	6	118.52	128.205	7.55%
1.5	4000	31.2	5	122.35	128.205	4.57%
1.0	4000	31.2	8	125.76	128.205	1.91%
0.5	4000	31.2	19	127.98	128.205	0.18%
0.1	4000	31.2	113	128.03	128.205	0.14%

Table 6-14 – Results of the element size sensitivity study used to create the finite element model of the tapered specimens.

To determine a suitable size of displacement a small study was undertaken with each material model where 1, 2, and 3 mm displacements were applied. To elastically relax the model the displacement is applied in a single step, and then in a second step the displacement boundary condition is supressed which allows the material model to relax into the deformed shape containing plastic strain. Peak plastic strain was measured in the straight, narrow section of the tapered specimens where cross sectional area is at a minimum. The results of this study are displayed in Table 6-15 and show that a 3 mm displacement provides a large peak plastic strain (~13%) without resulting in a stress above the UTS of 316L stainless steel.

The peak strain values in the y-direction are shown in Table 6-15 and a strain distribution map from Abaqus of the 1050°C heat treated model is shown in Figure 6-20. It was decided

from these results that a 3 mm displacement would be applied to the physical tapered specimens, as this provided a large peak level of plastic strain (>13%) without having an applied stress too close to the UTS so necking of the specimen should be avoided. A graph of the expected plastic strain distributions is shown in Figure 6-21 with data taken from the vertical centreline of the tapered specimen. As well has having the lowest peak predicted plastic strain, the specimen heat treated to 1050°C has higher levels of plastic strain when the strain is less than 4% at the same distance along the tapered specimen. At 3 mm displacement a sufficiently high level of plastic strain was predicted by the model, so was used as the experimental parameter.

Peak plastic strain	**Displacement**		
Specimen	**1 mm**	**2 mm**	**3 mm**
A/R	2.79%	8.78%	13.80%
900 H/T	2.55%	8.43%	13.35%
1050 H/T	1.65%	7.32%	12.11%

Table 6-15 – Peak plastic strain predictions for each model.

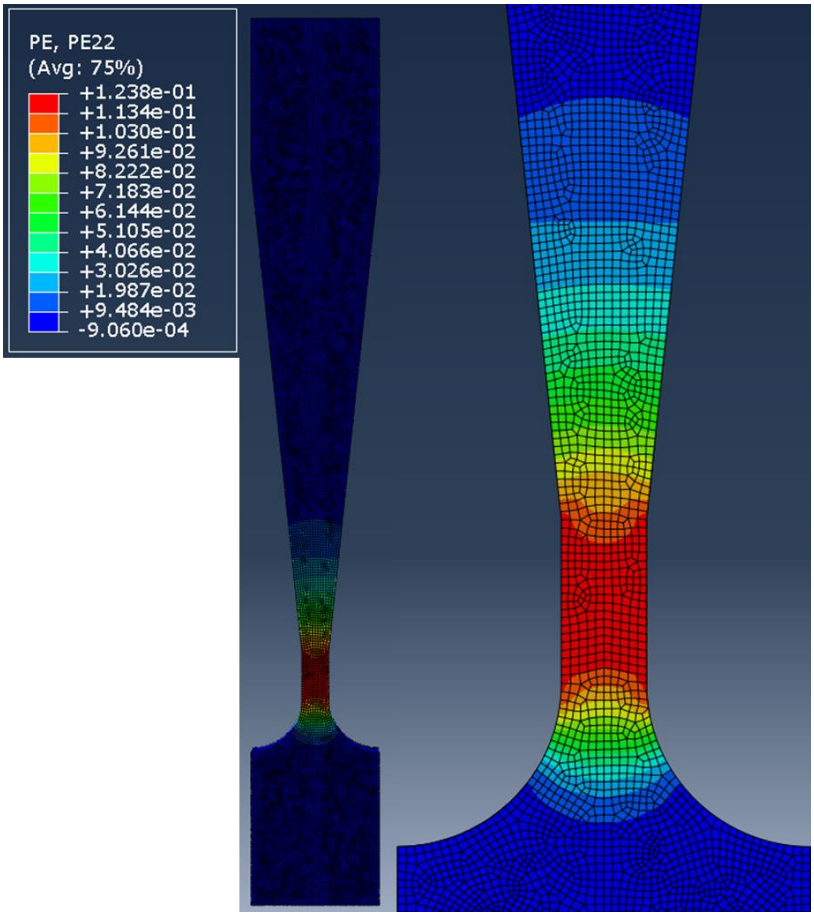

Figure 6-20 – 3D Abaqus model of the 1050°C heat treated tapered specimen, the taper is expanded to show the strain field in more detail.

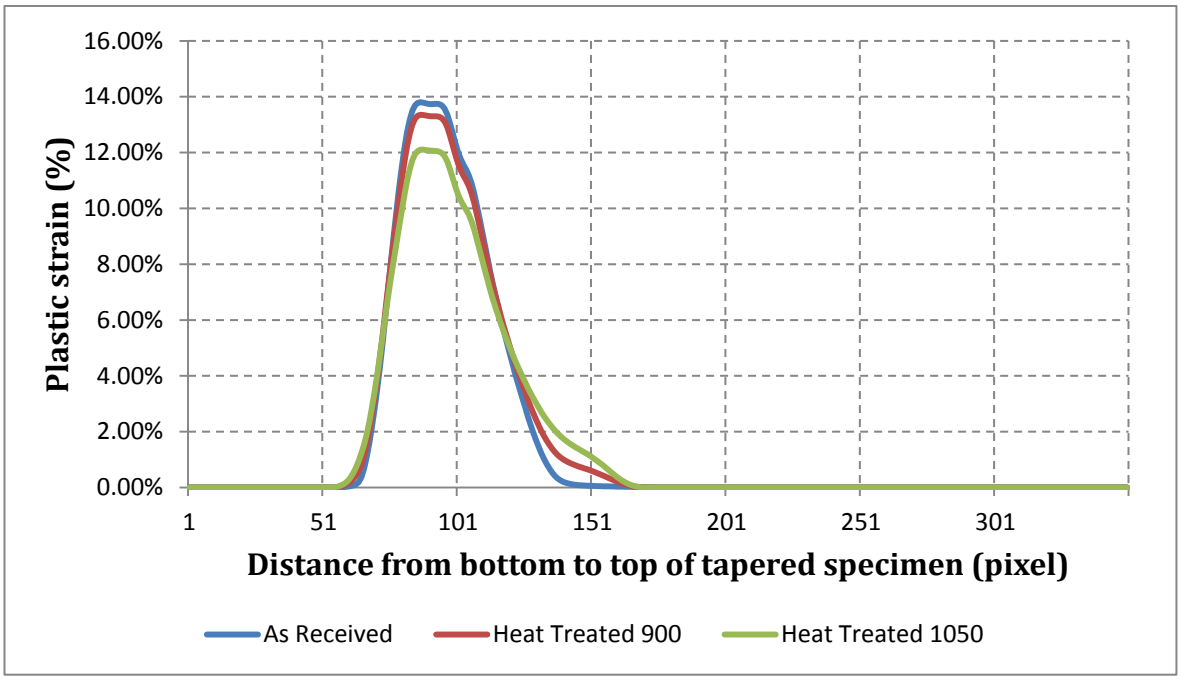

Figure 6-21 – Centreline plots of the plastic strain in each tapered specimen model.

6.3.4 Plastic deformation

Having made predictions of the plastic strain, the tapered specimens were plastically deformed. The specimens were prepared for DIC with a speckle pattern. DIC was used to extract the final plastic strain field from the deformed specimens. As in previous tests, an Instron 8800 servo-hydraulic test machine was used to plastically deform the tapered specimens. A test program of 3mm displacement at 0.5 mm/min was used to perform the deformation. The captured DIC data was processed using a subset size of 41 x 41 pixels and a step of 19. The strain map of the 1050°C heat treated specimen can be seen in Figure 6-22 and there is a strong qualitative correlation between the model strain prediction and the real strain.

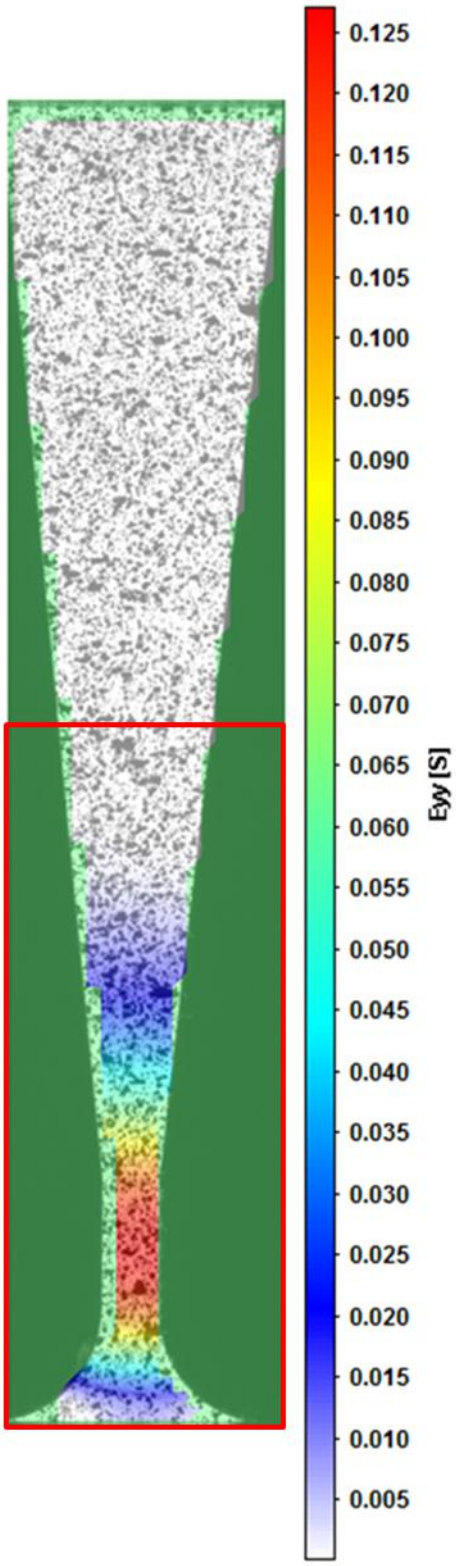

Figure 6-22 – DIC results of the 1050°C heat treated tapered specimen showing the strain in the y-direction.

A vertical profile was taken through each tapered specimen and the strain plotted against the strain predictions made by the model. The plastic strain in the tapered specimens only extends to about 1/3 of the way along the taper, therefore, the profile data was trimmed such that only vertical profile in the red box in Figure 6-22 is plotted in Figure 6-23. Figure 6-23

shows there was very good agreement with the model predictions; however, the specimen heat treated to 1050°C does contain 0.5% higher peak strain in the narrow section than the model predicts.

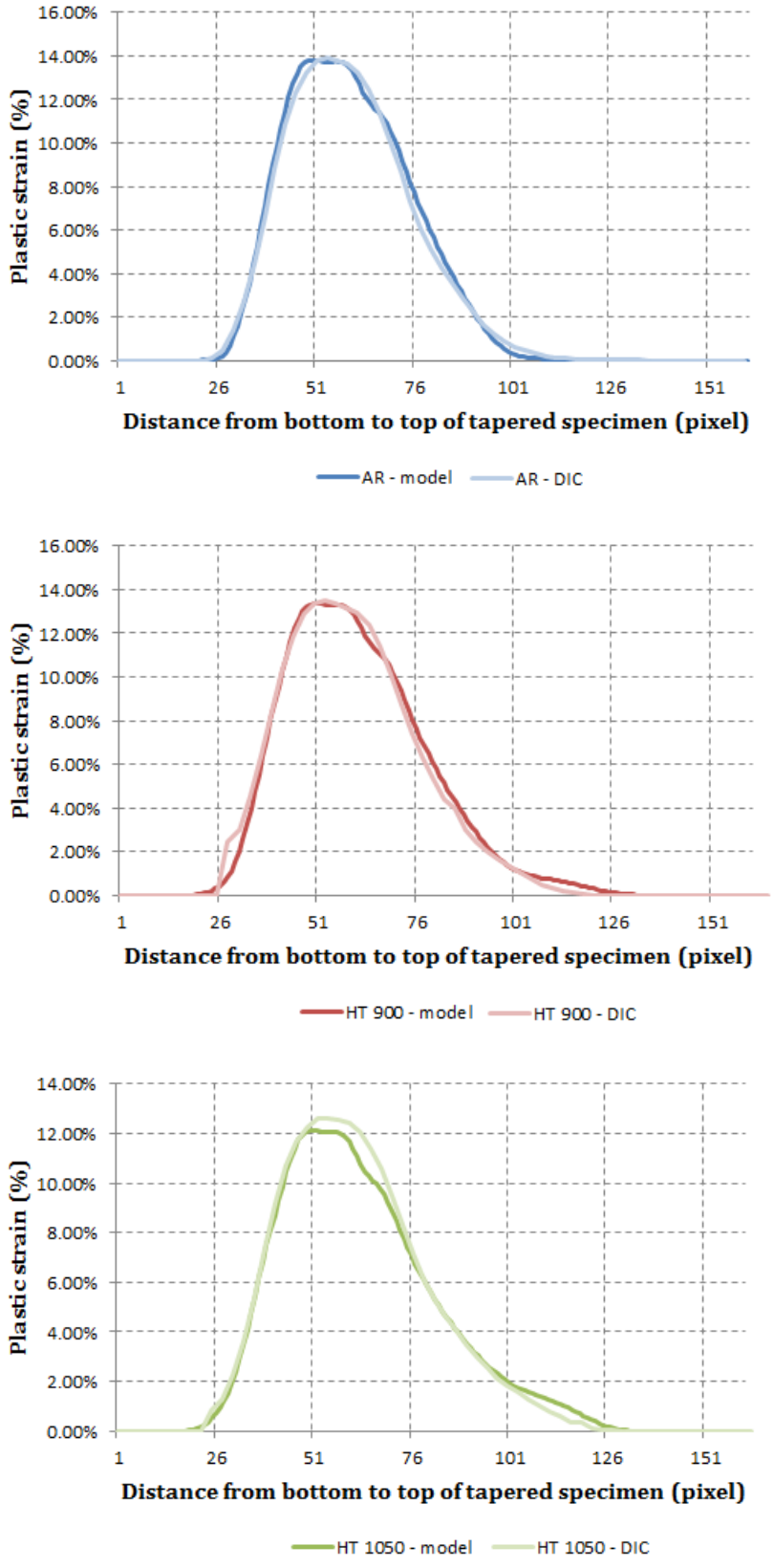

Figure 6-23 – Comparison of the model predictions for plastic strain and the DIC results of the plastic strain.

6.3.5 Thermoelastic stress analysis of tapered specimen

The tapered specimens, having been deformed, were prepared for TSA testing. This will allow the calculation of the thermoelastic response of 316L for a known plastic strain. The deformed shapes from the finite element models used to calculate the predicted plastic strain values were used to construct a second group of finite element models. This second group of models, containing the deformed geometry, was used to construct a synthetic bitmap of each heat treated specimen. Using the synthetic bitmap of the tapered specimens, the resultant thermoelastic response from each heat treatment can be calculated and then plotted against plastic strain. It is from this plot that the relationship between change in thermoelastic response and plastic strain can be calculated.

Methodology

The tapered specimens were cleaned of the speckle pattern previously used for DIC using acetone and had the residue rinsed using water. The thin coating of RS matt black paint was applied, details of which are shown in Table 6-16. Small marks were made away from the region containing peak plastic strain. The marks would allow motion compensation to be carried out using the Random Motion software. A load of 2 ± 1.5 kN (73.36 ± 55.26 MPa) was applied to each tapered specimen at a frequency of 15 Hz. This load was chosen to provide a stress range in the narrowest section of the tapered specimens of 110.52 MPa and a peak stress of 128.94 MPa. This ensured the tapered specimens were not loaded beyond their elastic limit whilst providing a large range of applied stress over which the thermoelastic response could be calculated. The data was processed using the Random Motion software described in Chapter 2 to remove a small amount of noise, and then Altair LI to extract the T and the ΔT datasets.

Specimen	Number of measurements	Mean (µm)	St. Dev. (µm)	Coefficient of Variation
As received	10	20.45	0.446	2.18%
Heat treat 900°C	10	21.03	0.494	2.35%
Heat treat 1050°C	10	20.86	0.388	1.86%

Table 6-16 – Paint thickness details of the RS matt black paint coating applied before TSA data was taken.

Results

As seen in other TSA data gathered throughout the PhD, in the tapered specimens there is a reflection of the IR camera visible in the T dataset of the processed IR data. Figure 6-24 shows the complete T data from the Altair software. A section is removed from the centre of each

specimen and viewed in Matlab. In each plot there is a small thermal gradient from the warmer, bottom actuator to the cold top grip. In the first two there is a cold spot in the data that is creating a large discrepancy in the temperature field recorded by the IR camera. To correct for this, as suggested in Chapter 4, a mean value of T has been calculated for each of the sections displayed in the right-hand side of Figure 6-24. This average value of T is used to calculate values of $\frac{\Delta T}{T}$ for each specimen.

The section of data (marked by the boxes in Figure 6-24) taken from the centre of the tapered specimens in the T dataset was also taken in the ΔT dataset. The values were divided to calculate a $\frac{\Delta T}{T}$ dataset that measured 10 x 204 pixels. Each row in the $\frac{\Delta T}{T}$ was averaged to give a single value along the centreline of the tapered specimen. A line plot of this averaged $\frac{\Delta T}{T}$ is shown in Figure 6-25. The plastic strain along the same centreline was taken from the DIC data collected during the plastic deformation of the tapered specimens. This was used to plot the thermoelastic response against plastic strain through the length of the specimen, see Figure 6-26. The specimen contains a large region without any plastic strain, which is shown by the cluster of data points at the 0% strain location on the line plot. The next step was to calculated the resultant thermoelastic response for each tapered specimen down the centreline. This value was calculated using the synthetic reference bitmap created in Abaqus.

The synthetic reference bitmap was created using the geometry of the deformed finite element model for each heat treated tapered model. The same 3 kN load from the TSA was applied in Abaqus to provide an output stress map of the tapered specimens. The stresses in the x- and y-direction were output from the nodes along the centreline of the finite element model and imported into Matlab. In Matlab, the value of thermoelastic constant measured from the dogbone specimens was applied to the stress data. This created a $\left(\frac{\Delta T}{T}\right)_{Syn}$ dataset that is the reference dataset needed for the synthetic bitmap approach this PhD has created. The resultant line plot, $\left(\frac{\Delta T}{T}\right)_{Resultant} = \left(\frac{\Delta T}{T}\right)_{TSA} - \left(\frac{\Delta T}{T}\right)_{Syn}$, for the centreline of each tapered specimen has been plotted against plastic strain and is shown in Figure 6-27. There is a small positive correlation within the two heat treated datasets. At small levels of plastic strain <2% the scatter is too large to plot a trend line. This suggests that the threshold of detectability is in the region of 2% plastic strain, however, further work is required before a final conclusion can be drawn.

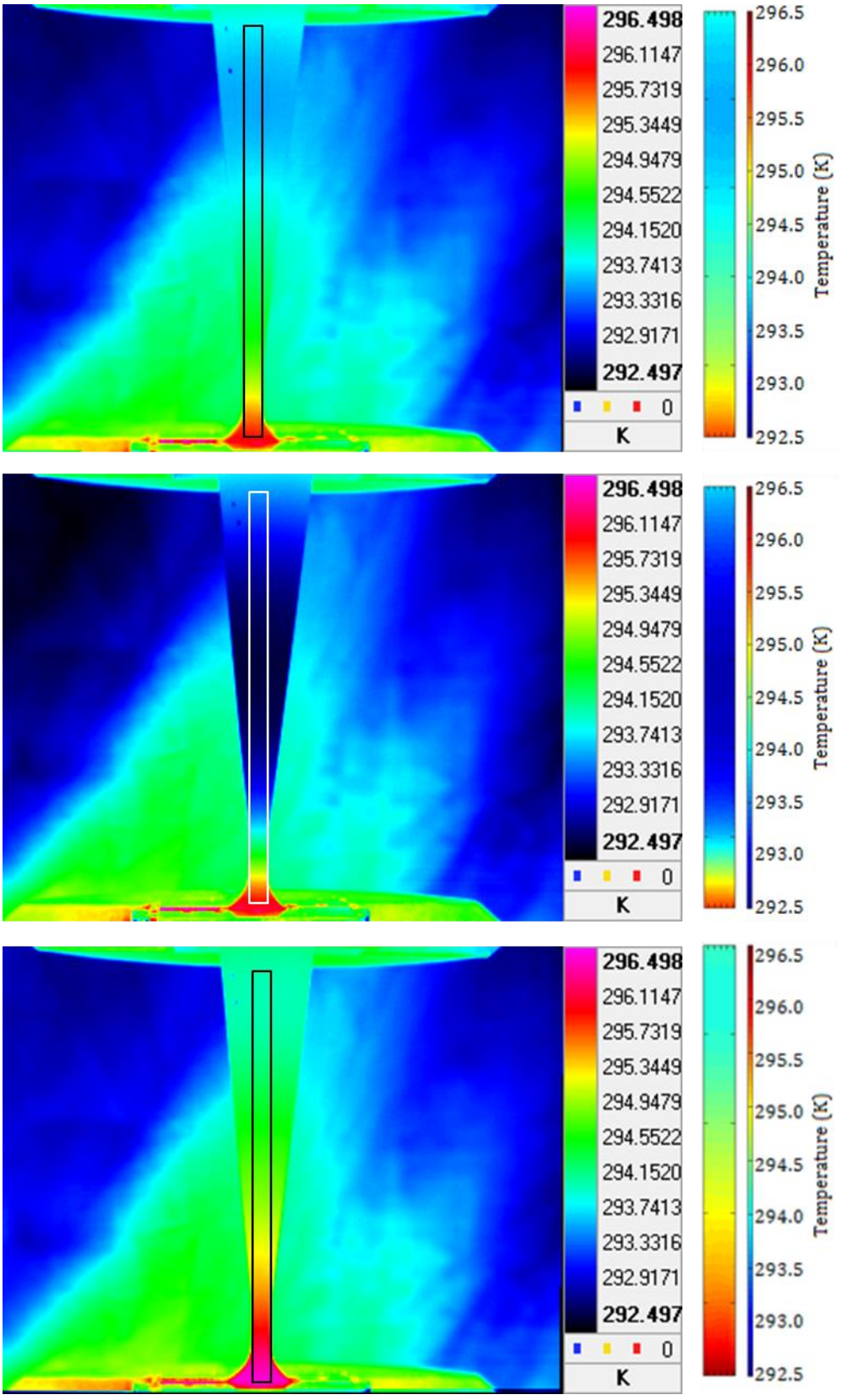

Figure 6-24 – Images of the *T* data from the tapered specimen TSA tests. Top to bottom is the "As received", "900°C heat treatment", and the "1050°C heat treatment" specimen. On the right is a section taken from the middle of each specimen.

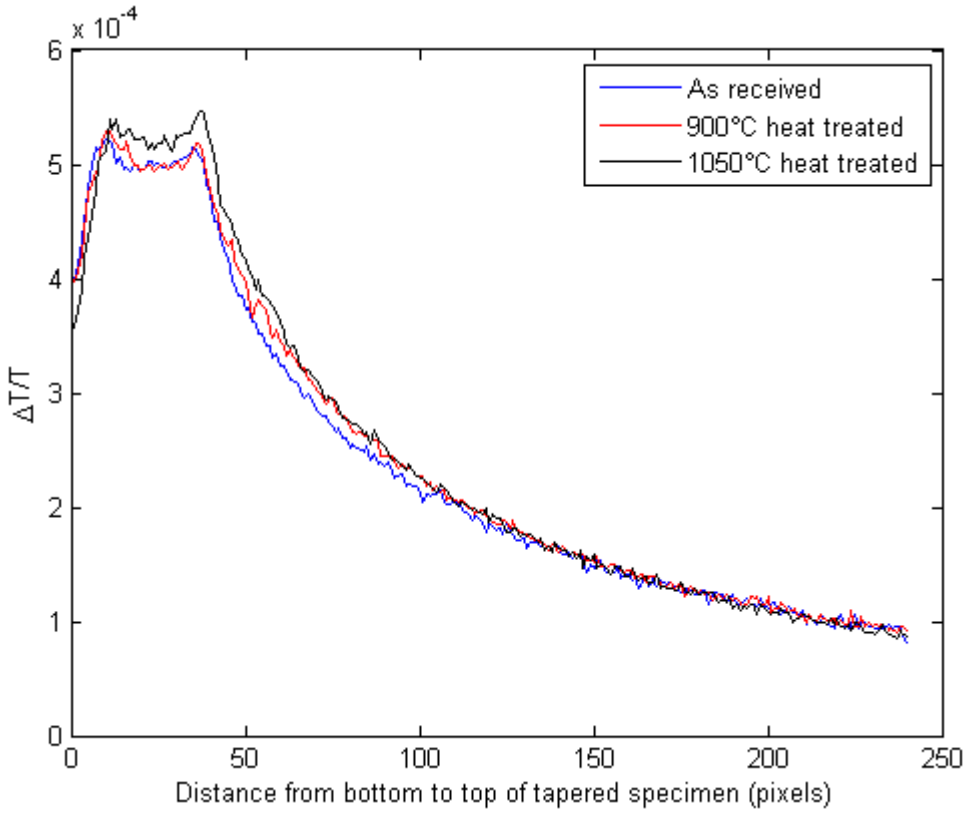

Figure 6-25 – *ΔT/T* of each tapered specimen plotted along the length of the tapered specimen from the bottom to the top.

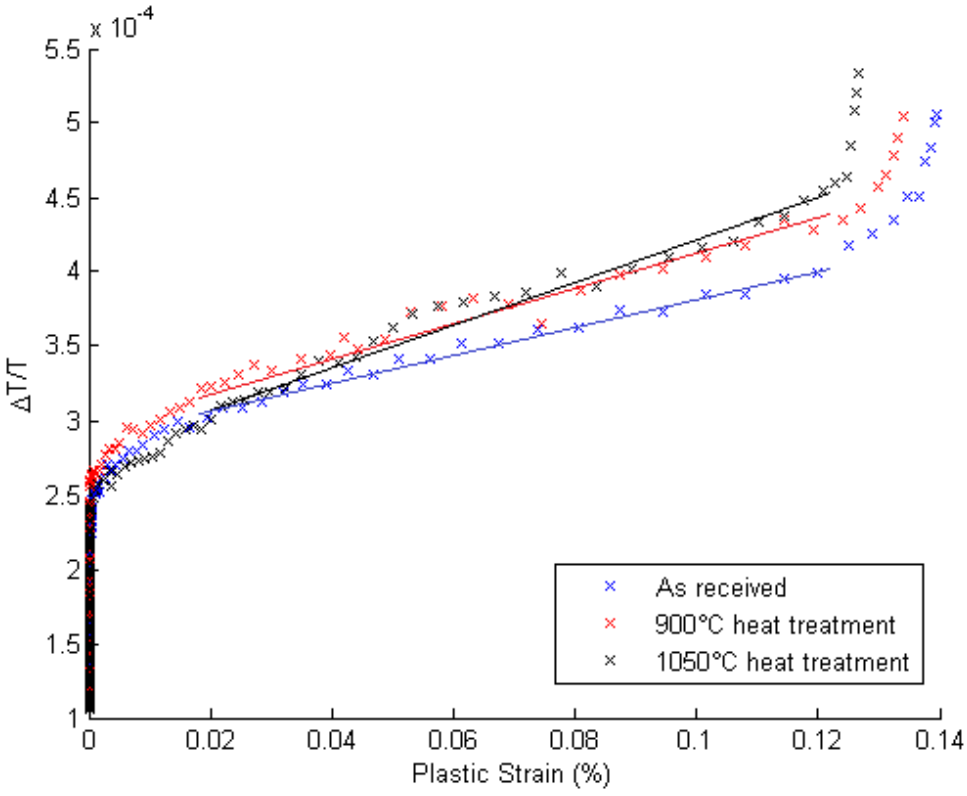

Figure 6-26 – *ΔT/T* of each tapered specimen plotted against the plastic strain recorded in the DIC data.

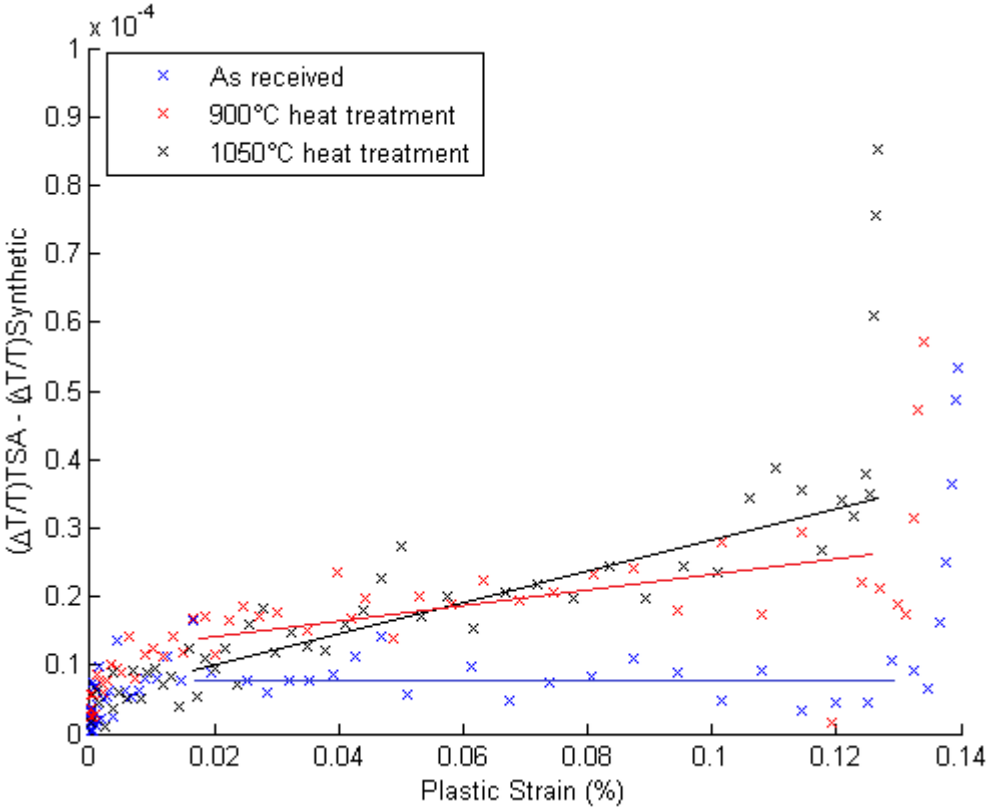

Figure 6-27 – Resultant thermoelastic response along the centreline of each specimen plotted against plastic strain recorded in the DIC data.

In both Figure 6-26 and Figure 6-27 the as received specimen presents a consistently lower $\frac{\Delta T}{T}$ when plotted against the plastic strain and also there appears to be no plastic strain dependency on the resultant $\frac{\Delta T}{T}$; therefore, no change in the thermoelastic constant with plastic strain. There are a couple of explanations for this, either the dislocations present in an as received specimen hide a dependency of the thermoelastic constant with plastic strain or during the heat treatment and subsequent abrasion of the tapered specimen to clean the residue deposited in the vacuum furnace the surface stress state was altered and the apparent relationship was revealed. The heat treatment was performed on only one tapered specimen, so these plots form a single data point. The sharp rise in the resultant thermoelastic response seen at around 13% plastic strain is potentially caused by the plane stress assumption no longer being true. The final 4 data points in each set have been removed for further analysis of the data. The section of data below 2% plastic strain has also been removed from the results because the increased scatter in the results below 2% plastic strain makes it difficult to draw sufficient correlation. It is required that additional specimens be manufactured and heat treated to further investigate if the relationship between the resultant $\frac{\Delta T}{T}$ in the heat treated specimens has a causal relationship with plastic strain. The normalised thermoelastic constant along each tapered specimen is plotted against plastic strain in

Figure 6-28 so that a comparison to the results of [17] can be made. As found in the results plotted in Figure 6-27, the as received specimen shows no dependence on plastic strain. The 900°C heat treated specimen displays a slight dependency, although there is only around a 1% increase in thermoelastic constant when 13% plastic strain is present in the specimen. The 1050°C heat treated specimen shows a comparable relationship to the results found in [17], there is a 3.5-4% increase in thermoelastic constant when 13% plastic strain is present. The results in Figure 6-4 display around a 5% increase in thermoelastic constant with 15% plastic strain present in the specimen. This is an encouraging result that warrants further investigation to better define the relationship between plastic strain and thermoelastic constant when heat treatment has been applied.

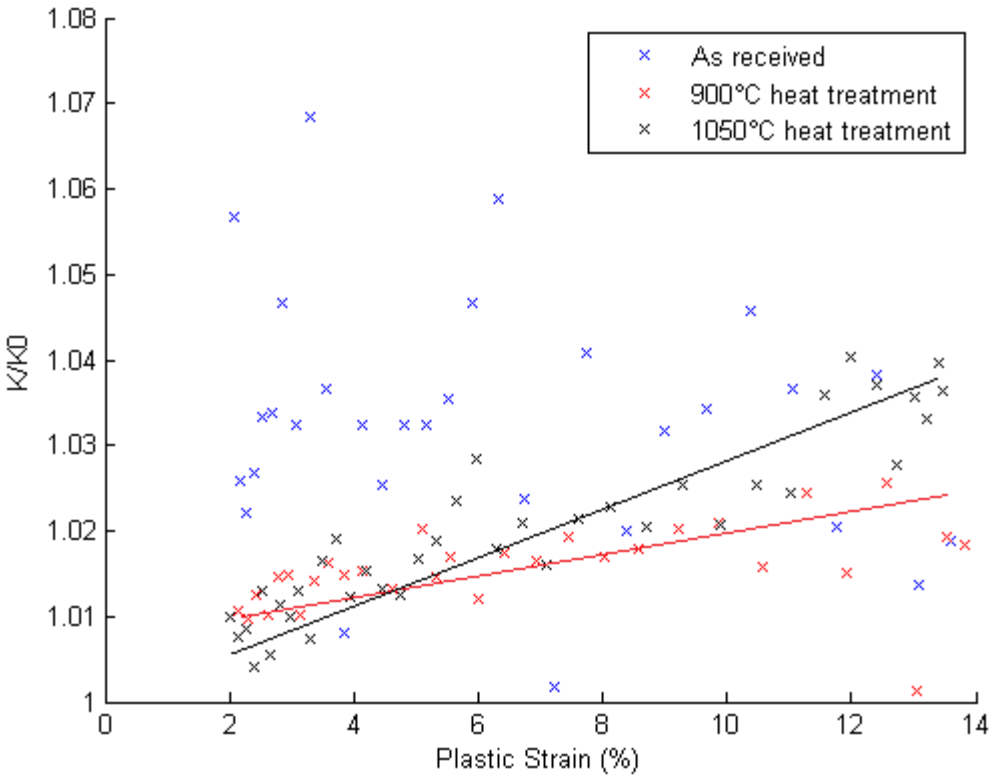

Figure 6-28 – Normalised K/K_0 plotted against plastic strain from each tapered specimen.

6.4 Extraction of the thermoelastic constant for a third generation welded mock-up

A pipe specimen measuring 1.5 m long and 48 mm in diameter made from 316L stainless steel was used to manufacture another welded mock-up. This specimen had a variety of realistic weld geometries included along its length, and was designed to be loaded using a shaker fixed to the pipe section rather than using a test machine to impart a load. This was to aid the development of the onsite testing described in Chapter 7. The pipe sections were in an

"as received" condition from the manufacturer and were too large to be heat treated in the furnaces available in a single heat treatment cycle. Therefore, it was required to establish whether there was any difference in thermoelastic constant between a non-heat treated section of the pipe and a section that had undergone heat treatment at 1050°C. Pipes that were to be investigated onsite would have been heat treated prior to installation and welding and if the $\frac{\Delta T}{T}$ data collected from the pipe section was to be converted into summed stress data the value of K needed to be known.

Two sections of 316L stainless steel pipe were used for this investigation, both pipe sections were cut from the pipe to be used for the large welded experimental test specimen. Both sections had 48 mm outer diameter and 38 mm inner diameter (therefore a wall thickness of 5 mm). Each section was 50 mm in length, but had to be squared off to give a final length of 42 mm. One specimen was heat treated in a vacuum furnace with a cycle of 200°C/hr heating to a temperature of 1050°C where it was held for 1 hour before cooling at a rate of 100°C/hr to room temperature.

Both specimens had surface dirt removed using acetone and were rinsed thoroughly. A thin coating of RS matt black paint was applied and the thickness of the paint checked, see Table 6-17 for details of the paint coating. The specimens were loaded into an Instron 8032 100 kN servo-hydraulic test machine between two compression plates bolted to the actuators of the test machine. A distance gauge was used to check the parallel nature of the plates and there was <0.1 mm of height difference between the left and right sides of the compression plates. Between the front and back there was no difference in height. The centre of the bottom compression plate was marked such that the pipe sections could be put in the same position, the centre of the test machine, every time they were put into the machine. Each specimen can be observed at 0°, 90°, 180°, and 270° and also two ways up; this results in the test matrix given in Table 6-18.

Specimen	Number of measurements	Mean (µm)	Standard Deviation (µm)	Coefficient of Variation
As received	14	18.45	0.310	1.68%
Heat treated 1050°C	14	19.20	0.424	2.21%

Table 6-17 – Paint thickness results of each pipe section.

Test number	Specimen	Load (kN)	Frequency (Hz)	Stress (MPa)	Elevation	Orientation
1	**AR**	-20±16.5	10	-30.29±24.99	A	Up
2	**AR**	-20±16.5	10	-30.29±24.99	B	Up
3	**AR**	-20±16.5	10	-30.29±24.99	C	Up
4	**AR**	-20±16.5	10	-30.29±24.99	D	Up
5	**AR**	-20±16.5	10	-30.29±24.99	A	Down
6	**AR**	-20±16.5	10	-30.29±24.99	B	Down
7	**AR**	-20±16.5	10	-30.29±24.99	C	Down
8	**AR**	-20±16.5	10	-30.29±24.99	D	Down
9	**HT**	-20±16.5	10	-30.29±24.99	A	Up
10	**HT**	-20±16.5	10	-30.29±24.99	B	Up
11	**HT**	-20±16.5	10	-30.29±24.99	C	Up
12	**HT**	-20±16.5	10	-30.29±24.99	D	Up
13	**HT**	-20±16.5	10	-30.29±24.99	A	Down
14	**HT**	-20±16.5	10	-30.29±24.99	B	Down
15	**HT**	-20±16.5	10	-30.29±24.99	C	Down
16	**HT**	-20±16.5	10	-30.29±24.99	D	Down

Table 6-18 – Test plan with applied loads and frequencies for both pipe sections. AR is the as received specimen, HT has been heat treated to 1050°C

The load applied was a compressive load, but the stress range used to calculate the thermoelastic constant is a Δ-value; therefore, it is just the magnitude of the stress range that is used. In the T data for the pipe sections it was noted that there was a reflection coming from a hydraulic hose of the test machine, see Figure 6-29. This resulted in a slightly elevated temperature reading on the right hand side of every T dataset. To correct for this an average from the central section, shown in the black box in Figure 6-29, was calculated and used for the $\frac{\Delta T}{T}$ calculation.

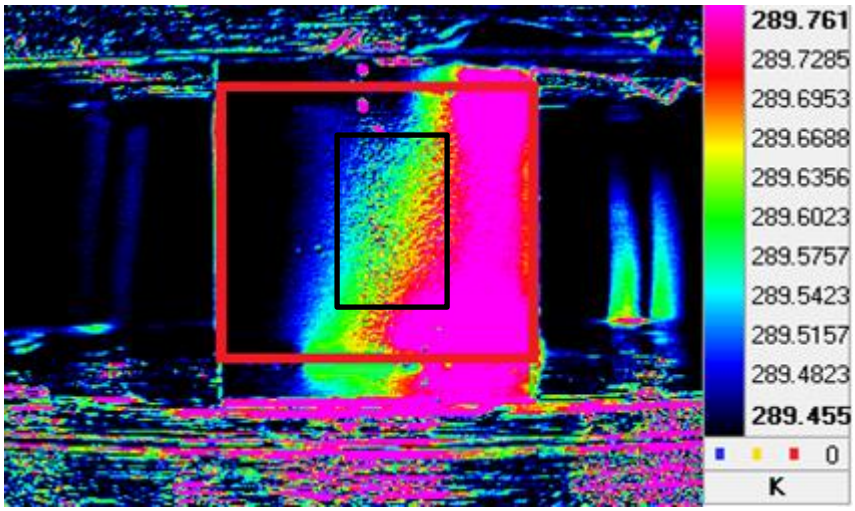

Figure 6-29 – *T* data of one of the pipe section TSA tests showing the influence of the warm hydraulic pipe. The red section shows the boundary of the specimen.

Results of the TSA tests on the pipe sections are shown in Table 6-19 with the averaged *K* and coefficient of variation shown in Table 6-20. These results agree with the results of the tests performed using the dogbone specimens in 6.3.2. The specimen which has been through a heat treatment cycle at 1050°C has a thermoelastic constant value of 4.63 x10^{-12} Pa^{-1} whilst the result for the as received specimen is 4.65 x10^{-12} Pa^{-1}. The tapered specimens show an apparent dependency on thermoelastic response with heat treatment. The dependency not seen in the results of the pipe sections and the dogbone specimens could be as a result of averaging which is carried out to define a single value of *K* for each specimen. The averaging could be masking any dependency in a relatively large scatter. The size of the difference between the two specimens is of a similar size to the scatter in the final results (the error bars are equal to 1 standard deviation), shown in Figure 6-30, therefore, more accurate measurements are required to conclude if there is a detectable difference between the thermoelastic constant for different heat treatments of 316L stainless steel.

Specimen	Test	ΔT (°C)	T (K)	$\frac{\Delta T}{T}$	K (Pa^{-1})
AR	**1**	0.0701	290.03	0.000242	4.84×10^{-12}
AR	**2**	0.0692	290.02	0.000239	4.77×10^{-12}
AR	**3**	0.0655	290.00	0.000226	4.52×10^{-12}
AR	**4**	0.0663	290.00	0.000229	4.57×10^{-12}
AR	**5**	0.0691	290.39	0.000238	4.76×10^{-12}
AR	**6**	0.0694	290.37	0.000239	4.78×10^{-12}
AR	**7**	0.0648	290.22	0.000223	4.47×10^{-12}
AR	**8**	0.0649	290.19	0.000224	4.48×10^{-12}
HT	**1**	0.0692	289.45	0.000239	4.78×10^{-12}
HT	**2**	0.0681	289.47	0.000235	4.71×10^{-12}
HT	**3**	0.0652	289.62	0.000225	4.50×10^{-12}
HT	**4**	0.0661	289.64	0.000228	4.57×10^{-12}
HT	**5**	0.0672	289.85	0.000232	4.64×10^{-12}
HT	**6**	0.0697	289.84	0.000240	4.81×10^{-12}
HT	**7**	0.0653	289.88	0.000225	4.51×10^{-12}
HT	**8**	0.0655	289.84	0.000226	4.52×10^{-12}

Table 6-19 – TSA test results for each row in Table 6-18.

Specimen	Mean K (Pa^{-1})	Standard Deviation (Pa^{-1})	Coefficient of Variation
AR	4.65×10^{-12}	1.54×10^{-13}	3.31%
HT	4.63×10^{-12}	1.25×10^{-13}	2.70%

Table 6-20 – Averaged values of K for each pipe section.

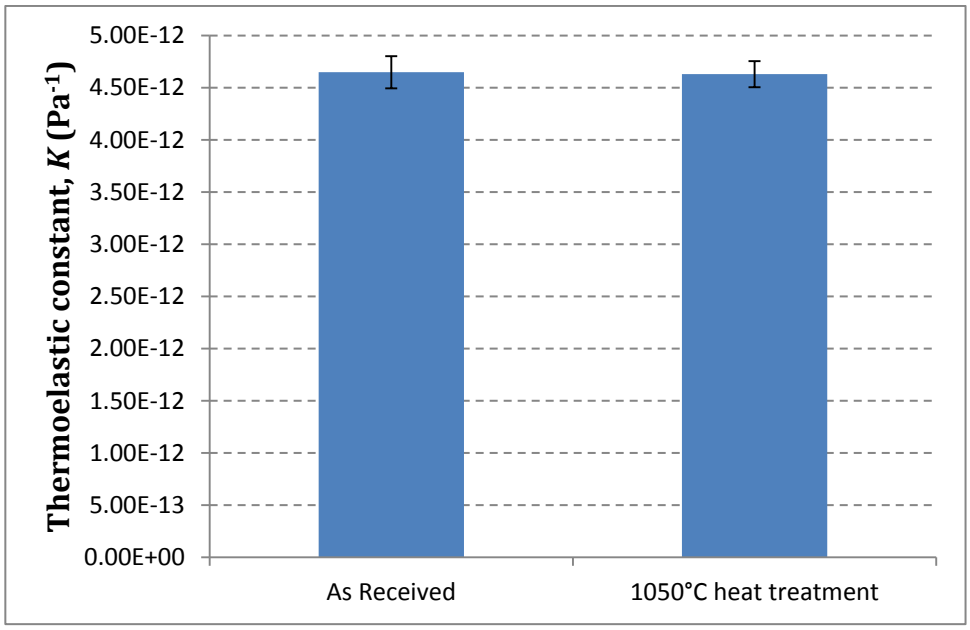

Figure 6-30 – Thermoelastic constant results of the two differently heat treated pipe sections.

6.5 Summary

This chapter aimed to determine the relationship between plastic strain and change in thermoelastic constant in 316L stainless steel. Results in [17] suggested that there was a linear relationship between plastic strain and a change in thermoelastic constant. However, when an attempt was made to replicate the results there were many sources of error and it was not possible to define the relationship using the large dumbbell specimens designed in [17]. A new specimen was designed that contains a gradient of plastic strain within a single specimen. This specimen only contained tensile plastic strain, not the compressive strain the dumbbells carried. However, by having the plastic strain gradient in a single specimen it removed many of the sources of error found in the dumbbell tests.

The results of the tapered specimen showed that there may be a relationship between plastic strain and thermoelastic constant. It also showed that there was a difference in the response between the heat treated and the as received material. When the normalised thermoelastic constant was plotted against plastic strain, a similar relationship was found in the 1050°C heat treated specimen as concluded by [17]. From the amount of scatter in the data recorded in the section of the specimens that experienced less than 2% plastic strain, a further conclusion can be drawn that 2% plastic strain is the detectability threshold for the current IR camera system. To improve this threshold with the current IR camera, and allow a detection of plastic strain of less than 2% plastic strain further investigation is required. These include defining the error caused by the movement of the specimen relative to the camera and devising better motion compensation routines. The error arising from the paint

coating, i.e. its thickness, the variability in thickness across a surface, and the quality of the bond between the paint and the effect of surface roughness.

As part of the investigation using the tapered specimens, it was necessary to investigate potential changes in thermoelastic constant when different stress relieving heat treatments are applied to components made from 316L stainless steel. There was a second body of work that also investigated this. The first set of experiments used dogbone specimens and applied a tensile cyclic load to perform TSA; the second set used sections of pipe and applied a compressive cyclic load. Both experiments showed a small reduction in thermoelastic constant when 316L is stress relieved; however, the difference between results was the same size as the scatter within each set of results so a definite relationship cannot be drawn.

Chapter 7: Application to a real, industrial component

7.1 Introduction

In Chapter 5 TSA was used to reveal regions within the cross section of a welded industrial mock up that contained plastic strain. These results were checked against model predictions of the welding and cutting process and correlation with the results was found. Chapter 6 attempted to use a specimen that contained a plastic strain gradient to determine the relationship between change in thermoelastic response and plastic strain. The results showed that there was a relationship, with an increase in plastic strain there is an increase in thermoelastic constant. The work of Chapter 6 did also reveal that there was around a 2% plastic strain threshold of detectability with the technique below which the scatter in the data was too large to observe any relationship.

The overall aim of the RESIST project was to create a new, onsite residual stress detection technique using TSA for the power generation industry. The work described in the previous two chapters demonstrates that regions containing plastic strain could be revealed using TSA, and the relationship between change in thermoelastic constant and plastic strain be established, once further investigation to define the size of errors within the technique has been carried out. Both sets of work were performed in a laboratory setting; therefore, it is necessary to take the equipment required for TSA onsite and determine if the TSA technique can be applied in-situ, as a tool for non-destructive evaluation in the first place. The target of this study was not to apply the plastic strain assessment, but to define what is achievable when TSA is applied outside the laboratory.

Two onsite visits were carried out to investigate the use of TSA equipment at power stations, EDF West Burton was visited in August 2015 and EDF Cottam was visited in August 2016. The results of the August 2015 visit to EDF West Burton, as well as the pre-site investigations, were reported in [77]. Both power stations have coal fired boilers and generate 2000 MW and 1000 MW respectively. The drain pipes coming from the boiler stacks were an ideal case study for implementing TSA onsite because they are relatively thin sections, outer diameter $40\text{mm}<d<50\text{mm}$, and contain a variety of weld types including T-junction welds between similar sized pipes, pipes joining with larger vessels, and girth welds to joint two lengths of pipe together. Unlike nuclear plant, the pipes are made from a ferritic steel so had an oxide coating that had to be removed before TSA could be performed, and the thermoelastic constant, K, had to be calculated for the material. It should be noted that it was not possible to

perform the work at EDF's nuclear sites, mainly because of health and safety restrictions. The tests at EDF West Burton and EDF Cottam were performed during outage, mainly on pipework that was scheduled to or had been replaced. A similar opportunity was not available at the nuclear power stations and there was concern about loading pipework that was to remain in service. The onsite work was led by Dr. Rachael Tighe who developed the onsite remote loading technique used; the determination of the thermoelastic constant and experiments into surface preparation technique were performed as part of the current PhD, alongside supporting the site visits and aiding in the set-up and data collection.

7.2 Pre-site visit investigations

Before going onsite it was required that some adjustments were made to the TSA methodology used within a laboratory environment. In general, specimens developed for tests within a laboratory have been manufactured for a specific purpose and as such arrive in an "as received" condition. Heat treatments and other material finishing techniques might be applied before testing, but the surface of test specimens usually only requires a small application of acetone to remove dirt before the matt black paint is applied. The pipes within a conventional power station however are made from ferritic steel that develops an oxide layer throughout the life cycle of the pipe. Therefore, the effects of this oxide layer on the thermoelastic response need to be established, and what degree of surface preparation is required to reduce the errors in TSA data associated with the pipe surface.

In a laboratory the load is usually applied to tensile specimens using a servo-hydraulic test machine to apply a cyclic load. Mounting a test machine around the pipework onsite is not a feasible solution. Therefore, a new loading approach had to be adopted that applies a small load at the fundamental frequency of the system to excite at the first mode and therefore increase the applied load. The first approach investigated used a permanent magnetic shaker to apply the cyclic load; the second used a pneumatic shaker. Both systems proved effective in the laboratory trials, though only the pneumatic shaker was used to apply the load to the pipes onsite.

7.2.1 Specimen preparation on-site

A sample of ferritic steel steam drain pipe was provided by EDF for performing laboratory trials. The section measured 600 mm and had an outer diameter of 42 mm and a wall thickness of 9 mm. The exterior of the pipe had a thick oxide layer with large flakes of rust composing the surface. Four different surface preparation techniques were trialled on the pipe and are referred to as L1-4, detailed in Table 7-1. The pipe was cyclically loaded using an Instron servo-hydraulic test machine with a tensile load of 99±81 kN (106±87 MPa) at a

loading frequency of 10 Hz. $\frac{\Delta T}{T}$ was calculated point by point for each level of surface finish and an average $\frac{\Delta T}{T}$ was determined for sections L1-4. K was then calculated by applying equation (1-1) giving four experimentally derived values of K for the ferritic steel pipe. Repeat tests were completed by turning the pipe upside-down to remove potential bias caused by pipe orientation. The reported value of K is the average of both tests.

Surface preparation	Description
L1	Application of a wire brush to remove flakes of rust and surface debris.
L2	Application of a wire brush and 80 grit SiC paper used to further prepare surface.
L3	Application of a wire brush and 120 grit SiC paper used to further prepare surface.
L4	Application of a wire brush and 180 grit SiC paper used to further prepare surface.

Table 7-1 – Details of each surface preparation level used on ferritic steel pipe.

L1 gave a much lower value of thermoelastic constant than L2-4 and also contained a larger standard deviation within the data. L2-4 provided very consistent values of K with much smaller standard deviation than L1. The pitting in the surface of the specimen increased the standard deviation more than would be expected from a TSA test, but this is to be expected and is one of the difficulties when applying TSA to real industrial components. The results of the thermoelastic constant tests are shown in Figure 7-1. The measured value of K does not improve beyond using surface preparation L2; therefore, it was decided to use a wire brush and 80 grit SiC paper for the onsite inspections. The exact grade of steel is not known, so K was calculated from literature values of its component parameters for a general steel [78] as 3.04 x10^{-12} Pa^{-1}. This is shown in Figure 7-1 as the dotted red line. The average thermoelastic constant of surface preparation L2-4 was measured as 3.20 x10^{-12} Pa^{-1}; this is shown in Figure 7-1 as the solid red line. The difference between the experimental value and literature estimation is less than 6%. This gives confidence to the experimentally derived value of K and so 3.20 x10^{-12} Pa^{-1} was used when converting onsite $\frac{\Delta T}{T}$ data into summed stress data.

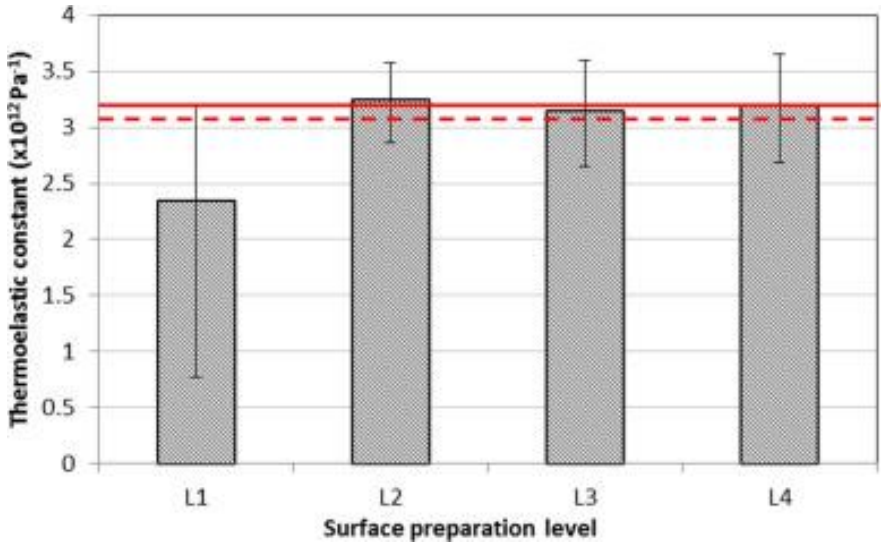

Figure 7-1 – Experimentally calculated *K* values of each surface preparation level L1-4. Literature value (red, dashed line) and mean experimental value (red, solid line) [77].

7.2.2 Load application to the pipe

To test the application of load another section of ferritic steel pipe was provided by EDF. This was 1.5 m in length with the same external diameter as the previous section, 42 mm. To mount the pipe section end plates were welded on and connections bolted to allow it to be attached to a metal strong floor. The pipe has the welds at both ends prepared using surface preparation technique L2 and then coated with a layer of Electrolube EMB400 paint. Electrolube was used rather than RS matt black because at the time the RS matt black paint was not readily available. As it was shown in Chapter 4 that the Electrolube paint performed almost as well this was chosen for the site visit, which had to take place at a specifically arranged date during the outage.

Two loading techniques were considered for the onsite application of load for TSA. The first was a Ling V406 permanent magnetic shaker weighing 14.1 kg. The mass of the shaker is important because it has to be carried onsite so cannot weigh too much otherwise it will not be a portable solution for onsite TSA. An instrumented hammer was used to calculate the first natural frequency, found to be 100 Hz. A signal generator was needed to drive the shaker, and a force transducer attached to the rigid stinger connected the shaker and the pipe was used to provide the load signal needed for data processing of the TSA data [77]. A picture of the shaker position and schematic of the experimental set-up is shown in Figure 7-2. The shaker is aligned to provide a load horizontally onto the pipe. The direction of applied load determines the load and hence the stress distribution in the weld at the end of the pipe. Results in Figure 7-3a) show the $\frac{\Delta T}{T}$ results for the pipe. Peak thermoelastic response is located in the horizontal axis, as expected from the load position, and the neutral axis shown

in Figure 7-3b) is through the vertical axis of the pipe. The experimentally calculated value of K is used to calculated the summed stresses along the profile taken from the $\frac{\Delta T}{T}$ image in Figure 7-3a).

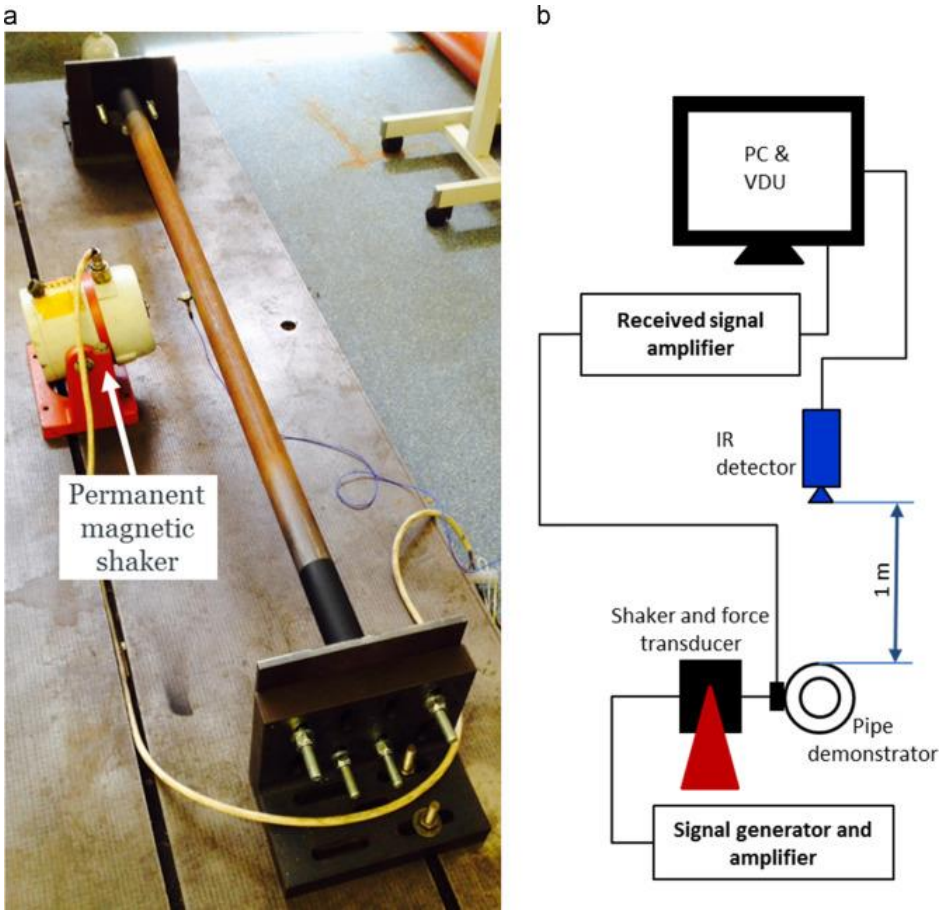

Figure 7-2 – a) Photo of the shaker position. b) Schematic showing the experimental set up [77].

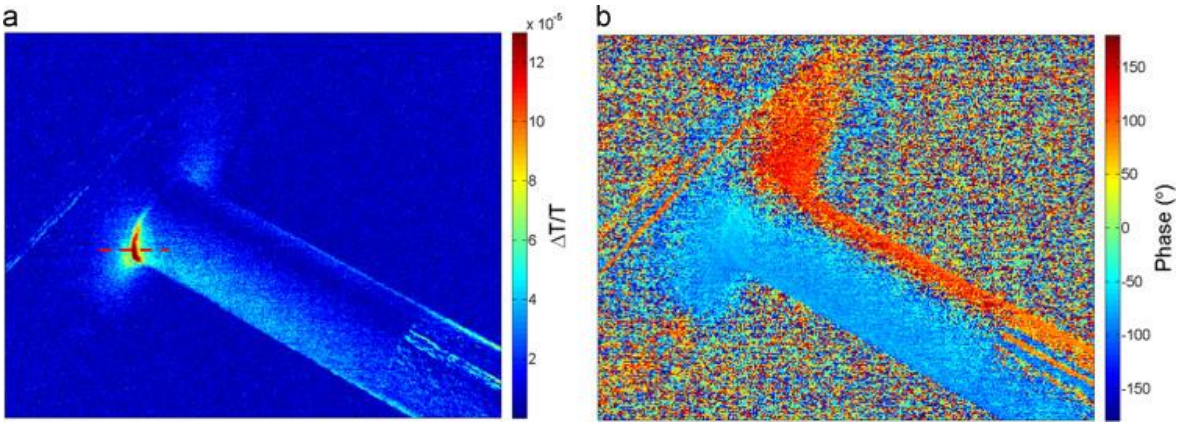

Figure 7-3 – a) $\Delta T/T$ and b) phase results during TSA using the permanent magnetic shaker [77].

The second approach used a Vibtec GT36 pneumatic shaker to excite the pipe. The two advantages of using the pneumatic shaker over a permanent magnetic shaker are the

reduction in mass and the reduction in amount of equipment required to take onsite. The GT36 uses a conventional workshop air supply to rotate an off centre mass turbine wheel that creates a vibration within an object to which it is clamped. The frequency and amplitude of the load are controlled through variation in the air flow. The shaker is attached to the pipe by a clamping system that was manufactured to accommodate pipes of outer diameter between 35 and 50 mm. The combined mass of the shaker and the clamp is 5 kg, so around a third of the mass of the permanent magnetic shaker. The experimental setup is shown in Figure 7-4, the shaker is clamped to the centre of the pipe and a valve is attached to the airline allowing fine control over the pressure of air through the shaker.

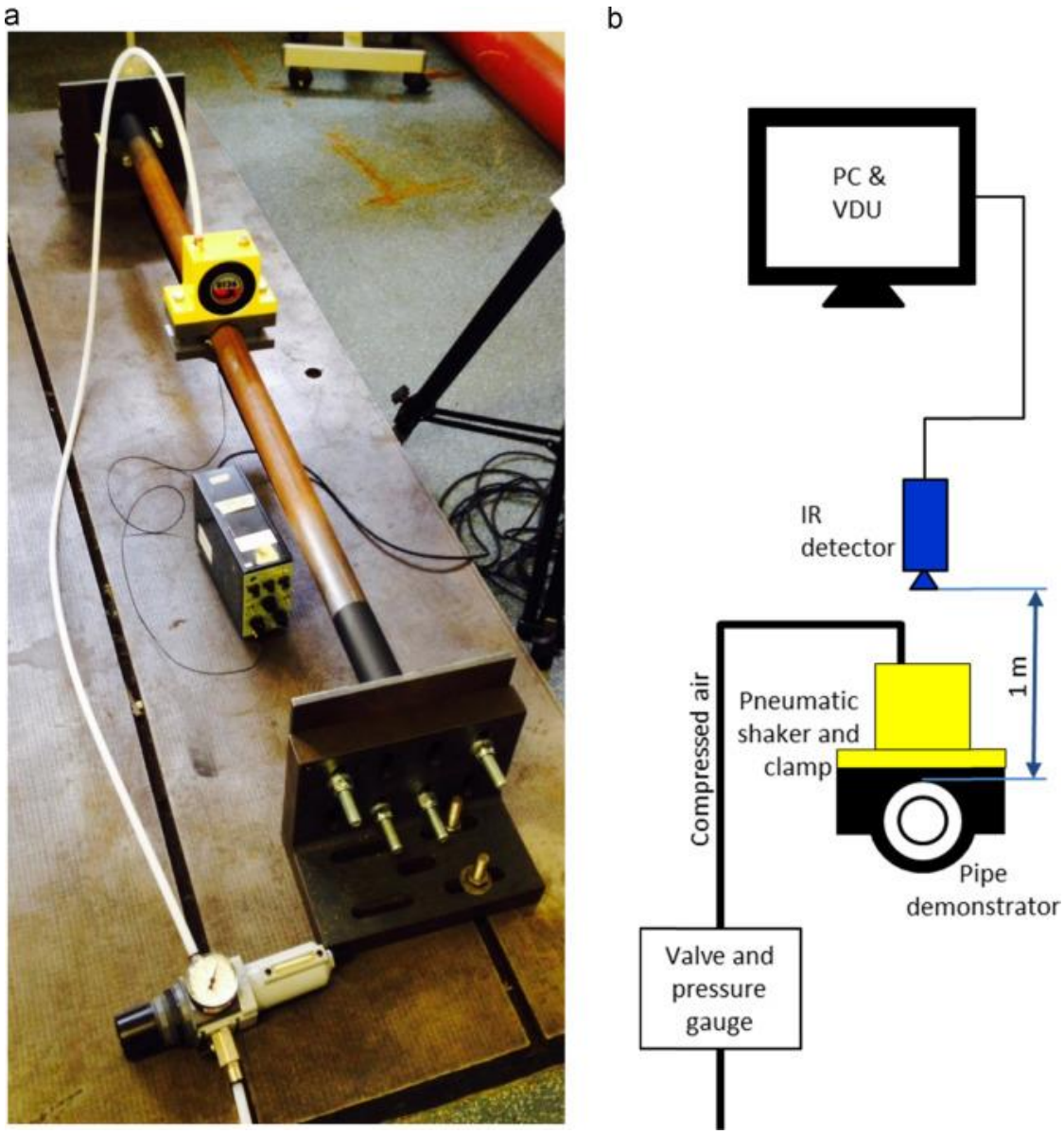

Figure 7-4 – a) Photo of the shaker position. b) Schematic showing the experimental set up of the pneumatic shaker [77].

There are difficulties in using an accelerometer onsite to collect the frequency of applied load so a different approach is used. A self-reference lock-in approach has been adapted from the

work in [79]. An area of pixels in the IR video is selected and the mean temperature of the pixels is calculated over time. This data is processed using a Fast Fourier transform (FFT) to calculate the frequency spectrum; the largest amplitude in the frequency of the reference signal. The approach developed in [77] differs from that in [79] by using a the thermography data to determine the reference signal frequency such that the lock-in approach described in Chapter 2 can be used to calculate $\frac{\Delta T}{T}$.

The $\frac{\Delta T}{T}$ and phase data from the tests with the pneumatic shaker are shown in Figure 7-5. The action of the turbine wheel in the pneumatic shaker causes an elliptical load pattern to be applied to the pipe rather than a cyclic load transverse to the pipe length, as applied by the magnetic shaker; this is seen in the phase data in Figure 7-5b). Despite this, the stress distribution in Figure 7-5a) shows the same pattern as Figure 7-3a). The summed stresses along the profile in Figure 7-5a) have been calculated and are compared to the summed stresses from Figure 7-3a) in Figure 7-6. The permanent magnetic shaker provided a higher peak stress of 53MPa compared to 41MPa, however, the overall stress in the data from the pneumatic shaker is larger.

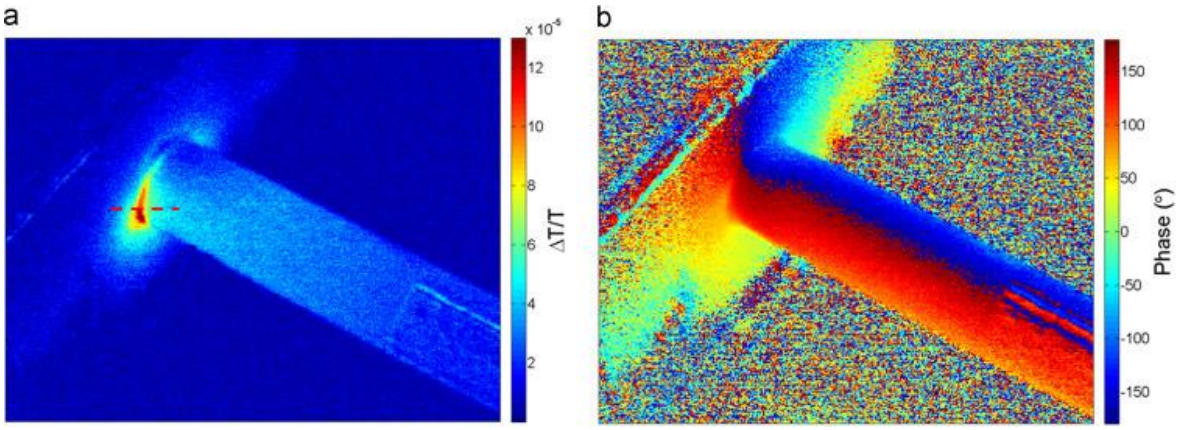

Figure 7-5 – a) *ΔT/T* and b) phase results during TSA using the pneumatic shaker [77].

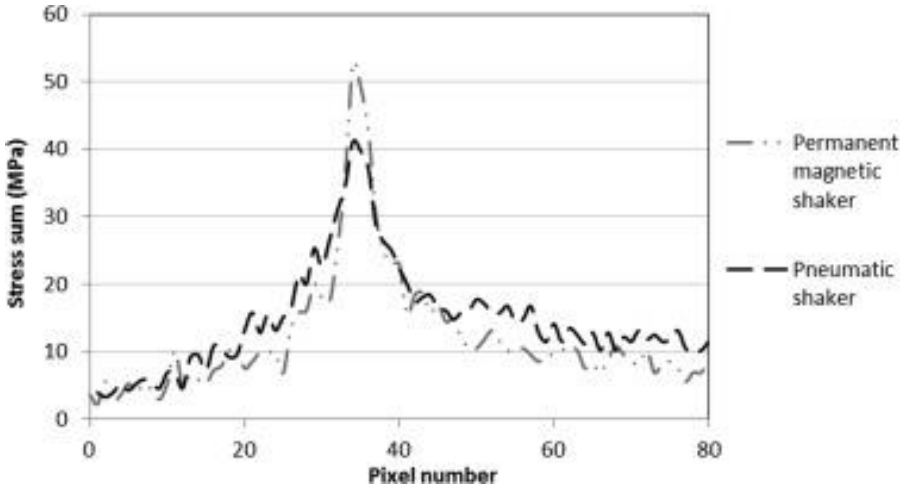

Figure 7-6 – summed stress profiles across the weld using the permanent magnetic shaker and the pneumatic shaker [77].

Both means of applying the load have been shown to function well under laboratory conditions. Therefore, it was decided to take only the pneumatic shaker onsite as this device had a much smaller mass and the amount of equipment required to set up the pneumatic shaker was a lot less than the permanent magnetic shaker.

7.3 On-site tests

Two visits were conducted to assess the onsite capability of the pneumatic shaker and TSA equipment. The first, to EDF West Burton, used relatively easily accessible high pressure steam drain lines in one location to perform the initial tests of the equipment. The second visit, to EDF Cottam, had multiple sites located where TSA could be performed and would provide a measure of the set-up time required. Both visits were carried out during the outage of the power stations, so the pipes being inspected were at ambient temperature before testing. There was minimal background vibration within the pipe systems due to the boilers being switched off for the duration of the onsite tests.

7.3.1 EDF West Burton

There were a range of different pipes and welds that could be assessed at EDF West Burton as shown in Figure 7-7a). Pipe 1 had an outer diameter of 48 mm and at the end was multi-pass fillet welded to a larger section of pipe creating a T-junction geometry, this is designated weld 1.1. Three butt welds were located along the length of pipe 1 joining different sections of pipe together. These were designated 1.2-1.4 [77]. The weld locations of 1.1 and 1.2, alongside the shaker location, are shown in Figure 7-7b) welds 1.3 and 1.4 are located in the vertical section of pipe 1 in Figure 7-7a). Pipe 2, see Figure 7-7a) was an 8 m long section of drain

pipe with an outer diameter of 43.5 mm; pipe 2 contained a series of girth welds along its length.

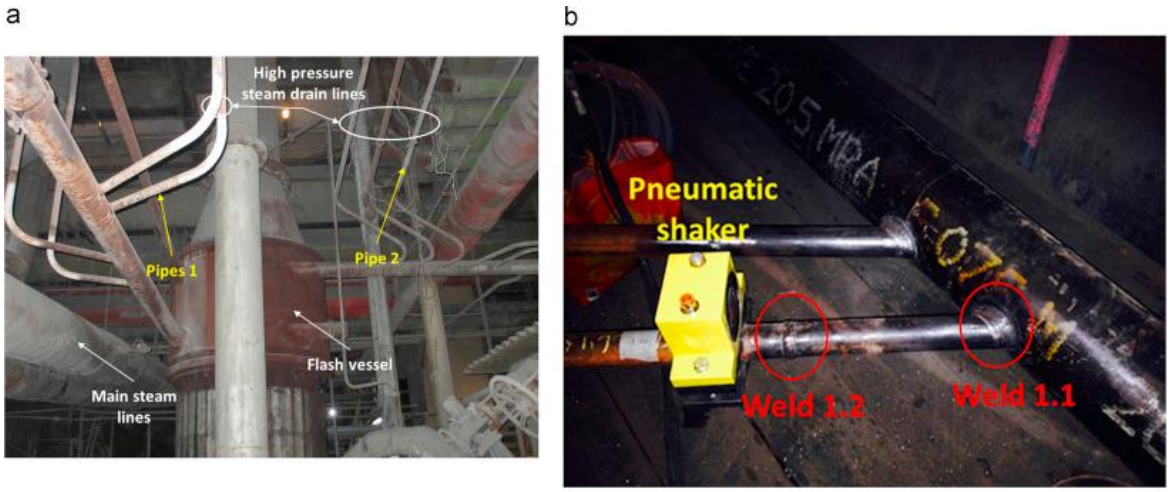

Figure 7-7 – a) Overview image of the inspection sites at EDF West Burton. b) Weld 1.1 and 1.2 locations, position of pneumatic shaker. The welds have not been prepared for TSA in this image [77].

Pipe 1 was a relatively new installation and had little corrosion to remove, shown in Figure 7-7b). Therefore, only a light abrasion using 80 grit SiC paper was required before acetone and Electrolube EMBP400 were used to finish the pipe preparation for TSA. Pipe 2 was more heavily corroded being over 10 years old; therefore, a wire brush was used to remove the largest surface debris and a battery powered grinder with an 80 grit disc was used to remove the surface corrosion. This process took 3-5 minutes to complete before acetone was used to clean the surface and the matt black paint applied. Due to time constraints onsite the shaker was attached in one position for the inspection of all welds on pipe 1, and then attached in a second location for the inspection of welds on pipe 2. The shaker was operated with a constant pressure of 1.5 bar for all tests, the excitation frequency for performing the lock-in analysis of the TSA data was calculated using the self-referential process.

The $\frac{\Delta T}{T}$ and phase data for welds 1.1-1.4 were obtained. In Figure 7-8 they are displayed with different scales on each image. This was performed intentionally to try and resolve as much information within each plot as possible.

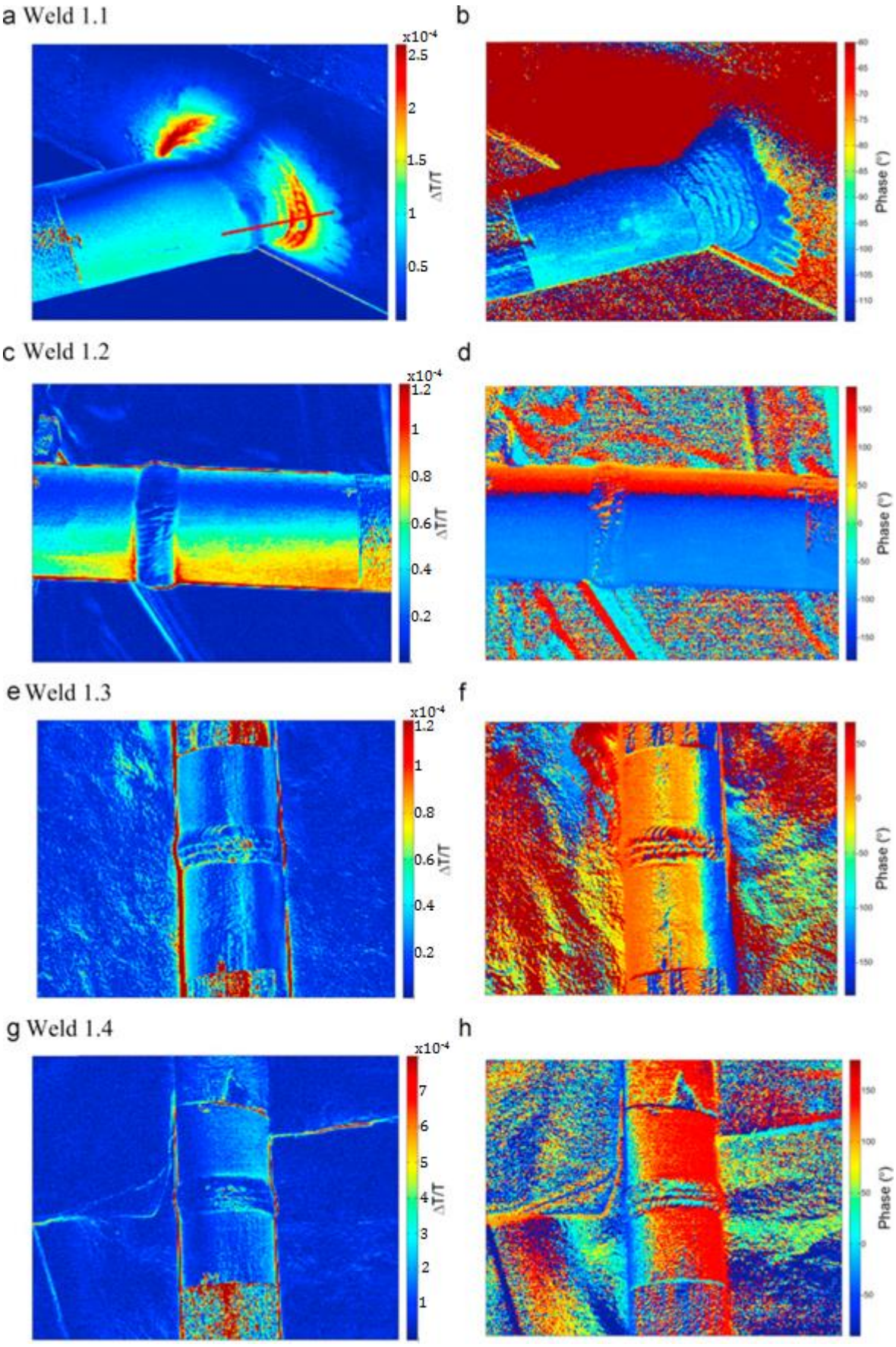

Figure 7-8 – *ΔT/T* and phase data for welds 1.1-1.4 on pipe 1 [77].

The T-junction geometry of weld 1.1 shows a clear neutral axis in the phase data, due to the fixed boundary condition at the weld, and there is a stress concentration in the horizontal axis. In the T-junction, peak stress is located within the fillet weld closest to the larger end pipe. Weld 1.2 shows a stress concentration in the pipe metal below the weld bead rather than in the weld bead itself. Welds 1.3 and 1.4 both show inconclusive results. This is partly due to the angle of view, the size of applied load range, and the motion within the image. The dark red bands on either side of the pipe in Figure 7-8e) and g) are indicative of motion and during the test it was noted that there were large vibrations in the sections of pipe 1 and pipe 2 away from any fixation point. In a weld at a junction, such as weld 1.1, there will be a stress concentration effect due to the restraint on motion of the pipe; however, the butt welds along the length of a pipe, welds 1.2-1.4, are free to move and hence the stress is relatively small. This is also seen in the $\frac{\Delta T}{T}$ data from weld 2.1 where the peak thermoelastic response is 1.2 x10^{4}, see Figure 7-9a), and the peak thermoelastic response in weld 1.1 is 2.6 x10^{-4}, see Figure 7-8a). There is also a large amount of noise in the results from weld 2.1, again this is due to the nature of the pipe and it being a long span without fixed points to restrict motion of the pipe when the shaker is applying a load.

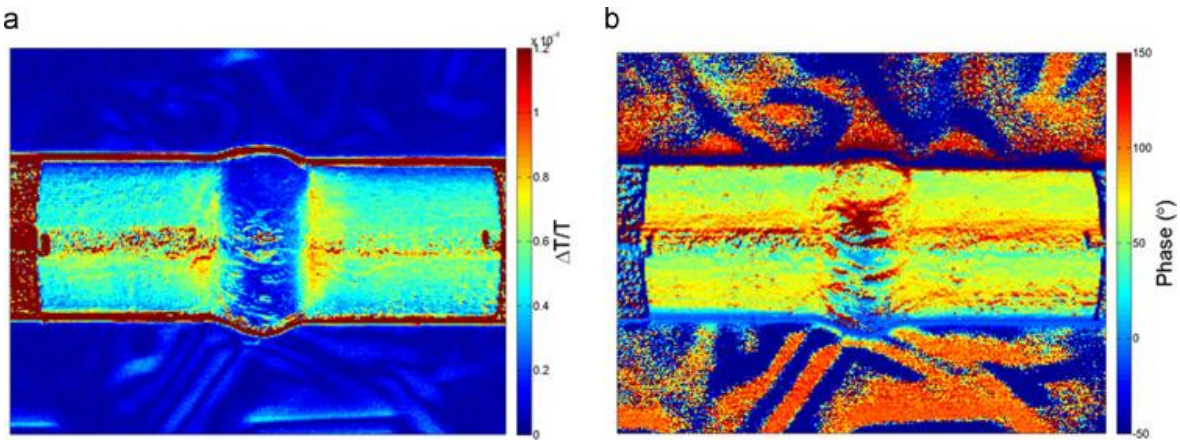

Figure 7-9 – *ΔT/T* and phase data for weld 2.1 on pipe 2 [77], clearly showing the blurring effects of motion.

As markers were not used during the collection of data, it was not possible to remove the motion, so stress data was calculated only from weld 1.1. The $\frac{\Delta T}{T}$ was converted into values of summed stress using *K* and a line plot taken through the multi-fillet weld in Figure 7-8a). The stress peak, shown in Figure 7-10 correspond with the weld bead geometry as expected, although there is an unexpected peak in the stress sum at pixel 75 (the centre yellow line in Figure 7-10). This is a possible defect that was unknown before TSA had been applied to the weld.

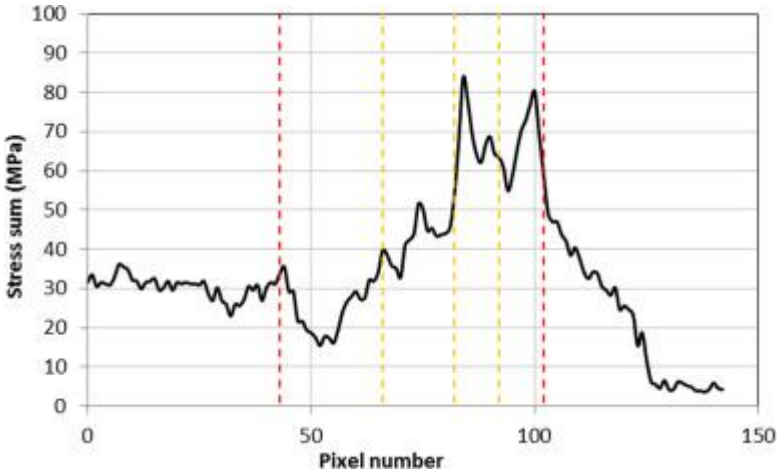

Figure 7-10 – Stress sum data plotted along the line in Figure 7-8a). The edges of the weld are shown by the red lines, the position of each weld bead is shown by the yellow lines.

The visit to EDF West Burton was the first stage in developing the onsite technique of applying TSA for residual stress assessment purposes. The loading system functioned as expected, and the surface preparation approach developed in the laboratory worked in-situ to provide a clean, emissive surface from which a thermoelastic response could be recorded. However, the effect of motion in welds that were not T-junction welds was a lot more than expected from the laboratory trials and meant that stress data could not be calculated from the majority of the welds inspected during the onsite trial. In the second onsite visit, to EDF Cottam, motion compensation was attempted to try and reduce the influence of motion in the thermoelastic data.

7.3.2 EDF Cottam

The second on-site test took place at EDF Cottam a year after the initial on-site trials. EDF Cottam was chosen because the nature of the refurbishment work taking place at EDF West Burton meant gaining access on-site was difficult to achieve. In total three sites at EDF Cottam were examined, all containing pipes made from the same ferritic steel as the pipes investigated at EDF West Burton. The pipes at each site were all old pipes, so every welded joint had to have large surface debris removed using a wire brush before a battery powered grinder with an 80 grit grinding wheel was used to remove the surface corrosion back to the base metal in preparation for painting with a thin layer of RS matt black paint. Motion compensation markers were placed onto the black paint around each weld so that displacement vectors could be calculated using the Random Motion software as described in Chapter 2.

Site 1

The pipes at site one were two parallel pipes of different external diameter. Pipe 1 had a diameter of 55 mm, pipe 2 had a diameter of 30 mm; both pipes had a wall thickness of between 4.7 – 6.3 mm taken from single point measurements using a wall thickness probe. The two pipes were connected to a main steam drain with a multi-fillet butt weld creating a T-junction at the base of each pipe, see Figure 7-11. Girth welds along the length of the pipe were accessible and captured using TSA.

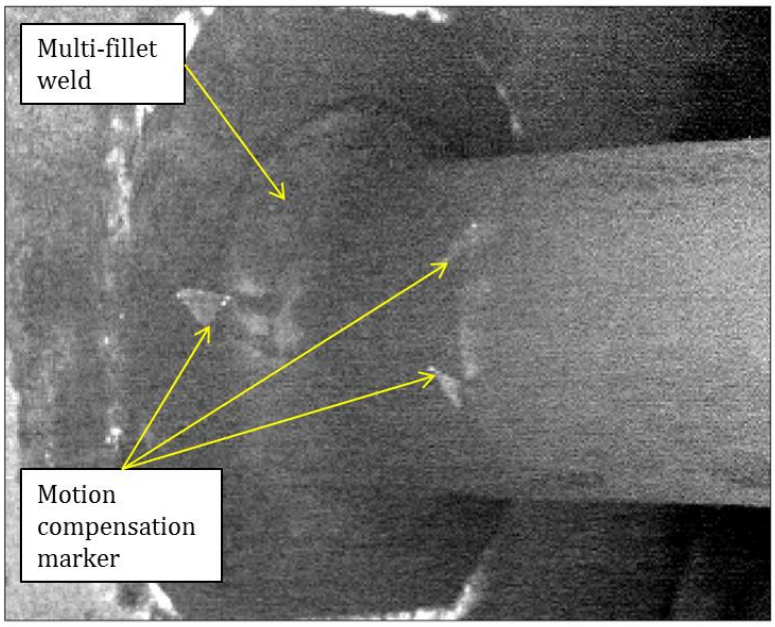

Figure 7-11 – A thermal image of the butt weld at the end of pipe 1 with motion compensation markers attached.

The movement in the welds along the length of both pipes was visible in the $\frac{\Delta T}{T}$ datasets shown in Figure 7-12. Both pipe sections showed significant movement, presented by the large, pink sections on either side of the pipes. Motion compensation marks had been applied, and an attempt to reduce the effect of motion in the images was made. However, whilst the in plane rigid body motion was reduced and the boundary of each pipe was more clearly defined the size of the motion provided by the pneumatic shaker resulted in a much noisier dataset, see Figure 7-13; therefore, the motion compensation was not successful at site 1.

a) b)

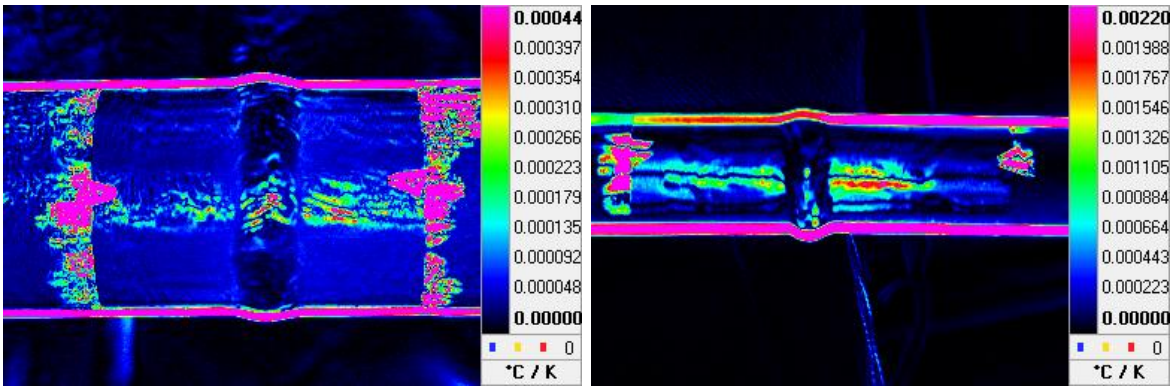

Figure 7-12 – *ΔT/T* data from a) pipe 1 and b) pipe 2. The effect of motion shown in the pink bands along the top and bottom edge of each pipe.

a) b)

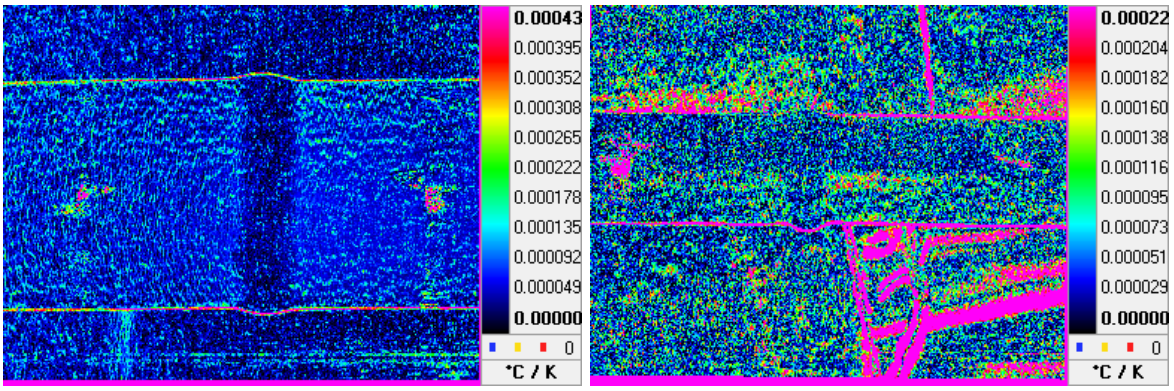

Figure 7-13 – *ΔT/T* data from a) pipe 1 and b) pipe 2. Motion compensation has been applied and the boundary of the pipes is better defined, but the noise in the data has increased.

At the junction with the larger main steam drain the stress concentration around the weld was much larger and the effect of motion in the thermoelastic response data was greatly reduced. Both can be attributed to the restriction on movement the connection to the much larger drain pipe put on pipes 1 and 2. The $\frac{\Delta T}{T}$ of the junction weld on pipe 1 was converted into summed stress data using the experimentally derived value of *K* from section 7.2.1. This data is shown in Figure 7-14a) without any motion compensation being applied. The stresses are concentrated over the weld geometry, as shown in Figure 7-14b).

a) b)

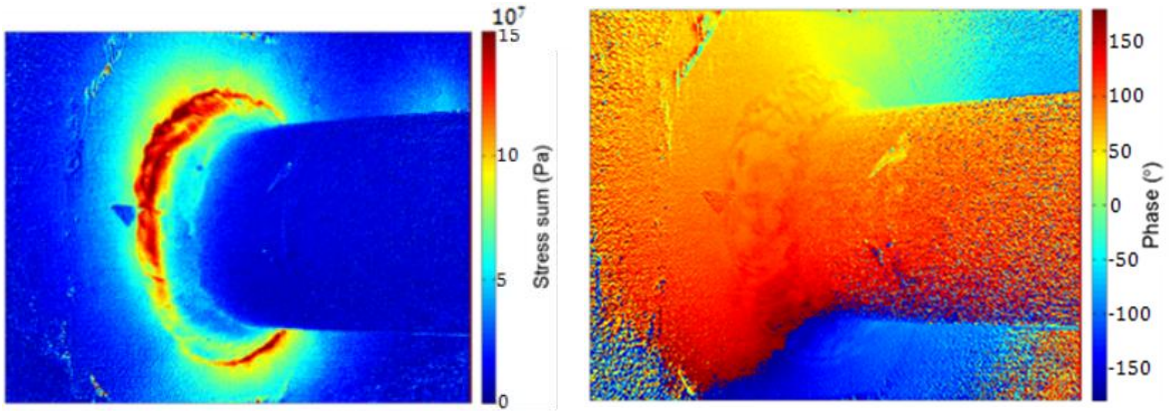

Figure 7-14 – Data taken from the weld joining the end of pipe 1 to the large steam drain. a) stress sum data calculated from the $\Delta T/T$ in the TSA data. b) Phase data showing neutral axis of loading.

Site 2

The second site contained a much more complex geometry for analysis. The pipes were connected in a double T-joint, see Figure 7-15; all pipes had an outer diameter of 51 mm and wall thicknesses between 5.2 – 6.8 mm. In Figure 7-15 the pipes have been prepared for testing using the 80 grit grinder used at EDF West Burton. The shaker was clamped onto the left hand vertical section in Figure 7-16 beyond the section painted in matt black paint; the triangles are motion compensation markers cut from metallic tape that provide a strong contrast to the thermoelastic response of the metal.

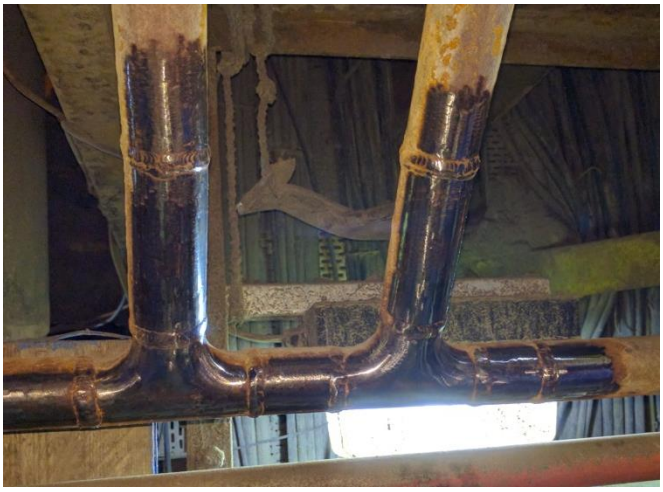

Figure 7-15 – Ferritic steel pipes at site 2, prepared using an 80 grit grinder ready for painting

Figure 7-16 – Site two prepared with coating of matt black paint. Motion compensation markers stuck on either side of every weld to be investigated.

There were no fixed points at site 2, so there was no welded joint where displacement was restrained and stress amplified. This was common across the power station and therefore provided an opportunity to assess how successfully TSA could be applied to these "boundary condition free" geometries. An investigation was carried out on the right hand T-junction and using different combinations of the motion compensation marks, seen in Figure 7-17 the standard deviation at a point of high mean $\frac{\Delta T}{T}$ and of low mean $\frac{\Delta T}{T}$ was calculated for each motion compensation used. Overall every attempt at motion compensation improved the definition of the boundary of the pipes but increased the overall noise level as shown in Table 7-2. The standard deviation across both small areas was increased by a factor between 3.5 and 9.4. Both the selection of the motion compensation marks used to remove the rigid body motion, and the use of a global frame-by-frame vector shift motion compensation using the Random Motion software provided by FLIR needs further consideration.

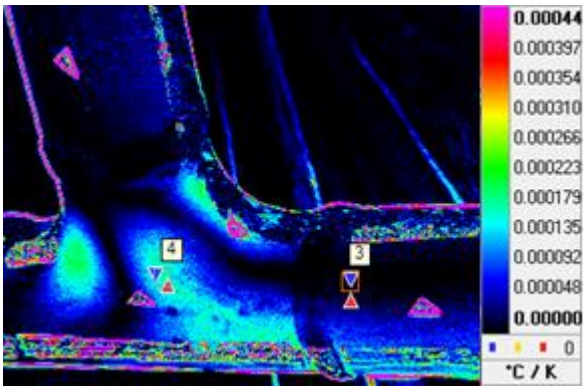

Figure 7-17 – *ΔT/T* plot of the right T-junction at site 2 with four motion compensation marks visible within the image.

File	Low mean $\frac{\Delta T}{T}$ S.D. (x10^{-5})	High mean $\frac{\Delta T}{T}$ S.D. (x10^{-5})
No MC	0.7	0.6
MC01	2.8	1.8
MC02	5.5	3.9
MC03	7.4	4.6
MC04	5.1	3.7
MC05	5.7	4.2
MC06	7.6	4.6
MC07	5.4	4.6

Table 7-2 – Standard deviations calculated from a point of high *ΔT/T* and low *ΔT/T* in Figure 7-17.

Site 3

Site 3 contained another mixture of motion constrained junction welds and girth welds in the middle of pipe lengths that saw large displacements during loading. The two sites investigated at shown in Figure 7-18 alongside the approximate location of the shaker and clamp to put the load into the pipes.

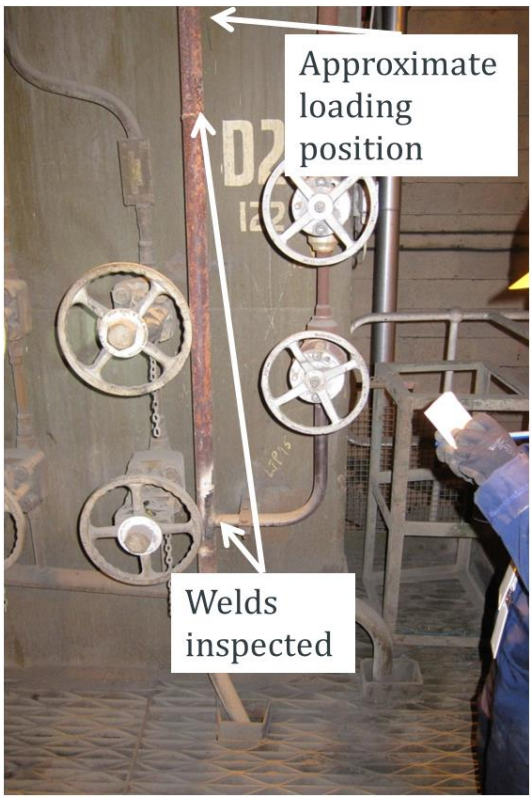

Figure 7-18 – Photograph showing the location of the welds and shaker at site 3.

Analysis of the pipes using TSA was undertaken and as expected a motion free dataset was captured at the lower weld location where a smaller pipe of outer diameter 42 mm exited the larger pipe of outer diameter 48 mm. There was also a bracket attached to the smaller pipe approximately 200 mm from the junction, further reducing the motion of the pipe. The $\frac{\Delta T}{T}$ from the T-junction is shown in Figure 7-19. There is a large concentration in the $\frac{\Delta T}{T}$ at the base of the weld toe, and a smaller spike at the edge of the weld on the smaller diameter pipe. The weld midway along the length of the pipe had a large displacement applied during the loading from the shaker. This created a large region on either side of the $\frac{\Delta T}{T}$ that could not be resolved, see Figure 7-20a). Motion compensation was applied to this dataset, and provided a much better final dataset than previous attempts at onsite motion compensation, see Figure 7-20b). It more clearly defines the boundary of the pipe, and the weld location and thermal hotspot at the base of the weld is still visible in the motion compensated dataset. The shaker was clamped very close to this weld, and so the displacement within the image is a simpler vector for the motion compensation software to calculate as it is dominated by the movement of the shaker; this has led to the improvement in the motion compensated data although more investigations need to be carried out to better understand how motion compensation can be successfully carried out in onsite tests.

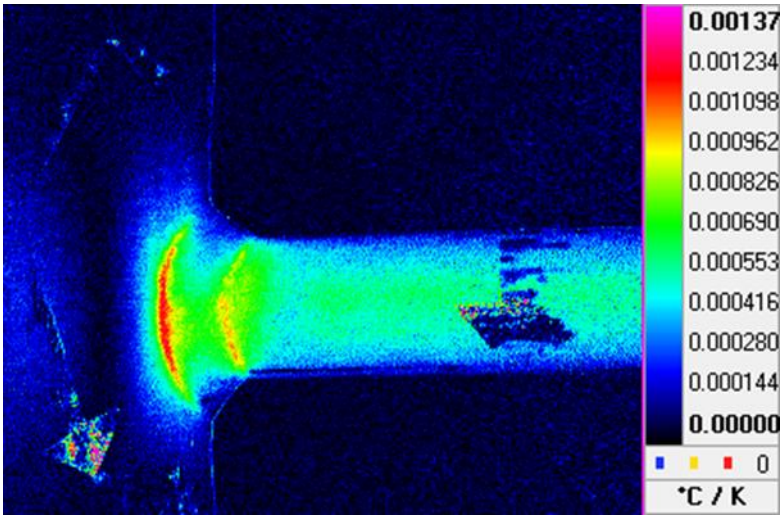

Figure 7-19 – *ΔT/T* data of the lower weld location at site 3.

a) b)

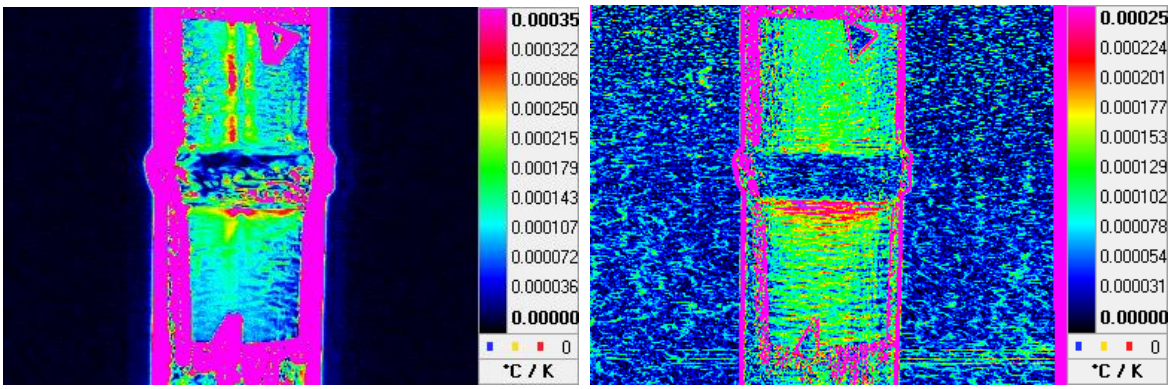

Figure 7-20 – *ΔT/T* plots of the upper weld location at site 3. The weld was midway along the larger diameter pipe. a) no motion compensation applied. b) motion compensation applied.

7.3.3 Conclusions of on-site testing

The onsite testing at EDF West Burton demonstrated that the TSA equipment could be taken onsite and used with a pneumatic shaker to extract $\frac{\Delta T}{T}$ results from welds. The thermoelastic data was converted into stress sum data and profiles across welds could be taken showing the stress distribution across the surface of the weld. Thermoelastic data could be recorded at each location every year allowing the evolution of the surface stress distribution to be plotted. Any changes in the stress distribution suggesting crack formation or other damage to the weld could be quickly seen in the datasets by using the first year measurements as a reference and finding the resultant thermoelastic bitmap for the welds each time new data is collected. However, this was only possible at locations that did not contain large movements.

The onsite testing at EDF Cottam attempted to demonstrate using motion compensation onsite to reduce the effects of pipe displacement during loading and allow the same analysis to be undertaken at welds midway along the length of a pipe. However, the displacement of each weld was not a simple one-directional movement because the motion applied by the pneumatic shaker is an elliptical motion. Therefore, the motion compensation did not function as hoped and analysis of the data taken was restricted.

7.4 Laboratory demonstrator of realistic pipe welds

To improve the motion compensation methodology and to apply TSA on a wide variety of welds, a laboratory demonstrator has been designed that can be loaded using the pneumatic shaker. The demonstrator, named mock-up C (MU-C), is a 1.5 m x 48 mm 316L stainless steel pipe. At the centre of the length an autogenous weld (heat from a weld torch without filler

material) has been created, and at the quarter length positions on either side two V-notches have been cut. One has been filled with a single pass weld, the other with a multi-pass weld. The ends are attached to mounting plates with single pass fillet welds. The pneumatic shaker can be attached at different points along the length of MU-C to provide different loading patterns into the welds. Therefore, motion compensation of the complex displacement given by the pneumatic shaker can be refined in a more controlled setting, and it is hoped that classification of different weld types can be made from the thermoelastic response profiles generated using MU-C.

The design and manufacture of MU-C was performed by Dr. Rachael Tighe and MU-C is now being tested by Elise Chevallier.

Chapter 8: Conclusions and Future Work

8.1 Conclusions

The primary aim of the research was to develop a plastic strain assessment technique using TSA and a synthetic reference bitmap that can be used onsite for industrial application in the UK nuclear power generation industry. The motivation for the work has arisen from the lack of full-field and portable non-destructive evaluation techniques. The work has been carried out using 316L stainless steel in the laboratory; however, onsite work has been performed on ferritic steel due to only having access to coal-fired power stations rather than nuclear power stations. The work in the thesis is divided into 4 main sections:

1. The development of synthetic data to reveal areas in a test specimen that have experienced plastic straining.
2. Determining the threshold of detectability for changes in the thermoelastic response caused by changes in plastic strain.
3. Constructing a calibration between plastic strain and change in thermoelastic response to assess the level of plastic strain a component has experienced.
4. The use of TSA away from a laboratory environment.

The main findings in each area are summarised in the following sections.

8.1.1 The development of the synthetic bitmap

The work conducted in Chapter 3 has fulfilled the first objective, a synthetic bitmap of the reference thermoelastic response was constructed. The approach was used a second time in Chapter 5 to reveal regions containing plastic strain in the HAZ of a welded specimen. The synthetic bitmap was validated against the thermoelastic response of a physical reference specimen, and the resultant bitmap calculated using the synthetic bitmap was validated against a prediction of plastic strain within the HAZ of the welded specimen. For future users of the synthetic bitmap approach there are the following recommendations:

- Elastic-plastic material properties have to be applied to the FE model used to construct the synthetic bitmap. Sensitivity to effects of localised plasticity is very high; therefore, accurate modelling of the material behaviour to applied loads is required.
- The actual geometry of the component, rather than the design geometry, being investigated should be used for the construction of the synthetic bitmap. Accurately mapping the geometry will provide a proper representation of the stress raisers within a component and enable a more accurate synthetic bitmap to be created.

- A submodel should be used to generate the synthetic bitmap. This submodel should be the same shape as the region observed by the IR camera during TSA. This will allow better image matching to ensure the resultant bitmap generated from the synthetic bitmap is accurately portraying the changes in thermoelastic response.
- A submodel allows a higher mesh density to be used in the synthetic bitmap. There can be sharp stress gradients within the FE model and a greater density mesh will allow a higher fidelity calculation of the stress field.

8.1.2 Determining the threshold of detectability

The investigation into experimental errors in Chapter 4 and the tapered specimen experiments in Chapter 6 demonstrated how difficult it is to produce data with a small amount of scatter such that a change in thermoelastic response due to plastic strain can be revealed by the data. Chapter 4 investigated the influence of test machine alignment, rigid body motion, reflections, the type of paint used during TSA, and the condition of the surface before the paint was applied. A threshold of 2% plastic strain detection was concluded after the experiments in Chapter 6, although additional experiments are required to determine how accurate this threshold is because a single set of specimens was used to derive this conclusion.

- The type of paint used during TSA was re-investigated due to a change in formulation of RS matt black paint. After extensive studies into the emissivity of the paints testing it was concluded that RS matt black should still be used for TSA tests in the future where available.
- The effect of acetone residue on the bond between the paint coating and the metal substrate was found to be very significant. Previously the acetone was wiped from the specimen with a thin residue resulting from this process. However, it is now recommended that users of TSA rinse the surface with water after cleaning to remove the acetone residue.
- The alignment of the grips in the test machine and the amount of rotation during a TSA test of the load actuator was found to cause a large difference in the thermoelastic response. An anti-rotation collar was constructed for the Instron 8800 used in the majority of tests in the current work and the grip alignment was corrected by an Instron engineer to remove the sources of error from future measurements.
- Rigid body motion is present in all TSA data because a cyclic load has to be applied to a specimen, and the IR camera is kept in a fixed position. Two different methods for removing the rigid body motion were found in the literature, the point mapping

approach was adopted as it did not require additional cameras to monitor the specimen and the motion in the laboratory tests was mainly vertical.

8.1.3 Calibration of the change in thermoelastic response with plastic strain

In Chapter 5 a bitmap containing the change in thermoelastic constant in a welded specimen was constructed using TSA and the synthetic bitmap approach. To calculate a bitmap of the plastic strain within the welded specimen a calibration between plastic strain and the change in thermoelastic response must be determined. However, the results of Chapter 6 using the tapered specimens contained too much scatter in the thermoelastic response along the length of the taper so a calibration could not be calculated from the datasets generated. There does appear to be a correlation between plastic strain and thermoelastic constant, but further experiments are required to reduce the scatter and better define the relationship.

- A gradient was found when the change in thermoelastic response for both heat treated tapered specimens was plotted against plastic strain, however, no gradient was seen in as received material dataset. The reason for this is unknown, and must be determined in future work; a more detailed examination of the surface of the material alongside a micrographic investigation is required.
- When the normalised thermoelastic constant through each tapered specimen was plotted against plastic strain the 1050°C heat treated specimen displayed a similar relationship to that found in [17]. Below 2% plastic strain the relationship was not visible, further suggesting that this is the current threshold of detectability of the technique.
- In experiments performed on dogbone test coupons loaded in tension and pipe sections loaded in compression, no difference in thermoelastic constant was found between heat treated or as received 316L stainless steel. However, there was a clear difference between the heat treated and as received tapered specimens, which requires further investigation.

8.1.4 Using TSA away from a laboratory environment

The equipment needed to perform TSA was successfully taken onsite to two fossil fuel power stations and used to gather thermoelastic images of pipes with different weld types. It was found that motion was the biggest source of error in the data collected, and an attempt was made to reduce the effect of rigid body motion but was unsuccessful with further tests required to refine the thermoelastic data.

- A portable loading device that provided excitation by pneumatic means was trialled and then successfully used onsite. It was shown that the pneumatic shakers could provide a stress range sufficient for TSA to be performed.
- The specimen preparation methodology was adapted for onsite purposes. Trials in the lab showed that a small amount of surface abrasion using 80 grit SiC paper was required to reveal the original metal surface before painting of the surface was carried out. Further finishing of the surface before painting did not improve the results of TSA.
- Using the pneumatic shaker, IR camera, and a laptop TSA could be performed onsite on welds on pipes up to 50 mm in diameter. The total time taken from arriving on site to leaving was under 3 hours, for comparison it can take up to a day to collect ultrasound data from welds of similar geometry.

8.2 Recommendations for future work

- The development of the synthetic bitmap approach in this thesis has revealed that there are a significant number of variables in the modelling that have an influence of unknown magnitude on the validity of the final synthetic bitmap. Therefore, detailed studies should be carried out to investigate the following points:
    - How important is it to have exact material properties? Can literature values of Young's modulus, Poisson's ratio, yield stress and hardening behaviour be used or does each material property have to be determined for every experiment?
    - What influence does having an imperfect, assumed geometry have on the synthetic bitmap? Accurate measurement of exterior surfaces is possible, using laser profilometers, though this will be expensive and difficult to carry out on site. Measurement of interior geometry of welds and pipes may be possible using ultrasound, however, this will not be possible/practicable along an entire pipe run. Therefore, the influence of assuming uniform wall thickness throughout a welded junction must be investigated.
    - How much of an influence will assumptions of boundary conditions and applied loads have on the final synthetic bitmap?
    - What is the best approach to accurately map the FE model to the real world thermoelastic data? How will slight misalignments effect the identification of regions having experienced plastic strain?
- Following an extensive literature survey an explicit relationship between plastic strain and a change in thermoelastic response was not found in the literature. There

was evidence to suggest plastic strain does not affect the density of a metal, neither was there evidence of plastic strain affecting the specific heat of a metal. However, the coefficient of thermal expansion does appear to be affected by plastic strain. Future work should investigate this relationship more deeply and if possible establish what is driving a change in the coefficient of thermal expansion when a material is subjected to plastic strain.

- The work in Chapter 6 suggested that there is currently a threshold of detectability of 2% plastic strain. Further experiments should be carried out to establish what effect the different sources of experimental error have on the thermoelastic response and whether this threshold can be reduced. The experimental errors are largely those investigated in Chapter 4, the paint coating, surface preparation, and application of load. Whilst Chapter 4 showed the current threshold, a better understanding of the magnitude of errors that each source causes may allow the threshold to be reduced.
- The final aim of the thesis was to take TSA onsite and apply the approach to welded pipework in situ. The feasibility was demonstrated but further evaluation is necessary to refine the approach.
    - The surface preparation of the pipes was performed in a much less controlled fashion than in the lab, experiments need to be performed to assess the size of the effect this will have on the results.
    - The angle of load relative to the IR camera needs to be investigated to determine the optimal viewing angle to collect the clearest thermoelastic response.
    - The motion of the pipe during loading is a lot more significant than when loading specimens in a test machine. An onsite motion compensation routine needs to be established that reduces the relative motion of the welded joint to the IR camera.

Appendix

Matlab script used to interpolate the stress data from an FE model into a $\frac{\Delta T}{T}$ bitmap

This script loads the .csv files containing 3 columns (x,y,sigma) of an FEA output. It then interpolates them into a 320*256 grid that matches the size of the TSA data.
Script written by Geoff Howell (G.Howell@soton.ac.uk)
This file runs in Matlab 2013a, does not function in 2012a as 'scatteredInterpolant' does not exist.

```
% Load data
a = load('3D coordinate and stress data.csv');
% Loads the raw data as arrays. Change the input file, has to be in ".csv" format.
% Separate data and build grid
x = a(:,1);    % Separates out the data into three datasets.
y = a(:,2);
s = a(:,3);
F = scatteredInterpolant(x,y,s);       % Interpolates the sigma values.
[xgrid,ygrid] = meshgrid(linspace(min(x),max(x),320),linspace(min(y),max(y),255));
sigmagrid = F(xgrid,ygrid);    % Creates the array of interpolated sigma values.

% Masking
% centerx = 0;
% centery = 0;
% r = 8;
% dist = sqrt((xgrid-centerx).^2 + (ygrid-centery).^2);
% sigmagrid(find(dist<=r)) = NaN;

% Image display
figure;
imagesc(sigmagrid)     % Plots a figure output of the data.
h = colorbar; set(get(h,'ylabel'),'string','MPa');

% Convert stress to absolute stress values
sigmagrid = abs(sigmagrid);

% Image display
figure;
imagesc(sigmagrid)     % Plots a figure output of the data.
h = colorbar; set(get(h,'ylabel'),'string','MPa')

% Convert to dT/T
k = 9.85E-12;
thermal = 1000000*k.*sigmagrid;

% Image display
figure;
imagesc(thermal)           % Plots a figure output of the data.
h = colorbar; caxis([0 0.0009]); set(get(h,'ylabel'),'string','\DeltaT / T');
```

References

[1] J. M. Dulieu-Barton and P. Stanley, “Development and applications of thermoelastic stress analysis”, *Journal of Strain Analysis,* vol. 33, pp. 93-104, 1998.

[2] P. J. Withers and H. K. D. H. Bhadeshia, “Overview: Residual stress part 2 - nature and origin”, *Materials Science and Technology,* vol. 17, pp. 366-375, 2001.

[3] P. J. Withers and H. K. D. H. Bhadeshia, “Overview: Residual stress part 1 - measurement techniques”, *Materials Science and Technology,* vol. 17, pp. 355-365, 2001.

[4] M. Steinzig and T. Takahashi, “Residual stress measurement using the hole drilling method and laser speckle interferometry”, *Experimental Techniques,* vol. 27, no. 6, pp. 59-63, 2006.

[5] M. Turski and L. Edwards, “Residual stress measurement of 316L stainless streel bead-on-plate specimen utilising the contour method”, *International Journal of Pressure Vessels and Piping,* vol. 86, pp. 126-131, 2009.

[6] D. E. Bray, W. Tang and D. Grewal, “Ultrasonic stress evaluation in a compressor rotor”, *Journal of Testing and Evaluation,* vol. 25, pp. 503-509, 1997.

[7] M. C. Smith, A. C. Smith, R. C. Wimpory, C. Ohms, B. Nadri and P. J. Bouchard, “Optimising residual stress measurements and predictions in a welded benchmark specimen: A review of phase 2 of the NeT task group 1 single bead on plate round robin”, in *ASME 2009 Pressure Vessels and Piping Conference*, Prague, 2009.

[8] M. C. Smith and A. C. Smith, “NeT bead-on-plate round robin: Comparison of residual stress predictions and measurements”, *International Journal of Pressure Vessels and Piping,* vol. 86, no. 1, pp. 79-95, 20019.

[9] A. K. Wong, S. A. Dunn and J. G. Sparrow, “Residual stress measurement by means of the thermoelastic effect”, *Nature,* vol. 332, pp. 613-615, 1988.

[10] S. Quinn, J. M. Dulieu-Barton and J. M. Langlands, “Progress in thermoelastic residual stress measurement”, *Strain,* vol. 40, pp. 127-133, 2004.

[11] A. K. Wong, J. G. Sparrow and S. Dunn, “On the revised theory of the thermoelastic effect”, *Journal of Physics and Chemistry of Solids,* vol. 49, pp. 395-400, 1988.

[12] J. M. Eaton-Evans, J. M. Dulieu-Barton, E. G. Little and I. A. Brown, "Thermoelastic studies on Nitinol stents", *Journal of Strain Analysis,* vol. 41, pp. 481-495, 2006.

[13] S. Quinn, J. M. Dulieu-Barton, J. M. Eaton-Evans, R. K. Fruehmann and P. J. Tatum, "Thermoelastic assessment of plastic deformation", *Journal of Strain Analysis,* vol. 43, pp. 451-468, 2008.

[14] J. M. Dulieu-Smith, "Alternative calibration techniques for quantitative thermoelastic stress analysis", *Strain,* vol. 31, no. 1, pp. 9-16, 1995.

[15] A. F. Robinson, J. M. Dulieu-Barton, S. Quinn and R. L. Burguete, "The potential for assessing residual stress using thermoelastic stress analysis: A study of cold expanded holes", *Experimental Mechanics,* vol. 53, no. 2, pp. 299-317, 2013.

[16] Y. Du, D. Backman and E. Patterson, "A new approach to measuring surface residual stress using thermoelasticity", in *Proceedings of the XIth International Congress and Exposition (SEM)*, Orlando, 2008.

[17] A. F. Robinson, "Assessment of residual stress using thermoelastic stress analysis [PhD Thesis]", University of Southampton, Southampton, 2011.

[18] A. F. Robinson, J. M. Dulieu-Barton, S. Quinn and R. L. Burguete, "Paint coating characterization for thermoelastic stress analysis of metallic materials", *Measurement Science and Technology,* vol. 21, no. 8, 2010.

[19] M. Kobayashi, T. Matsui and Y. Murakami, "Mechanism of creation of compressive residual stresses by shot peening", *International Journal of Fatigue,* vol. 20, no. 5, pp. 351-357, 1998.

[20] R. W. Landgraf and R. A. Chernenkoff, "Residual stress effects on fatigue of surface processed streels", *American Society for Testing and Materials,* vol. Analytical and Experimental Methods for Residual Stress Effects in Fatigue, pp. 1-12, 1988.

[21] E. J. Hearn, Mechanics of materials vol. 1, Oxford, New York: Pergamon Press, 1985.

[22] J. H. Faupel and F. Fisher, Engineering Design: Synthesis of stress analysis and materials engineering, John Wiley & Sons Inc, 1981.

[23] J. L. Cunningham, D. J. Medlin and G. Krauss, "Effects of induction hardening and prior cold work on a microalloyed medium carbon steel", *Journal of Materials Engineering and*

Performance, vol. 8, no. 4, pp. 401-408, 1999.

[24] T. L. Teng, C. P. Fung, P. H. Chang and W. C. Yang, "Analysis of residual stresses and distortions in T-joint fillet welds", *International Journal of Pressure Vessels and Piping,* vol. 75, no. 8, pp. 523-538, 2001.

[25] S. S. Babu, J. W. Elmer, J. M. Vitek and S. A. David, "Time-resolved X-ray diffraction investigation of primary weld solidification in Fe-C-Al-Mn steel welds", *Acta Materialia,* vol. 50, no. 19, pp. 4763-4781, 2002.

[26] C. Neelamegam, V. Sapineni, V. Muthukumaran and J. Tamanna, "Hybrid intelligent modeling for optimizing welding process parameters for reduced activation ferritic-martensitic (RAFM) steel", *Journal of Intelligent Learning Systems and Applications,* vol. 5, pp. 39-47, 2013.

[27] X. Shan, C. M. Davies, T. Wangsdan, N. P. O'Dowd and K. M. Nikbin, "Thermo-mechanical modelling of a single-bead-on-plate weld using the finite element method", *Internatinoal Journal of Pressure Vessels and Piping,* vol. 86, no. 1, pp. 110-121, 2009.

[28] M. C. Smith, P. J. Bouchard, M. Turski, L. Edwards and R. J. Dennis, "Accurate prediction of residual stress in stainless steel welds", *Computational Materials Science,* vol. 54, pp. 312-328, 2012.

[29] R. J. Dennis, N. A. Leggatt and A. Gregg, "Optimisation of weld modelling techniques: Bead-on-plate analysis", in *ASME 2006 Pressure Vessels and Piping/ICPVT-11 Conference*, Vancouver, 2006.

[30] M. C. Smith, A. C. Smith, R. Wimpory and C. Ohms, "A review of the NeT Task Group 1 residual stress measreuments and analysis round robin on a single weld bead-on-plate specimen", *International Journal of Pressure Vessels and Piping,* Vols. 120-121, pp. 93-140, 2014.

[31] M. Machizuki, M. Hayashi and T. Hattori, "Numerical analysis of welding residual stress and its verification using neutron diffraction measurement", in *Transactions of the ASME*, 2000.

[32] T. W. Clyne and S. C. Gill, "Residual stresses in thermal spray coatings and their effect on interfacial adhesion: A review of recent work", *Journal of Thermal Spray Technology,* vol. 5, no. 4, pp. 401-418, 1996.

[33] A. T. Parklyn and G. Jeronimidis, "Residual stresses in carbon fibre-thermoplastic matrix

laminates", *Journal of Composite Materials,* vol. 22, no. 5, pp. 401-415, 1998.

[34] B. S. Yilbas and A. F. M. Arif, "Residual stress analysis for HVOF diamalloy coating on Ti-6Al-4V alloy", *Surface and Coatings Technology,* vol. 202, no. 3, pp. 559-568, 2007.

[35] A. Mezin, "Coasting internal stress measurement through the curvature method: a geometry-based criterion delimiting the relevance of stoney's formula", *Surface and Coatings Technology,* vol. 200, no. 18-19, pp. 5259-5267, 2006.

[36] G. S. Schajer, B. Winiarski and P. J. Withers, "Hole drilling residual stress measurement with artifact corrections using full field DIC", *Experimental and Applied Mechanics,* vol. 4, pp. 403-414, 2012.

[37] C. Trautner, M. McGinnis and S. Pessiki, "Development of the incremental core-drilling method of non-destructive investigation of stresses in concrete structures", *ATLSS Reports,* p. Paper 107, 2008.

[38] F. Faure and R. H. Leggatt, "Residual stresses in austenitic stainless steel primary coolant pipes and welds of pressurized water reactors", *International Journal of Pressure Vessels and Piping,* vol. 65, no. 3, pp. 265-275, 1996.

[39] G. Schajer, Encyclopedia of Materials Science and Technology, Oxford: Pergamon Press, 2001.

[40] M. B. Prime, "Residual stress measurement by successive extension of a slot: The crack compliance method", *Applied Mechanics Review,* vol. 52, no. 2, pp. 75-96, 1999.

[41] W. Cheng, I. Finnie, M. Gremaud, A. Rosselet and R. D. Streit, "The compliance method for measurement of near surface residual stresses - Application and validation for surface treatment by laser and shot-peening", *Journal of Engineering Materials and Technology,* vol. 116, no. 4, pp. 556-560, 1994.

[42] M. B. Prime and A. R. Gonzales, "The contour method: Simple 2D mapping of residual stresses", in *Procedure 6th International Conference on Residual Stresses*, Oxford, 2000.

[43] M. B. Prime, "Cross-sectional mapping of residual stresses by measuring the surface contour after a cut", *Transactions of the ASME,* vol. 123, pp. 162-168, 2001.

[44] P. J. Webster and P. J. Withers, "Nautron and synchrotron X-ray strain scanning", *Strain,* vol. 37, pp. 19-33, 2001.

[45] I. C. Noyan, T. Huang and B. R. York, "Residual stress/strain analysis in thin films by X-ray diffraction", *Critical Reviews in Solid State and Materials Science,* vol. 20, no. 2, pp. 125-177, 1995.

[46] Archana, "X-Ray Diffraction Presentation", 29 09 2014. [Online]. Available: https://image.slidesharecdn.com/81347482-x-ray-diffraction-technique-140929002756-phpapp01/95/xraydiffractiontechnique-9-638.jpg?cb=1411953232. [Accessed 04 04 2017].

[47] NPL, M. E. Fitzpatrick, A. T. Fry, P. Holdway, F. A. Kandil, J. Shackleton and L. Suominen, "A National Measurement Good Practice Guide: No. 52 Determination of reisudla stresses by X-ray diffraction", National Physical Laboratory, Teddington, 2005.

[48] Pulstec Industrial Co. Ltd., "μ-X360 Portable X-ray Residual Stress Analyzer", Pulstec, [Online]. Available: http://www.pulstec.co.jp/en/pr/xray/pr_x01.html. [Accessed 03 04 2017].

[49] Pulstec, μ-X360 Portable X-ray Residual Stress Analyzer: Basic Instruction Manual, Hamamatsu City: Pulstec Industrial Co. Ltd. , 2012.

[50] P. J. Withers, "Depth capabilities of neutron and synchrotron diffraction strain measurement instruments. The maximum feasible path length", *Journal of Applied Crystallography,* vol. 37, pp. 596-606, 2004.

[51] J. Shackleton, "Presentations and handouts for the residual stress workshop hosted by University of Manchester", *British Society for Strain Measurement,* 2009.

[52] S. Eldevik, A. A. F. Olsen and P. Lunde, "Sound velocity change owing to the acousto-elastic/plastic effect in steel measured using acoustic resonance technology (ART)", in *Scandinavian Symposium on Physical Acoustics*, Geilo, 2012.

[53] B. Xu, Z. Shen, X. Ni, J. Lu and Y. Wang, "Finite element model of laser-generated surface acoustic waves in coating-substrate system", *Journal of Applied Physics,* vol. 95, no. 4, 2004.

[54] A. Ruiz and P. Nagy, "Laser-ultrasonic surface wave dispersion measurements on surface-treated metals", *Ultrasonics,* vol. 42, pp. 665-669, 2004.

[55] Y. Javardi, M. Hasani and S. Sadeghi, "Investigation of clamping effects on the welding sub-surface residual stress and deformation by using the eltrasonic stress measurement

and finite element method", *Journal of Nondestructive Evaluation,* vol. 34, no. 3, 2015.

[56] J. Gough, "A description of a property of Caoutchoucor Indian rubber; with some reflections of the cause of the elasticity of this substance", *Manchester Phil. Mem., Second Series,* vol. 1, pp. 288-295, 1805.

[57] W. K. Thomson (Lord Kelvin), "On the dynamical theory of heat", *Transactions of the Royal Society of Edinburgh,* vol. 6, pp. 49-53, 1853.

[58] S. A. Dunn, D. Lombardo and J. G. Sparrow, "The mean stress effect in metallic alloys and composites", in *SPIE: Stress and Vibration: Recent Developments in Industrial Measurement and Analysis*, London, 1989.

[59] A. L. Gyekenyesi and G. Y. Baaklini, "Thermoelastic stress analysis: The mean stress effect in metallic alloys", *NASA,* pp. NASA-TM-1999-209376, 1999.

[60] A. L. Gyekenyesi, "Thermoelastic stress analysis: An NDE tool for residual stress assessment in metallic alloys", *Journal of Engineering for Gas Turbines and Power,* vol. 124, pp. 383-387, 2002.

[61] R. K. Fruehmann, J. M. Dulieu-Barton and S. Quinn, "On the thermoelastic response of woven composite materials", *Journal of Strain Analysis,* vol. 43, pp. 435-450, 2008.

[62] W. Wang, R. K. Fruehmann and J. M. Dulieu-Barton, "Application of Digital Image Correlation to address complex motions in Thermoelastic Stress Analysis", *Strain,* vol. 51, pp. 405-418, 2015.

[63] E. Toussaint, X. Balandraud, J.-B. Le Cam and M. Grédiac, "Combining displacement, strain, temperature and heat source fields to investigate the thermomechanical response of an elastomeric specimen subjected to large deformations", *Polymer Testing,* vol. 31, no. 7, pp. 916-925, 2012.

[64] J. R. Samaca Martinez, X. Balandraud, E. Toussaint, J.-B. Le Cam and D. Berghezan, "Thermomechanical analysis of the crack tip zone in stretched crystallizable natural rubber by using infrared thermography and digital image correlation", *Polymer,* vol. 55, no. 24, pp. 6345-6353, 2014.

[65] J. L. F. Freire, R. C. Waugh, R. Fruehmann and J. M. Dulieu-Barton, "Using thermoelastic stress analysis to detect damaged and hot spot areas in structural components", *Journal of Mechanics Engineering and Automation,* vol. 5, pp. 623-634, 2015.

[66] A. K. Wong, “Seeing the invisible: Takeing a look at stresses in aircraft fatigue analysis and testing”, in *27th ICAF Symposium*, Jerusalem, 2013.

[67] J. Rosenholtz and D. Smith, “The effect of compressive stresses on the linear thermal expansion of magnesium and steel”, *Journal of Applied Physics,* vol. 21, pp. 396-399, 1950.

[68] A. R. Rosenfield and B. L. Averbach, “Effect of stress on the expansion coefficient”, *Journal of Applied Physics,* vol. 27, pp. 154-156, 1956.

[69] J. Lord, *Private correspondence,* 2014.

[70] R. Nave, “Law of Dulong and Petit”, Hyperphysics.phy-astr.gsu, [Online]. Available: http://hyperphysics.phy-astr.gsu.edu/hbase/thermo/Dulong.html. [Accessed 20 03 2017].

[71] B. Wuensch, *Shear and Thermal Expansion Tensors - Part 1,* Massachusetts: MIT Open Courseware, 2005.

[72] H. J. Fecht, E. Hellstern, Z. Fu and W. L. Johnson, “Nanocrystalline metals prepared by high-energy ball milling”, *Metallurgical Transactions,* vol. 21, pp. 2333-2337, 1990.

[73] S. K. Bate, R. Charles and A. Warren, “Finite element analysis of a single bead-on-plate specimen using SYSWELD”, *International Journal of Pressure Vessels and Piping,* vol. 86, no. 1, pp. 73-78, 2009.

[74] E. C. Chevallier, “Assessment of welding induced plastic strain using the thermoelastic stress analysis technique [PhD Thesis]”, University of Southampton, Southampton, 2017.

[75] British Stainless Steel Association, “Stress relieving heat treatments for austenitic stainless steels”, British Stainless Steel Association, 2016. [Online]. Available: http://www.bssa.org.uk/topics.php?article=76. [Accessed 11 05 2017].

[76] O. Muransky, C. J. Hamelin, C. I. Patel, V. Luzin and C. Braham, “The influence of constitutive material models on accumilated plastic strain in finite element weld analyses”, *International Journal of Solids and Structures,* Vols. 69-70, pp. 518-530, 2015.

[77] R. C. Tighe, G. P. Howell, J. P. Tyler, S. Lormer and J. M. Dulieu-Barton, “Stress based non-destructive evaluation using thermographic approaches: From laboratory trials to on-site assessment”, *NDT&E International,* vol. 84, pp. 76-88, 2016.

[78] ThyssenKrupp Materials International, “Material data sheet ASTM A53”, 2011.

[79] T. Sakagami, Y. Izumi, N. Mori and S. Kubo, “Development of self-reference lock-in thermography and its application to remote nondestructive inspection of fatigue cracks in steel bridges”, *Quantitative InfraRed Thermography Journal,* vol. 7, no. 1, pp. 73-54, 2010.